

# Toward the Commercialisation of LiNi<sub>0.5</sub>Mn<sub>1.5</sub>O<sub>4</sub> for a Diversified Battery Supply Chain: Revealing Key Properties for Enhanced Performance

Beth Murdock, MChem (Hons)

Department of Chemistry

Lancaster University

A thesis submitted in partial fulfilment of the requirements for the degree of *Doctor of Philosophy* 

September 2024

#### **Abstract**

Lithium-ion batteries (LIBs) have become a vital technology within modern society. With the increasing demand for LIBs, however, comes a drastic increase in demand for the materials inside of them—particularly the cathode material, which is typically high in critical metal content. This PhD thesis aims to advance cathode development toward a more diverse battery supply chain to alleviate supply risk, by providing a deep understanding of their structure-property-performance relationships. Initially, an evaluation of the criticality and sustainability of state-of-the-art and advanced cathode materials was performed to identify a material that could diversify the demand for battery metals. It was found that current NMC materials pose a future supply risk due to high Ni demand. LNMO emerged as a promising candidate with low Co, Li, and Ni content, alongside benefits such as high energy density and good rate performance. However, commercialisation of LNMO is limited by its poor capacity retention.

Subsequent chapters focused on improving LNMO's capacity retention through cationic substitution, where Fe and Mg were chosen as earth-abundant substituents. Structural investigations revealed that Fe and Mg substitution led to an increasing concentration of Lisite defects, with Mg showing a distinct preference for the Li sites. The increased Mn³+ content did not significantly impact rate performance or cycling stability, although high Fe and Mg concentrations led to capacity loss. At elevated temperatures, Mg-substituted LNMO demonstrated improved cycling stability due to the formation of a corrosion-resistant surface layer rich in C–O functionality.

The findings highlight that Mg-substituted LNMO can achieve better capacity retention through the presence of Mg<sub>Li</sub> defects and a stable surface layer. The similarity in structure and morphology of unsubstituted and Fe-substituted LNMO meant that Fe offered little improvement to the electrochemical performance.

#### **Declaration and Statement of Authorship**

I declare that this thesis has not been submitted in support of an application for another degree at this or any other university and that all the work presented is my own, unless otherwise specified with adequate acknowledgement and references.

Chapter 2 includes a reprint of the material as it appears in "Murdock, B.E., Toghill, K.E., and Tapia-Ruiz, N. (2021). A Perspective on the Sustainability of Cathode Materials used in Lithium-ion Batteries. Adv. Energy Mater. *11*, 1–27." This dissertation author was the primary investigator and first author of this paper.

Chapter 4 includes a reprint of the material as it appears in "Murdock, B.E., Cen, J., Squires, A.G., Kavanagh, S.R., Scanlon, D.O., Zhang, L., and Tapia-Ruiz, N. (2024). Li-Site Defects Induce Formation of Li-Rich Impurity Phases: Implications for Charge Distribution and Performance of LiNi<sub>0.5-x</sub>M<sub>x</sub>Mn<sub>1.5</sub>O<sub>4</sub> Cathodes (M = Fe and Mg; x = 0.05-0.2). Adv. Mater. *36*, 2400343." This dissertation author was the primary investigator and first author of this paper. The computational results presented in figures 4.3, 4.5, 4.7 and 4.9 are the work of Dr. Jiayi Cen. Specifically, figures 4.3, 4.5 and 4.9 (in part) have been previously submitted in support of Jiayi's thesis. However, in the context of this thesis, they allow novel insights into the structure of the experimental samples which are unique to this work. Interpretation of these results in this context, as presented as part of Chapter 4, is, therefore, entirely my own. For completeness the computational methods, as published, are provided in Appendix B.

Chapter 5 presents the manuscript "Murdock, B.E., Menon, A.S., Booth, S.G., Fitzpatrick, J., Zhang, L., Piper, L.F.J., Cussen, S.A., and Tapia-Ruiz, N. Surface Stability of High-Voltage Spinel Cathodes Improved Through Mg Substitution Under Accelerated Ageing Conditions. *In Preparation*." which has been submitted for publication. This dissertation author was the primary investigator and first author of this manuscript. Co-authors assisted in collecting HAXPES and sXAS measurements.

### **Table of Contents**

Acknowledgements	vii
List of Figures	viii
List of Tables	xiii
Chapter 1   Introduction	1
1.1 An Age of Energy Storage	1
1.2 How Do Rechargeable Batteries Store Energy?	2
1.3 Battery Degradation	5
1.4 Strategies to Limit Cathode Degradation	7
1.4.1 Surface Coatings	7
1.4.2 Advanced Electrolytes	8
1.4.3 Doping/Substitution	9
1.4.4 Particle Engineering	10
1.5 Material Social Futures	10
1.6 Scope of Thesis	11
1.7 References	12
Chapter 2   Assessing the Sustainability of State-of-the-Art Cathodes	16
Abstract	17
2.1 Introduction	17
2.2 Current Cathode Technology and Material Development	19
2.2.1 Layered Cathode Materials	21
2.2.2 Non-layered Cathode Materials	23
2.3 Mining and Material Management	25
2.3.1 Mining	25
2.3.2 Supply vs Demand	26
2.3.3 Supply risk	32
2.3.4 Environmental, Social and Governance (ESG) Impacts	34
2.3.5 End-of-life and Waste Management	38
2.3.6 Recycling	39

	2.4 Conclusion and Outlook	. 43
	2.5 References	. 44
С	hapter 3   Theory and Experimental Methods	. 52
	3.1 Material Synthesis	. 52
	3.2 Electrochemical Characterisation	. 54
	3.2.1 Electrode Preparation	. 54
	3.2.2 Coin Cell Assembly	. 54
	3.2.3 Galvanostatic Cycling	. 55
	3.2.4 Cyclic Voltammetry	. 56
	3.2.5 Potentiostatic Electrochemical Impedance Spectroscopy	. 58
	3.3 Ex-situ Surface Characterisation	. 61
	3.3.1 X-ray Photoelectron Spectroscopy	. 61
	3.3.2 Soft X-ray Absorption Spectroscopy	. 64
	3.4 Characterisation of Bulk (Micro)structure and Morphology	. 65
	3.4.1 Scanning Electron Microscopy	. 65
	3.4.2 Exploring Crystal Structures Using Bragg Diffraction	. 66
	3.5 Full details for the refinements carried out in this work are provided in Chapte References	
С	hapter 4   Understanding the Structure and Performance of Substituted LNMO Cathode:	
	Abstract	
	4.1 Introduction	. 80
	4.2 Experimental Methods	. 83
	4.2.1 Material Synthesis and Electrochemical Characterisation	
	4.2.2 Powder X-ray and Neutron Diffraction	. 83
	4.2.3 Mn <sup>x+</sup> calculations (Figure 4.8)	. 85
	4.2.4 Estimation of impurity phase fractions from Li deficiencies (Figure 4.13)	. 86
	4.3 How Substitution Alters Site Preference and Defect Concentrations	. 86
	4.3.1 Mg and Fe site Preference in Substituted LNMO Materials	. 86
	4.3.2 Li (8a) Site Defect Response to Increased Substituent Concentration	. 88

4.4 Origin and Possible Charge Compensators for the Presence of Mn³+ ions in S	
4.4.1 Mn <sup>3+</sup> Concentration Increases with Fe/Mg Content	
4.4.2 Ni <sup>3+</sup> Concentration is Present in Substituted Samples and Independent content	•
4.4.3 V₀ are Almost Negligible	95
4.4.4 Off-Stoichiometry Drives an Increase in [Mn³+]	96
4.4.5 Impurity Phases Exacerbate Off-stoichiometry	99
4.5 Influence of Fe and Mg Substitution on Electrochemical Performance	103
4.6 Conclusions	108
4.7 References	109
Chapter 5   Exploring the Surface Stability of Substituted LNMO Cathodes at Temperatures	
Abstract	115
5.1 Introduction	116
5.2 Experimental Methods	118
5.2.1 Material Synthesis and Electrochemical Characterisation	118
5.2.2 Surface Characterisation	119
5.3 Electrochemical Performance	119
5.4 Ex-situ Surface Analysis	125
5.4.1 Hard X-ray Photoelectron Spectroscopy	125
5.4.2 Soft X-ray Absorption Spectroscopy	131
5.5 Contribution of Cell Resistance to Voltage Polarisation	135
5.6 Conclusions	139
5.7 References	140
Chapter 6   Conclusions	144
Chapter 7   Future Work	147
Appendix A   Supporting Experimental Data for Chapter 4	149
Estimated material intensity (kg kWh <sup>-1</sup> )	149
Supporting Figures	150

Supporting Tables	156
Appendix B   Supporting Computational Methods and Data for Chapter 4	159
Computational Methods	159
Supporting Figures and Tables	160
Supporting references	161
Appendix C   Supporting Experimental Data for Chapter 5	164
Consolidated List of References	166

#### Acknowledgements

First and foremost, I would like to express my deepest gratitude to my supervisors, Dr Nuria Tapia-Ruiz and Prof. Kathryn Toghill, for their guidance and support throughout my PhD journey, as well as the directors of the Materials Social Futures CDT program—Prof. Rob Short and Prof. Richard Harper—for creating and running a program which nurtured a broadened research perspective.

The work in this thesis was primarily conducted at the Lancaster University Chemistry Department, funded by the Leverhulme Trust. Key data presented throughout the thesis was collected at the Diamond Light Source and ISIS national facilities. This work was also supported by the Faraday Institutions FutureCat project and, in the later stages, research was conducted at the Molecular Sciences Research Hub at Imperial College London. A huge thank you to all the institutions involved and the people who are so vital to their operation.

A special mention goes to all my colleagues, friends and collaborators in the Tapia-Ruiz group, the Toghill group, the MSF cohort and across the Faraday Institution whose camaraderie and collaboration made the research process enjoyable and fulfilling. I am particularly grateful to Sarah McKinney, Alexandra Michial, Jack Fitzpatrick and Dr Li Zhang from the Tapia-Ruiz group for their advice and moral support, as well as Hannah Lynn for cheering me on through the final stages of my PhD and being the greatest friend a girl could ask for. I would like to express my sincere gratitude to all the collaborators of the work presented, particularly Dr Jiayi Cen, for your computational contributions, and Dr Ashok Menon, for assisting with the spectroscopic data collection and processing.

Finally, to my friends and family—thank you for your encouragement. To my sister, Hannah, thank you for always being there and making the impossible feel a little more possible.

### **List of Figures**

Figure 1.1: Battery schematic showing the flow of Li <sup>+</sup> ions (purple) and electrons (orange during the charging process
Figure 2.1: a) Schematic of a LIB, showing the movement of electrons and Li <sup>+</sup> ions (green during charge (purple) and discharge (orange) processes. Crystal structures of various cathode chemistries are indicated: i) layered structure, where teal octahedra represent M (Ne Ni, Mn, Co for NMC and M = Ni, Co, Al for NCA), ii) spinel structure, where purple octahedra represent M (M = Mn for LMO and M = Ni, Mn for LNMO), iii) olivine structure, in which M = Fe for LFP, and iv) disordered rock salt structure, where cation mixing of M(d <sup>0</sup> ) (grey) and L (green) between the layers is observed (M = Fe, Mn, Ti). b) Typical mass and cost breakdown of an NMC battery pack, where CAM = cathode active material, AAM = anode active material NCC = negative current collector and PCC = positive current collector. Charts produced with data from reference 15
Figure 2.2: a) Estimated cell material cost based on production capacity of 1 GWh, data reproduced from $^{24}$ , b) selected electrochemical performance parameters (volumetric and gravimetric energy) from full cells with graphite (Gr) as anode and a variety of LIB cathodes such as NMC111, 442, 532, 622 and 811, LR-NMC (Li-rich NMC), NCA, LMO, LNMO and LFP. Reproduced with permission from $^{24}$ , and c) Cost breakdown of an NMC811 prismatic cell produced in China considering costs related to mining and refining, production of Cathode Active Material (CAM), production of other cell components and cell manufacturing (SG&A selling and general & administrative expenses, FG&A = factors that account for general & administrative expense, Li <sub>2</sub> O = Li spodumene concentrate 6%, $^{1}$ = mark up of $\approx$ 6.3% to account for efficiency losses between theoretical vs nominal voltage.) Adapted with permission from $^{25}$
Figure 2.3: Schematic highlighting the considerations required for supply (purple, top) and demand (orange, bottom) modelling. Turquoise arrows indicate factors that influence the outcome of projections. Differences in factors chosen for modelling can result in significant differences in projected supply and demand.
Figure 2.4: Predicted changes in battery and non-battery demand of Ni, Li, and Co. Figures produced using data from references 12 and 24. LCE = lithium carbonate equivalents 29. Figure 2.5: a) Price fluctuations of Co and Ni from 2016-2021 (USD/T). b) Price fluctuations of Li <sub>2</sub> CO <sub>3</sub> traded in China, from 2017-2021 (CNY/T). Data from collected from references [77]

the scores for the seven dimensions (first seven columns), in which environmental risk is comprised of waste, water and conservation and social risk is comprised of communities, land uses and social vulnerability. b) The breakdown of total risk scores by resource tonnage Colours respond to risk level, with red showing higher risk and blue showing lower risk Reproduced with permission from <sup>86</sup>
<b>Figure 2.7:</b> a) Schematic illustrating the closed-loop approach to LIB EOL through recycle and reuse. Reproduced with permission from <sup>95</sup> (copyright Wiley Materials), b) Breakdown or recycling cost for a 240 Wh kg <sup>-1</sup> NCA battery pack, reproduced with permission from <sup>114</sup> 4
Figure 3.1: Comparison of a) a full-cell and b) a cathode half-cell coin-cell setup5
<b>Figure 3.2</b> : a) Schematic illustrating features typically observed in a Nyquist plot, highlighting that the ideality of capacitance influences the shape of the semi-circle. Here, the solid, black semicircles indicate ideal capacitance $C$ , as shown in the equivalent circuit model (b). The grey, dashed semi-circles, on the other hand, indicate non-ideal capacitance ( $Q \approx C^{n<1}$ ) and are depressed in comparison. The impedance response can instead be modelled by the equivalent circuit model (c); d) schematic illustrating the three-electrode PAT cell in which working electrode (WE), and counter electrode (CE) are compressed either side of a polypropylene (PP) insulation sleeve which houses the glass fibre separator and ring reference electrode (RE)
Figure 3.3: Simplified schematic illustrating the fundamental electron excitation and decaprocesses that govern a) X-ray photoelectron spectroscopy, b) X-ray absorption in c) total fluorescence yield (TFY) mode and d) total electron yield (TEY) mode, as described in detain Sections 3.3.1–3.3.2. For each technique, the value that is measured is provided in brackets.
<b>Figure 3.4:</b> a) Unit cell with lengths $(a, b, c)$ and angles $(\alpha, \beta, \gamma)$ . Exemplar atoms in place with fractional coordinates x, y, z = 1, 0, 0 and $\frac{1}{4}$ , 0, $\frac{1}{2}$ . b) schematic highlighting lattice plane within the crystal lattice (grey dots), with Miller indices $(hkl) = (010)$ and $(120)$ and d-spacing of $d_{010}$ and $d_{120}$ , respectively.
Figure 3.5: Schematic representation of diffraction, used to derive Bragg's law 6
<b>Figure 4.1:</b> Comparing the intensity of different elements/materials (kg kWh <sup>-1</sup> ) of LNMO to state-of-the-art NMC cathodes at the material level (i.e., this calculation does not consider the weight of inactive cell components. Material intensity at the cell level will be greater). See Appendix A for calculation details

<b>Figure 4.2:</b> LNMO crystal structures: a) disordered ( <i>Fd3m</i> ); and b) ordered ( <i>P4</i> <sub>3</sub> 32) LNMO.
<b>Figure 4.3:</b> The distribution of formation energies of intrinsic ( $Ni_{Li}$ and $Mn_{Li}$ ) and extrinsic defects ( $M_i$ , $M_{Li}$ , $M_{Mn}$ , $M_{Ni}$ ) for $M = Mg$ (a) and Fe (b) over all growth conditions (chemical potentials), see Computational Methods in SI for details. Results and figure provided by Dr J. Cen.
<b>Figure 4.4:</b> Changes in 8a site occupancy for samples LNMO, Fe $x$ and Mg $x$ ( $x$ = 0.1 and 0.2) in different Li-site defect scenarios: (a) no defect; (b) Ni <sub>Li</sub> defect; and (c) M <sub>Li</sub> defect (M = Mg or Fe). Li-deficiencies (1-f <sub>Li(8a)</sub> ) are indicated as percentages
<b>Figure 4.5, DFT calculated Li deficiencies:</b> Calculated total concentration of $X_{Li}$ defects, consisting of contributions from $V_{Li}$ , $Mn_{Li}$ , $Ni_{Li}$ and $M_{Li}$ defects as a function of increasing concentration of extrinsic defect species $Mg_{Ni}$ (a) and $Mg_{Li}$ (b) in $Mg$ -doped system ( $M = Mg$ ) and defect species $Fe_{Ni}$ (c) and $Fe_{Mn}$ (d) in $Fe$ -doped system ( $M = Fe$ ), respectively. Results and figure provided by $Prover$ $Prove$ $Prover$ $Prover$ $Prover$ $Prove$ $Pro$
<b>Figure 4.6, Mn</b> <sup>3+</sup> <b>concentration increases with Fe/Mg content:</b> First-cycle voltage profiles of spinel/Li half cells (1C, 3.5–4.9 V) for a) Mg $x$ and b) Fe $x$ ( $x$ = 0–0.2), where the capacity below 4.375 V as shown in (c) is used to derive the specific charge capacity related to Mn <sup>3+</sup> (4 V region) in Mg $x$ and Fe $x$ samples, where error bars represent deviation between cells ( $n$ = 3) d); and the corresponding changes in the lattice parameter, $a$ , as a function of substituent concentration for samples Mg $x$ , Fe $x$ e). The lattice parameter, $a$ , was determined either through combined ND-XRD Rietveld refinement (filled symbol; $x$ = 0, 0.1, and 0.2) or Le Bail refinement against XRD data (hollow symbol; $x$ = 0.05 and 0.15)
<b>Figure 4.7, DFT calculated Ni<sup>3+</sup>:</b> Calculated [Mn <sup>3+</sup> ] and [Ni <sup>3+</sup> ] in response to increased substituent concentration through tuning the concentration of extrinsic defect species Mg <sub>Ni</sub> (a) and Mg <sub>Li</sub> (b) in Mg-doped system and defect species Fe <sub>Ni</sub> (c) and Fe <sub>Mn</sub> (d) in Fe-doped systems, respectively. Results and figure provided by Dr J. Cen
<b>Figure 4.8:</b> Estimated Mn <sup>x+</sup> oxidation state from the 4 V specific charge capacity region in the galvanostatic data (OCV–4.375 V, Echem data) and Rietveld refinements (Li-site defects: None, $M_{Li}$ and $Ni_{Li}$ ) both with (hollow) and without (filled) oxygen vacancies ( $V_o$ ). The comparison between structural refinements and electrochemical data suggests that $V_o$ are overestimated within the refinement, resulting in overestimated Mn <sup>3+</sup> concentrations. Due to such anticipated overestimation, refinements with $V_o$ are discounted. Refinements in which $Mn^{x+} > Mn^{4+}$ are also discounted as they result from large, refined Li deficiencies (Figure 4.4).

<b>Figure 4.9, DFT calculated Ni deficiency</b> : Calculated total concentration of $X_{Ni}$ defect decomposed into contributions from $V_{Ni}$ , $Mn_{Ni}$ and $Li_{Ni}$ defects as a function of increasing concentration of extrinsic defect species $Mg_{Ni}$ (a) and $Mg_{Li}$ (b) in $Mg$ -doped system ( $M = Mg$ and defect species $Fe_{Ni}$ (c) and $Fe_{Mn}$ (d) in $Fe$ -doped system ( $M = Fe$ ), respectively. Result and figure provided by $Dr J$ . Cen
<b>Figure 4.10, Charge surplus</b> : % charge surplus from the expected +8 cation charge require to balance oxygen in full occupancy, as calculated from refined stoichiometries in scenario that consider Ni <sub>Li</sub> and M <sub>Li</sub> (M = Mg and Fe).
<b>Figure 4.11, Identification of impurity phases:</b> a) XRD and c) ND-TOF patterns of as synthesised LNMO and calculated patterns of typical Ni-rich impurity phases: Ni <sub>6</sub> MnO <sub>8</sub> (ICS #41890) and Li <sub>x</sub> Ni <sub>1-x</sub> O (ICSD #40584). The location of impurity peaks present in LNMO as highlighted by yellow asterisks; b) XRD and d) ND-TOF patterns of Mg0.2 synthesised here and calculated patterns of Li <sub>2</sub> MO <sub>3</sub> -type impurity phases: Li <sub>2</sub> MnO <sub>3</sub> (ICSD #132578), Li <sub>2</sub> NiO (ICSD #29337) and Li <sub>2</sub> Ni <sub>0.25</sub> Mn <sub>0.75</sub> O <sub>3</sub> (ICSD #252826). Li <sub>2</sub> MO <sub>3</sub> impurity peaks present in Mg0. are highlighted by green arrows. XRD patterns of c) Fex and d) Mgx, where $x = 0.05-0.3$ Insets show selected 2θ range in which impurity peaks are observed, indicated by yellow asterisks (Ni <sub>6</sub> MnO <sub>8</sub> ) or green arrows (Li <sub>2</sub> MO <sub>3</sub> , M = Ni or Mn)
<b>Figure 4.12:</b> First-cycle cyclic voltammograms of a) Mg $x$ and b) Fe $x$ ( $x = 0.05$ –0.2) collected in spinel/Li half-cells, using a voltage window of 3.5–5 V and a sweep rate of 0.1 mV s <sup>-1</sup> . Note that a higher cut-off voltage was used in these measurements compared to the galvanostate cycling data shown in the manuscript to identify the Fe <sup>3+/4+</sup> redox reaction and thus, illustrate the successful incorporation of Fe in the spinel substituted samples (b)
Figure 4.13, Estimated impurity phase fraction from refined Li deficiencies: Impurity phase fraction of Li <sub>2</sub> MO <sub>3</sub> in Fe0.1, Fe0.2*, Mg0.1 and Mg0.2, as determined through combined Rietveld refinements (refined), and as estimated from refined Li deficiencies in refinement that consider sole-Li 8a site occupancy (None), Ni <sub>Li</sub> and M <sub>Li</sub> site defects (M = Fe and Mg). * 0.5 wt.% impurity is assumed for Fe0.2 as it is present in the XRD data but not in the NP data. In the XRD pattern, the amount is too small to refine yet data collection on moder detectors, under conditions to provide a good signal-to-noise ratio allows detection of impurity phases as low as 0.5–1 wt.%. <sup>52</sup>
<b>Figure 4.14, Electrochemical performance:</b> Capacity retention of a) Mg $x$ and b) Fe $x$ ( $x$ = 0.2) (1C, 3.5–4.9 V, 28°C); c) Average capacity retention after 300 cycles ( $n$ = 3); and capacity retention at different rates for Fe $x$ and Mg $x$ from waterfall plots shown in Figure A (Appendix A)

<b>Figure 5.1</b> : Long-term cycling performance of spinel/Li half-cells at 50 °C (1C, 3.5–4.9 V): a) cycling stability and b) corresponding coulombic efficiency values of LNMO (grey), Mg0.05 (orange) and Fe0.05 (blue) over 300 cycles; and c) average cycle-to-cycle variations (n > 3) in capacity retention ( $CR = (Cn + 1Cn) \times 100$ ), with insets highlighting the different rates of degradation from cycles 1–50 and 200–300.
<b>Figure 5.2:</b> Voltage profiles of the 1 <sup>st</sup> (solid) and 300 <sup>th</sup> cycle (dashed) for a) LNMO, b) Fe0.05 and c) Mg0.05, obtained at 50 °C (1C, 3.5–4.9 V; dQ/dV vs. V plots corresponding to cycles 1 and 300 for d) LNMO, e) Fe0.05 and f) Mg0.05); enlarged dQ/dV vs. V, in the 4 V region mapping, the evolution of Mn <sup>3+/4+</sup> -related capacity from cycles 1–300 for g) LNMO, h) Fe0.05 and i) Mg0.05, where increases/decreases in intensity are indicated by red/yellow arrows respectively.
Figure 5.3: a) C1s, b) O1s and c) F1s HAXPES spectra of C/PVDF-P, LNMO-P, Fe0.05-P and Mg0.05-P
<b>Figure 5.4:</b> C1s, O1s and F1s HAXPES spectra, collected using an incident X-ray energy of 2.2 keV, for a) LNMO, b) Fe0.05 and c) Mg0.05 at various points of cycling as well as d) C/PVDF at OCV (50°C, 1C, 3.5–4.9 V). Electrodes for <i>ex-situ</i> characterisation were extracted before cycling (OCV) and at the end of cycles 1, 150 and 300. Spectra are area normalised to aid with the visualisation of relative intensity changes.
<b>Figure 5.5:</b> Ni <i>L</i> -edge (a-c) and Mn <i>L</i> -edge (d-f) sXAS-TEY spectra of <i>ex-situ</i> LNMO (grey; a, d, h), Fe0.05 (blue; b, e, i) and Mg0.05 (orange; c, f j) electrodes at various points of cycling (50°C, 1C, 3.5–4.9 V): before cycling (OCV); and after cycles 1, 150 and 300. The intensity normalised Mn <i>L</i> -edge h) LNMO, i) Fe0.05 and j) Mg0.05 highlight changes in relative intensity
<b>Figure 5.6</b> : O <i>K</i> -edge sXAS-TEY spectra of <i>ex-situ</i> LNMO (grey), Fe0.05 (blue) and Mg0.05 (orange) electrodes at various stages of cycling (50°C, 1C, 3.5–4.9 V): before cycling (OCV), and after cycles 1, 150 and 300.
<b>Figure 5.7:</b> Exemplar Nyquist plot highlighting $R_{sol}$ , $R_{Contact}$ and $R_{cathode}$ under blocking (4.9 V) and non-blocking conditions (4.4 V), where the high-frequency semi-circle ( $R_{contact}$ ) is independent of state of charge, whereas the mid-frequency semi-circle ( $R_{cathode}$ ) is dependent on state of charge.
<b>Figure 5.8:</b> Evolution of resistances in spinel/Li/Li 3-electrode half cells (50°C, 1C, 3.5–4.9 V) from EIS collected at 4.4 V (discharge) for a) LNMO using the detailed program, b) LNMO using the simplified program and c) a comparison of LNMO and Mg0 05 using the simplified

program, where the evolution of EIS spectra can be found in Appendix C, Figure C3. The
detailed program involves measuring EIS at 4.9 V and at 4.4 V (discharge) for every cycle,
while the simplified program involves measuring EIS at 4.4 V, only for selected cycles. While
the detailed program collects multiple datasets per cycle, only data which corresponds to those
collected in the simplified program are presented in (b). EIS fitting was performed using the
equivalent circuit model (d)
List of Tables
Table 3.1: List of samples and abbreviations.    53
<b>Table 3.2:</b> Peak assignments for HAXPES fittings in accordance with references [ <sup>28–30</sup> ] 64
<b>Table 3.3:</b> The seven crystal systems and their corresponding d <sub>nkl</sub> expressions <sup>39</sup>
<b>Table 3.4:</b> Coherent neutron scattering lengths of elements relevant to this thesis. 43 70
Table 4.1: Summary of X-ray and neutron diffraction data collected for each sample
Table 4.2: Polovant data comparison of LNMO performance reported in the literature 105

#### **Chapter 1 | Introduction**

#### 1.1 An Age of Energy Storage

The rapidly changing climate is fast approaching a point of crisis. Despite targets set out in the 2015 Paris Agreement "to limit the temperature increase to  $1.5^{\circ}$ C above pre-industrial levels",  $CO_2$  emissions continue to climb, with record highs once again reported in 2023 (35.8  $\pm$  0.3 Gt).<sup>1,2</sup> Energy-related emissions play an immense role in the rise in  $CO_2$ , due to the global reliance on fossil fuels as the principal energy source.<sup>2</sup> The largest sources of energy-related emissions are electric power and transportation. The strong dependence between economic growth and increased consumption, however, makes reducing consumption particularly challenging.<sup>3</sup> The challenge then becomes providing large amounts of energy with negligible  $CO_2$  emissions, by decarbonising the grid and decarbonising transportation, thus ending our reliance on fossil fuels.

Renewable energy acts as an alternative, low-to-no emissions energy source, which, unlike fossil fuels, comes from renewable sources such as wind and solar energy. These energy sources, however, are intermittent and the energy they generate must be stored to allow access to energy during times of insignificant energy generation. Energy storage devices will, therefore, be instrumental in providing low-carbon energy through renewable sources.4 Amongst these energy storage devices is the rechargeable battery—a device that stores chemical energy and converts it into electrical energy. Their rechargeable nature means that they can be charged (to store the energy) and discharged (to release the energy) many times over their lifetime. As a result, rechargeable batteries will not only be instrumental in decarbonising the grid, but they have already begun to infiltrate almost every aspect of daily life from transportation (electric vehicles, E-bikes) to entertainment (smartphones, laptops), health (smart watches, electric toothbrushes, hearing aids) and construction (cordless power tools). Each application, however, has different battery performance requirements necessitating the careful design/selection of both the battery technology and the battery materials to ensure optimal performance under specific operating conditions. Such selection requires a comprehensive understanding of how rechargeable batteries store energy and the unique properties of the materials inside of them.

#### 1.2 How Do Rechargeable Batteries Store Energy?

Rechargeable batteries store energy by harnessing the reversible redox reactions that take place at their electrodes upon charge and discharge. Perhaps the most ubiquitous rechargeable battery is the lithium-ion battery (LIB). First commercialised by Sony in 1991, LIBs were historically based on a separator soaked in carbonate-based electrolyte sandwiched between a  $LiCoO_2$  cathode (positive electrode) and a graphite anode (negative electrode, **Figure 1**).<sup>5</sup> This setup works by harnessing the difference in stability provided when lithium (Li) is intercalated into the cathode vs the anode. When intercalated into  $LiCoO_2$ ,  $Li^+$  ions occupy specific sites within the crystal structure where  $Li^+$  is coordinated within the oxide framework, thus providing a low-energy state for the  $Li^+$  ions. In contrast, when intercalated into the graphitic layers, the interaction between the  $Li^+$  ions and the graphite host is relatively weak.<sup>6</sup> Therefore, the structure of the cathode provides a more thermodynamically stable environment for the  $Li^+$  ions. As a result, a higher electrochemical potential is required to extract Li from the cathode ( $\mu_C$ ), creating a potential difference between the two electrodes ( $E_{cell}$ , Equation 1.1, where e is the elemental charge of an electron).<sup>7</sup>

$$E_{cell} = \frac{\mu_A - \mu_C}{e} \tag{1.1}$$

During charge, an external power source applies energy to the battery, forcing the Li<sup>+</sup> ions to transport through the electrolyte from their low-energy state in the cathode to a higher-energy state in the anode. As Li<sup>+</sup> ions leave the LiCoO<sub>2</sub> structure, Co<sup>3+</sup> oxidises to Co<sup>4+</sup> to maintain electroneutrality.<sup>5</sup> The lost electrons then move from the cathode to the anode through the external circuit, and the anode becomes reduced. To drive this non-spontaneous reaction, the applied potential must be greater than E<sub>cell</sub>. The energy is then stored as chemical potential energy in the battery. During discharge, the opposite is true; powering an external device causes the anode to oxidise, allowing Li<sup>+</sup> ions to transport back to the cathode, which reduces back to LiCoO<sub>2</sub>. Here, LiCoO<sub>2</sub> and graphite are examples of intercalation materials. Today, several intercalation cathode and anode materials exist—most commonly a Li transition metal (TM) oxide cathode paired with a graphite anode—but the working principle remains the same.

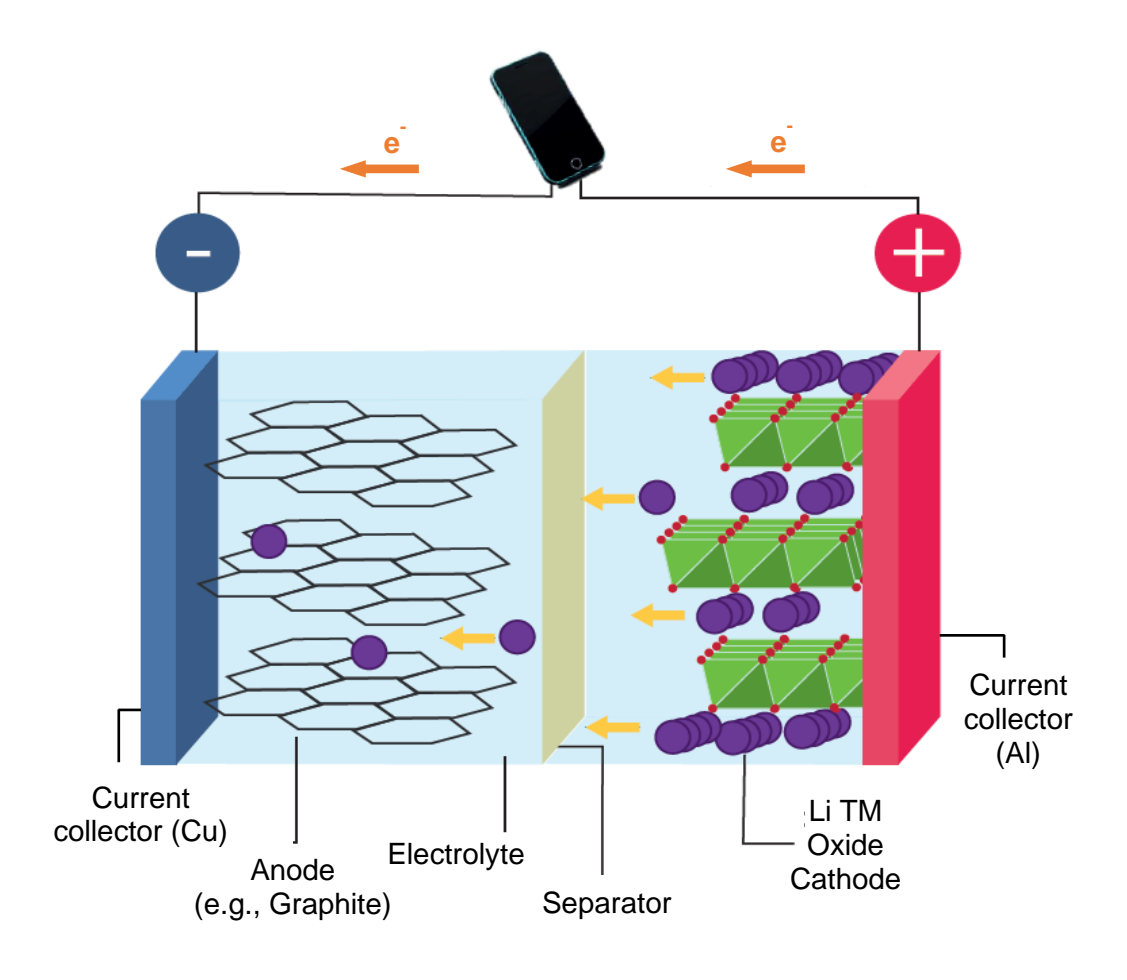


**Figure 1.1:** Battery schematic showing the flow of Li<sup>+</sup> ions (purple) and electrons (orange) during the charging process.

Different intercalation materials can store different amounts of energy, where energy is a product of capacity (Q) and potential difference (V).<sup>7</sup> The amount of energy a battery can store is often expressed in terms of gravimetric or volumetric energy density. The gravimetric energy density (i.e., the amount of energy stored per kg, Wh kg<sup>-1</sup>, Equation 1.2) is more important for applications that require low weights, whereas volumetric energy density (i.e., the amount of energy stored per L, Wh L<sup>-1</sup>, Equation 1.3) is more important for applications where space is limited.<sup>7</sup> For example, electric vehicles are not only limited by the size of the vehicle but also by the weight, since more energy is required to move objects i) that are heavier and ii) by further distances. Both high volumetric and gravimetric energy densities are, therefore, required. Stationary storage applications, on the other hand, are less restricted in space, meaning that gravimetric capacity becomes more important. Improvements in energy density can be offered by i) increasing capacity (Q), ii) increasing the average operating potential (V), or iii) decreasing mass (m)/volume (Vol).

$$ED_g = \frac{Q \cdot V}{m} \tag{1.2}$$

$$ED_{Vol} = \frac{Q \cdot V}{Vol} \tag{1.3}$$

$$Q_g = \frac{n \cdot F}{M_{w}} \tag{1.4}$$

$$Q_{Vol} = Q_g \cdot \rho \tag{1.5}$$

A materials theoretical gravimetric (Equation 1.4) and volumetric capacity (Equation 1.5) describes the amount of charge it can store per unit mass/volume, where *n* is the number of electrons transferred per formula unit, *F* is the Faraday constant, M<sub>w</sub> is the molecular weight and ρ is the density. The theoretical capacity is therefore related to i) the mass/volume of the constituent elements, ii) the amount of Li that can be stored in the host structure and iii) the capability of the host to change valence state to accommodate for changes in Li content.<sup>6</sup> Anodes typically have higher theoretical capacity than cathodes since they can store more Li<sup>+</sup>.<sup>6</sup> The cathode is, therefore, the limiting factor for cell energy density, and its structure and composition can have a significant influence on performance. Practical specific capacity is typically lower than theoretically predicted and can be limited by the reversibility of intercalation, the rate of Li<sup>+</sup> ion diffusion, and the rate of charge transfer.<sup>7</sup> As such, the practical capacity is highly correlated to the rate at which the cell is charged/discharged. To maximise practical capacity, the rate of Li<sup>+</sup> ion diffusion/charge transfer must be faster than the rate of charge/discharge. As such, good reversibility alongside fast diffusion and charge-transfer kinetics can allow for high practical capacity, even at fast charge/discharge rates.<sup>7</sup>

Charging/discharging rates are usually described by their C-rate, which is inversely proportional to the time of charge/discharge. As such, charging at a C-rate of 1C means that the battery fully charges within 1 hour. Higher C-rates mean faster charging and lower C-rates mean slower charging. When related to the EV use case, fast charging ( $\geq$  2C) is required for 'on-the-go' charging, at services for example, whereas slow, overnight charging (0.1C) can be achieved in residential areas.<sup>8</sup> Fast discharge can be related to fast acceleration ( $\geq$  1C) and slow discharge to more steady driving (0.5–0.2C).<sup>8</sup> Power tools, on the other hand, require much faster charge (2C) and discharge rates (5–15C).<sup>9</sup> In an ideal world, a battery would be able to perform at high C-rates all the time. However, not only does this decrease the lifetime

of the cell but can lead to potentially dangerous dendrite formation and cell failure (see Section 1.3).<sup>10</sup>

Practical capacity can also depend on the operating potential window, which is typically selected to encapsulate the potentials at which the redox reactions occur, without inducing degradation that can be caused by excessively high/low voltages (e.g., electrolyte oxidation/Li plating, see Section 1.3). For example, limiting the upper-cut-off voltage to improve capacity retention can prevent full oxidation of the cathode structure, thus lowering practical capacity. The potentials at which redox reactions take place are specific to each material and are determined by i) the energy required to extract Li<sup>+</sup> ions from a given site in the host structure, where lower site energy leads to higher potentials, and ii) the energy required for redox reactions to occur in the host material.<sup>6</sup> To maximise cell voltage and subsequent cell energy density, it is desirable to match a high-voltage cathode with a low-voltage anode.

While high capacities and cell voltages are desirable for maximising energy density, it is important to be able to maintain high energy density over many charge/discharge cycles (i.e., have a long cycle life). Another important battery metric is therefore capacity retention, where industry standards require that 80% of initial capacity be retained after 500 cycles. <sup>11</sup> Unfortunately, high energy density cathodes typically come at the expense of cycle life, where a plethora of battery degradation mechanisms contribute to decay in both reversible capacity and voltage.

#### 1.3 Battery Degradation

Battery degradation is a complex phenomenon that describes the chemical and physical changes that occur in the cell during operation and storage. Despite the success of LIBs, almost every component of the battery can experience degradation. However, all battery degradation can be broadly categorized into 4 degradation modes; loss of Li inventory (LLI), loss of active cathode/anode material (LAM), loss of electrolyte (LE), and increase in resistance (RI).<sup>12</sup>

LLI refers to the loss of cyclable Li that arises because of side reactions that occur at the cathode/anode. One such example is Li plating, which describes the metallic Li that deposits on the anode surface as opposed to intercalating into the material. Li plating is most severe under fast-charging conditions, and not only consumes active Li but poses a safety concern since the subsequent formation of Li dendrites can penetrate through the separator, ultimately leading to an internal short circuit.<sup>10</sup>

The formation of interphases at the cathode/anode also contributes to LLI. Interphases on the respective electrodes form when the electrode potentials are beyond the electrolyte stability

window (ESW), where the ESW is the potential range in which the electrolyte can operate without being oxidised (upper-voltage limit) or reduced (lower-voltage limit).¹³ Graphite—the most commonly used anode in LIBs—operates at a potential (≈ 0.1 V) which is lower than the ESW of commercial electrolytes (1–4.2 V).¹ These commercial electrolytes are typically composed of a LiPF<sub>6</sub> salt dissolved into a mixture of cyclic and linear carbonates, such as ethylene carbonate (EC) and dimethyl or ethyl methyl carbonate (DMC, EMC). As the electrolyte becomes reduced on the anode, it forms a series of organic and inorganic species at the surface.¹³ This surface layer is known as the solid electrolyte interphase (SEI) and its formation consumes electrolyte during the initial cycle.¹³ The formation of a stable SEI layer can prevent further electrolyte reduction while facilitating the transport of Li⁺ ions. However, other degradation mechanisms, such as particle cracking that occurs due to volume expansions in the host material, can open fresh surfaces allowing for continued electrolyte reduction.¹²

A similar phenomenon occurs at the cathode, where operating at a high voltage can lead to electrochemical electrolyte oxidation at the cathode surface and the formation of what is known as the cathode electrolyte interphase (CEI).<sup>14</sup> When at the cathode, however, the electrolyte can undergo both chemical and electrochemical oxidation. Chemical oxidation can occur when structural instability in the cathode leads to O<sub>2</sub> release which subsequently reacts with the electrolyte.<sup>15</sup> Similarly to the SEI, the formation of a stable CEI can prevent further oxidation. The CEI, however, can be unstable at high operating voltages due to corrosion by acidic species that form as a by-product of electrolyte degradation (e.g., HF).<sup>16</sup> Significant build-up of the CEI can impede Li<sup>+</sup> ion transport to the cathode, contributing to increases in cell resistance.<sup>14</sup>

HF formed as a by-product of electrolyte degradation has several negative effects on the performance of the cell. Firstly, HF can corrode the Al current collector on the cathode side. As a result of corrosion, the cathode material loses electrical and mechanical contact with the current collector, contributing to increases in the cell resistance.<sup>17</sup> HF can also attack the cathode itself, leading to surface etching and facilitating the dissolution of TMs (e.g., Mn<sup>2+</sup>, Ni<sup>2+</sup>, Co<sup>2+</sup>). Dissolved TMs contribute to LAM and can either react with electrolyte and deposit on the cathode, as TMF<sub>2</sub> for example, or they can migrate towards the anode, interfering with the anode surface chemistry.<sup>18</sup> Mn<sup>2+</sup> is particularly problematic for the stability of the SEI, opening up the anode surface to further degradation.<sup>19</sup> TM dissolution can, therefore, indirectly contribute to LLI.

Structural degradation at the cathode also contributes to battery degradation and refers to the physical changes and damage that occur in the electrode materials during cycling. For

example, phase transitions that occur upon cycling can lead to mechanical stress and the formation of microcracks within the cathode particles.<sup>20</sup> The mechanical degradation not only compromises the structural integrity of the cathode but also exposes fresh surfaces to the electrolyte, which can result in continuous electrolyte decomposition and the formation of resistive interphases.<sup>20</sup> Repeated phase transitions can cause a breakdown of the cathode's electronic and ionic pathways, leading to increased internal resistance and diminished capacity.<sup>20</sup> In addition to changes in the bulk phase, the surface can experience surface reconstruction as TM ions migrate into vacant sites in the cathode structure. This not only alters the electronic/ionic pathways but can also facilitate TM dissolution from the cathode surface.<sup>21</sup>

The extent to which these degradation processes occur is largely dependent on the materials chosen. However, they can also be influenced by external factors such as C-rate, state of charge (SoC) and temperature.<sup>12</sup> Therefore, to limit degradation, it is often important to understand how a specific material responds to a range of external conditions.

#### 1.4 Strategies to Limit Cathode Degradation

Degradation at the cathode can be mitigated using a variety of strategies. Those most investigated throughout the literature include surface coatings, advanced electrolytes, substitution/doping, and particle engineering—all of which will be briefly summarised.

#### 1.4.1 Surface Coatings

Surface coatings act as a physical barrier to unwanted surface reactions that occur between the cathode and the electrolyte, while also preventing the dissolution of active metals. They should be both ionically and electronically conducting to allow Li<sup>+</sup>-ion diffusion and electron migration during cycling.<sup>22</sup> The success of each coating is highly dependent on the cathode morphology, the coating technique and composition. However, common coating materials investigated included metal oxide coating, ionically conductive coatings, hybrid coatings and polymer coatings.

Many oxide-based coatings, such as  $Al_2O_3$ , ZnO, and  $SnO_2$ , are amphoteric, meaning that they can react with both acids and bases.<sup>22</sup> They can therefore react beneficially with a wide range of chemical species in the electrolyte and are particularly useful for their ability to scavenge HF.<sup>22</sup> This can protect the cathode material from HF surface-etching, and dissolution of active metals. The metal within the coating is typically inactive and so does not take part in the electrochemical reactions. However, the coatings typically possess low ionic conductivities which can decrease capacity, particularly at higher C-rates.<sup>22</sup> In contrast, good ionic conductors, such as (e.g.,  $Li_3PO_4$ ,  $Li_4P_2O_7$ , and  $Li_2SiO_3$ ), are also investigated as surface

coatings and can allow high performance, even at high C-rates.<sup>23–25</sup> These surface coatings, however, typically have poor electronic conductivities. Hybrid coatings—which typically combine a metal oxide coating with an ionically conductive coating—are therefore being investigated to combine the benefits offered by both components.<sup>26</sup> Being able to produce a homogenous coating which is thin enough so as not to inhibit ion transport can be challenging. For this reason, conducting polymer coatings can be beneficial. Due to their flexible nature, they can also accommodate volume changes that occur as Li<sup>+</sup> ions are de/inserted into the material.<sup>26</sup>

#### 1.4.2 Advanced Electrolytes

High-voltage electrolytes with improved anodic stability are being developed to avoid degradation of the electrolyte at high operating voltages. Amongst the electrolytes considered are sulfones, phosphates, fluorinated carbonates as well as ionic liquids and concentrated electrolytes.<sup>27–38</sup> Despite their high anodic stability, sulfones suffer from high viscosities, resulting in low ionic conductivities, and require complex synthesis thus inflating costs. Phosphates, on the other hand, display inferior solubility of many Li-based salts.<sup>27</sup> Another issue often presented by such high-stability electrolyte alternatives is their inability to form sufficient CEI layers, in which electrolyte additives are often required.<sup>27</sup> In order to satisfy all that is required of an electrolyte, solvent mixtures are often considered to present the advantages of each.<sup>28</sup>

Concentrated electrolytes are gaining particular attention due to their unique solvation chemistry in which anion molecules take precedence over solvent molecules. This allows greater flexibility in choosing solvents, opening possibilities for solvents previously disregarded and creating diversity in potential designs.<sup>39,40</sup> In addition to wide operating voltage windows (> 5 V), they show an enhanced ability to suppress both side reactions and the corrosion of the Al current collector, caused by high proton concentrations generated as the electrolyte rapidly oxidises at high potentials.<sup>39,40</sup> The use of high salt concentrations, however, results in inherently high costs and viscosities. The introduction of an 'inert' solvent—with low viscosity, volatility and cost (e.g., hexafluoroisopropyl methyl ether, HFME)—provides a potential solution whereby the electrolyte mobility is enhanced whilst maintaining a 'concentrated' solvation structure.<sup>37</sup> Lower salt concentrations can, therefore, be used to provide the same advantages of high operating voltages and rate capability. This approach is known as 'dilution of concentrated electrolytes' or 'pseudo-concentration'.

Additives can also be added to the electrolyte to alleviate degradation. These additives are typically small amounts of compounds incorporated into the electrolyte to form protective films on electrode surfaces, suppress unwanted side reactions, and improve overall battery life. For

example, additives like Li bis(oxalato)borate (LiBOB) can form protective layers on the cathode, reducing TM dissolution and stabilizing the CEI.<sup>41</sup> Phosphorus-based additives, such as tris(trimethylsilyl) phosphite (TMSPi), act as scavengers for HF, reducing its corrosive impact on the electrodes and current collectors.<sup>42</sup> By tailoring the choice of electrolyte additives, it is possible to significantly enhance the longevity and safety of LIBs, addressing critical issues related to high-voltage operation, thermal stability, and cycling efficiency.

#### 1.4.3 Doping/Substitution

Cationic substitution involves substituting TMs in the cathode with another cation and is often referred to as doping when using low-concentration levels of the element. This substituting cation could either be another TM, metals such as Na and Mg, or non-metals such as P. 43-45 This improvement method is adopted across the varying cathode materials available to enhance conductivities, stabilize crystal structures and mitigate phase transitions. For example, substituting a TM in the cathode with an alternative TM that shows stronger TM-O bonding can weaken neighbouring Li-O bonding. This not only makes the structure more stable but can facilitate Li-ion transport. 46 Substituents that show a preference for a given structural site can also be employed to prevent phase transitions that occur due to TM migration, by occupying the site to which the TM usually migrates.<sup>45</sup> Substitution can also influence the defect chemistry, for example, substituting with ions of a different valence state can introduce vacancy sites which can influence the Li<sup>+</sup> ion diffusion pathways.<sup>47</sup> Finally, in some cases, substitution can alleviate electrolyte degradation at the surface by modifying the surface chemistry, or by reacting with the electrolyte to form a protective surface layer. 48 The improvement enabled by each substituent, however, is highly dependent on the concentration, the cathode material under investigation, and the synthetic method that is adopted.

Anionic substitution in cathode materials is also investigated, where oxygen with the TM oxide cathode is partially substituted with another anion. For example, partial substitution of oxygen with fluorine in the lattice structure can improve the material's electrochemical stability and conductivity.<sup>49</sup> Fluorine, being highly electronegative, helps to stabilize the TM oxidation states and reduces the likelihood of oxygen release at high voltages, thereby enhancing the safety and longevity of the battery.<sup>49</sup>

In addition to bulk doping strategies, advanced concentration-gradient doping strategies are being adopted to maintain high capacity while increasing longevity. The concentration gradient approach involves varying the concentration of TMs within a single particle, creating a gradient from the core to the surface.<sup>43</sup> Typically, the core has a higher concentration of a particular metal that provides high capacity, while the outer layers have metals that offer structural stability and mitigate side reactions. This gradient design helps reduce the internal stress and

strain during cycling, thereby minimizing particle cracking and enhancing the overall structural integrity of the material.<sup>50</sup>

#### 1.4.4 Particle Engineering

Several aspects of the particle morphology can significantly influence the electrochemical performance including the shape, size and crystal orientation. Smaller particles can shorten the Li-ion diffusion pathway, but with smaller particles comes a larger surface area and a potential increase in surface reactions. The particle size must often be balanced to accommodate faster Li-ion kinetics with minimised degradation.<sup>51</sup> The crystal orientation can also influence the extent of degradation, where high-energy surface facets can be more prone to degradation/dissolution, while surface facets which expose Li-ion diffusion pathways can be beneficial for facilitating Li-ion transport.<sup>52</sup> Some research, therefore, focused on engineering different particle shapes to expose the desired surface facets.

Advanced cathode morphologies, such as single crystal morphologies, are also being developed to alleviate degradation. This is because cathodes typically adopt a polycrystalline morphology, in which primary particles agglomerate to form secondary particles. This results in numerous grain boundaries that can act as sites for undesired reactions and accumulation of mechanical stress. <sup>53,54</sup> These grain boundaries are prone to cracking and can facilitate the dissolution of TMs, contributing to capacity fade and increased resistance over time. <sup>53,54</sup> In contrast, single crystal cathodes, which are composed of a single, continuous crystalline structure, exhibit fewer grain boundaries and therefore reduced susceptibility to these degradation mechanisms. <sup>53,54</sup> Single crystal cathodes typically demonstrate superior cycling stability due to their enhanced structural integrity and reduced tendency for particle fracture and surface reconstruction. <sup>53,54</sup> However, single-crystal materials can be more challenging and costly to synthesize. <sup>52</sup> Balancing the benefits and drawbacks of polycrystalline versus single-crystal cathodes is crucial for optimizing battery performance and longevity, particularly for high-energy applications where long-term stability is paramount.

#### 1.5 Material Social Futures

While materials research and development is primarily focused on performance characteristics, the 'Material Social Futures' CDT program aims to explore critical dimensions that can be easily overlooked. These include environmental impact, societal behaviours, economics, and policy. Such dimensions can be explored through a series of analytical lenses:

• Futures thinking is an explorative process that defines the key factors that drive change. This allows countless possible futures—ranging in both probability and

- extremity—to be imagined. Such futures thinking can be used to explore the implications on the decisions made today.<sup>55</sup>
- Ecological modernisation, argues that a co-prosperous relationship can exist between the market and the environment. For example, decisions can be made by a company that not only saves money but also reduces environmental impact.<sup>56</sup>
- Political ecology is a field of environmental research that studies the inherent relationship between policy/economics/culture and environmental change.<sup>57</sup>
- *Embodied energy*, considering not only the energy embodied within the battery itself but also the energy that goes into making the battery.<sup>58</sup>

Viewing the development of battery technologies from several different angles allows a more complete assessment of their impact beyond the final consumer use case.

#### 1.6 Scope of Thesis

Framed by these analytical lenses, this thesis aims to advance the development of cathode materials toward a more diverse battery supply chain, by understanding their structure-property-performance relationships.

While Chapter 1 has provided a broad overview of battery fundamentals, Chapter 2 introduces state-of-the-art cathode materials in more detail and assesses their sustainability to identify promising advanced cathode materials that can act as a bridge toward a more sustainable battery supply chain. From this assessment, LiNi<sub>0.5</sub>Mn<sub>1.5</sub>O<sub>4</sub> is selected for further development and forms the basis of the experimental investigations presented in Chapters 3–5, which, through the use of cationic substitution, aim to increase the cycle-life of this high-voltage cathode: Chapter 3 outlines the underlying theory and provides a broad overview of the characterisation techniques and methods adopted throughout Chapters 4–5, with specific parameters being provided in the respective Chapters; Chapter 4 presents an in-depth investigation into the influence of the substituents on the bulk structure and their room temperature performance; while Chapter 5 evaluates the performance under conditions that accelerate electrolyte degradation (i.e., elevated temperature, 50°C), using a combination of surface characterisation and electrochemical impedance spectroscopy to understand the influence of cationic substitution on electrolyte degradation and CEI formation at high voltage.

#### 1.7 References

- 1 United Nations, Paris Declaration on Electro-Mobility and Climate Change & Call to Action, https://unfccc.int/news/the-paris-declaration-on-electro-mobility-and-climate-change-and-call-to-action.
- 2 Z. Liu, Z. Deng, S. J. Davis and P. Ciais, *Nat. Rev. Earth Environ.*, 2024, **5**, 253–254.
- 3 E. Klinenberg, M. Araos and L. Koslov, Annu. Rev. Sociol., 2020, 46, 649–669.
- C. T. M. Clack, S. A. Qvist, J. Apt, M. Bazilian, A. R. Brandt, K. Caldeira, S. J. Davis, V. Diakov, M. A. Handschy, P. D. H. Hines, P. Jaramillo, D. M. Kammen, J. C. S. Long, M. G. Morgan, A. Reed, V. Sivaram, J. Sweeney, G. R. Tynan, D. G. Victor, J. P. Weyant and J. F. Whitacre, *Proc. Natl. Acad. Sci. U. S. A.*, 2017, 114, 6722–6727.
- 5 Y. Nishi, *J. Power Sources*, 2001, **100**, 101–106.
- 6 C. Liu, Z. G. Neale and G. Cao, *Mater. Today*, 2016, **19**, 109–123.
- 7 J. B. Goodenough and K. S. Park, *J. Am. Chem. Soc.*, 2013, **135**, 1167–1176.
- 8 Distinguishing charge rates for next-generation batteries, https://www.quantumscape.com/resources/blog/distinguishing-charge-rates-for-next-generation-batteries/, (accessed 12 August 2024).
- 9 W. Weydanz and S. Ag, *Siemens AG*, 2009, 46–52.
- X. Lin, K. Khosravinia, X. Hu, J. Li and W. Lu, *Prog. Energy Combust. Sci.*, 2020, 87,
   DOI:10.1016/j.pecs.2021.100953.
- 11 Z. Lin, T. Liu, X. Ai and C. Liang, *Nat. Commun.*, 2018, **9**, 8–12.
- J. S. Edge, S. O'Kane, R. Prosser, N. D. Kirkaldy, A. N. Patel, A. Hales, A. Ghosh, W. Ai, J. Chen, J. Yang, S. Li, M. C. Pang, L. Bravo Diaz, A. Tomaszewska, M. W. Marzook, K. N. Radhakrishnan, H. Wang, Y. Patel, B. Wu and G. J. Offer, *Phys. Chem. Chem. Phys.*, 2021, 23, 8200–8221.
- 13 H. Adenusi, G. A. Chass, S. Passerini, K. V. Tian and G. Chen, *Adv. Energy Mater.*, 2023, **13**, 2203307.
- 14 H. Wang, X. Li, F. Li, X. Liu, S. Yang and J. Ma, *Electrochem. commun.*, 2021, **122**, 106870.
- B. L. D. Rinkel, D. S. Hall, I. Temprano and C. P. Grey, *J. Am. Chem. Soc.*, 2020, **142**, 15058–15074.

- 16 T. Yoon, J. Soon, T. Jin, J. Heon and S. M. Oh, *J. Power Sources*, 2021, **503**, 230051.
- D. Pritzl, A. E. Bumberger, M. Wetjen, J. Landesfeind, S. Solchenbach and H. A. Gasteiger, *J. Electrochem. Soc.*, 2019, **166**, A582–A590.
- 18 J. H. Kim, N. P. W. Pieczonka, Z. Li, Y. Wu, S. Harris and B. R. Powell, *Electrochim. Acta*, 2013, **90**, 556–562.
- 19 H. Shin, J. Park, A. M. Sastry and W. Lu, *J. Power Sources*, 2015, **284**, 416–427.
- 20 F. Xia, W. Zeng, H. Peng, H. Wang, C. Sun, J. Zou and J. Wu, *J. Mater. Sci. Technol.*, 2023, **154**, 189–201.
- 21 M. Lin, L. Ben, Y. Sun, H. Wang, Z. Yang, L. Gu, X. Yu, X. Q. Yang, H. Zhao, R. Yu, M. Armand and X. Huang, *Chem. Mater.*, 2015, **27**, 292–303.
- 22 G. Kaur and B. D. Gates, *J. Electrochem. Soc.*, 2022, **169**, 043504.
- 23 J. Chong, S. Xun, X. Song, G. Liu and V. S. Battaglia, *Nano Energy*, 2013, **2**, 283–293.
- 24 J. Chong, S. Xun, J. Zhang, X. Song, H. Xie, V. Battaglia and R. Wang, *Chem. A Eur. J.*, 2014, **20**, 7479–7485.
- 25 Y. Deng, J. Mou, H. Wu, N. Jiang, Q. Zheng, K. H. Lam, C. Xu and D. Lin, *Electrochim. Acta*, 2017, **235**, 19–31.
- U. Nisar, N. Muralidharan, R. Essehli, R. Amin and I. Belharouak, *Energy Storage Mater.*, 2021, **38**, 309–328.
- Z. Zou, H. Xu, H. Zhang, Y. Tang and G. Cui, ACS Appl. Mater. Interfaces, 2020, 12, 21368–21385.
- 28 F. Wu, H. Zhou, Y. Bai, H. Wang and C. Wu, *ACS Appl. Mater. Interfaces*, 2015, **7**, 15098–15107.
- T. Doi, Y. Shimizu, M. Hashinokuchi and M. Inaba, *J. Electrochem. Soc.*, 2017, **164**, A6412–A6416.
- 30 Q. Zheng, Y. Yamada, R. Shang, S. Ko, Y. Y. Lee, K. Kim, E. Nakamura and A. Yamada, *Nat. Energy*, 2020, **5**, 291–298.
- Y. Yamada, K. Furukawa, K. Sodeyama, K. Kikuchi, M. Yaegashi, Y. Tateyama and A. Yamada, *J. Am. Chem. Soc.*, 2014, **136**, 5039–5046.
- 32 C. Li, Y. Zhao, H. Zhang, J. Liu, J. Jing, X. Cui and S. Li, *Electrochim. Acta*, 2013, **104**, 134–139.

- 33 C. C. Su, M. He, P. C. Redfern, L. A. Curtiss, I. A. Shkrob and Z. Zhang, *Energy Environ. Sci.*, 2017, **10**, 900–904.
- J. Alvarado, M. A. Schroeder, M. Zhang, O. Borodin, E. Gobrogge, M. Olguin, M. S. Ding, M. Gobet, S. Greenbaum, Y. S. Meng and K. Xu, *Mater. Today*, 2018, 21, 341–353.
- 35 L. Xue, K. Ueno, S. Y. Lee and C. A. Angell, *J. Power Sources*, 2014, **262**, 123–128.
- Z. Zeng, V. Murugesan, K. S. Han, X. Jiang, Y. Cao, L. Xiao, X. Ai, H. Yang, J. G. Zhang, M. L. Sushko and J. Liu, *Nat. Energy*, 2018, 3, 674–681.
- 37 G. Ma, L. Wang, X. He, J. Zhang, H. Chen, W. Xu and Y. Ding, *ACS Appl. Energy Mater.*, 2018, **1**, 5446–5452.
- 38 T. Doi, Y. Shimizu, M. Hashinokuchi and M. Inaba, *J. Electrochem. Soc.*, 2016, **163**, A2211–A2215.
- 39 Y. Yamada, *Electrochemistry*, 2017, **85**, 559–565.
- 40 M. Li, C. Wang, Z. Chen, K. Xu and J. Lu, *Chem. Rev.*, , DOI:10.1021/acs.chemrev.9b00531.
- 41 Z. Xiao, J. Liu, G. Fan, M. Yu, J. Liu and X. Gou, *Mater. Chem. Front.*, 2020, **4**, 1689–1696.
- 42 H. Liu, A. J. Naylor, W. R. B. Ashok Sreekumar Menon, K. Edström and R. Younesi, *Adv. Mater. Interfaces*, 2020, **7**, 2000277.
- 43 G. Ko, S. Jeong, S. Park, J. Lee, S. Kim, Y. Shin, W. Kim and K. Kwon, *Energy Storage Mater.*, 2023, **60**, 102840.
- 44 T. Fu, Y. Li, Z. Yao, T. Guo, S. Liu, Z. Chen, C. Zheng and W. Sun, *Small*, 2024, 2402339.
- G. Liang, Z. Wu, C. Didier, W. Zhang, J. Cuan, B. Li, K. Ko, P. Hung, C. Lu, Y. Chen, G. Leniec, S. M. Kaczmarek, B. Johannessen, L. Thomsen, V. K. Peterson, W. K. Pang and Z. Guo, *Angew. Chemie*, 2020, **132**, 10681–10689.
- 46 J. Liu and A. Manthiram, *J. Phys. Chem. C*, 2009, **113**, 15073–15079.
- 47 B. Zhang, S. Xu, Z. Lu, Z. Zhang, L. Chen and D. Zhang, *Mater. Lett.*, 2023, **350**, 134870.
- 48 Z. W. Lebens-Higgins, D. M. Halat, N. V. Faenza, M. J. Wahila, M. Mascheck, T. Wiell,

- S. K. Eriksson, P. Palmgren, J. Rodriguez, F. Badway, N. Pereira, G. G. Amatucci, T. L. Lee, C. P. Grey and L. F. J. Piper, *Sci. Rep.*, 2019, **9**, 1–12.
- 49 Y. Luo, H. Li, T. Lu, Y. Zhang, S. S. Mao, Z. Liu, W. Wen, J. Xie and L. Yan, *Electrochim. Acta*, 2017, **238**, 237–245.
- Y. Zhang, J. Liu, W. Xu, Y. Lu, H. Ma, F. Cheng and J. Chen, *J. Power Sources*, 2022,
   535, 231445.
- G. Liang, V. K. Peterson, K. W. See, Z. Guo and W. K. Pang, *J. Mater. Chem. A*, 2020,8, 15373–15398.
- 52 Z. Q. Li, Y. F. Liu, H. X. Liu, Y. F. Zhu, J. Wang, M. Zhang, L. Qiu, X. D. Guo, S. L. Chou and Y. Xiao, *Chem. Sci.*, 2024, **15**, 11302–11310.
- W. N. Wang, D. Meng, G. Qian, S. Xie, Y. Shen, L. Chen, X. Li, Q. Rao, H. Che, J. Liu,
   Y. S. He, Z. F. Ma and L. Li, *J. Phys. Chem. C*, 2020, 124, 27937–27945.
- F. Zhang, X. Zhou, X. Fu, C. Wang, B. Wang, W. Liang, P. Wang, J. Huang and S. Li, *Mater. Today Energy*, 2021, **22**, 100873.
- 55 Government Office for Science, A brief guide to futures thinking and foresight, 2022.
- 56 Z. Sezgin, *Int. J. Energy Econ. Policy*, 2013, **3**, 93–101.
- 57 B. K. Sovacool, *Energy Res. Soc. Sci.*, 2021, **73**, 101916.
- T. R. Hawkins, B. Singh and A. H. S. Guillaume Majeau-Bettez, *J. Ind. Ecol.*, 2013, **17**, 53–64.

## Chapter 2 | Assessing the Sustainability of State-of-the-Art Cathodes

This chapter presents the article "Murdock, B.E., Toghill, K.E., and Tapia-Ruiz, N. (2021). A perspective on the Sustainability Cathode Materials used in Lithium-ion Batteries. Adv. Energy Mater. 11, 1–27." under the terms of the Creative Commons CC BY license with minor edits for clarity and cohesion. The review was published in the peer-reviewed journal of Advanced Energy Materials in September 2021. It provides a perspective on cathode sustainability, framed through the analytical lenses presented in Section 1.5, with a focus on material management as well as highlighting the interdependence between society, policy and the environmental impacts of cathode materials.

A transition from internal combustion engines to electric vehicles (EVs), powered by lithium-ion batteries (LIBs), will be crucial in achieving CO<sub>2</sub> emission targets outlined by the 2015 Paris Agreement. With the large-scale adoption of EVs, however, comes a drastic demand increase for the various metals used in commercial LIB cathodes—primarily lithium (Li), cobalt (Co), nickel (Ni), and manganese (Mn). In particular, concerns surrounding Co, including high cost, low natural abundance, and unethical mining practices have prompted a shift in the automobile industry to Ni-rich cathodes to allow for desirable electrochemical performance whilst minimising Co content. Although this appears to combat the Co predicament, the future implications and sustainability of such a transition to Ni-rich cathodes, amongst other future cathodes, are unclear.

Whilst EVs appear to be essential to reducing global CO<sub>2</sub> emissions, it is necessary to ensure this reduction is not at the expense of other environmental and social landscapes through mining and material mismanagement. In this critical review, the impact of LIB cathodes and the risk factors associated with critical metal supply are considered within the wider context of environmental, social, and governance impacts. This chapter shows that inadequate consideration is given to the long-term impacts within current research, particularly when considering Ni, amongst other metals for which demand may increase with new up-and-coming materials. Developing chemistries that show lower Ni content to state-of-the-art cathodes, with competitive electrochemical performance, will be key to diversifying the battery supply chain.

# A Perspective on the Sustainability of Cathode Materials Used in Lithium-ion Batteries

Beth E. Murdock<sup>a,b,c</sup>, Kathryn E. Toghill<sup>a</sup> and Nuria Tapia-Ruiz<sup>a,c\*</sup>

<sup>c</sup>The Faraday Institution, Quad One, Harwell Science and Innovation Campus, Didcot, OX11 0RA, United Kingdom

#### Abstract

Electric vehicles powered by lithium-ion batteries (LIBs) are viewed as a vital green technology required to meet CO<sub>2</sub> emission targets, as part of a global effort to tackle climate change. Positive electrode (cathode) materials within such batteries are rich in critical metals—particularly Li, Co, and Ni. The large-scale mining of such metals, to meet increasing battery demands, poses concerns surrounding material exhaustion in addition to further environmental, social and governance (ESG) issues. In particular, unethical mining practices and political instability within the Democratic Republic of the Congo (the world's largest Coproducer) have prompted research into low-Co and Co-free alternatives. This review aims to provide a holistic view of LIB cathode development and inform advancements by highlighting the interdependencies across mining, material development, and end-of-life management. While material sustainability is reported through supply and demand projections, the potential socio-environmental impacts of LIB technology represent a hugely under-researched area among the aforementioned themes. Notably, the lack of attention paid toward future implications of increased Ni use across material management and development disciplines is also discussed.

#### 2.1 Introduction

High energy density lithium-ion batteries (LIBs) facilitate portable behaviours in modern society, contrived by a high-speed culture, that requires us to communicate, work, and even charge 'on the go'. Beyond convenience, such technologies are taking centre stage in the environmental revolution through the ever-growing adoption of electrified modes of transport, as transportation currently accounts for 23% of global energy-related CO<sub>2</sub> emissions. Electric vehicles (EVs) thus represent a rapidly expanding market, with at least 20% of road vehicles estimated to be electrically powered by 2030. LIB technology takes great prominence within the automobile industry, due to its unbeatable electrochemical performance and lightweight,

<sup>&</sup>lt;sup>a</sup> Department of Chemistry, Lancaster University, LA1 4YB, Lancaster

<sup>&</sup>lt;sup>b</sup> Materials Science Institute, Lancaster University, LA1 4YB, Lancaster

portable nature. Its impressive performance can be attributed, in part, to the low weight and small ionic radius of the Li<sup>+</sup> ions (0.76 Å), allowing fast ion transport. This fast transport, along with its low reduction potential (-3.04 V vs standard hydrogen electrode (SHE)),<sup>2</sup> allows for high power density as well as volumetric and gravimetric capacity. Such properties are of critical importance for EVs.<sup>3</sup> With the increased demand for high energy density LIBs for EVs, comes reductions in battery cost and subsequent volatility in material supply. In light of the immense scale of transport electrification that is being proposed in order to meet CO<sub>2</sub> emission targets, considerable attention is being directed toward the socio-environmental and economic impact of such an increase in material demand. Of particular focus are LIB cathode materials, many of which are composed of lithium (Li), nickel (Ni), manganese (Mn), and cobalt (Co), in varying concentrations (**Figure 2.1a**). The cathode constitutes more than 20% of LIBs overall cost and is a key factor in determining the energy and power density of the battery (**Figure 2.1b**).<sup>3,4</sup> It is, therefore, vital to maximising the cathode's performance while minimising its cost, to make EVs more accessible for society.

The high cost of cathode materials is largely attributed to the presence of Co—a rare and expensive element mined primarily in the Democratic Republic of the Congo (DRC)—which has been deemed necessary in the past to deliver high energy densities in LIBs. For example, the active material within the commercial NMC111 cathode (LiNi<sub>0.33</sub>Mn<sub>0.33</sub>Co<sub>0.33</sub>O<sub>2</sub>) costs ≈ £17 kg<sup>-1</sup>, producing 3.88 kWh kg<sup>-1</sup>.5 This high cost is largely attributed to the relatively large amount of Co within the electrode (£ 25 kg<sup>-1</sup>). This cost is over 350 times greater than that of Fe (£0.068 kg<sup>-1</sup>), which reflects its relatively high natural abundance. A combination of political instability within the DRC, social impacts within the mining sector, and supply chain volatility and ambiguity have driven a decrease in Co content in NMC cathodes (e.g. going from NMC 111 to NMC811 (LiNi<sub>0.8</sub>Mn<sub>0.1</sub>Co<sub>0.1</sub>O<sub>2</sub>)) and zero-Co alternatives such as LiNi<sub>0.5</sub>Mn<sub>1.5</sub>O<sub>4</sub> spinels, LiMO<sub>2</sub> disordered rock-salts, and LiNi<sub>1-x</sub>M<sub>x</sub>O<sub>2</sub> layered Ni-rich oxides.<sup>8</sup> Such a drastic shift to Ni-rich alternatives begs the question: "In what way will decreasing Co and increasing Ni demand affect future supply amongst other environmental effects?" Although this question remains largely undiscussed throughout the literature, the precarious environmental state and dire acceleration of EV consumption highlight the need for battery developers to place their research into a wider context to better inform material progression. With this in mind, this review aims to provide a more holistic insight into low-Co and Co-free cathode materials, thus considering material supply and demand among other environmental, social and governance (ESG) issues to provide a perspective on the future cathodes under development.

#### 2.2 Current Cathode Technology and Material Development

The high transition metal (TM) content required to induce redox reactions to store charge in LIB cathodes leaves their formulations open to scrutiny, where the literature often highlights concerns surrounding Li and Co supply risk. Research to overcome the main challenges faced by LIBs is underway with the exploration of alternative monovalent battery technologies such as sodium-ion<sup>9</sup> and divalent batteries, e.g. magnesium<sup>10</sup> and calcium<sup>11</sup> batteries. Yet, LIB technology will remain the market leader for the foreseeable future until such alternatives can offer parity in performance. Although the removal of Li from cathode materials is unfeasible for present implementation, materials that require less Li per kWh are preferable.

The start of the EV influx in 2015 saw that much of the LIB market was dominated by cathodes with high Co content, such as NMC111.<sup>12</sup> However, increased consciousness toward Co supply risk within the field of LIB development has resulted in the adoption of cathodes with reduced Co content, such as NMC811. Beyond reducing Co content, much research is invested in Co-free alternatives. Commercialised options available include lithium iron phosphate (LiFePO<sub>4</sub>)<sup>13</sup> and lithium manganese oxide (LiMn<sub>2</sub>O<sub>4</sub>, LMO)<sup>14</sup>—the use of which has often been limited to certain applications due to unsatisfactory electrochemical performance for use in EVs (i.e., low energy density and power density, and poor cycle life in the case of LMO). This prompts research into further improving such cathodes for long-range EV applications in addition to developing other potential future cathode materials. The aim for future LIB cathodes is, therefore, to minimise Co and Li required while still maintaining, or better yet improving, electrochemical performance including energy density, power density, and long-term cycling stability. Such material development will be briefly outlined below.

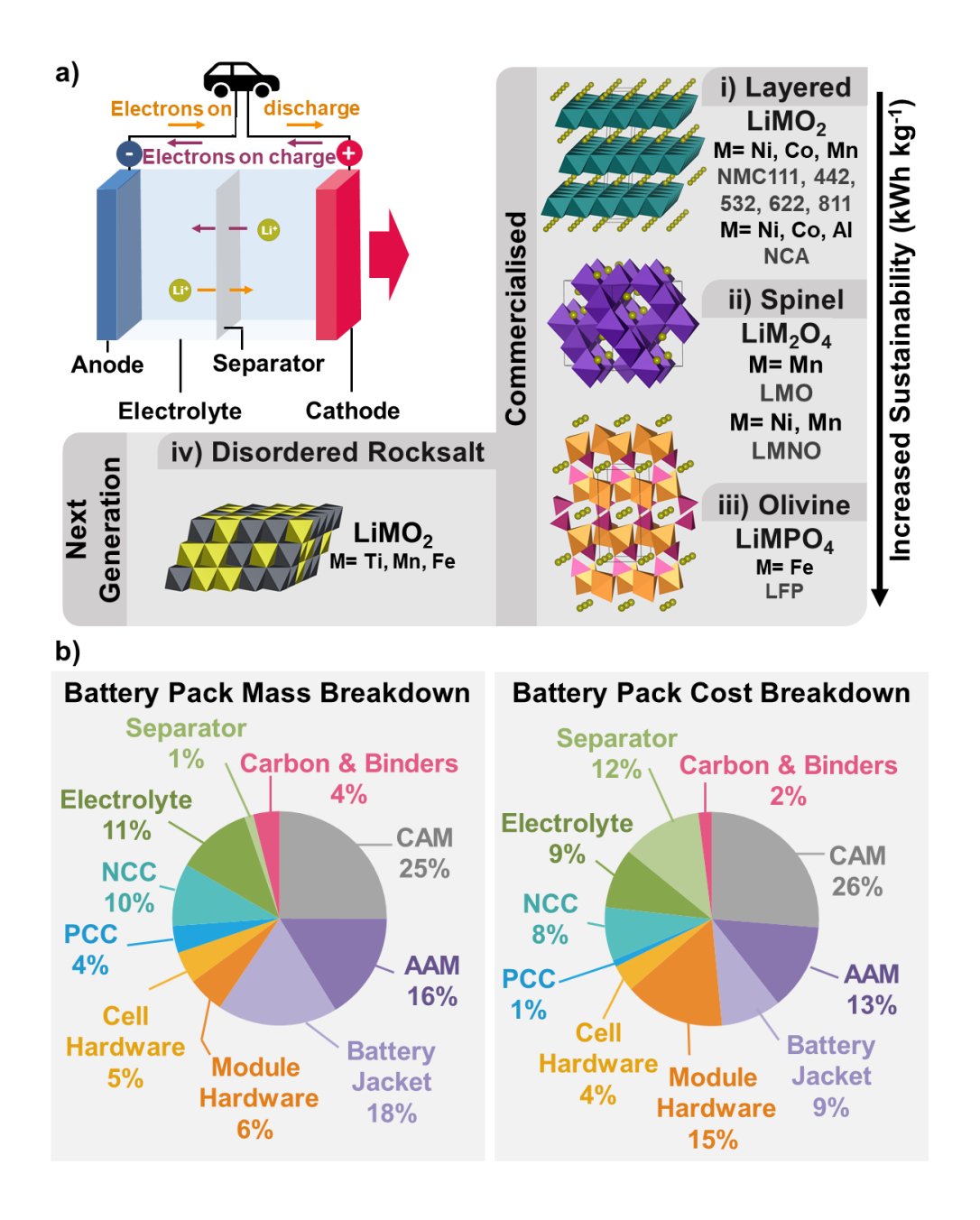


**Figure 2.1:** a) Schematic of a LIB, showing the movement of electrons and Li<sup>+</sup> ions (green) during charge (purple) and discharge (orange) processes. Crystal structures of various cathode chemistries are indicated: i) layered structure, where teal octahedra represent M (M = Ni, Mn, Co for NMC and M = Ni, Co, Al for NCA), ii) spinel structure, where purple octahedra represent M (M = Mn for LMO and M = Ni, Mn for LNMO), iii) olivine structure, in which M = Fe for LFP, and iv) disordered rock salt structure, where cation mixing of M(d<sup>0</sup>) (grey) and Li (green) between the layers is observed (M = Fe, Mn, Ti). b) Typical mass and cost breakdown of an NMC battery pack, where CAM = cathode active material, AAM = anode active material, NCC = negative current collector and PCC = positive current collector. Charts produced with data from reference 15.

#### 2.2.1 Layered Cathode Materials

Layered cathodes (Figure 2.1a) represent the most widely researched cathode type for LIBs, where NMC-type cathodes (LiNi<sub>1-x-v</sub>Co<sub>x</sub>Mn<sub>v</sub>O<sub>2</sub>) show particular prominence. The combination of Ni, Mn, and Co provides high specific capacity, low internal resistance, and high stability, respectively. 12 Although NMC111 is the most common, NMC-type cathodes with reduced Co content are gaining importance to mitigate sustainability and cost implications associated with the critical element supply risk (see *Mining and Material Management* section). Progression through low-Co NMC cathodes has seen a variety of formulations including NMC442, NMC523, NMC622 and NMC811, which result in lowered pristine material costs (Figure 2.2a), where in the case of NMC811, raw materials make up approximately 30% of production costs (Figure 2.2c). In addition to the benefits related to decreasing Co concentration, the increased Ni concentration enhances capacity, with NMC811 showing an improved specific capacity of 200 mAh g<sup>-1</sup> when compared to NMC111 (160 mAh g<sup>-1</sup>, both 4.3 V vs Li<sup>+</sup>/Li).<sup>12</sup> Increasing the Ni content in these NMC-type cathodes, however, increases the reactivity of the cathodes due to the instability of Ni ions towards the liquid organic electrolyte and any trace moisture. 12 This prompts the need for additional cathode components to prevent degradation, such as electrode coatings, for example.

Beyond simple surface coatings are advanced particle design strategies such as core-shell<sup>15,16</sup> and concentration gradient particles 16,17, in which Ni-rich NMC occupies the particle core to provide desirable electrochemical performance, whilst less reactive manganese-rich NMC dominates the particle surface (shell), providing enhanced stability against the electrolyte. 12 Commercially, NMC-type cathodes are often synthesised through a two-step co-precipitation reaction in which the metal hydroxide or carbonate is precipitated before sintering with stoichiometric amounts of Li source (Li<sub>2</sub>CO<sub>3</sub> or LiOH). 18 Whilst material costs may decrease due to reducing Co concentration, the manufacturing cost may increase due to the greater processing cost related to Ni and the use of, more expensive, LiOH as the Li source required for the synthesis of Ni-rich cathodes (\$9.50 kg<sup>-1</sup> LiOH compared to \$7.75 kg<sup>-1</sup> Li<sub>2</sub>CO<sub>3</sub>, 2021). 19,20 NMC 712 shows an optimal elemental composition when considering a variety of factors including cost and abundance.<sup>21</sup> Considerations towards the increased SO<sub>x</sub> emissions associated with Ni increase are also not to be overlooked (see ESG Impacts section).<sup>22</sup> Furthermore, the thermal safety of the NMC cathode with higher Ni contents, such as NMC811, is more hazardous due to the earlier exothermic onset temperature and largest exothermic heat generated.<sup>23</sup>

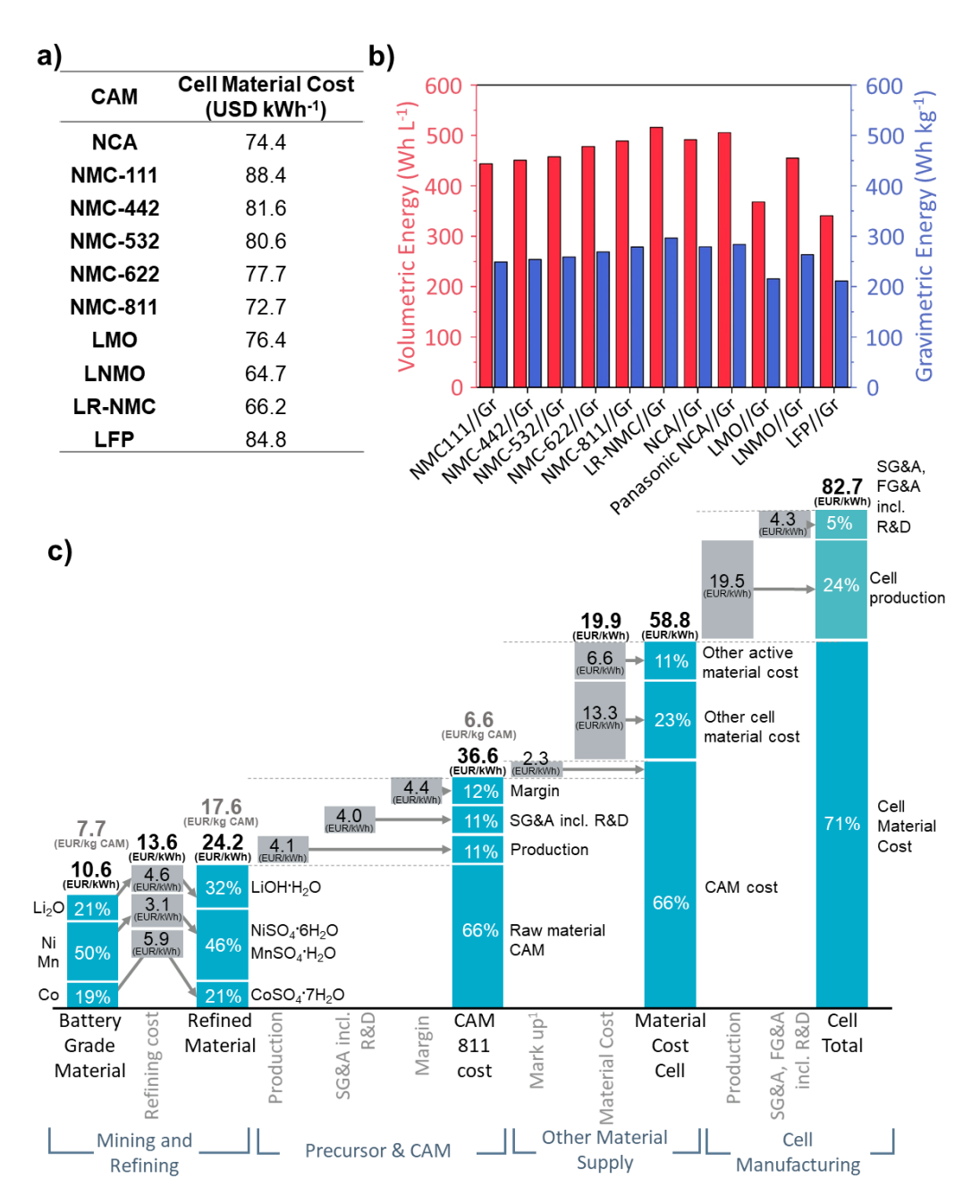


**Figure 2.2:** a) Estimated cell material cost based on production capacity of 1 GWh, data reproduced from  $^{24}$ , b) selected electrochemical performance parameters (volumetric and gravimetric energy) from full cells with graphite (Gr) as anode and a variety of LIB cathodes such as NMC111, 442, 532, 622 and 811, LR-NMC (Li-rich NMC), NCA, LMO, LNMO and LFP. Reproduced with permission from  $^{24}$ , and c) Cost breakdown of an NMC811 prismatic cell produced in China considering costs related to mining and refining, production of Cathode Active Material (CAM), production of other cell components and cell manufacturing (SG&A = selling and general & administrative expenses, FG&A = factors that account for general & administrative expense, Li<sub>2</sub>O = Li spodumene concentrate 6%,  $^{1}$  = mark up of ≈ 6.3% to account for efficiency losses between theoretical vs nominal voltage.) Adapted with permission from  $^{25}$ .

NCA cathodes (LiNi<sub>1-x-y</sub>Co<sub>x</sub>Al<sub>y</sub>O<sub>2</sub>) join NMC-type cathodes as front runners within the automobile industry. The NCA formulation has been optimised to 5 wt% aluminium (NCA-80, LiNi<sub>0.8</sub>Co<sub>0.15</sub>Al<sub>0.05</sub>O<sub>2</sub>), showing a comparable specific capacity to NMC811 (200 mAh g<sup>-1</sup>, 4.3 V vs Li<sup>+</sup>/Li).<sup>19</sup> The lack of Mn in NCA materials (i.e. NCA-80,81 and 82) results in desirable capacity retention when compared to NMC811 as Mn-ion dissolution is eliminated, whilst the incorporation of aluminium ions provides enhanced thermal stability.<sup>19</sup> Correspondingly, NCA is often the choice for 'long-range' EVs provided by Tesla, which boast ranges > 500 km.<sup>12</sup>

Li-rich (LR) NMC type cathodes (Li(Li<sub>w</sub>Ni<sub>x</sub>Co<sub>y</sub>Mn<sub>z</sub>)O<sub>2</sub>) exploit both cationic (Ni<sup>2+/4+</sup>, Co<sup>3+/4+</sup>) and anionic (2O<sup>2-</sup>/O<sub>2</sub>n- [n < 4]) redox activity allowing further improvements in capacity when compared to conventional NMCs (> 270 mAh g<sup>-1</sup>).<sup>18,26</sup> Such a significant increase in capacity results in lower cell material cost (**Figure 2.2a**).<sup>24</sup> These materials, however, suffer from capacity and voltage fade as well as voltage hysteresis and slow kinetics that result from the anionic redox. LR-NMC's with higher Ni content (i.e. LR-NMC811) are more effective at mitigating such issues.<sup>26</sup> More recently, disordered rock-salt (DRX) LiMO<sub>2</sub> cathodes (**Figure 2.1a**) offer a Co-free layered cathode that requires d<sup>0</sup> metal species and excess Li.<sup>27</sup> These are, however, at a very early stage of research development. For sustainability reasons, Fe-,<sup>28,29</sup> Mn-<sup>30</sup> and Ti-based<sup>28,29,31</sup> oxides are of particular interest. Substitution of oxygen by fluoride anions has shown to allow high reversible capacities (> 300 mAh g<sup>-1</sup>) and energy densities (≈ 1000 Wh kg<sup>-1</sup>, 1.5-5.0 V vs Li+/Li)<sup>27</sup> by preventing irreversible oxygen redox reactions and/or O<sub>2</sub> loss.

#### 2.2.2 Non-layered Cathode Materials

LiFePO₄ (LFP), a cathode with an olivine structure (**Figure 2.1a**), exhibits excellent cycle life and high thermal and electrochemical stability, due to the strong bond energy of the PO₄ tetrahedral units. These properties, along with its inherently low cost and use of naturally abundant Fe, make it an attractive cathode option for several battery applications. Its widespread adoption in EVs, however, is limited by its low energy density (120 Wh kg⁻¹) and poor electronic conductivity (≈ 10⁻⁰ S cm⁻¹), which despite low material cost results in relatively high cost per kWh. 19,24,32 LFP is typically synthesised through a two-step route in which the precursor is prepared through spray drying followed by calcination in an inert or mildly reducing atmosphere. This is often coated with conductive carbon to improve the poor electronic conductivity. The synthesis of nano-sized particles is also considered to improve electronic conductivity by decreasing the Li⁺ ion diffusion pathway. Despite these drawbacks, LFP cathodes in a traditional cell format may still have a role in public transport, due to their high safety and fast charging times of ≈ 2.5 h, and in less power-demanding stationary storage.

Despite the drawbacks of traditional cylindrical/prismatic cell formats, the increased energy density of LFP (comparable to low-Ni NMCs at pack level) has been demonstrated by Chinese company BYD, when using their Blade Battery technology. This simplifies the pack design by mitigating the need for modules—as the thin blade cells are stacked directly into the pack (cell-to-pack)—which reduces the overall weight of inactive components.<sup>35</sup> This has prompted a new surge in academic and industrial research into LFP. Improved energy density at the material level is also being investigated by incorporating Mn into the formulation LiMn<sub>x</sub>Fe<sub>1-x</sub>PO<sub>4</sub> (LMFP). This allows higher theoretical energy density since the Mn redox reactions occur at a higher potential than the Fe redox reactions. High Mn concentrations are desirable to increase the average operating potential. However, high-Mn LMFP is plagued by Mn-dissolution and resulting capacity decay.<sup>36</sup>

Spinel-type cathodes (**Figure 2.1a**) provide an additional opportunity to eliminate Co, within certain battery applications, whilst also benefitting from decreased wt. % of Li when compared to layered TM oxides (e.g. NMC, NCA).<sup>37</sup> Their three-dimensional structure allows for facile Li<sup>+</sup> ion diffusion and thus high-rate capability.<sup>37</sup> LiMn<sub>2</sub>O<sub>4</sub> (LMO) represents the most widely researched spinel to have penetrated the EV market. The use of LMO is limited, however, by its low capacity and energy density, and short lifetime (due to structural instabilities upon cycling). Thus, LMO is often blended with NMC-type cathodes (for example, by automotive manufacturers Mitsubishi) to provide the high rate capability and low cost of LMO alongside the high capacity and improved cycling stability of NMC-type cathodes.<sup>19</sup>

More recent research efforts have turned to focus on the high-voltage LiNi<sub>0.5</sub>Mn<sub>1.5</sub>O<sub>4</sub> spinel. The incorporation of Ni into the parent LMO spinel allows for high operating voltage and high energy density, through a two-electron Ni<sup>2+/4+</sup> redox couple (≈ 4.75 V vs Li<sup>+</sup>/Li).<sup>37</sup> This increase in energy density results in a decrease in cell material cost, despite the incorporation of a more expensive component (Ni), as less material is required per kWh.<sup>24</sup> Its high voltage also offers an opportunity to simplify the pack, as fewer cells in series are required to provide the same pack voltage.<sup>38</sup> As with LMO, however, LNMO is limited by structural instabilities on cycling in addition to incompatibility with commercial electrolytes resulting in electrolyte oxidation at such high voltage (> 4.5 V).<sup>37</sup> In order to compete with commercial Co-containing cathode materials, methods to improve such failure mechanisms are under investigation. These methods include various doping strategies,<sup>39,40</sup> high-voltage electrolytes,<sup>41,42</sup> surface coatings<sup>43</sup> and particle morphology optimisation.<sup>44</sup> Doping with abundant elements, such as Fe at low concentrations, has not only shown to improve electrochemical performance, (particularly at high C rates) but could alleviate Ni demand which may prove beneficial when considering long-term supply vs demand (see *Supply vs Demand* section).<sup>45</sup>

#### 2.3 Mining and Material Management

### **2.3.1 Mining**

The mining of raw materials can have significant consequences for the resulting environmental, economic, and social impact of LIBs. Cathode materials constitute a considerable amount of the raw materials required for, and the cost of, LIBs. High cathode costs are a consequence of using critical elements such as Li and Co. On the other hand, Ni and Mn are considered to be far less critical. Nevertheless, it is worthwhile to consider supply, demand, and wider consequences of all constituent elements in cathodes to best project the outcome of rapid EV adoption.

Mining of Li occurs primarily in South American countries, such as Chile and Argentina, in which Li is extracted from brines and largely processed to form Li<sub>2</sub>CO<sub>3</sub>, which can then be converted into LiOH. Brines containing Li are estimated to represent 66% of global Li resources (estimated to be 81 Mt by the U.S. Geological Survey, 2020).<sup>46,47</sup> Hard-rock extraction, on the other hand, from minerals such as spodumene, is largely employed in Australia. While each of these countries focuses on only one extraction method, China uniquely produces Li from both brine and hard-rock.<sup>48</sup> Unlike brines, spodumene can be directly transformed into LiOH, being approximately \$ 500 t<sup>-1</sup> cheaper than LiOH from brine.<sup>48</sup> It is predicted that LiOH will constitute a large share of future demand due to its preferred use for long-range batteries.<sup>48</sup> The preferred use of LiOH over Li<sub>2</sub>CO<sub>3</sub> is due to the instability of high Ni content NMC cathodes (NMC811) when synthesised with Li<sub>2</sub>CO<sub>3</sub>.<sup>19</sup> The use of LiOH in their synthesis, compared to Li<sub>2</sub>CO<sub>3</sub>, allows the use of lower synthetic temperatures, helping to maximise stability.<sup>19</sup> In addition to conventional sources such as hard-rock and brines, Tesla is hoping to extract Li from clays using salt (sodium chloride). However, this source is often deemed unfeasible due to the low grade and high extraction cost.<sup>49</sup>

Co mining is geographically concentrated in The DRC—home to the copper belt—where it is heavily mined, with China and Canada following as the 2<sup>nd</sup> and 3<sup>rd</sup> largest producers.<sup>50</sup> Co is primarily produced as a co-product of copper (Cu) mining (70% current supply, > 30% Cu mine revenue) and a by-product of Ni mining (20% current supply, < 5% Ni mine revenue).<sup>48,50</sup> An estimated 15–20% of the DRCs Co supply is produced by small-scale artisanal miners who are not officially employed.<sup>50</sup> The role of the DRC as the main Co provider is predicted to remain stable, where they are projected to supply 62–70% from 2018 to 2030.<sup>51</sup> Future projections, however, suggest that Co supply as a by-product of Ni mining will increase. Shifting from co-product supply to by-product supply will ultimately reduce the interdependencies of Co on primary metal mining.<sup>51</sup> This, in turn, should improve the security of Co supply.

Ni is mined—primarily in the Philippines, followed by Indonesia and Canada—as sulphide and laterite (oxide) ores.<sup>22</sup> Although laterites are more abundant, representing 70% of global stock, sulphides represent 60% of Ni supply due to the more complex, and thus more expensive, processing of laterites.<sup>22</sup> Unlike the aforementioned metals required for electromobility, Mn is plentiful, representing the third most abundant TM in the Earth's crust, of which 80% is mined in South Africa followed by Australia and China.<sup>52</sup>

The possibility of deep-sea mining is also being considered. However, widespread exploration of such mining is limited by the high upfront cost.<sup>53</sup> Furthermore, automotive companies such as BMW and Volvo have committed to avoid deep-sea mining due to the unclear effects on the fragile ocean eco-systems that are already under significant stress from overfishing, pollution and global warming.<sup>53</sup> Work across the social sciences aims to highlight and understand further issues surrounding social justice, vulnerability and ownership of deep-sea mining and mining areas.<sup>54</sup>

## 2.3.2 Supply vs Demand

Various literature reports have attempted to predict supply vs demand for metals used in LIB cathode materials in order to elucidate potential future limitations. Such modelling and predictions prove difficult as the quantification of potential metal resources are highly dependent on public information provided by mining companies and other relevant sources, such as the U.S. and British geological surveys (USGS<sup>55</sup> and BGS<sup>56</sup>). Potential metal sources are often described in terms of resources and reserves. Resources represent a location in which a given metal is present in the Earth's crust. Reserves, on the other hand, represent resources that are economically feasible to mine.<sup>57</sup> Such feasibility is dependent on the deposit size, metal content and the extraction process required. For example, Bolivia contains the largest known Li reserve (≈ 21 Mt<sup>47</sup>). However, the lack of transportation and mining infrastructure, the limited quality of Li-containing ore, and political barriers result in this area being under-mined.<sup>58</sup> Reserves are, therefore, dynamic—changing according to current socioeconomics, environmental policy and technology.<sup>59</sup> Estimations of supply are reliant on the number of deposits included from existing sources, sources that have announced future mining operations as well as projections towards potential unannounced mining operations (Figure 2.3).<sup>51</sup> Demand modelling also depends on a large variety of factors including the time frame considered, the projected number of vehicles manufactured within this time frame, the share of different EV technologies in the market, the size of the EVs in question (kWh), the cathode material used and the weight of each metal per kWh (Figure 2.3).<sup>57</sup> Any difference in the parameters chosen can result in significant modifications in the proposed supply vs demand scenarios.

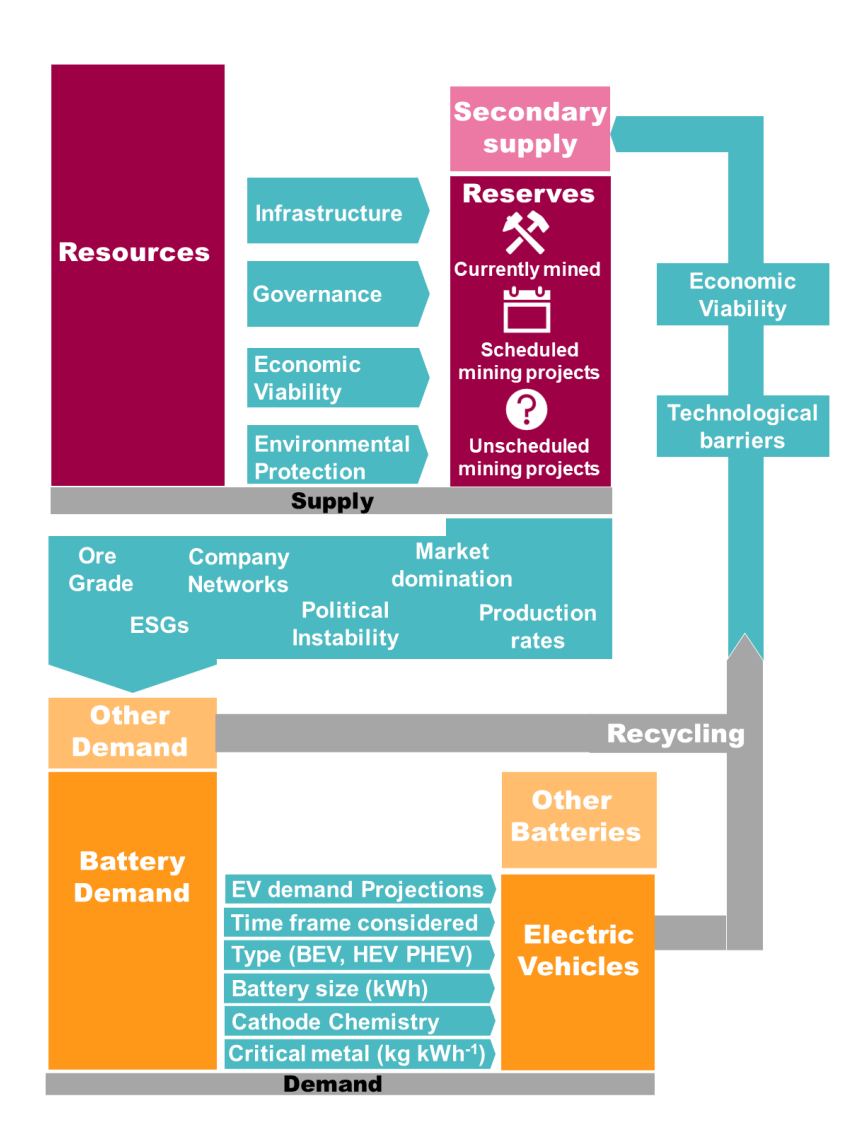


**Figure 2.3**: Schematic highlighting the considerations required for supply (purple, top) and demand (orange, bottom) modelling. Turquoise arrows indicate factors that influence the outcome of projections. Differences in factors chosen for modelling can result in significant differences in projected supply and demand.

Gruber *et al.* projected a total Li demand over a period from 2010–2100 by modelling EV penetration, where annual EV growth beyond 2030 is anticipated to remain constant. <sup>46</sup> Such projections predict 100% EV penetration between 2083–2087. This results in an estimated Li demand of 19.6 Mt, in which batteries dedicated to automotive applications account for approximately 65% of this demand. In this scenario, LIB recycling is estimated at 90%, with

90% recoverable Li. Such recycling operations would significantly lower the strain on Li mining. Evaluating Li supply vs demand, for 39 Mt of estimated in-situ Li resources, suggest that supplies are sufficient to meet demand until at least 2100. This, however, is highly dependent on the success and implementation of LIB recycling technology. Calisaya-Azpilcueta *et al.* took a different approach to model the Li supply chain through stochastic modelling, combining material flow analysis with both global sensitivity analysis and uncertainty analysis.<sup>60</sup> This allowed the identification of variables that had the most important effect on Li distribution and EV production; LiOH production, from both Li<sub>2</sub>CO<sub>3</sub> and hard rock, and traditional battery production. However, this work did not consider stages beyond production. From their findings arose a probable scenario in which increasing demand is not covered by supply. For the time frame considered (2019–2025), this undersupply scenario was shown to be more likely to occur in 2025 than in 2021.<sup>60</sup> As a time frame beyond 2025 was not considered, that is not to say that Li resources are predicted to be depleted by this time.

Fu et al. applied a series of scenario models for estimating the supply and demand of Co over of short-term period (2015-2030). Their results indicated that—based on a high compound annual growth rate (CAGR)—Co demand for EV LIBs accounts for 70% of battery demand by 2030 at 250 kt.<sup>51</sup> In addition to other battery applications and non-battery applications, in an aggressive high-demand scenario, it is projected that Co demand will reach 430 kt by 2030. This is closely matched to the projected 458 kt of supplied Co, under the same scenario conditions.<sup>51</sup> This work, therefore, envisages that Co supply will meet short-term demand. The possibility of recovering secondary Co through the recycling of electronics is estimated to provide an additional 17 kt into the supply chain (at a recovery efficiency of 100%).<sup>51</sup> Elshkaki et al. postulate four different future scenarios and model the changes in Ni demand for each, where a collaborative 'Equability world's scenario' resulted in the highest demand (350% increase on 2010 by 2050) and lowest demand in a 'security foremost' scenario in which significant disparities exist (215% increase on 2010 by 2050).<sup>22</sup> In each of the four scenarios demand is expected to exceed reserves whilst remaining within the constraints of the estimated resources (150 Mt). This work predicts that Ni supplies will be sufficient to meet demand within the timeframe considered (2050). Concerns surrounding Ni for battery applications are often minor as battery demand represents only a small percentage of overall Ni demand when compared to Li and Co required for battery applications (Figure 2.4).<sup>22</sup> Nonetheless, reports have highlighted that although initial Ni supply may seem high, constraints defined by ore grade, governmental control, as well as environmental and social pressures, significantly limit the amount of Ni available for use in EVs.<sup>61</sup> For example, only 46% of Ni produced globally is of sufficiently high purity for EV applications, where 70% of battery-grade Ni comes from sulphide ores. 61 Their projections indicate limitations to Ni supply as early as 2027 when considering a low-demand scenario. Conclusions and comparisons to literature reports for these scenarios, however, are not possible as the basis for such projections is not outlined. Despite this, it raises the importance of considering ore grade within supply and demand modelling as failure to do so may lead to misleading results.

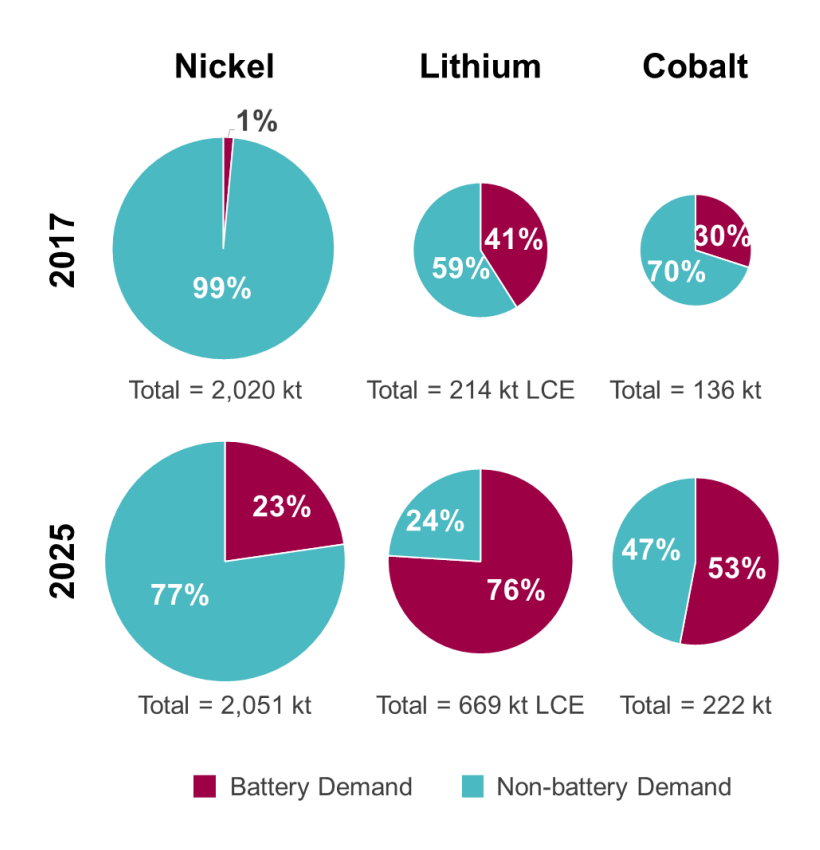


**Figure 2.4:** Predicted changes in battery and non-battery demand of Ni, Li, and Co. Figures produced using data from references 12 and 24. LCE = lithium carbonate equivalents.

Being the third most abundant TM in the Earth's crust, supply vs demand studies that focus on Mn alone are unsurprisingly difficult to come by. Unlike the literature above that discusses the supply and demand of one focus element, work conducted by Habib *et al.* considered a range of materials required for EV production with a particular focus on cathode constituents. <sup>62</sup> This provides the benefit of comparing different elements under the same applied conditions. Three scenarios were modelled, based on representative concentration pathways (trajectories to predict climate futures, RCPs), which indicate the global warming delivered by a given concentration of CO₂ emissions (measured in W m<sup>-2</sup>). Those considered are as follows: (1) 4.5 W m<sup>-2</sup> (baseline), where CO₂ emissions are required to start declining ≈ 2045 and are expected to half between 2050 and 2100, (2) 2.6 W m<sup>-2</sup> (stringent), where CO₂ emissions are required to start declining by 2020 and reach 0 by 2100, and (3) 3.4 W m<sup>-2</sup> (moderate),

representing a scenario between 1 and 2.63 Increased stringency to meet RCPs resulted in EVs constituting increased proportions of total 2050 passenger vehicles (23% of all vehicles electric in a baseline scenario, 32.6% in moderate and 73% in stringent). As expected, the increased in-use EV stocks significantly accelerate the reserve depletion of Co, Li, and Ni, with Co reserves being depleted by 2035 under stringent modelling conditions. Other battery and EV constituents such as Mn, Al, Fe, and Cu, on the other hand, experience less significant depletion, retaining 90% (Mn, Al, Fe) and 74% (Cu) of original stocks up to 2050. As modelling followed an S-curve trend, all scenarios saw the highest demand for materials in 2035. A great disparity in material demand was seen between models, however, where Co demand was 11 times higher in the stringent scenario when compared with the baseline. This work identified Ni as well as Li and Co as having high potential supply risk in the future.<sup>62</sup> No mention of ore grade is supplied within Habib *et al.*'s report, suggesting this supply risk is based on total Ni reserves as opposed to the 46% of Ni reserves that are acceptable for battery use.<sup>61,62</sup> With increasing Ni content in LIB cathodes, greater attention must be paid to improving supply and demand modelling of not only Li and Co but also, crucially, Ni.

Comparison between different models of supply vs demand outlined above shows a large disparity in projected outcomes. Earlier attempts of modelling supply vs demand lacked detail, often only considering one battery chemistry and EV type. Fr Recent developments show increased attention to specific EV and battery technologies employed, considering various cathode chemistries and relative EV battery sizes (kWh). Another area for uncertainty is non-battery applications. Whilst some works tried to also model non-battery applications, others do not, which would result in a gross underestimate of materials demand. The inclusion, however, adds further complexity and uncertainty to demand calculations. The sensitivity of modelling supply vs demand renders outcomes doubtful, thus comparison studies, as conducted by Habib *et al.*, may prove more beneficial. Various time-frames used in reports make comparison difficult. As may be expected, with increased time, uncertainty increases due to the greater probability of significant changes in the supply and demand landscape.

Material demand is often modelled on different scenarios. These scenarios, however, are not consistent between reports. Whilst Speirs *et al.*<sup>57</sup> and Habib *et al.*<sup>62</sup> both considered scenarios based on CO<sub>2</sub> emission targets, the targets used were different with the former using IEA scenarios in which CO<sub>2</sub> emissions should see a 50% reduction by 2050 and the latter employing scenarios based on shared socio-economic pathways outlined by climate change researchers targeting different RCPs. This leads to significant differences in the anticipated EV and subsequent Li demand. Speirs *et al.* consider an EV market made up of BEVs and PHEVs, totalling 109 M vehicles in 2050. Varying material intensity within the EVs batteries resulted in a wide range of Li demand from 184–989 kt. Habib et al, on the other hand, predict

EV demand between 2–3 M, with Li demand <100 kt for 2050. In addition to different scenarios used, different trends in EV adoption lead Habib *et al.* to predict a peak EV demand  $\approx$  2030, whereas Speirs *et al.* observed a continual growth until 2050. Furthermore, Habib *et al.* included HEVs into their projections which use Ni-metal hydride batteries that are non-reliant on Li and so this will further reduce Li demand projections.

Focusing on projected Co demand for 2030, Habib *et al.*, using RCP-based projections, predict EV demand from 30–70 million.<sup>62</sup> Fu *et al.* instead used compound annual growth rates (CAGR) of 5 and 10% when projecting EV demand, suggesting a range of approximately 10-21 million vehicles.<sup>51</sup> The former suggests a demand of approximately 500–5000 kt in 2030. The latter, on the other hand, predicts 235–430 kt of Co demand, where the higher limit is in line with the lower baseline limit projections of the former. Such a drastic increase in projected demand may be explained due to the far greater estimations of EV adoption to meet CO<sub>2</sub> targets where baseline efforts may be more probable unless significant policy is put in place. Despite the use of different scenarios, all recent works agree that supply will be sufficient for short-term to mid-term demand. A further drawback is that, although demand may appear to be within supply constraints, models often do not consider the rate of production for such critical metals. Lags in production rate may, therefore, pose a limiting supply factor.<sup>64</sup> It is evident from the works summarised, however, that Co poses the biggest depletion concerns followed by Li.

Despite research efforts towards replacing LIBs with more sustainable alternatives (e.g. sodium-ion, magnesium, and calcium batteries), the requirement of LIBs for high energy density applications is likely to remain necessary for the foreseeable future as alternative technologies lag. This makes the complete removal of Li unfeasible at present. Optimising formulations to minimise Li content per kWh, however, can be investigated to minimise strain on Li demand. Unlike Li, Co can, and is, being substituted, largely by Ni and/or Mn (see *Material Development* section).<sup>8</sup> Despite no significant limitations predicted by literature reports on Ni supply in the near to mid-future, it would be worthwhile for modelling attempts to consider long-term supply vs demand.

As seemingly abundant materials, Fe (natural abundance (NA) = 56,300 ppm), Ti (NA = 5,650 ppm), and Mn (NA = 950 ppm) are viewed as worthwhile alternatives to Ni (NA = 190 ppm) and Co (NA = 25 ppm). <sup>65</sup> Studies that consider supply and demand for Fe and Mn, focus on their use in steel and those that consider Ti, consider its use in pigments and within the aerospace industry. <sup>66–68</sup> From such studies it is difficult to extrapolate supply and demand to battery applications. As with Ni, however, battery applications form a small percentage of Fe, Ti, and Mn demand. Supply and demand studies for Fe focused entirely on supply and

demand for steel, as it is estimated that 99% of the Fe market lies within the steel industry.<sup>67</sup> As with Ni, widespread adoption of Ti- and Fe- and Mn-based cathode materials will add further strain on to resources with already high demand. Here, we highlight the dangers of defining any given battery material as sustainable, as in doing so we lose foresight to future sustainability issues. It is clear from the extensive amount of resources required for successful EV penetration that a variety of cathode materials, used in conjunction throughout the industry, will be required to optimise sustainable development. More research into the potential impacts of increased Fe, Ti and Mn battery demand should be considered pre-development, once again, to better inform materials development. Modelling approaches may be wise to consider a variety of up-and-coming materials (see *Material Development* section) to model the optimal share of each within the EV sector to best sustain resources. Such modelling attempts should allow anticipation of future bottlenecks. The undetermined electrochemical performance of novel materials when implemented in EV systems may, however, present some challenges and additional uncertainties.

#### 2.3.3 Supply risk

Supply risk is often assessed through product concentration, by-product dependency and political country risk (Figure 2.3).50 Whilst Li and Co are both largely concentrated in South America and the DRC, respectively, companies located in China are largely responsible for the refinement of these raw materials for battery material production. 69,70 China has significantly increased investment into Co mining activities overseas in order to provide a domestic and steady downstream supply of raw materials. Chinese dominance of both raw and battery materials may lead to supply shortages if critical materials are leveraged in diplomatic disputes or reserved for their domestic use.<sup>70</sup> Therefore, country-level disruption to South American countries, the DRC or China could result in a significant impact on global Li and Co supply resulting in high supply risk.<sup>50</sup> In addition to Li and Co, environmental policies appearing throughout Southeast Asia banning raw ore exports or suspending Ni extraction in certain regions may pose a notable risk to Ni supply.71 Increased insight into the environmental, social and governance (ESG) impacts of critical metal mining (see below) has led to increased consciousness towards responsible sourcing, which may further restrict resources available for use. Tesla has demonstrated the need for a secure supply chain by securing supply of both Ni and Li as these metals pose the greatest risk within their Ni-rich chemistries.49,72

Helbig *et al.* attempted to quantify the supply risk associated with a selection of metals used for battery applications.<sup>73</sup> From this study, it was determined that Li and Co posed the most significant supply risk (54% risk). Risk to Li supply was largely impacted by a lack of sufficient

recycling opportunities, whereas high Co risk was a result of political instability and by-product dependence. From the data presented, Ni (50%) and Mn (52%) show similar supply risk scores, with Ni risk largely dependent on supply reduction. Mn, on the other hand, shows a high score, despite its high natural abundance, due to its lack of substitutability. Ti was also evaluated, due to its use in Li titanate anode materials (Li<sub>4</sub>Ti<sub>5</sub>O<sub>12</sub>), and was shown to have a lower supply risk (43%). This work highlights the need to include Mn into supply considerations. Furthermore, understanding the impact of increased demand for Ti may be interesting for understanding the future implications of moving to Co- and Ni-free chemistries.

In order to reinforce supply chains, a more diverse stream of Co and Li will be particularly necessary. Diversifying Co supply can be achieved through improved artisanal Co mining from >150 Co sites currently unmined, located in countries that do not presently mine. Significant efforts should be made to improve the working conditions of artisanal mining through social and environmental sustainability measures as increased supply chain resilience could be achieved. The emergence of Co-primary mines, which has resulted from increased demand in the electronics sector, should help further improve Co security. Investment into Li mining in Bolivia by foreign companies will considerably extend Li reserves. Believed.

In addition to geographical supply risk, company-based supply risk poses a potential threat. Companies that possess multiple links to other companies within the supply chain pose the biggest risk as a collapse in their supply could result in large-scale disruption. A large network of companies in the supply chain is, therefore, favourable to minimise such large-scale damage. 50 Any such shortages in supply may result in price increases. Co shortages experienced between 2016 and 2017 saw Co prices approximately double (Figure 2.5a). It is estimated that the cost of NCA and NMC increased by roughly 12.5%, as a result. A further decrease in Co content would limit the propagation of price and supply volatility to LIBs.<sup>74</sup> In contrast, Ni prices are far less volatile yet have seen a recent increase in prices, to their highest in six years due to increased demand for EVs (Figure 2.5a). Li<sub>2</sub>CO<sub>3</sub>, on the other hand, experienced a drop in price between 2018 and late 2020 as increased production was not met by the required demand within EVs (**Figure 2.5b**).<sup>75</sup> In order to sustain supply and demand, efforts must focus on developing electrode materials that are not reliant on scarce materials, extending battery lifetimes and improving reuse, repurpose, recycling and remanufacturing frameworks.<sup>76</sup> Recycling offers a reduced burden on mining by feeding into supply, reducing the primary metals required to meet demand. Supply risk also has the potential to benefit from recycling as secondary metal production can be exploited in countries without geological supply, thus diversifying the current supply chain. If, however, secondary supply is dominated by primary supplying countries, such as China, risks to supply would remain.<sup>62</sup> That being said, recycling will not alleviate strain within the near future given the lifetime of LIBs, rendering large material quantities in use until significant numbers of batteries reach end-of-life.<sup>64</sup>

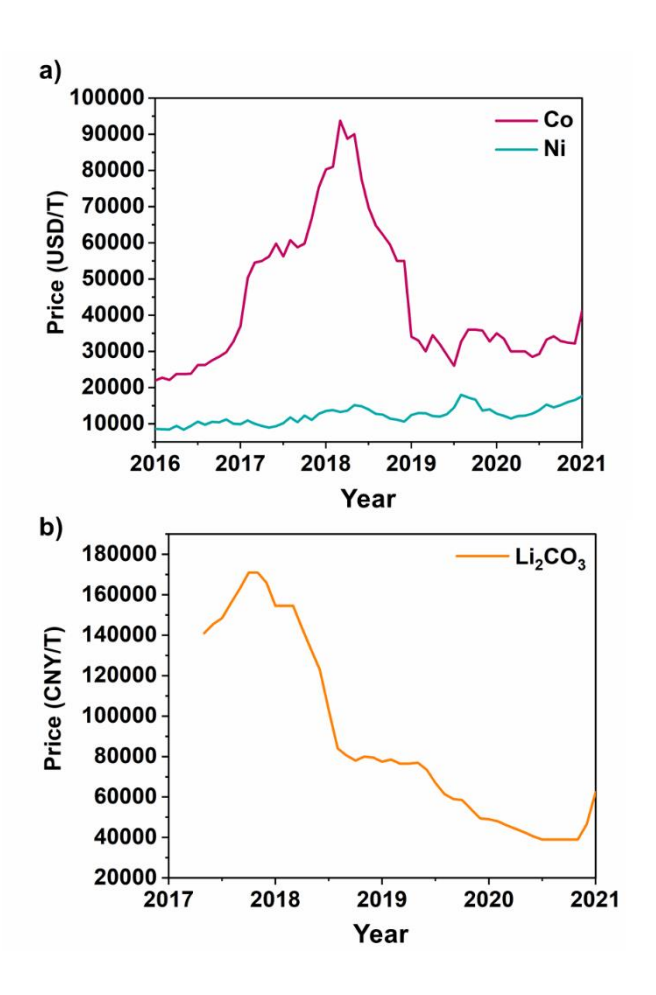


**Figure 2.5**: a) Price fluctuations of Co and Ni from 2016-2021 (USD/T). b) Price fluctuations of Li<sub>2</sub>CO<sub>3</sub> traded in China, from 2017-2021 (CNY/T). Data from collected from references [<sup>77–79</sup>].

# 2.3.4 Environmental, Social and Governance (ESG) Impacts

Issues surrounding economics, supply, and demand appear to be the focus of LIB concerns, with a modest amount of literature reports on further environmental and societal matters. Sovacool *et al.* revealed the extreme risks to both environmental and public health, as well as social implications of gender discrimination and child labour in the DRC, exacerbated by the increasing adoption of 'green technologies' such as EVs. <sup>80</sup> Gender inequality in such areas, is allowed through mining hierarchies in which women appear very low, thus often carrying out the most strenuous yet poorly paid activities. <sup>80</sup> An estimated 23% of children within the DRC (many of whom are orphans) work within Co mining where they are exposed to physical, physiological and sexual abuse in order to provide for themselves and their families. <sup>80</sup> The long-lasting health impacts to societies within the vicinity of Co mines has been made apparent

through the elevated Co levels in their blood and urine resulting in potential heart, lung, thyroid and blood complications. 74 Handling mining waste appropriately is also of utmost importance for ensuring the welfare of local residents. Waste from a previous mining plant, after long storage, was shown to have polluted surface and groundwater, atmospheric air, and soils with waste metals. The large number of heavy metals in water systems resulted in their presence within local foods.<sup>81</sup> In addition to toxicity concerns, tunnels dug for mining purposes lead to soil erosion and land instability.<sup>80</sup> Thies et al. considered child labour, corruption, occupational toxicity and hazards, and poverty as social risk factors throughout the supply chain of LIBs, through a social life cycle analysis—all of which were significantly reduced through the responsible sourcing of raw materials.82 The supply chains investigated considered raw materials, cell components, battery cell production and battery pack production. Comparisons between supply chains that consisted of China- and Germany-based battery cell and battery pack production indicated greater risks in all the aforementioned areas from China-based battery production.<sup>82</sup> This highlights the value of responsibly sourcing and producing batteries and battery materials for the health and wellbeing of residents. Artisanal mining within the DRC has been highlighted in recent years due to child labour and unsafe mining conditions.83 Banning of artisanal mining may, however, result in unintended harmful consequences as in poorer areas as it can be the only source of income for local residents.<sup>83</sup> In such communities more money can be earned through Co mining than through agriculture, creating a desire to mine with the hope of escaping poverty.<sup>80</sup> Although such issues accounted for a small amount of artisanal mining, further regulations and control are required to prevent such atrocities.83

Mining holds influence over ≈ 50 million km² of terrestrial surface area, with 82% of mining area targeting critical materials required for clean energy production.<sup>84</sup> As the demand for different metals changes, the mining landscape will evolve with new mines opening, where desired ores are concentrated, and other mines closing due to declines in demand. The forced relocation of local residents to allow for mining expansion and the inhabitancy of old mining areas, due to decreased land quality, leaves a profound social and health impact on the local community.<sup>85</sup> In addition to residential areas, agricultural land and forestry also suffer due to mine expansion, with 14% of protected areas being within, or close to, metal mining areas.<sup>85</sup> The density of mining areas extracting critical metals that overlap with protected areas is far greater than the density of other mining areas which overlap. This indicates that with increased demand for critical metals for LIBs comes increased threats to biodiversity.<sup>84</sup> This provides additional ecological and environmental concerns beyond material exhaustion. Such socioenvironmental considerations are often beyond the scope of the supply, demand, and economic concerns of mining activities. New and developing mining activities are thus encouraged to formulate considered mining plans that aim to assess nearby eco-systems,

long-term effects and possible rehabilitation strategies.85 It should be noted that issues will arise from the mining of most metals. It is, however, important to critically assess each in order to select those which pose minimal damage pre-use, during use and post-use. A comparative analysis into the ESG risk of a variety of TMs used in green technologies, performed by Lèbre et. al, indicated that 70% of Co resources reside in areas with high ESG risks that are associated with a variety of factors across social vulnerability, land use, governance and waste.86 Li, on the other hand, shows 65% of resources are in areas with low to medium ESG risk, where water use presents the biggest concern among the ESG factors (Figure 2.6).86 Ni and Fe show mining projects that are evenly divided across both high- and low-risk areas, where management and mitigation of ESG risks prove to be of critical importance for a global strategy to ensure minimal environmental and social impact with increasing demand.86 Fe, when compared to Ni, Co and Li shows very low ESG risk, with the biggest concerns stemming from toxic waste and land use (Figure 2.6).86 Primary environmental concerns related to Co, other than material exhaustion, are eutrophication and global warming potential, due to large amounts of electricity consumption for extraction. For Ni and Mn, on the other hand, greenhouse gas emissions (GHG) pose the biggest concern due to fossil fuel usage in mining, extraction and refining.<sup>87</sup> Access to sufficient renewable energy on the mining sites poses a hurdle for reducing GHG and global warming potential (GWP) as replacing existing supplies will prove time-consuming and costly.87 Using high-grade ores can both economically and environmentally beneficial as processing requirements are lowered. As resources deplete, however, the extraction from low-grade ores will be inevitable.87

Ni production, particularly from Ni sulphate (NiSO<sub>4</sub>), is a very energy-intensive process that generates large amounts of sulphur dioxide (SO<sub>2</sub>) during refinement.<sup>88</sup> This significantly increases the emissions related to LIB production. For this reason, the source of Ni production was shown to have a significant effect on the environmental impact through varying stringency on SO<sub>x</sub> capture, with Canadian refined Ni producing 0 kg SO<sub>x</sub> per kg NiSO<sub>4</sub> and Russian refined producing 2,902,991 kg SO<sub>x</sub> per kg NiSO<sub>4</sub>.<sup>88</sup> This is dependent on the use of sufficient technology to capture and convert SO<sub>x</sub> emissions and highlights the importance of responsible sourcing. These figures are particularly alarming when considering that Russia produced 21.1% of battery-grade Ni I in 2019, the largest producer of that year.<sup>61</sup> Life-cycle analysis conducted by Kallitsis *et al.* modelled three scenarios based on different NMC cathode chemistries (111, 622 and 811). Similar threats to humans and ecosystems are presented by novel chemistries.<sup>89</sup> NiSO<sub>4</sub> production, however, resulted in an increase in all ecotoxicity categories considered as cathode Ni content increased. An overall decrease in the impact of LIBs using novel Ni-rich cathodes is provided through expected increased capacities. The prospect that the initial lifespan of novel positive electrodes may be inferior to existing ones

should be considered and may limit the reduction of impact over the whole lifetime. Of the aspects considered—namely mining, extraction, processing, manufacture and assembly—battery production was found to have the most profound environmental impacts. This is largely a consequence of non-renewable energy use in battery production.<sup>89</sup> The energy-intensive processing of Ni and Co ores accounts for a large proportion of energy consumption required to produce NMC-type cathodes. LMO and LFP cathodes, on the other hand, consume the most energy during the cathode preparation stage.<sup>20</sup>

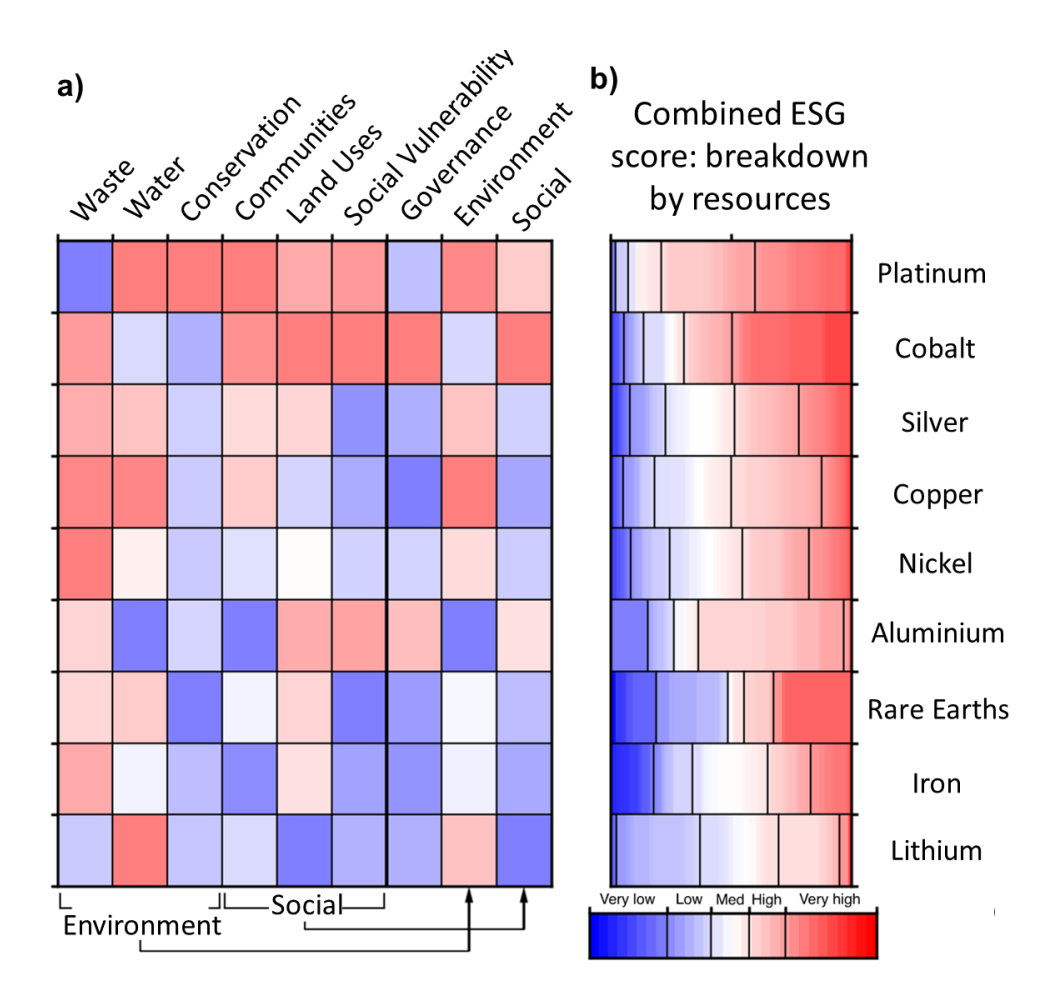


**Figure 2.6:** a) ESG risk matrix for nine metals ranked by total score, defined as the sum of the scores for the seven dimensions (first seven columns), in which environmental risk is comprised of waste, water and conservation and social risk is comprised of communities, land uses and social vulnerability. b) The breakdown of total risk scores by resource tonnage. Colours respond to risk level, with red showing higher risk and blue showing lower risk. Reproduced with permission from <sup>86</sup>

With regards to the Ti dioxide (TiO<sub>2</sub>) precursor, for which demand may increase if disordered rock-salt cathodes are to be successfully commercialised, production from starting materials such as rutile, ilmenite or Ti slag can be achieved through two methods: the chloride route and

the sulphate route.<sup>66</sup> As with Ni processing, the use of sulfuric acid in the sulphate route poses potential environmental issues, which as previously mentioned can be eliminated through the use of sufficient mitigation practices.<sup>90</sup> Acid treatment, however, renders the sulphate route more costly.<sup>90</sup> The sulphate route is predicted to be the most common throughout Europe and China, whereas the chloride route dominates America.<sup>66</sup> The chloride route produces TiO<sub>2</sub> with higher purity and so such routes may be necessary to provide battery grade TiO<sub>2</sub>.<sup>66</sup> Greater understanding into the impacts of Ti processing, and subsequent comparison with Ni, and Co, would be beneficial for understanding the true environmental gain of replacing Ni- and Co-rich chemistries.

### 2.3.5 End-of-life and Waste Management

The possibility of a secondary metal supply from spent LIBs is commonly considered as a necessary addition to the extraction of raw materials in order to meet future demand. Waste LIBs from EVs, and other portable devices, are rapidly accumulating with little regulation in place to ensure safe and sufficient disposal within a coherent waste hierarchy scheme: prevention, reuse, repurpose, recycle, disposal. Prevention, as previously discussed (see *Current Cathode Technology and Material Development* section), can be realised through material development, in which the amount of critical raw metal within cathode materials can be minimised. Subsequent improvement in performance of such materials is vital for lowering overall long-term demand.

Reuse involves the repair and/or remanufacture of spent LIBs for use in the same applications, whilst repurposed LIBs are to be used for less demanding energy storage (i.e. second-use).<sup>91</sup> For effective re-use, efficient battery management will be required in order to retrieve LIBs with approximately 80% state of health for subsequent repair and recirculation, likely as part of a battery leasing scheme.<sup>91</sup> LIB repair can involve identifying the cells within the battery pack (≈ 10%) with the poorest state of health (SOH).<sup>92</sup> The identified cells can then be replaced, with fresh cells, avoiding replacement of the whole pack. Research into alternative charging methods illustrates a possibility of rejuvenating spent LIBs without disassembly, potentially reducing costs when compared to remanufacture and recycling waste streams. One such charging method is sinusoidal wave charging, as opposed to constant current charging, in which cycling to negative currents allows the reduction of solid electrolyte interface species at the anode surface, improving passivation.<sup>93</sup> This method has been shown to revive aged LiFePO₄-based cells with SOH of 60−70%, 70−80%, and 80−90% by 18.7%, 9.5% and 4.2%, respectively.<sup>93</sup>

Whilst reuse would be intuitively favoured over repurposing due to less processing required, a study into the eco-efficiency of end-of-life (EOL) routes showed that repurposing allowed for

greater reductions in cumulative energy demand, eco-toxicity, metal input and economic benefit. This outcome largely came from the replacement of Pb-acid stationary storage with LIB stationary storage. However, the quantity of LIBs that can be repurposed for second-use will far outweigh the second-use demand, due to the large amount of EVs going into circulation. Furthermore, such repurposing will delay the retrieval of critical metals before the LIBs are eventually discarded. The successful implementation of battery recycling and critical metal recovery is, therefore, crucial for providing a sustainable supply of battery materials.

Each of the aforementioned EOL scenarios is limited by low collection rates (0-25% across different EU countries). <sup>96</sup> Such rates are proposed to be a result of insufficient EOL policy and public awareness of disposal protocols from which spent LIBs are often incorrectly disposed of or left as hibernating stock within society. <sup>96</sup> Under UK regulation the battery producer is responsible for paying for waste battery collection, treatment, recycling and disposal. <sup>97</sup> Whilst the disposal of LIBs into landfill is illegal under UK law<sup>97</sup>, insufficient public awareness and lack of accessible disposal routes, such as curbside collection, renders such practices inevitable. <sup>98</sup> The incorrect disposal of LIBs poses a significant safety concern due to the associated electrical, chemical and fire hazards that arise from damage to the battery packs and the leaching of internal chemicals. Such events have seen approximately 48% of UK annual waste fires to be a result of waste LIBs. <sup>98</sup> This risk results in high transportation and processing costs such as manual disassembly, limiting the possibility for automated systems. <sup>99</sup> Whilst such manual disassembly may suffice in the short term, it will fail to cope with the greater influx of spent LIBs that is expected to come. <sup>99</sup> Automation within the disassembly line will, therefore, be paramount to the success of recycling operations. <sup>99</sup>

#### 2.3.6 Recycling

In addition to extending resources, the successful recycling of LIBs is suggested to alleviate other environmental concerns surrounding metal extraction, such as pollution, energy use and water use. <sup>20,95,96,99–110</sup> Beyond the environment, and as previously discussed (see *Supply Risk* section), a domestic secondary supply will reduce supply risk and mitigate price fluctuations, in addition to avoiding high transportation and processing costs of exporting and disposing of E-waste. <sup>104</sup> The price of recycled materials, however, may struggle to be competitive with primary resources, especially at the early stages of recycling development. This calls for incentives from policymakers to internalise social and environmental costs or subsidise recycled materials. <sup>91</sup> The benefits that recycling has on the social impacts of metal extraction, however, are largely unknown and may be a worthwhile investigation for future works to ensure the desired positive social impact.

Numerous reviews have been published within the last couple of years, in which various recycling methods under development are critically analysed. 20,95,106–110,96,99–105 Whilst an indepth review of recycling methods is beyond the scope of the work presented herein, the technologies under development are briefly discussed and the trends in challenges identified and future outlooks proposed within a series of reviews are considered.

A variety of different recycling methods exist within the literature namely pyrometallurgy, hydrometallurgy, biometallurgy (Figure 2.7) and direct recycling. Recycling first requires LIBs to be discharged, typically through the use of saturated sodium chloride solutions. If disassembling under inert conditions (e.g. under argon), however, such discharging is not necessary. 108 Mechanical separation is then used to dismantle the battery into its different components, from which the cathode material is extracted and further treated. Pyrometallurgy involves the heat treatment of recovered cathode materials to form an alloy of Cu, Co, Ni and Fe. Li and Al, on the other hand, are contained with the remaining slag from which they are difficult to extract. Due to the simplicity of pyrometallurgy, it is an attractive choice for recycling operations. However, the use of high temperatures and the release of significant greenhouse gasses limits its eco-friendliness. Hydrometallurgy involves the selective dissolution, leaching, separation and purification of metals from waste cathode materials. Typical leaching agents include H<sub>2</sub>SO<sub>4</sub>, HNO<sub>3</sub> and HCl. <sup>108</sup> Research into organic leaching agents, however, (such as oxalic and citric acid) is gaining importance in order to provide a more environmentally friendly alternative.111 Bio-metallurgy uses microbiological processes that can produce organic or inorganic acids to extract critical metals. 100 Cathodes can then be resynthesized from the leachate solution via a co-precipitation or sol-gel method, which can simplify separation and purification steps. 111 Both hydrometallurgy and bio-metallurgy have the advantage of being able to recover Li, unlike pyrometallurgy. However, the high volumes of effluents produced require treatment before disposal. 108 Whilst bioleaching provides an eco-friendly and energyefficient method, its poor adaptability and leaching conditions required currently limit its suitability for industrial applications. 111 Direct recycling poses a method in which the crystal structure can be retained thus improving the economic feasibility in addition to lowering environmental impacts. 112,113

The cost of different recycling methods is comprised of labour costs, material costs and utilities amongst additional expenses such as tax, rent, insurance, and maintenance (**Figure 2.7b**).<sup>114</sup> Leaching chemicals required for hydrometallurgical recycling result in higher material costs, whereas pyrometallurgical recycling is more labour-intensive with higher utility costs, resulting in a higher overall cost in comparison. The financial viability of hydrometallurgical,

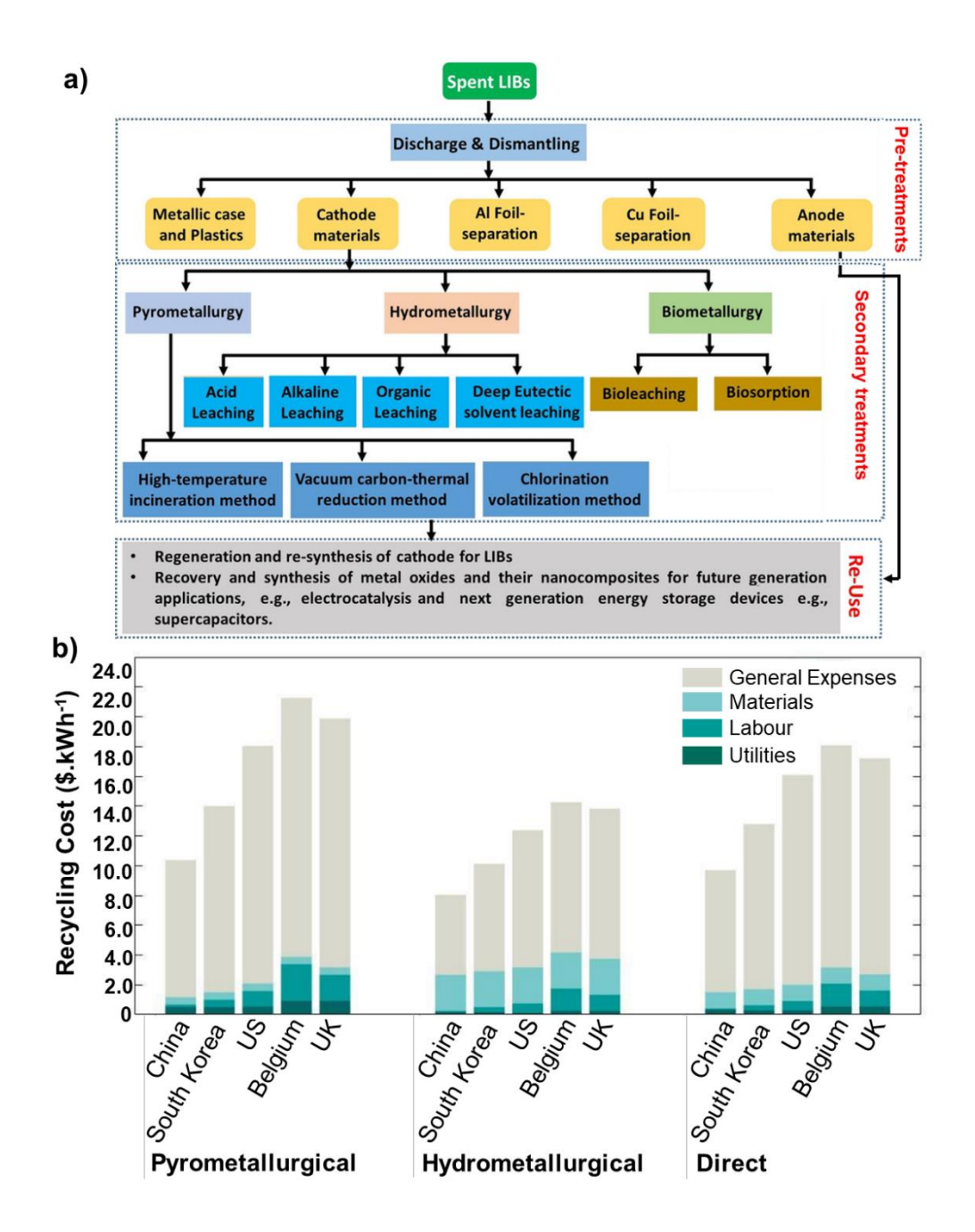


**Figure 2.7:** a) Schematic illustrating the closed-loop approach to LIB EOL through recycle and reuse. Reproduced with permission from <sup>95</sup> (copyright Wiley Materials), b) Breakdown of recycling cost for a 240 Wh kg<sup>-1</sup> NCA battery pack, reproduced with permission from <sup>114</sup>.

pyrometallurgical and direct recycling methods are impacted by a series of factors including transport distances, labour cost, disassembly cost, recycling capacity and revenue generated from recovered materials. Although direct recycling is predicted to be slightly more expensive than hydrometallurgical recycling, higher net profit is anticipated with increased scaling due to increased revenue through higher material recovery. In comparison to European countries, such as Belgium and the UK, China and South Korea show lower recycling costs due to lower labour and general expenses costs. Despite this, an analysis into possible recycling routes for

spent UK LIBs revealed that, due to high transportation costs, recycling abroad is uneconomic regardless of the cell chemistry and recycling method adopted. 114 The EOL of LIBs is confronted with many challenges spanning across social, environmental, economic, political, technical and chemical domains. Technical concerns dominate recent reviews, with barriers to automation seen as significant challenges. 20,95,106-110,96,99-105 Such barriers include the nonuniformity in cell designs adopted by different manufacturers. Furthermore, the large variety of cell chemistries used in LIBs requires sorting before recycling can begin. Whilst a mixed market of battery materials may be beneficial for conserving resources, a wide variety of chemistries in circulation renders highly specific recycling techniques inadequate. The lack of labelling systems on battery packs makes pre-sorting challenging, and introduces additional safety concerns as LIBs can enter Pb-acid battery waste streams accidentally. 102 Of the reviews considered, 20,95,106-110,96,99-105 the technical barriers to widespread adoption of LIB recycling identified were ubiquitous, with each highlighting the need for; 1) sufficient labelling systems for easy identification, 2) standardisation of cell material, cell design and processing, and/or greater flexibility in the recycling processes, 3) minimisation of components, 4) screening, health monitoring and sorting methods and 5) automation in the disassembly line. It was acknowledged by the majority of reviews that many of these challenges require necessary intervention from policy-makers to provide a clear recycling industry chain and introduce sufficient regulations for the safe transport and handling of waste LIBs. 94,95,99-103,107,109

Whilst recycling offers a potential secondary supply of materials, amongst other benefits, it is important to consider net changes in energy consumption when recycled materials are implemented. With a few exceptions, 100,109,115 environmental concerns related to recycling are largely underexamined and, if so, addressed qualitatively. Conclusions made by Huang *et al.* highlighted the need for further quantification of environmental damage/benefit including the quantification of waste and emissions. 109 For example, a study by Ciez *et al.* indicates pyrometallurgical and hydrometallurgical recycling processes do not pose significant environmental benefits when considering resulting reductions in greenhouse gas emissions. 74 For more environmentally friendly cathode technologies, such as LiFePO<sub>4</sub> (LFP), no amount of recovered LFP is sufficient to offset GHG emissions that result from both the recycling process and the incineration of other waste components. Furthermore, the decrease in Co concentration reduces the economic viability of such processes, perhaps limiting the recyclability of Li and Ni. Having said that, if Ni resources begin to deplete to the levels that Co is currently experiencing, the economic viability of such recycling will inevitably increase.

As previously mentioned, direct recycling poses a method with greater economic and environmental benefits. 112,113 Recent works demonstrated the possibility of directly recycling

LFP<sup>113</sup> and LMO<sup>112</sup> cathodes, in which life-cycle analysis showed a reduction in both GHG emissions (≈ 70%) and energy usage (> 75%). A critical review of recycling techniques, performed by Piątek et. al, revealed that, within the principles of green chemistry and circular economy, solutions presented are often very unsustainable. Whilst recycling is key for materials sustainability, this adds another level of complexity to the holistic LIB sustainability problem whereby recycling efforts must employ technologies that do not pose additional negative environmental and social issues.

#### 2.4 Conclusion and Outlook

The issues presented by the widespread use of LIBs cover a wide range of sectors from onset through to end-of-life. Amongst them, mining and material management, socio-environmental life cycle analysis, material development and end-of-life management, outlined herein, are crucial for understanding and mitigating concerns surrounding supply risk and environmental, social and governance (ESG) issues. Whilst each one of these sectors plays an important role in LIB research, they are often considered as individual entities without additional thought to the other contributors. This review aims to place such material development into the wider context of ESG factors, in order to better inform cathode material development.

Progression towards 'sustainable' cathode materials within the industry has seen a shift to Nirich chemistries. However, the dependence of LIBs on high-grade Ni ore may pose a limit to supply. Supply and demand projections that consider ore grade will, therefore, be vital in assessing the Ni resources available for battery applications. The increasing complexity of the EV and wider battery market results in an increased number of parameters to be considered, in which ore grade, the various EV battery types and sizes used, as well as non-battery applications will demand greater attention. With an increased number of parameters, however, comes increased uncertainty in the results obtained. It is therefore important to critically analyse previous models against real-time supply and demand data in order to determine their accuracy and provide an explanation for discrepancies to allow for the development of improved, and eventually standardised models. Standardisation of such modelling would prove beneficial for comparing between different elements and can be translated to other elements contained within newer cathode chemistries, to highlight changes in material sustainability with cathode composition. Due to the dynamic nature of available reserves, increased efforts to strengthen supply chains (e.g. establishment of more Co-primary mines), and the exploration of new mining opportunities (e.g. deep-sea and Li clay mining), long-term models previously considered may require reassessment to account for such changes.

While the market is dominated by Ni-rich cathodes, new cell architectures (e.g., the Blade Battery) have prompted a surge in industrial interest into LFP and LMFP. Promising future

cathode materials such as LNMO spinels and disordered rock-salts, however, require further research to allow widespread commercialisation before they can alleviate supply constraints.

The potential limit to supply, in addition to geopolitical and company-based supply risk, may add further strain to cathode and LIB supply chains. Such supply may, however, benefit from the successful implementation of reuse, repurposing and recycling in order to extend the use of critical metals in stock and better distribute secondary resources that do not have such a significant dependence on geographical location. Implementation at a large scale, however, is limited by poor financial viability and lack of automation. Thus, developing simple and low-cost methods with increased recovery rates is vital for ensuring a secondary supply. Financial viability can be further improved by establishing domestic LIB waste schemes by avoiding high transportation costs, in which sufficient policy surrounding LIB waste management, increased recycling capacity and increased public awareness will be key. Whilst a secondary supply is crucial, the additional environmental impacts of recycling, such as waste and emissions, adds further complexity. Current literature lacks quantification of such impacts which is necessary for critically assessing and comparing various recycling methods.

Beyond material sustainability, further efforts are required to ensure environmental sustainability of Ni used in LIBs by introducing sufficient international regulation on sulphate capture to prevent additional damage caused by NiSO<sub>4</sub> processing emissions. It is therefore expected that in the future, more sustainable battery chemistries based on Co-free and low-Ni content materials focused on Fe, Mn and Ti elements will provide both socio-economic and environmental gain. However, a foreseeable practical research challenge will be engineering cathode materials with adequate elemental compositions that can achieve comparable or even better performance metrics than well-established and commercialised cathode materials. Similarly, these new materials will require a critical assessment on ESG issues to encourage sustainability progression and successful and responsible use in LIBs for EVs.

#### 2.5 References

- 1 United Nations, Paris Declaration on Electro-Mobility and Climate Change & Call to Action, https://unfccc.int/news/the-paris-declaration-on-electro-mobility-and-climate-change-and-call-to-action.
- 2 K. Vignarooban, R. Kushagra, A. Elango, P. Badami, B. E. Mellander, X. Xu, T. G. Tucker, C. Nam and A. M. Kannan, *Int. J. Hydrogen Energy*, 2016, **41**, 2829–2846.
- 3 N. Nitta, F. Wu, J. T. Lee and G. Yushin, *Mater. Today*, 2015, **18**, 252–264.
- 4 J. Desjardins, The Cathode is the Key to Advancing Lithium-Ion Technology, https://www.visualcapitalist.com/cathode-advancing-lithium-ion/.

- 5 S. Ahmed, P. A. Nelson, K. G. Gallagher, N. Susarla and D. W. Dees, *J. Power Sources*, 2017, **342**, 733–740.
- 6 Cobalt Price, https://www.metalary.com/cobalt-price, (accessed 23 January 2020).
- Metallary, Iron Price, https://www.metalary.com/iron-price/, (accessed 11 January 2021).
- 8 S. W. D. Gourley, T. Or and Z. Chen, *iScience*, 2020, **23**, 101505.
- 9 S. W. Kim, D. H. Seo, X. Ma, G. Ceder and K. Kang, *Adv. Energy Mater.*, 2012, **2**, 710–721.
- 10 R. Mohtadi and F. Mizuno, *Beilstein J. Nanotechnol.*, 2014, **5**, 1291–1311.
- 11 R. J. Gummow, G. Vamvounis, M. B. Kannan and Y. He, *Adv. Mater.*, 2018, **30**, 1–14.
- 12 X. Zeng, M. Li, D. Abd El-Hady, W. Alshitari, A. S. Al-Bogami, J. Lu and K. Amine, *Adv. Energy Mater.*, 2019, **9**, 1–25.
- A. Yamada, S. C. Chung and K. Hinokuma, J. Electrochem. Soc., 2001, 148, A224.
- 14 R. J. Gummow, A. de Kock and M. M. Thackeray, Solid State Ionics, 1994, 69, 59–67.
- 15 Y. K. Sun, S. T. Myung, B. C. Park and K. Amine, *Chem. Mater.*, 2006, **18**, 5159–5163.
- 16 P. Hou, H. Zhang, Z. Zi, L. Zhang and X. Xu, *J. Mater. Chem. A*, 2017, **5**, 4254–4279.
- 17 S.-J. Yoon, K.-J. Park, B.-B. Lim, C. S. Yoon and Y.-K. Sun, *J. Electrochem. Soc.*, 2015, **162**, A3059–A3063.
- 18 R. Schmuch, R. Wagner, G. Hörpel, T. Placke and M. Winter, *Nat. Energy*, 2018, **3**, 267–278.
- 19 W. Li, E. M. Erickson and A. Manthiram, *Nat. Energy*, 2020, **5**, 26–34.
- J. B. Dunn, C. James, L. Gaines, K. Gallagher, Q. Dai and J. C. Kelly, *Argonne Natl. Laborartory*, 2015, **53**, 1689–1699.
- 21 K. Shang, Nickel sulphate: In high-nickel batteries, safety comes into question, https://roskill.com/news/nickel-sulphate-in-high-nickel-batteries-safety-comes-into-question/.
- 22 A. Elshkaki, B. K. Reck and T. E. Graedel, *Resour. Conserv. Recycl.*, 2017, **125**, 300–307.
- 23 J. Gong, Q. Wang and J. Sun, *Thermochim. Acta*, 2017, **655**, 176–180.

- 24 M. Wentker, M. Greenwood and J. Leker, *Energies*, 2019, **12**, 1–18.
- W. Bernhart, Battery Recycling is a Key Market of the Future: Ist it also an Oppourtunity for Europe?, https://www.rolandberger.com/en/Insights/Publications/Battery-recycling-is-a-key-market-of-the-future-Is-it-also-an-opportunity-for.html.
- 26 R. N. Ramesha, D. Bosubabu, M. G. Karthick Babu and K. Ramesha, *ACS Appl. Energy Mater.*, 2020, **3**, 10872–10881.
- 27 R. J. Clément, Z. Lun and G. Ceder, *Energy Environ. Sci.*, 2020, **13**, 345–373.
- 28 M. Yang, X. Zhao, C. Yao, Y. Kong, L. Ma and X. Shen, *Mater. Technol.*, 2016, **31**, 537–543.
- 29 R. Chen, R. Witte, R. Heinzmann, S. Ren, S. Mangold, H. Hahn, R. Hempelmann, H. Ehrenberg and S. Indris, *Phys. Chem. Chem. Phys.*, 2016, **18**, 7695–7701.
- M. Freire, M. Diaz-Lopez, P. Bordet, C. V. Colin, O. I. Lebedev, N. V. Kosova, C. Jordy, D. Chateigner, A. L. Chuvilin, A. Maignan and V. Pralong, *J. Mater. Chem. A*, 2018, 6, 5156–5165.
- 31 A. KITAJOU, K. TANAKA, H. MIKI, H. KOGA, T. OKAJIMA and S. OKADA, *Electrochemistry*, 2016, **84**, 597–600.
- 32 S. T. Myung, F. Maglia, K. J. Park, C. S. Yoon, P. Lamp, S. J. Kim and Y. K. Sun, *ACS Energy Lett.*, 2017, **2**, 196–223.
- 33 Y. Ding, Z. P. Cano, A. Yu, J. Lu and Z. Chen, *Electrochem. Energy Rev.*, 2019, **2**, 1–28.
- Z. Lei, A. Naveed, J. Lei, J. Wang, J. Yang, Y. Nuli, X. Meng and Y. Zhao, *RSC Adv.*,
   2017, 7, 43708–43715.
- S. Hasan, M. S. Islam, S. M. A. Bashar, A. Al Noman Tamzid, R. Bin Hossain, M. A. Haque and M. F. Rahaman, *E3S Web Conf.*, 2023, **469**, 00005.
- 36 R. Yang, L. Chang, S. Luo, X. Bi, W. Yang, K. Cai, A. Wei and Z. Hou, *J. Mater. Chem. C*, 2024, **12**, 4961–4976.
- 37 G. Liang, V. K. Peterson, K. W. See, Z. Guo and W. K. Pang, *J. Mater. Chem. A*, 2020,8, 15373–15398.
- Jeppe Winther Hedegaard, The Cathode Material for Next-Generation Lithium ion Batteries is Ready, https://www.topsoe.com/blog/the-cathode-material-for-next-generation-lithium-ion-batteries-is-ready.

- 39 D. W. Shin, C. A. Bridges, A. Huq, M. P. Paranthaman and A. Manthiram, *Chem. Mater.*, 2012, **24**, 3720–3731.
- 40 G. T. K. Fey, C. Z. Lu and T. Prem Kumar, *J. Power Sources*, 2003, **115**, 332–345.
- 41 Q. Zheng, Y. Yamada, R. Shang, S. Ko, Y. Y. Lee, K. Kim, E. Nakamura and A. Yamada, *Nat. Energy*, 2020, **5**, 291–298.
- 42 Z. Zou, H. Xu, H. Zhang, Y. Tang and G. Cui, *ACS Appl. Mater. Interfaces*, 2020, **12**, 21368–21385.
- 43 S. Deng, B. Wang, Y. Yuan, X. Li, Q. Sun, K. Doyle-Davis, M. N. Banis, J. Liang, Y. Zhao, J. Li, R. Li, T. K. Sham, R. Shahbazian-Yassar, H. Wang, M. Cai, J. Lu and X. Sun, *Nano Energy*, 2019, **65**, 103988.
- Y. Shu, Y. Xie, W. Yan, S. Meng, D. Sun, Y. Jin and K. He, *J. Power Sources*, 2019,433, 226708.
- N. Kiziltas-Yavuz, M. Yavuz, S. Indris, N. N. Bramnik, M. Knapp, O. Dolotko, B. Das, H. Ehrenberg and A. Bhaskar, *J. Power Sources*, 2016, **327**, 507–518.
- 46 P. W. Gruber, P. A. Medina, G. A. Keoleian, S. E. Kesler, M. P. Everson and T. J. Wallington, *J. Ind. Ecol.*, 2011, **15**, 760–775.
- 47 Lithium statistics and information, 2020, vol. 53.
- 48 McKinsey&Company, McKinsey&Company Met. Min.
- 49 A. Grant, M. Whittaker and C. Aaron, Inside Tesla 's Lithium Clay Salt Extraction Process, https://www.jadecove.com/research/teslasaltclay, (accessed 10 February 2021).
- 50 S. van den Brink, R. Kleijn, B. Sprecher and A. Tukker, *Resour. Conserv. Recycl.*, 2020, **156**, 104743.
- X. Fu, D. N. Beatty, G. G. Gaustad, G. Ceder, R. Roth, R. E. Kirchain, M. Bustamante,C. Babbitt and E. A. Olivetti, *Environ. Sci. Technol.*, 2020, **54**, 2985–2993.
- 52 S. H. Farjana, N. Huda, M. A. P. Mahmud and C. Lang, *Sci. Total Environ.*, 2019, **688**, 1102–1111.
- F. Jordans, Why automakers are joining the push against deep seabed mining, https://www.csmonitor.com/Environment/2021/0331/Why-automakers-are-joining-the-push-against-deep-seabed-mining.

- 54 R. Carver, J. Childs, P. Steinberg, L. Mabon, H. Matsuda, R. Squire, B. McLellan and M. Esteban, *Ocean Coast. Manag.*, 2020, **193**, 105242.
- 55 U.S. Geological Survey, Commodity Statistics and Information, https://www.usgs.gov/centers/nmic/commodity-statistics-and-information, (accessed 11 January 2021).
- 56 BGS, Uk and World Mineral datasets and statistics, https://www.bgs.ac.uk/datasets/uk-and-world-mineral-statistics-datasets/, (accessed 11 January 2021).
- J. Speirs, M. Contestabile, Y. Houari and R. Gross, *Renew. Sustain. Energy Rev.*, 2014, **35**, 183–193.
- 58 T. P. Narins, Extr. Ind. Soc., 2017, 4, 321–328.
- 59 H. Vikström, S. Davidsson and M. Höök, *Appl. Energy*, 2013, **110**, 252–266.
- D. Calisaya-Azpilcueta, S. Herrera-Leon, F. A. Lucay and L. A. Cisternas, *Minerals*, 2020, **10**, 1–20.
- A. Marcelo, N. Goffaux and K. Hoffman, *McKinsey insights*, 2020, 1–6.
- 62 K. Habib, S. T. Hansdóttir and H. Habib, Resour. Conserv. Recycl., 2020, 154, 104603.
- 63 Climate Change 2014 Synthesis Report, 2014.
- 64 E. A. Olivetti, G. Ceder, G. G. Gaustad and X. Fu, *Joule*, 2017, 1, 229–243.
- W. M. Haynes, CRC Handbook of Chemistry and Physics, CRC Press, 97th edn., 2016.
- 66 C. Perks and G. Mudd, *Ore Geol. Rev.*, 2019, **107**, 629–646.
- 67 Y. Song, N. Wang and A. Yu, Resour. Policy, 2019, **64**, 101506.
- 68 S. Li, J. Yan, Q. Pei, J. Sha, S. Mou and Y. Xiao, Sustain., 2019, 11, 1–23.
- 69 G. M. LaRocca, .
- 70 A. L. Gulley, E. A. McCullough and K. B. Shedd, *Resour. Policy*, 2019, **62**, 317–323.
- 71 McKinsey, 2021, 2019.
- 72 Tesla partners with nickel mine amid shortage fears, https://www.bbc.co.uk/news/business-56288781.
- 73 C. Helbig, A. M. Bradshaw, L. Wietschel, A. Thorenz and A. Tuma, *J. Clean. Prod.*, 2018, **172**, 274–286.

- 74 R. E. Ciez and J. F. Whitacre, *Nat. Sustain.*, 2019, **2**, 148–156.
- Roberto Sifon-arevalo, Why lithium has turned from gold to dust for investors, https://www.spglobal.com/en/research-insights/articles/why-lithium-has-turned-from-gold-to-dust-for-investors.
- 76 C. W. Babbitt, Clean Technol. Environ. Policy, 2020, 22, 1213–1214.
- 77 Cobalt, https://tradingeconomics.com/commodity/cobalt.
- 78 Nickel, https://tradingeconomics.com/commodity/nickel.
- 79 Lithium, https://tradingeconomics.com/commodity/lithium.
- 80 B. K. Sovacool, A. Hook, M. Martiskainen, A. Brock and B. Turnheim, *Glob. Environ. Chang.*, 2020, **60**, 102028.
- 81 I. V. May, S. V. Kleyn and S. A. Vekovshinina, *IOP Conf. Ser. Earth Environ. Sci.*, , DOI:10.1088/1755-1315/315/6/062024.
- 82 C. Thies, K. Kieckhäfer, T. S. Spengler and M. S. Sodhi, *Procedia CIRP*, 2019, **80**, 292–297.
- 83 S. Gifford, Faraday Insights.
- 84 L. J. Sonter, M. C. Dade, J. E. M. Watson and R. K. Valenta, *Nat. Commun.*, 2020, **11**, 6–11.
- 85 S. Wang, 2020, 21–31.
- 86 É. Lèbre, M. Stringer, K. Svobodova, J. R. Owen, D. Kemp, C. Côte, A. Arratia-Solar and R. K. Valenta, *Nat. Commun.*, 2020, **11**, 1–8.
- 87 S. H. Farjana, N. Huda, M. A. Parvez Mahmud and R. Saidur, *J. Clean. Prod.*, 2019, **231**, 1200–1217.
- 88 J. C. Kelly, Q. Dai and M. Wang, Mitig. Adapt. Strateg. Glob. Chang., 2019, 371–396.
- 89 E. Kallitsis, A. Korre, G. Kelsall, M. Kupfersberger and Z. Nie, *J. Clean. Prod.*, 2020, **254**, 120067.
- 90 Titanium Dioxide (TiO2) Production and Manufacturing Process.
- 91 R. Lee and S. Gifford, Faraday Insights, 2020, 8.
- 92 K. Richa, C. W. Babbitt and G. Gaustad, *J. Ind. Ecol.*, 2017, **21**, 715–730.
- 93 P. Chen, F. Yang, Z. Cao, J. Jhang, H. Gao, M. Yang and K. D. Huang, Batter.

- Supercaps, 2019, 2, 673–677.
- 94 G. Harper, R. Sommerville, E. Kendrick, L. Driscoll, P. Slater, R. Stolkin, A. Walton, P. Christensen, O. Heidrich, S. Lambert, A. Abbott, K. Ryder, L. Gaines and P. Anderson, *Nature*, 2019, 575, 75–86.
- D. J. Garole, R. Hossain, V. J. Garole, V. Sahajwalla, J. Nerkar and D. P. Dubal, *ChemSusChem*, 2020, **13**, 3079–3100.
- 96 A. Nordelöf, S. Poulikidou, M. Chordia, F. B. de Oliveira, J. Tivander and R. Arvidsson, *Batteries*, DOI:10.3390/batteries5030051.
- gov.uk, Waste batteries: producer responsibility, https://www.gov.uk/guidance/waste-batteries-producer-responsibility#:~:text=It's illegal to send waste,sale on the UK market.
- 98 D. Moore, Lithium-ion battery waste fires costing UK over 150m a year, https://www.circularonline.co.uk/news/lithium-ion-battery-waste-fires-costing-uk-over-150m-a-year/.
- 99 L. Gaines, K. Richa and J. Spangenberger, MRS Energy Sustain., 2018, 5, 1–14.
- J. Piątek, S. Afyon, T. M. Budnyak, S. Budnyk, M. H. Sipponen and A. Slabon, *Adv. Energy Mater.*, , DOI:10.1002/aenm.202003456.
- X. Zhang, L. Li, E. Fan, Q. Xue, Y. Bian, F. Wu and R. Chen, *Chem. Soc. Rev.*, 2018,
   47, 7239–7302.
- 102 L. Gaines, Sustain. Mater. Technol., 2014, 1, 2–7.
- 103 A. Mayyas, D. Steward and M. Mann, Sustain. Mater. Technol., 2019, 19, e00087.
- 104 D. Steward, A. Mayyas and M. Mann, *Procedia Manuf.*, 2019, **33**, 272–279.
- T. Fujita, H. Chen, K. tuo Wang, C. lin He, Y. bin Wang, G. Dodbiba and Y. zhou Wei, *Int. J. Miner. Metall. Mater.*, 2021, **28**, 179–192.
- 106 K. M. Winslow, S. J. Laux and T. G. Townsend, *Resour. Conserv. Recycl.*, 2018, **129**, 263–277.
- 107 X. Guo, J. Zhang and Q. Tian, Renew. Sustain. Energy Rev., 2020, 110461.
- 108 Z. A. Kader, A. Marshall and J. Kennedy, *Emergent Mater.*, 2021, 725–735.
- 109 B. Huang, Z. Pan, X. Su and L. An, *J. Power Sources*, 2018, **399**, 274–286.

- 110 C. Liu, J. Lin, H. Cao, Y. Zhang and Z. Sun, *J. Clean. Prod.*, 2019, **228**, 801–813.
- Y. Yao, M. Zhu, Z. Zhao, B. Tong, Y. Fan and Z. Hua, *ACS Sustain. Chem. Eng.*, 2018,6, 13611–13627.
- 112 H. Gao, Q. Yan, P. Xu, H. Liu, M. Li, P. Liu, J. Luo and Z. Chen, *ACS Appl. Mater. Interfaces*, 2020, **12**, 51546–51554.
- 113 P. Xu, Q. Dai, H. Gao, H. Liu, M. Zhang, M. Li, Y. Chen, K. An, Y. S. Meng, P. Liu, Y. Li, J. S. Spangenberger, L. Gaines, J. Lu and Z. Chen, *Joule*, 2020, **4**, 2609–2626.
- 114 L. Lander, T. Cleaver, M. A. Rajaeifar, V. Nguyen-Tien, R. J. R. Elliott, O. Heidrich, E. Kendrick, J. S. Edge and G. Offer, *iScience*, 2021, **24**, 102787.
- 115 D. H. S. Tan, P. Xu and Z. Chen, MRS Energy Sustain., 2020, **7**, 1–13.

# **Chapter 3 | Theory and Experimental Methods**

As discussed in Chapter 2, the increasing reliance on Ni-rich cathode chemistries raises concerns over future Ni supply risk, in addition to the existing challenges surrounding Li and Co. As such the rapid development and commercialisation of low-Ni and Co-free alternatives will be crucial for ensuring a diversified battery supply chain. To this end, LFP has since become of huge industrial interest. LNMO cathodes, on the other hand, lack substantial industrial backing due to their poor cycling stability, despite being a well-established cathode chemistry that offers ESG benefits over NMC-based cathodes (see Chapter 4 for further details). The remainder of this thesis, therefore, focuses on understanding the structure-property-performance relationships in LNMO cathodes, to help these materials break their barriers to commercialisation. This chapter provides a broad overview of the characterisation techniques and methods adopted throughout Chapters 4–5.

### 3.1 Material Synthesis

Several methods exist for cathode material synthesis. The solid-state method—perhaps the most common in literature—is a simple and low-cost method.¹ It involves mixing reagents in a planetary mixer before sintering, typically at high temperatures, for long durations. The resulting material, however, is inhomogeneous with wide particle distribution and poor crystallinity—all attributes that can lead to poor electrochemical performance.¹ As a result, much research has been devoted to alternative methods. Such methods include molten-salt, sol-gel, hydrothermal, spray drying, microwave, and co-precipitation.

Co-precipitation is widely used in industry as it provides good homogeneity and morphological control while being easy to scale.<sup>2</sup> The general process involves mixing TM salts (e.g., TMSO<sub>4</sub>) with a chelating agent (e.g., NH<sub>3</sub>) and precipitating agent (e.g., NaOH) in an aqueous solution, in which the stirring speed, duration, temperature, and pH must be carefully controlled.<sup>2</sup> The resulting precipitate is then filtered, washed, and dried before mixing with a Li source and sintering at high temperatures. Several co-precipitation methods have been studied, such as the hydroxide co-precipitation and the carbonate co-precipitation. NiCO<sub>3</sub>, however, is difficult to form as a stable precipitate, while in hydroxide co-precipitation Mn tends to over-oxidise to MnOOH, making it difficult to control the stoichiometry.<sup>3,4</sup>

Unlike the aforementioned co-precipitation methods, oxalate coprecipitation uses oxalic acid as both the precipitating agent and the chelating agent, mitigating the need for NH<sub>3</sub>. Previous work has demonstrated that Ni and Mn oxalate both precipitate at high efficiencies, allowing better stoichiometric control.<sup>5</sup> Similar to the hydroxide co-precipitation, the oxalate precursor is synthesised before adding the Li source. Some literature, however, reports a one-step

method, in which Li acetate, Ni acetate, and Mn acetate are added to the initial reaction solution and precipitated simultaneously, allowing further control of the stoichiometry.<sup>6</sup> LNMO synthesised by this method produces large chamfered polyhedral particles which can promote Li<sup>+</sup> ion diffusion whilst reducing the surface area and minimising side reactions, thus leading to desirable electrochemical performance and high-tap density.<sup>6–9</sup> As a result, this work uses the one-step oxalate co-precipitation method previously reported as the basis for synthesising LiNi<sub>0.5</sub>Mn<sub>1.5</sub>O<sub>4</sub> (LNMO), LiNi<sub>0.5-x</sub>Fe<sub>x</sub>Mn<sub>1.5</sub>O<sub>4</sub> (Fex) and LiNi<sub>0.5-x</sub>Mg<sub>x</sub>Mn<sub>1.5</sub>O<sub>4</sub> (Mgx) (x = 0.05, 0.1, 0.15 and 0.2). A full list of samples and sample abbreviations can be found in (**Table 3.1**).

The oxalate co-precipitation method adopted in this work involves stirring stoichiometric amounts of Li acetate (Alfa Aesar, 99%), Ni acetate (Aldrich, 99%), Mn acetate (Aldrich, 99%), and either Mg or Fe nitrate (Alfa Aesar, 98%) in deionised water (1h) and precipitating with oxalic acid (Alfa Aesar, 98%). The molar ratio of oxalic acid:cation was 1:1. The solution was stirred for 2 h at room temperature and dried overnight in a water bath (50°C) with continual stirring to produce a mixed-metal oxalate [LiNi<sub>0.5-x</sub>M<sub>x</sub>Mn<sub>1.5</sub>]C<sub>2</sub>O<sub>4</sub>.<sup>6</sup> At this point, the successful precipitation of Fe/Mg is clearly visible; with increased Fe concentration the green precipitate becomes more yellow because Fe oxalate is yellow, and with increased Mg concentration the green precipitate becomes lighter because Mg oxalate is white. The dried precipitate was heated at 500°C for 6 h (heating and cooling rate of 10°C min<sup>-1</sup>) to decompose the precursors into a mixed-metal oxide, allowing the release of CO<sub>2</sub> prior to pellet formation. The resulting mixed-metal oxide was then pressed into pellets (5 tons cm<sup>-2</sup>) before sintering at 900°C for 24 h (heating and cooling rate of 10°C min<sup>-1</sup>) to produce the final cathode active material (CAM).

**Table 3.1:** List of samples and abbreviations.

Sample	Target formulation	Substituent	Substituent mole fraction
abbreviation			
LNMO	LiNi <sub>0.5</sub> Mn <sub>1.5</sub> O <sub>4</sub>	-	-
Mg0.05	$LiNi_{0.45}Mg_{0.05}Mn_{1.5}O_{4}\\$	Mg	0.05
Mg0.1	$LiNi_{0.4}Mg_{0.1}Mn_{1.5}O_4$	Mg	0.1
Mg0.15	$LiNi_{0.35}Mg_{0.15}Mn_{1.5}O_{4}\\$	Mg	0.15
Mg0.2	$LiNi_{0.3}Mg_{0.2}Mn_{1.5}O_4$	Mg	0.2
Fe0.05	$LiNi_{0.45}Fe_{0.05}Mn_{1.5}O_{4}$	Fe	0.05
Fe0.1	$LiNi_{0.4}Fe_{0.1}Mn_{1.5}O_4$	Fe	0.1
Fe0.15	$LiNi_{0.35}Fe_{0.15}Mn_{1.5}O_{4}$	Fe	0.15
Fe0.2	$LiNi_{0.3}Fe_{0.2}Mn_{1.5}O_4$	Fe	0.2

#### 3.2 Electrochemical Characterisation

### 3.2.1 Electrode Preparation

Electrodes were prepared for both electrochemical testing and spectroscopic measurements. Electrode preparation involves coating the CAM onto the Al current collector. Al is the most commonly used positive current collector because of its low cost, high electrical conductivity, and chemical/electrochemical inertness (< 4.5 V). To allow sufficient adhesion of the active cathode material to the current collector, a polymer-based binder is typically required. Polyvinylidene fluoride (PVDF) is the most commonly used because of its wide electrochemical stability window (0–5 V), and excellent mechanical properties while providing high adhesion to the current collector. The Finally, TM oxides typically suffer from poor electronic conductivity. Therefore, to facilitate efficient transport to/from the current collector, a conductive additive is typically used, (e.g., carbon black, CB). The PVDF binder and CB additive are known as inactive components and must be added in small amounts. To produce a homogeneous coating, the CAM, PVDF, and CB are mixed in solution to make a slurry. The selected solvent must be able to effectively dissolve the active/inactive components. For this reason, *N*-methyl pyrrolidone (NMP) is typically used as a strongly polar aprotic solvent that is particularly effective at dissolving the PVDF binder.

In this work, electrodes were prepared by casting a mixture of 80% CAM, 10% Super-P (TOBMachine), and 10% PVDF (Alfa Aesar) in NMP (AcrosOrganics, 99.5%) onto Al foil. The cast slurry was dried at 80°C overnight, punched in 12 mm discs and pressed at 5 tons cm<sup>-2</sup>, before drying under vacuum at 120°C for a further 12 h to remove any residual H<sub>2</sub>O/solvent. The resulting CAM loading was typically 3–3.5 mg cm<sup>-2</sup>.

### 3.2.2 Coin Cell Assembly

As described in Section 1.2, a Li-ion cell consists of a cathode and an anode separated by a separator soaked in electrolyte. This is known as a full-cell configuration (i.e., the cathode is coupled with an anode, **Figure 3.1a**). When using a full-cell configuration, however, it can be difficult to decouple the influence of both the anode and the cathode on the resulting performance. For initial materials research and development, a half-cell configuration is therefore adopted to allow the influence of the respective electrodes to be decoupled (**Figure 3.1b**). In a half cell, the material of interest (e.g., cathode) acts as the working electrode and is paired with a Li counter electrode/pseudo-reference electrode to complete the electrical circuit. While the working electrode undergoes oxidation/reduction, the Li counter electrode can undergo complementary oxidation/reduction ( $Li^+ + e^- \rightleftharpoons Li(s)$ ). It is typically oversized compared to the working electrode to limit polarisation and provide a large source of Li so as

not to become a limiting factor during electrochemical testing.<sup>15</sup> The potential of the cathode is then measured against the Li (V vs Li<sup>+</sup>/Li) which also acts as a reference electrode, often described as a 'pseudo-reference' since its potential is not always stable and well-defined.<sup>16</sup> All potentials reported in this work are vs Li<sup>+</sup>/Li.

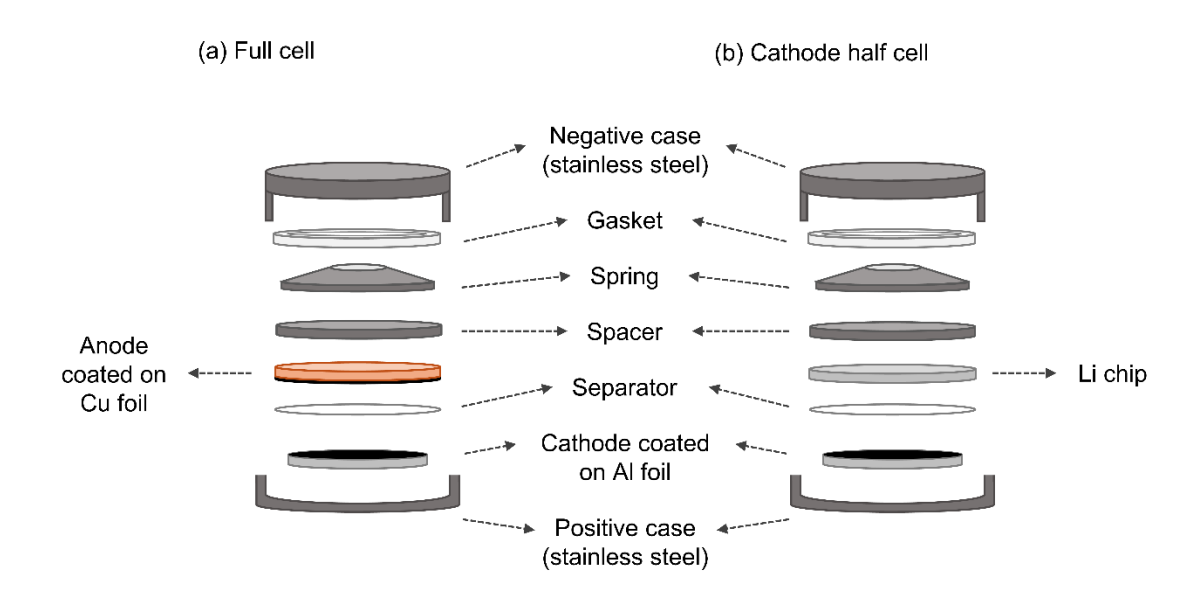


Figure 3.1: Comparison of a) a full-cell and b) a cathode half-cell coin-cell setup.

In this work, a two-electrode coin-cell type cell geometry is adopted (unless otherwise stated) due to its simplicity and small material requirements. The coin cell consists of a stainless steel casing (2032-type, Tob New Energy) which houses: the positive electrode (CAM coated onto AI foil); a glass fibre separator soaked in 1 M LiPF<sub>6</sub> in ethylene carbonate (EC)/dimethyl carbonate (DMC) (1:1, V:V) as electrolyte (Aldrich, battery grade); the Li counter/pseudoreference electrode; a spacer and spring to ensure sufficient and homogenous contact between the cell components. All cells were prepared in an argon-filled glovebox (< 0.1 ppm H<sub>2</sub>O and O<sub>2</sub>) and left to rest for 12 h before conducting electrochemical experiments.

### 3.2.3 Galvanostatic Cycling

Galvanostatic cycling was performed to evaluate the electrochemical performance of the studied cathodes. During cycling, a constant current is applied to the cell within a specified voltage window. The applied current is calculated based on CAM mass (m), desired charge/discharge rate (C-rate, C, h<sup>-1</sup>), and the theoretical specific capacity ( $Q_{th}$  = 147 mAh g<sup>-1</sup>), by Equation 3.1. Throughout the experiment, time (t) is recorded as a function of the voltage. Time is then related to capacity through Equation 3.2.

$$I = m \cdot C \cdot Q_{th} \tag{3.1}$$

$$Q = \frac{It}{m} \tag{3.2}$$

The voltage response with respect to capacity, also known as the voltage profile, can provide information relating to possible phase transitions occurring within the material. A voltage plateau indicates the co-existence of two phases. For example, the voltage profile of LNMO is dominated by two high-voltage plateaux. This is because, at different states of lithiation, LNMO experiences three phases that correspond to the three possible oxidation states of Ni (Ni<sup>2+</sup>, Ni<sup>3+</sup>, Ni<sup>4+</sup>): LiNi<sub>0.5</sub>Mn<sub>1.5</sub>O<sub>4</sub> (Li<sub>1</sub>), Li<sub>0.5</sub>Ni<sub>0.5</sub>Mn<sub>1.5</sub>O<sub>4</sub> (Li<sub>0.5</sub>) and Ni<sub>0.5</sub>Mn<sub>1.5</sub>O<sub>4</sub> (Li<sub>0</sub>). This results in two regions of two-phase coexistence, namely, Li<sub>1</sub> and Li<sub>0.5</sub> coexistence at the lower potential plateau ( $\approx 4.70$  V) and Li<sub>0.5</sub> and Li<sub>0</sub> coexistence at the higher potential plateau ( $\approx 4.74$  V). Two-phase co-existence occurs because the energies of the two phases overlap, at the applied voltage. A sloping voltage profile, on the other hand, indicates solid-solution behaviour, where a continuous change in composition occurs without distinct phase separation.

Galvanostatic cycling stability and rate capability studies were carried out on a multichannel battery cycler (Neware) between 3.5–4.9 V. Cycling stability studies (1C) were conducted both at room temperature (RT, 28°C) and high temperature (HT, 50°C). Cycling was carried out in a temperature-controlled climate chamber (Memmert). To evaluate the performance at high rates, rate capability studies were performed (RT, 28°C), in which the charging/discharging rate was increased every 5 cycles from 0.1C–10C, before returning to 0.1C, to determine if the capacity loss at high rates was reversible or irreversible. Note that the rate of charge was equal the the rate of discharge.

For selected samples, the recorded capacity was differentiated with respect to the recorded voltage. In the resulting dQ/dV vs V plot, plateaus in the voltage profiles manifest as peaks. These peaks enable a clearer analysis of the capacity fade and voltage polarization associated with individual electrochemical processes.

## 3.2.4 Cyclic Voltammetry

Cyclic voltammetry was used to investigate the electron transfer reactions that occur at the cathode. It involves applying a potential to the cell and measuring the output current, where the applied potential is linearly changed throughout the measurement between predefined voltage limits. In this work, the potential was scanned from the open circuit potential (≈ 3 V vs Li⁺/Li) to the upper potential limit (5 V vs Li⁺/Li) and then back down to the lower potential limit (3.5 V vs Li⁺/Li).

When the potential is increased during a CV experiment, Li<sup>+</sup> ions are extracted from the cathode, and the TMs in the cathode material are oxidized. This oxidation process involves the release of electrons from the TMs, which then flow into the external circuit, resulting in a positive current. The current increases as the potential rises, reaching a peak current ( $I_p$ ), which represents the maximum rate of the electrochemical reaction under the given conditions. The peak current ( $I_p$ ) is influenced by several factors, including the concentration of electroactive species, the rate of Li extraction from the cathode structure, and the oxidation of TMs.<sup>19</sup> The specific potential at which  $I_p$  occurs depends on the thermodynamic and kinetic aspects of the Li extraction and the oxidation process of the TMs. As the oxidation proceeds and the amount of electroactive species (such as Li<sup>+</sup> and TM ions in the reduced state) at the surface decreases, the current begins to decline. This decline occurs because the concentration of the species that can be oxidized diminishes, thus lowering the rate of the reaction.<sup>19</sup>

During the reverse scan, when the potential is decreased, Li<sup>+</sup> ions are reinserted into the cathode, and the TMs are reduced. This reduction process involves the acceptance of electrons from the external circuit, which results in a negative current. The occurrence of a negative current during reduction reflects the flow of electrons into the cathode.

By comparing the peak currents ( $I_p$ ) and the positions of the peaks during the oxidation and reduction processes, one can assess the reversibility of the electrochemical reactions. In a perfectly reversible system, the oxidation and reduction peaks would occur at the same potential (with symmetrical currents).<sup>19</sup> In practice, however, there can be slight shifts due to kinetic barriers and overpotentials. The separation and symmetry of the peaks, as well as the relative magnitudes of the oxidation and reduction peak currents, provide insights into the efficiency and reversibility of the redox processes. The width of the peak in the CV curve can also indicate the rate at which the electrochemical reaction occurs. A sharper peak suggests a faster reaction rate, as the electroactive species are consumed over a narrower potential range, corresponding to a shorter time in the experiment. Conversely, a broader peak indicates a slower reaction rate.<sup>19</sup>

The scan rate, which is the speed at which the potential is swept during a CV experiment, significantly influences the observed current and peak characteristics.<sup>19</sup> At higher scan rates, the peaks in the CV curve generally become broader and shift to higher (for oxidation) or lower (for reduction) potentials. This shift occurs because, at faster scan rates, there is less time for the electrochemical reaction to reach equilibrium, leading to increased overpotentials. The scan rate is, therefore, a crucial parameter in CV experiments. In non-aqueous systems, such

as LIBs that use organic solvents, slow scan rates are required (0.1–0.5 mV s<sup>-1</sup>). This is because non-aqueous electrolytes typically have higher viscosities and lower ionic conductivities than aqueous electrolytes. This leads to slower ion mobility and so by using slower scan rates the ions are allowed sufficient time to transport.<sup>19</sup>

## 3.2.5 Potentiostatic Electrochemical Impedance Spectroscopy

Potentiostatic electrochemical impedance spectroscopy (PEIS) is used to understand the electrical, electrochemical, and physical processes that occur in an electrochemical system. These processes include diffusion of redox species from the solution to the surface of the electrode, faradaic reactions, and the charging/discharging of the electric double layer at the electrode/electrolyte interface.<sup>20</sup>

During the PEIS experiment, a small-amplitude alternating voltage is applied to a system in steady-state. To avoid nonlinearities and large signal distortions, the amplitude of the alternating signal must kept small (5–10 mV).<sup>20</sup> When using such small amplitudes the system's response can be considered linear. Since the aforementioned processes occur on different timescales, the frequency of the AC signal is applied over a given frequency range (Hz), where frequency is the inverse of time (s) (Equation 3.3).<sup>20</sup> As such, slow processes, such as diffusion, can be probed at low frequencies and fast processes, such as charging of the electric double layer, can be probed at higher frequencies.<sup>20</sup> At each frequency, the resulting alternating current is measured.

$$f = \frac{1}{t} \tag{3.3}$$

$$Z = Z' + jZ'' \tag{3.4}$$

Current within an electrical circuit can become obstructed by impedance  $Z(\omega)$ , where the impedance (Z) is a combination of reactance and resistance. Resistance (Z) is the real part of impedance and reactance (Z") is the imaginary part, as shown by Equation 3.4, where j is an imaginary number such that f = -1. Resistance, found in resistors, opposes the flow of current, causing energy to be lost as heat. Reactance, instead, opposes a change in current. It is, therefore, specific to alternating current and is found in inductors and capacitors.

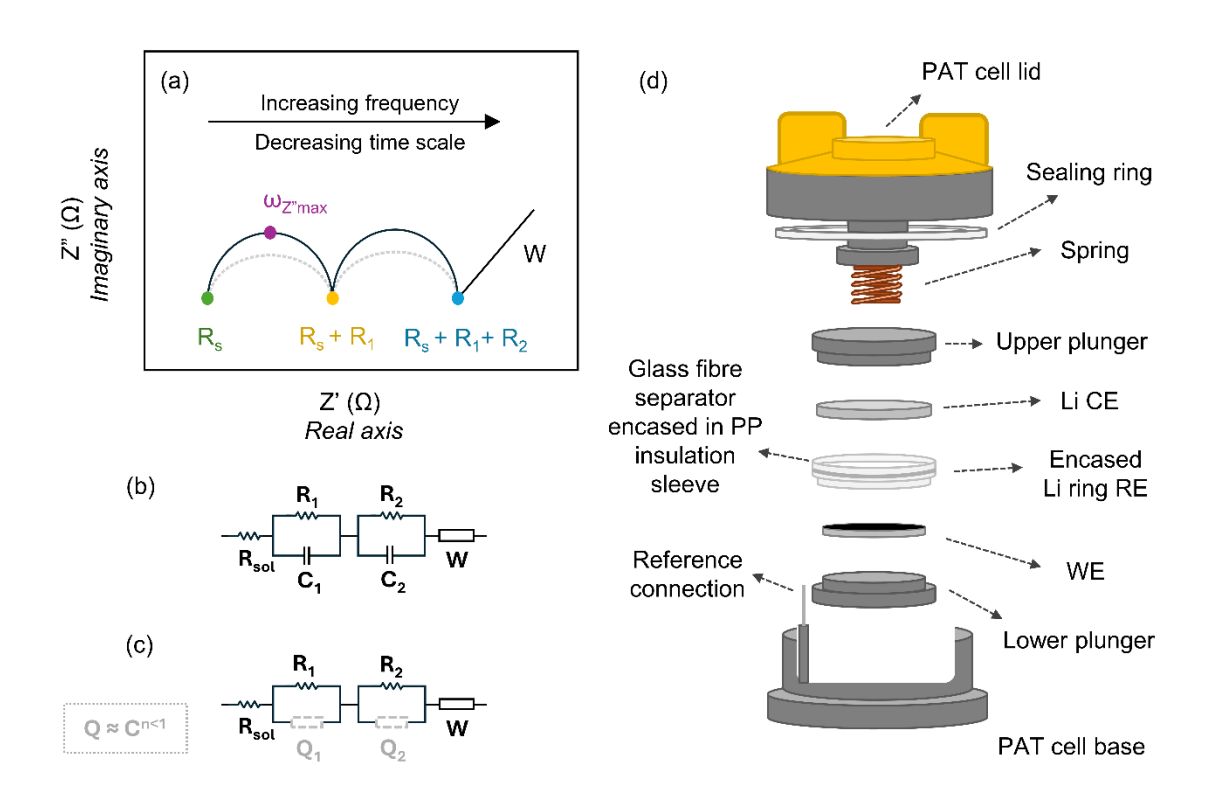


**Figure 3.2**: a) Schematic illustrating features typically observed in a Nyquist plot, highlighting that the ideality of capacitance influences the shape of the semi-circle. Here, the solid, black semicircles indicate ideal capacitance C, as shown in the equivalent circuit model (b). The grey, dashed semi-circles, on the other hand, indicate non-ideal capacitance ( $Q \approx C^{n<1}$ ) and are depressed in comparison. The impedance response can instead be modelled by the equivalent circuit model (c); d) schematic illustrating the three-electrode PAT cell in which working electrode (WE), and counter electrode (CE) are compressed either side of a polypropylene (PP) insulation sleeve which houses the glass fibre separator and ring reference electrode (RE).

One of the most common ways to display EIS data of battery materials is using Nyquist plots, in which Z (resistance) is plotted on the *x*-axis and Z" (reactance) is plotted on the *y*-axis (**Figure 3.2a**). The Nyquist plot typically consists of a semi-circle, or a series of semi-circles, at higher frequencies (left side of the plot) and a 'tail' at lower frequencies (right side of the plot). Solution resistance ( $R_{sol}$ ) is observed at high frequencies (i.e., short time scale).<sup>20</sup> Only resistance is present in the solution. Therefore, reactance equals 0, and the impedance is equal to the resistance ( $Z' = R_{sol}$ ). As a result,  $R_s$  is a single point that intercepts the x-axis at high frequency.<sup>20</sup>

As the frequency decreases, a semi-circle appears in the Nyquist plot, representing the combined effects of a parallel resistor-capacitor (RC) circuit (**Figure 3.2b**).<sup>20</sup> In this region, the current flows through the resistor and the capacitor, at varying ratios. The peak of the semi-

circle represents the point at which the contribution of capacitive reactance is at its maximum  $(\omega_{z''max}, \text{ Figure 3.2a})$ . At the low-frequency intercept (right), all the current passes through the resistor  $(Z' = R_{sol} + R_1)$ , creating a low-frequency intercept in the x-axis. It is possible to observe several semi-circles in the Nyquist, each corresponding to a different RC process, which—because they are seen at different frequencies—occur at different time scales. Processes that occur on similar time scales will overlap, making their response difficult to distinguish from one another. This is a problem experienced during the EIS analysis of LNMO and is discussed in detail in Chapter 5. Finally, the low-frequency tail represents slow Li<sup>+</sup> diffusion within the electrode. On the control of the

Equivalent circuit models are often used to simulate impedance spectra to determine the resistances. Each semi-circle is typically modelled using a parallel RC element. However, due to surface roughness, capacitance in a practice is non-ideal leading to a semi-circle that appears depressed. To model this non-ideal capacitance, a constant phase element (Q) is used, where  $Q \approx C^{n,20}$  Here, n represents the deviation from ideality; for an ideal capacitor n = 1, for a non-ideal capacitor n < 1 (**Figure 3.2c**). The tail at low frequency, representing semi-infinite diffusion, typically appears at a 45° angle to the x-axis, in which case it is modelled using a Warburg element (W). However, non-ideal systems can experience finite diffusion leading the angle to deviate from 45°. In these cases, the tail can be modelled using a constant phase element (Q), allowing the angle to be changed by adjusting the value of n, where the Warburg is a unique case where  $Q \approx C^{0.5}$  (n = 0.5). n = 0.5

To collect useful impedance data, it is often necessary to use a three-electrode setup. This is because when using a two-electrode setup, as described in Section 3.2.2, it is hard to deconvolute the impedance response that is coming from the cathode side and the anode side.<sup>21</sup> The inclusion of a third reference electrode allows the impedance response of the individual electrodes to be measured separately against the reference electrode. Since the reference electrode doesn't participate in the reactions this can also improve the stability of the reference itself.<sup>21</sup>

In this work, PEIS was performed (Biologic, VMP-300) in a three-electrode cell (PAT-Cell, El-Cell®) using a spinel working electrode, Li counter electrode, and Li reference electrode (**Figure 3.2d**). The reference is a pre-assembled Li ring (El-Cell®) enclosed in the cell around the glass fibre separator. The use of ring-type reference electrode geometry can ensure uniform potential distribution across the working electrode while allowing ease of handling. Full PEIS program details are provided in Chapter 5.

#### 3.3 Ex-situ Surface Characterisation

To understand how battery cycling influences the surface/interphases of the cycled electrode, it is necessary to perform *ex-situ* surface characterisation, in which the cell is dissembled and the electrodes are extracted at various states of charge/cycling. *Ex-situ* surface characterisation was carried out at the Diamond Light Source's Surface and Interface Structural Analysis beamline (I09) which offers the unique capability of being able to perform hard and soft X-ray measurements on the same sample, allowing good correlation between the techniques.<sup>22</sup> The I09 beamline makes use of the synchrotron light source which provides a high-intensity X-ray beam that is beneficial for measuring low-intensity signals with a low signal-to-noise ratio.<sup>22</sup> The ability to tune the energy of the X-ray beam makes it possible to scan across a specific range of photon energies, which is particularly useful for X-ray absorption measurements.<sup>22</sup> In this work, a combination of hard X-ray photoelectron spectroscopy and soft X-ray absorption spectroscopy was employed (**Figure 3.3**).

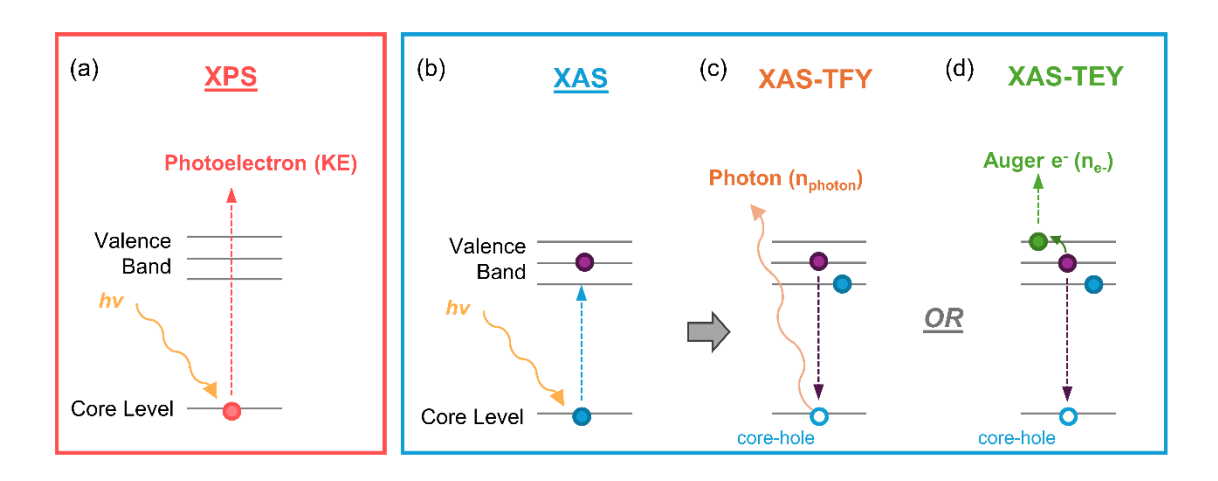


**Figure 3.3:** Simplified schematic illustrating the fundamental electron excitation and decay processes that govern a) X-ray photoelectron spectroscopy, b) X-ray absorption in c) total fluorescence yield (TFY) mode and d) total electron yield (TEY) mode, as described in detail in Sections 3.3.1–3.3.2. For each technique, the value that is measured is provided in brackets.

#### 3.3.1 X-ray Photoelectron Spectroscopy

X-ray photoelectron spectroscopy (XPS) is a surface-sensitive technique which can reveal the chemical functionality of the analysed surface. This makes it particularly useful for understanding the electrode-electrolyte interphase layers that form during electrochemical cycling. XPS typically uses soft X-rays—that is to say X-rays with energy < 2 keV.<sup>23</sup> The use of a synchrotron source, however, allows the use of higher excitation energies (2–8 keV) that can probe deeper into the sample and provide more sub-surface information. This is known

as hard X-ray photoelectron spectroscopy (HAXPES), and like standard XPS, works off the basic principle of the photoelectric effect (Equation 3.5) which describes the emissions of photoelectrons from a sample that is irradiated by X-rays—of energy E = hv—when the electrons have sufficient energy to overcome their binding energy (BE) and the work function of the material (**Figure 3.3a**). BE describes how tightly an electron is bound to the atom to which it is attached and can be affected by both chemical environment and oxidation state.<sup>24</sup> The kinetic energy (KE) of the emitted photoelectrons is then measured and, through Equation 3.5, the BE of the emitted photoelectron is derived. Spectra are denoted by the element and orbital from which the photoelectron has been ejected (e.g., O1s).

$$BE = hv - (KE + \phi_{spectrometer})$$
 (3.5)

Energy, or BE, resolution is affected by the photon source, the electronic state being excited and the instrument, as determined by the resolution of the hemispherical electron analyser.<sup>24</sup> The purpose of the hemispherical analyser is to i) bend the trajectory of the photoelectrons, that enter the analyser through a narrow slit, such that their final radii are dependent on their KE and ii) retard the photoelectrons to a selected pass energy, by applying opposing voltages to the inner and outer hemispheres.<sup>24</sup> The hemispherical radius, the width of the entrance, the angle at which the electrons enter the analyser, and the pass energy all influence the energy resolution.<sup>24</sup> However, the pass energy is the only extrinsic parameter that allows user control and must be selected based on the requirements for spectral resolution. Higher pass energies (>150 eV) allow for higher count rates (intensity) but limit energy resolution since electrons are bent to a greater extent as they pass around the analyser, resulting in energy peaks that are closer together. Lower pass energies, on the other hand, improve energy resolution but come at the cost of worsening signal-to-noise ratio.<sup>24</sup> It is, therefore, necessary to balance pass energy to ensure both sufficient signal-to-noise ratio and BE resolution.

The BEs recorded during an XPS experiment can appear shifted towards higher BEs, due to sample charging.<sup>24</sup> Charging of the sample surface can occur when the loss of photoelectrons causes a build-up of positive charge.<sup>24</sup> Although charge compensation can be used during an experiment, it is not always possible to fully neutralize the samples. Some reference must, therefore, be used to charge reference the resulting spectra and provide BEs that are more comparable to literature and/or databases. Perhaps the most common reference is the C1s peak for adventitious carbon, which is typically placed at 284.8 eV, allowing all other spectra to be shifted by the same degree.<sup>25</sup> The use of a carbon reference is a particularly useful method when using electrodes prepared using a carbon black additive, as described above. Carbon black, however, has a lower BE, since it is sp<sup>2</sup> hybridised (284.4).<sup>26</sup>

In this work, HAXPES data were collected using an incident X-ray energy of 2.2 keV, with a probing depth < 10 nm, and a pass energy of 100 eV. Before measurements, beam damage tests were conducted in which a F1s scan was repeated on the same sample spot over 30 minutes to ensure that the F1s signal did not i) lose significant intensity or ii) change in shape. F1s scans were also taken both at the start and the end of a set of measurements.<sup>27</sup> In both tests, no significant change in F1s signal were observed and so beam damage is ruled out, assuming of course that any beam damage is not instantaneous. Once collected, spectra were calibrated to the sp<sup>2</sup> C1s peak present in all samples in the form of carbon black (284.4 eV).

Data processing and peak fitting were performed using the CasaXPS software, using a Shirley background. The spectral response of unknown surfaces requires careful and considered analysis. In this work, peak fitting of HAXPES data has been performed to provide a visual aid for the evolution of spectral features and not as a form of quantitative analysis. Spectral features have been assigned according to the literature, and correlating features (**Table 3.2**).<sup>28–30</sup> The FWHM of the surface species observed should be equal unless there is a chemical reason for the differences observed.<sup>31</sup> To determine reasonable FWHM for electrode species, electrodes without active material (C/PVDF reference) were fit, since they contained a known number of XPS peaks, with no chemical reason why these should be different between the species analysed in this work. FWHM in cycled samples was constrained to be within ± 0.1 eV of similar species in pristine electrodes to account for peak broadening that may arise due to the formation of a series of unknown surface species with varying composition.

The binding energy at which certain species appear in the high-resolution XPS spectra differs between literature reports. For example, several works report  $\text{Li}_x\text{PO}_y\text{F}_z$  species to appear at 534.5 eV in the O1s spectra, while others report these to appear at 532 eV. In some cases,  $\text{Li}_x\text{PO}_y\text{F}_z$  species are identified in only the O1s (F1s) spectrum, without the presence of correlating peaks in the F1s (O1s) spectrum. Furthermore, high energy binding peaks in the O1s spectra (> 534 eV) are sometimes assigned to polycarbonate species. However, correlating peaks in the C1s spectra are not observed in this work. As a result, peaks at 534.5 eV (O1s) and 686 eV (F1s) have been assigned to  $\text{Li}_x\text{PO}_y\text{F}_z$  because their intensity changes correlate well across all spectra.

**Table 3.2:** Peak assignments for HAXPES fittings in accordance with references [<sup>28–30</sup>]

Region	Binding Energy (eV)	Assignment
C1s	284.4	C-C (sp <sup>2</sup> ), CB
	284.8	C-C/C-H (sp <sup>3</sup> )
	286.0	$\underline{C}H_2$ – $CF_2$ (PVDF) / C–O
	287.8	C=O / O-C-O
	288.5	O-C=O
	290.2	CO <sub>3</sub> / CF <sub>2</sub> (PVDF)
O1s	529.1	TM-O
	531.5	C=O / TM-OH
	532.5	C-O
	534.6	$\text{Li}_{x}\text{PO}_{y}\text{F}_{z}$
F1s	684.5	LiF / MF
	686.6	$\text{Li}_x PO_y F_z$
	687.8	$CF_x$ (PVDF)
	688.5	Li <sub>x</sub> PF <sub>y</sub>

#### 3.3.2 Soft X-ray Absorption Spectroscopy

Soft X-ray Absorption Spectroscopy (sXAS) is a valuable technique for investigating the electronic structure of battery cathode materials. It involves the absorption of X-ray photons by the sample, which excites core-level electrons to unoccupied states (**Figure 3.3b**).<sup>23</sup> The energy range of soft X-rays (100 eV–2 keV) is particularly well suited for exciting electrons from the O1s (K-edge) or TM2p (L-edge) core levels to unoccupied orbitals.<sup>23</sup> The TM L-edge absorption ( $2p \rightarrow 3d$  transitions) provides direct information about the occupancy and configuration of the 3d orbitals, which are sensitive to the oxidation state.<sup>35</sup> The O K-edge, on the other hand, can provide useful insights into the extent of O2p-TM3d hybridisation.<sup>36</sup>

Despite the benefits of using soft X-rays, the soft X-ray attenuation length is small (<< 1 µm).<sup>23</sup> When trying to measure X-ray absorption directly, in transmission mode, this creates limitations on sample thickness that are difficult to realise in practice (i.e., the sample has to be thin enough to match the attenuation length).<sup>23</sup> Therefore, alternative detection modes are typically used to indirectly measure the absorption through the resulting decay processes: total fluorescence yield (TFY) and total electron yield (TEY).<sup>23</sup> TFY mode detects the number of photons ( $n_{photon}$ ) that are released as an electron from a higher-lying energy state relaxes to fill the core hole (**Figure 3.3c**).<sup>23</sup> TEY mode, on the other hand, detects the number of auger

electrons that are emitted from the sample ( $n_{e-}$ , **Figure 3.3d**). Auger electrons are emitted when the energy released during the electron decay process is transferred to an outer shell electron, allowing the outer shell electron to escape.<sup>23</sup> In both cases, the decay products are influenced by the number of core holes created in the absorption process.<sup>23</sup> However, TFY mode and TEY mode have different detection depths ( $\approx$  100 nm and  $\approx$  5 nm respectively).<sup>23</sup>

In this work, sXAS of the O K-edge, Ni L-edge, and Mn L-edge were collected in total electron yield (TEY) mode, providing surface-sensitive information about TM oxidation states and O2p-TM3d hybridisation. To account for lateral inhomogeneities, several electrode spots ( $n \ge 3$ ) were measured, and the average spectra are presented in all cases. Spectral processing is described in Chapter 5.

#### 3.4 Characterisation of Bulk (Micro)structure and Morphology

#### 3.4.1 Scanning Electron Microscopy

Scanning Electron Microscopy (SEM) is a powerful technique extensively used to examine the surface morphology of a material at high magnifications. SEM operates by directing a focused beam of high-energy electrons onto the surface of a sample.<sup>37</sup> These incident electrons interact with the atoms in the sample, generating various signals, including secondary electrons, backscattered electrons, and characteristic X-rays.<sup>37</sup> The secondary electrons, primarily emitted from the top few nanometers of the sample surface, are most commonly detected and used to form high-resolution images that reveal topographical details.<sup>37</sup> The intensity and distribution of these emitted electrons depend on the surface features and composition, allowing SEM to produce detailed, three-dimensional-like images of the sample surface. In this work, Scanning Electron Microscopy (SEM) was collected to confirm to particle morphology of the synthesised samples (JEOL JSM-7800F, acceleration voltage = 5 kV).

## 3.4.2 Exploring Crystal Structures Using Bragg Diffraction

Crystallography

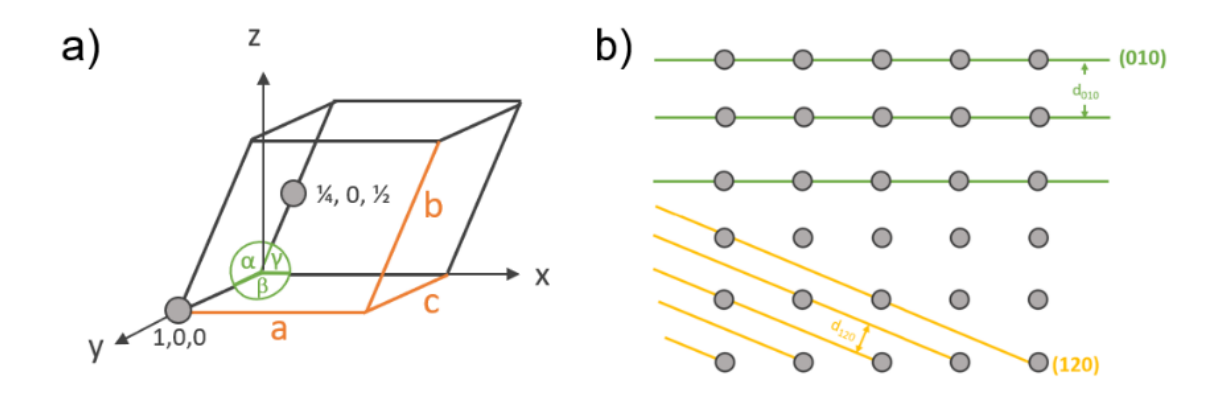


**Figure 3.4:** a) Unit cell with lengths (a, b, c) and angles ( $\alpha$ ,  $\beta$ ,  $\gamma$ ). Exemplar atoms in place with fractional coordinates x, y, z = 1, 0, 0 and  $\frac{1}{4}$ , 0,  $\frac{1}{2}$ . b) schematic highlighting lattice planes within the crystal lattice (grey dots), with Miller indices (hkl) = (010) and (120) and d-spacings of  $d_{010}$  and  $d_{120}$ , respectively.

Crystalline materials have a geometric array of atoms (lattice points) that repeat periodically to form a crystal lattice.<sup>38</sup> The arrangement of atoms within the lattice is described by the crystal structure and the lattice planes with which they intersect. The crystal structure is often defined by its smallest repeating unit, known as its unit cell where the unit cell itself is defined by three lengths (a, b, c) and three angles (a,  $\beta$ ,  $\gamma$ ) (**Figure 3.4a**). Different combinations in which these lengths and angles relate to one another result in seven possible crystal systems (**Table 3.3**). Centring of atoms on one face (base-centred), each face (face-centred), or in the centre of the crystal systems (body-centred) leads to 14 possible lattices, known as Bravais lattices. Atomic positions within the lattice are defined by fractional coordinates (x, y, z) that describe their distance from the origin as a fraction along each axis (**Figure 3.4a**). Crystal structures are also described by lattice planes—equidistant parallel planes—that appear at different orientations across the crystal lattice. Lattice planes, denoted by their Miller indices (hkl), are separated by a given distance,  $d_{hkl}$  (**Figure 3.4b**).  $d_{hkl}$  can be related to lattice parameters (a, b, c, a,  $\beta$ ,  $\gamma$ ) through  $d_{hkl}$  expressions which differ depending on the crystal system (**Table 3.3**).

**Table 3.3:** The seven crystal systems and their corresponding  $d_{hkl}$  expressions<sup>39</sup>

Crystal system	Unit Cell	Allowed lattices	d <sub>hkl</sub> expression
Cubic	$a = b = c$ $\alpha = \beta = \gamma = 90^{\circ}$	P <sup>a</sup> , F <sup>b</sup> , I <sup>c</sup>	$\frac{1}{d_{hkl}^2} = \frac{h^2 + k^2 + l^2}{a^2}$
Tetragonal	$a = b \neq c$ $\alpha = \beta = \gamma = 90^{\circ}$	P, I	$\frac{1}{d_{hkl}^2} = \frac{h^2 + k^2}{a^2} + \frac{l^2}{c^2}$
Orthorhombic	$a \neq b \neq c$ $\alpha = \beta = \gamma = 90^{\circ}$	P, F, I,  A <sup>d</sup> (B or C)	$\frac{1}{d_{hkl}^2} = \frac{h^2}{a^2} + \frac{k^2}{b^2} + \frac{l^2}{c^2}$
Hexagonal	$a = b \neq c$ $\alpha = \beta = 90^{\circ},$ $\gamma = 120^{\circ}$	Р	$\frac{1}{d_{hkl}^2} = \frac{h^2}{a^2} + \frac{k^2}{b^2} + \frac{l^2}{c^2}$
Trigonal	$a = b = c$ $\alpha = \beta = \gamma \neq 90^{\circ}$	R <sup>e</sup>	$\frac{1}{d_{\rm hkl}^2} =$ $\frac{\left(h^2 + k^2 + l^2\right)\sin^2\alpha + 2(hk + kl + hl)(\cos^2\alpha - \cos\alpha)}{\alpha^2(1 - 3\cos^2\alpha + 2\cos^3\alpha)}$
Monoclinic	$a \neq b \neq c$ $\alpha = \gamma = 90^{\circ},$ $\beta \neq 90^{\circ}$	P, C	$\frac{1}{d_{\text{hkl}}^2} = \frac{1}{\sin^2 \beta} \left( \frac{h^2}{a^2} + \frac{k^2 \sin^2 \beta}{b^2} + \frac{l^2}{c^2} - \frac{2hl \cos \beta}{\text{ac}} \right)$
Triclinic	a≠b≠c α≠β≠γ≠90°	Р	$\frac{1}{d_{hkl}^2} = \frac{1}{V^2} [h^2 b^2 c^2 \sin^2 \alpha + k^2 \alpha^2 c^2 \sin^2 \beta$ $+ l^2 \alpha^2 b^2 \sin^2 \gamma + 2hkabc^2 (\cos \alpha \cos \beta - \cos \gamma)$ $+ 2kl\alpha^2 bc (\cos \beta \cos \gamma - \cos \alpha)$ $+ 2hlab^2 c (\cos \alpha \cos \gamma - \cos \beta)]$

<sup>&</sup>lt;sup>a</sup> Primitive centering (P): lattice points on the cell corners only; <sup>b</sup> Face centered (F): one additional lattice point at centre of each of the faces of the cell; <sup>c</sup> Body centered (I): one additional lattice point at the centre of the cell; <sup>d</sup> Base centered (A, B or C): one additional lattice point at the centre of each of one pair of the cell faces. <sup>e</sup> Rhombohedral.

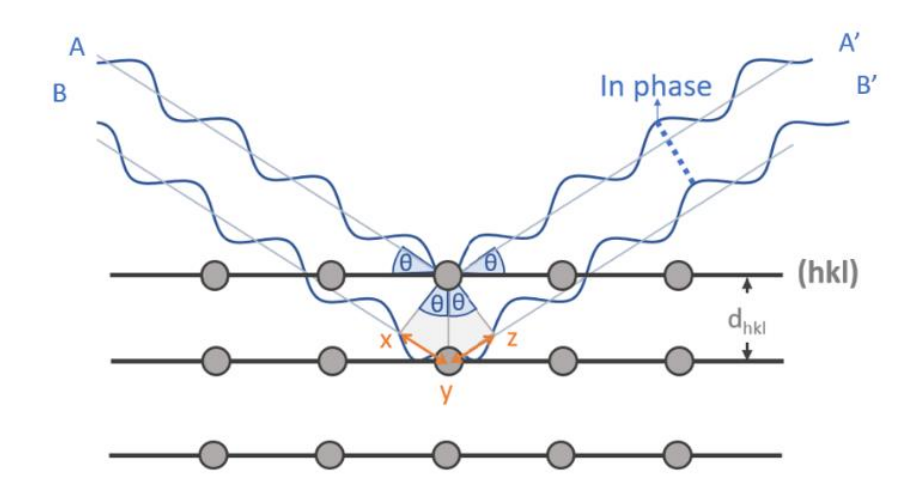


Figure 3.5: Schematic representation of diffraction, used to derive Bragg's law.

The structures of crystalline electrode materials are routinely probed using powder X-ray and/or neutron diffraction. During the diffraction experiment, the incident X-ray, or neutron, beam interacts with the sample and becomes elastically scattered (**Figure 3.5**). To observe Bragg diffraction, the reflected beams must be in phase with one another, allowing constructive interference (**Figure 3.5**). However, beam B travels xy + yz further than beam A. For the beams to remain in phase with one another, the additional distance travelled by B must be an integer number of wavelengths

$$xyz = n\lambda \tag{3.6}$$

Through trigonometry, the distance xyz can be related to  $d_{hkl}$  and incident angle  $\theta$  as follows:

$$xyz = 2d_{hkl}sin\theta (3.7)$$

such that

$$n\lambda = 2d_{hkl}\sin\theta \tag{3.8}$$

Thus, a series of Bragg peaks at specific  $d_{hkl}$ , and  $\theta$ , values will be measured when Braggs' law is satisfied (Equation 3.8). For this reason, they are also known as (hkl) reflections, denoted by the (hkl) Miller index of the lattice plane which reflects the incident beam. The position of these Bragg peaks is determined by the size of the unit cell (**Table 3.3**). Cases exist where translational symmetry elements and/or centring in the lattice can result in destructive interference of certain reflections, despite Braggs' Law being satisfied. These are known as systematic absences. Indexing peak positions can therefore provide information regarding the unit cell size, symmetry, and crystal system.

The intensity of a given peak is directly related to the intensity of the reflected beam that is detected in a diffraction experiment.<sup>40</sup> The intensity of the beam itself is dependent on the location of different elements within a crystal system. It is therefore influenced by their atomic position (x, y, z) in which each position has an associated site occupancy factor (f) and atomic displacement parameter (U).<sup>41</sup> U describes the mean atomic displacement about the atomic position (x, y, z) that occurs because of static disorder or atomic vibrations. It is therefore higher for lighter elements or atoms that are less strongly bound.<sup>42</sup> Atomic displacement can be isotropic  $(U_{iso})$  or anisotropic  $(U_{ij}, ij = 11, 22, 33, 12, 23, 13)$ . Site occupancy factors describe the average fraction of a given atomic position that is occupied by a given element. Different elements within the structure are distinguished based on the difference in their scattering power: scattering factor (f) for X-rays and scattering length (b) for neutrons. Elements with higher scattering power, therefore, contribute to higher peak intensity in the diffraction pattern.<sup>40</sup> Determining these parameters is not trivial, and the right beam must be selected to have the best chance of establishing the crystal structure.

## X-ray Diffraction vs Neutron Diffraction

The wavelength of the X-ray/neutron beams used in diffraction experiments is similar to the interatomic spacing within a crystal lattice, allowing diffraction to occur in both cases. However, how X-rays and neutrons interact with the sample differs, resulting in different experimental capabilities.

The most notable difference between X-ray and neutron diffraction is the relationship between different elements and their scattering power.<sup>40</sup> The X-ray scattering factor of the elements increases proportionally with the number of electrons as the incident X-ray beam interacts with the electron cloud surrounding the constituent atoms. As a consequence, light elements (e.g., Li and O) are weak X-ray scatterers, making their contribution difficult to distinguish from stronger-scattering elements within the structure (e.g., TMs).<sup>40</sup> A second consequence is that elements with similar atomic numbers (e.g., Ni and Mn) have similar X-ray scattering lengths and are therefore hard to differentiate from one another.<sup>40</sup> In such cases, neutron diffraction

can help to differentiate between elements as the neutron beam interacts with the atomic nuclei as opposed to the electron cloud. This makes coherent neutron scattering length independent of atomic number. Thus, neutron diffraction is often better suited to determining site occupancy by allowing differentiation between elements of low and/or similar atomic numbers (**Table 3.4**). Coherent scattering is not the only scattering observed from neutron-nucleus interactions. Spin-spin interactions between the neutron (spin =  $\frac{1}{2}$ ) and the nucleus also lead to incoherent scattering. Incoherent scattering in powder neutron diffraction contributes to general background noise in the data.

**Table 3.4:** Coherent neutron scattering lengths of elements relevant to this thesis, which represent averages based in the natural isotopic abundances of each element.<sup>43</sup>

Element	Coherent neutron Dominant isotopes and		
	scattering length [fm]	abundances (%)	
Li	-1.9	<sup>6</sup> Li (7.59 %), <sup>7</sup> Li (92.41 %)	
0	5.803	<sup>16</sup> O (99.76 %), <sup>17</sup> O (0.04 %),	
		<sup>18</sup> O (0.20 %)	
Mg	5.375	<sup>24</sup> Mg (78.99 %), <sup>25</sup> Mg (10.00 %),	
		<sup>26</sup> Mg (11.01 %)	
Ni	10.3	<sup>58</sup> Ni (68.08 %), <sup>60</sup> Ni (26.22 %)	
Mn	-3.73	<sup>55</sup> Mn (100 %)	
Fe	9.45	<sup>54</sup> Fe (5.8 %), <sup>56</sup> Fe (91.75 %)	
V	-0.3824	<sup>51</sup> V (99.75 %), <sup>50</sup> V (0.25 %)	

Interaction of the beam with the atomic nucleus vs the electron cloud also makes neutron diffraction better suited for determining U. In X-ray diffraction, the interaction of the X-rays with the electron cloud results in scattering factors that reduce as the scattering vector Q, and thus  $\theta$ , increase (Equation 3.9):<sup>40</sup>

$$Q = \frac{4\pi \sin\theta}{\lambda} \tag{3.9}$$

Therefore, at higher angles/smaller d-spacings, Bragg intensity is diminished. Unlike an electron cloud, an atomic nucleus is a finite pin-point scatterer, making neutron scattering length independent of Q, and by relation  $\theta$  and d.<sup>40</sup> Information related to smaller d-spacings is, therefore, better determined through neutron diffraction when compared to X-ray diffraction. This makes neutron diffraction more capable of determining U, which is often unresolved when analysing X-ray diffraction data.

Another practical effect on intensity to consider when conducting a diffraction experiment is X-ray/neutron absorption. Different elements have different absorption cross-sections. A high absorption cross-section results in a decrease in reflected intensity as the incident beam becomes partially absorbed. In the case of X-rays, both scattering and absorption increase with atomic number. Neutrons, on the other hand, are only absorbed by a handful of isotopes. Most notable for this work is the <sup>6</sup>Li isotope, which makes up approximately 7.5% of naturally occurring Li.<sup>40</sup> The main isotope (<sup>7</sup>Li), however, has an absorption cross-section that is two thousand times smaller than that of <sup>6</sup>Li. The relatively low proportion of highly absorbing <sup>6</sup>Li in naturally occurring Li, therefore, does not inhibit neutron diffraction of Li-containing samples. However, <sup>6</sup>Li absorption may need to be considered/corrected when analysing diffraction data.

For both X-ray and neutron diffraction, constant wavelength (CW) experiments are routinely conducted in which a monochromatic beam of known wavelength is used. Non-monochromatic wavelengths, however, can also be used in neutron diffraction. This is known as time-of-flight neutron diffraction and is the focus of all further discussions on neutron diffraction.

#### Time-of-Flight Neutron Diffraction

Time-of-flight powder neutron diffraction (ND-ToF) exploits the de Broglie equation (Equation 3.10) in which a neutron's wavelength is related to its momentum:<sup>44</sup>

$$\lambda = \frac{h}{mv} = \frac{ht}{mL} \tag{3.10}$$

where h is Planck's constant and m is the mass of the neutron; its velocity, v, is a measure of the distance travelled by the neutron, L, in a given time, t. By combining de Broglie's equation and Bragg's Law (Equation 3.8), we can use ToF measurements to determine crystal structures through:<sup>44</sup>

$$\frac{ht}{mL} = 2d\sin\theta \tag{3.11}$$

In practice, this means that to determine  $d_{nkl}$  we must measure the time it takes for a neutron to reach the detector, which is a fixed distance and angle from the source. To reduce counting times several detectors are arranged into different banks, placed at different angles with respect to the source. To accurately determine the time taken to travel distance L, the start time must be fixed. To fix the start time, the neutron source is pulsed into well-defined intervals. Pulsed neutrons can be provided by a spallation source in which  $H^-$  ions are bunched, accelerated, and stripped of their electrons. The result is a proton beam with discrete pulses, which is directed towards a tungsten target. Once the pulsed proton beam hits the tungsten target, neutrons are driven from the nuclei of the target atoms, producing a neutron beam. Moderators are then used to slow the resulting neutron beam, before conducting diffraction experiments, to wavelengths that allow diffraction and subsequent data collection/analysis.

#### Rietveld Refinement

Rietveld refinement is a least-squares fitting approach to refining structural models against experimental diffraction data.<sup>46</sup> The refinement of the structural model considers both instrumental and structural parameters. A first approximation of structural parameters is contained within an input file which outlines cell symmetry, lattice parameters, atomic positions, site occupancy, and displacement parameters. During the refinement of these parameters, the intensity that is calculated by the structural model  $Y_i(calc)$  is refined against its experimentally observed intensity  $Y_i(obs)$ , for each step (*i*) such that Equation 3.12 is minimised<sup>46</sup>:

$$\sum_{i} w_i \{ Y_i(\text{obs}) - Y_i(\text{calc}) \}^2$$
(3.12)

Once minimised, the quality of the fit can be assessed through R-factors ( $R_p$ ,  $R_{wp}$ ,  $R_{exp}$ ) and the goodness-of-fit parameter ( $\chi^2$ ).

The weighted-profile R-value,  $R_{wp}$  (Equation 3.13) becomes minimised as Equation 3.12 is minimised:

$$R_{wp} = \left\{ \frac{\sum_{i} w_{i} \{ Y_{i}(obs) - Y_{i}(calc) \}^{2}}{\sum_{i} w_{i} \{ Y_{i}(obs) \}^{2}} \right\}^{\frac{1}{2}}$$
(3.13)

Where  $w_i$  is the weighting of each data point with respect to the uncertainty,

$$w_i = \frac{1}{\sigma_i(y_i)} \tag{3.14}$$

For a given number of counts (N), the "best possible" value for  $R_{wp}$  is termed the expected R factor ( $R_{exp}$ ):

$$R_{exp} = \left(\frac{N}{\sum_{i} w_{i} \{Y_{i}(obs)\}^{2}}\right)^{\frac{1}{2}}$$
(3.15)

In an ideal scenario, the value of  $R_{wp}$  should approach  $R_{exp}$ . This leads to the goodness-of-fit parameter,  $\chi^2$ :

$$\chi^2 = \left(\frac{R_{wp}}{R_{exp}}\right)^2 \tag{3.16}$$

For a perfect fit, where  $R_{wp} = R_{exp}$ ,  $\chi^2 = 1$ . However,  $\chi^2$  should be interpreted with adequate knowledge of the data collection. To increase the statistical precision of the collected data, and thereby allow for the adaptation of better structural models, the total number of counts (*N*) is often increased.<sup>46</sup> This results in a decrease in the uncertainty of each data points. Therefore, by Equation 3.15, counting for longer causes  $R_{exp}$  to decrease, and  $\chi^2$  to increase. Minor imperfections in a fit with many points can lead to large increases in  $\chi^2$ . So, whilst counting longer will allow a better structural model to be developed, the fit will appear worse when judging solely on  $\chi^2$ .<sup>46</sup> Often visual comparison of the calculated and observed pattern can be more informative.

Another metric for assessing the refined parameters within the structural model is the estimated standard deviation (ESD,  $\sigma$ ), or standard uncertainty.<sup>47</sup> The ESD of each refined parameter,  $p_j$ , is calculated using the inverted least-squares matrix,  $A_{ij}$ :

$$\sigma(p_i) = \left[\chi^2 A_{ii}^{-1}\right]^{\frac{1}{2}} = \left[A_{ii}^{-1}\right]^{\frac{1}{2}} R_{wp} / R_{exp}$$
(3.17)

Through this relationship between  $\sigma$  and  $R_{exp}$ , ESDs are also related to number of profile points (N). However, N is overestimated for parameters that affect peak intensity, as the number of contributing reflections ( $N_{nkl}$ ) is less than the number of profile points. Therefore, the use of N in calculating ESDs leads to an underestimation in error, by Equation 3.17. This underestimation is generally accepted to be by a factor of  $\approx 3.48$ 

Le Bail refinement is a related least-squares fitting technique, but it focuses on the refinement of the unit cell parameters and peak intensities rather than the full atomic model. Unlike Rietveld refinement, where atomic positions, site occupancies, and displacement parameters are refined, Le Bail refinement adjusts the profile parameters (such as peak shapes, positions, and intensities) to fit the experimental data. This method is particularly useful when the structural model is not fully known or when the focus is on the phase identification and unit cell determination rather than a detailed refinement of atomic positions. In this work, Le bail refinements are applied to XRD patterns for samples which do not have corresponding ND patterns (see Section 4.2.2), since the similar X-ray scattering length off Ni/Mn make the refinement of a full atomic model unfeasible.

Full details for the refinements carried out in this work are provided in Chapter 4

#### 3.5 References

- 1 C. Liu, M. Wu, Y. Liu, Z. Lu, Y. Yang, S. Shi and G. Yang, *Mater. Res. Bull.*, 2018, **99**, 436–443.
- T. Entwistle, E. Sanchez-Perez, G. J. Murray, N. Anthonisamy and S. A. Cussen, *Energy Reports*, 2022, **8**, 67–73.
- 3 M. Noh and J. Cho, *J. Electrochem.* Soc., 2013, **160**, A105–A111.
- 4 S. Zhang, C. Deng, B. L. Fu, S. Y. Yang and L. Ma, *Powder Technol.*, 2010, **198**, 373–380.
- 5 H. Dong and G. M. Koenig, *J. Mater. Chem. A*, 2017, **5**, 13785–13798.
- 6 D. Liu, J. Han and J. B. Goodenough, *J. Power Sources*, 2010, **195**, 2918–2923.
- 7 Z. Liu, Y. Jiang, X. Zeng, G. Xiao, H. Song and S. Liao, *J. Power Sources*, 2014, 247, 437–443.
- 8 H. Liu, G. Zhu, L. Zhang, Q. Qu, M. Shen and H. Zheng, *J. Power Sources*, 2015, **274**, 1180–1187.
- 9 Y. Xiao, W. Xiang, J. Zhang, Y. Zhu and X. Guo, *Ionics (Kiel).*, 2016, **22**, 1361–1368.
- 10 P. Du, J. Wan, J. Qu, H. Xie, D. Wang and H. Yin, *npj Mater. Degrad.*, , DOI:10.1038/s41529-024-00453-x.
- 11 C. M. Costa, E. Lizundia and S. Lanceros-Méndez, *Prog. Energy Combust. Sci.*, 2020, **79**, 100846.
- 12 X. Lu, G. J. Lian, J. Parker, R. Ge, M. K. Sadan, R. M. Smith and D. Cumming, J. Power

- Sources, 2024, 592, 233916.
- M. Yue, S. Azam, N. Zhang, J. R. Dahn and C. Yang, *J. Electrochem. Soc.*, 2024, 171, 050515.
- 14 J. H. Kim, N. P. W. Pieczonka, Z. Li, Y. Wu, S. Harris and B. R. Powell, *Electrochim. Acta*, 2013, **90**, 556–562.
- L. Madec and H. Martinez, *Electrochem. commun.*, 2018, **90**, 61–64.
- B. E. Murdock, C. G. Armstrong, D. E. Smith, N. Tapia-Ruiz and K. E. Toghill, *Joule*, 2022, **6**, 928–934.
- 17 C. Liu, Z. G. Neale and G. Cao, *Mater. Today*, 2016, **19**, 109–123.
- H. Arai, K. Sato, Y. Orikasa, H. Murayama, I. Takahashi, Y. Koyama, Y. Uchimoto and Z. Ogumi, *J. Mater. Chem. A*, 2013, **1**, 10442–10449.
- N. Elgrishi, K. J. Rountree, B. D. McCarthy, E. S. Rountree, T. T. Eisenhart and J. L. Dempsey, *J. Chem. Educ.*, 2018, **95**, 197–206.
- 20 A. C. Lazanas and M. I. Prodromidis, ACS Meas. Sci. Au, 2023, 3, 162–193.
- J. Landesfeind, D. Pritzl and H. A. Gasteiger, *J. Electrochem. Soc.*, 2017, 164, A1773–
   A1783.
- 22 T. L. Lee and D. A. Duncan, Synchrotron Radiat. News, 2018, 31, 16–22.
- 23 X. Liu and T. C. Weng, MRS Bull., 2016, 41, 466–472.
- 24 G. Greczynski and L. Hultman, *J. Appl. Phys.*, , DOI:10.1063/5.0086359.
- T. R. Gengenbach, G. H. Major, M. R. Linford and C. D. Easton, *J. Vac. Sci. Technol. A Vacuum, Surfaces, Film.*, DOI:10.1116/6.0000682.
- 26 G. Greczynski and L. Hultman, *ChemPhysChem*, 2017, **18**, 1491–1660.
- 27 D. J. Morgan, Surf. Interface Anal., 2023, **55**, 331–335.
- E. Markevich, G. Salitra, K. Fridman, R. Sharabi, G. Gershinsky, A. Garsuch, G. Semrau, M. A. Schmidt and D. Aurbach, *Langmuir*, 2014, **30**, 7414–7424.
- E. Björklund, C. Xu, W. M. Dose, C. G. Sole, P. K. Thakur, T.-L. Lee, M. F. L. De Volder, C. P. Grey and R. S. Weatherup, *Chemistry Mater.*, 2022, **34**, 1987–2494.
- 30 S. Dalavi, M. Xu, B. Knight and B. L. Lucht, *Electrochem. Solid-State Lett.*, 2011, **15**, A28.

- 31 G. H. Major, N. Fairley, P. M. A. Sherwood, M. R. Linford, J. Terry, V. Fernandez and K. Artyushkova, *J. Vac. Sci. Technol. A*, DOI:10.1116/6.0000377.
- 32 J. N. Zhang, Q. Li, Y. Wang, J. Zheng, X. Yu and H. Li, *Energy Storage Mater.*, 2018, **14**, 1–7.
- 33 M. Xu, D. Lu, A. Garsuch and B. L. Lucht, *J. Electrochem. Soc.*, 2012, **159**, A2130–A2134.
- 34 D. T. Clark, W. J. Feast, P. J. Tweedale and H. R. Thomas, *J. Polym. Sci.*, 1980, **18**, 1651–2031.
- 35 M. L. Baker, M. W. Mara, J. J. Yan, K. O. Hodgson, B. Hedman and E. I. Solomon, Coord. Chem. Rev., 2017, 345, 182–208.
- 36 F. Frati, M. O. J. Y. Hunault and F. M. F. De Groot, *Chem. Rev.*, 2020, **120**, 4056–4110.
- W. Zhou, R. Apkarian, Z. L. Wang and D. Joy, *Scanning Microsc. Nanotechnol. Tech. Appl.*, 2007, 1–40.
- 38 P. W. Atkins, *Physical Chemistry*, 6519BC, vol. 625.
- 39 B. D. Cullity and S. R. Stock, *Elements of X-ray diffraction*, Prentice-Hall, 3rd ed., 2001.
- 40 H. Liu, H. Liu, S. H. Lapidus, Y. S. Meng, P. J. Chupas and K. W. Chapman, *J. Electrochem. Soc.*, 2017, **164**, A1802–A1811.
- 41 L. B. Mccusker, R. B. Von Dreele, D. E. Cox, D. Louër and P. Scardi, *J. Appl. Crystallogr.*, 1999, **32**, 36–50.
- 42 E. A. Merritt, Acta Crystallogr. Sect. D Biol. Crystallogr., 2012, 68, 468–477.
- 43 V. Sears, *Phys. Rev.*, 1992, **3**, 26–27.
- 44 S. E. Nagler, A. D. Stoica, G. M. Stoica, K. An, H. D. Skorpenske, O. Rios, D. B. Hendin and N. W. Bower, *J. Anal. Methods Chem.*, 2019, **2019**, 164058.
- W. G. Williams, R. M. Ibberson, P. Day and J. E. Enderby, *Phys. B Condens. Matter*, 1997, **241–243**, 234–236.
- 46 B. H. Toby, *Powder Diffr.*, 2006, **21**, 67–70.
- 47 J. F. Berar and P. Lelann, *J. Appl. Crystallogr.*, 1991, **24**, 1–5.
- 48 J. K. Cockcroft, Estimated Standard Deviations, http://pd.chem.ucl.ac.uk/pdnn/refine1/errors.htm, (accessed 5 May 2023).

# Chapter 4 | Understanding the Structure and Performance of Substituted LNMO Cathodes

This chapter presents the article "Murdock, B.E., Cen, J., Squires, A.G., Kavanagh, S.R., Scanlon, D.O., Zhang, L., and Tapia-Ruiz, N. (2024). Li-Site Defects Induce Formation of Li-Rich Impurity Phases: Implications for Charge Distribution and Performance of LiNi<sub>0.5-x</sub>M<sub>x</sub>Mn1.5O4 Cathodes (M = Fe and Mg; x = 0.05-0.2). Adv. Mater. *36*, 2400343." under the terms of the Creative Commons CC BY license with minor edits for clarity and cohesion. The supporting information has been incorporated into the main text where appropriate. The article was published in the peer-reviewed journal of Advanced Materials in April 2024.

As explored in Chapter 2, the development and adoption of high-performance cathodes that show low critical metal content is of both environmental and socioeconomic importance. To this end, the high-voltage spinel cathode (LNMO) is a promising material, with a reasonably high energy density that can be maintained with fast charging/discharging. Compared to more commonly used cathodes, LNMO balances the relatively low critical material content and highrate performance of LFP with the high-energy density of low-Ni NMCs (e.g. NMC111).1 The unique high voltage of LNMO, however, may allow simplification of the battery pack. The battery pack consists of many cells which are connected in series to provide a given voltage. Since the nominal voltage of LNMO (4.7V) is ≈ 25% higher than that of NMC-type cathodes (3.7V), 25% fewer cells would be required to reach the same voltage, ultimately lowering pack cost.2 Cost is also reduced through lowering material demands, where LNMO is not only Cofree but also contains less Ni, less Li, and less graphite per kWh (Figure 4.1). LNMO, therefore, offers a Co-free and Mn-rich counterpart to Ni-rich cathodes, to help alleviate supply risk and diversify supply chains. Successful commercialisation of LNMO, however, is hindered by poor capacity retention. Cationic substitution of LNMO (i.e., LiNi<sub>0.5-x</sub>M<sub>x</sub>Mn<sub>1.5</sub>O<sub>4</sub>) can, not only alleviate capacity degradation but can also further reduce Ni content.<sup>3</sup> The use of abundant substituents (e.g., M = Mg, Fe) is, therefore, key to promoting overall sustainability.

While it is generally accepted within the literature that cationic substitution (i.e.,  $LiNi_{0.5-x}M_xMn_{1.5}O_4$ ) can improve the electrochemical performance of LNMO, a clear and systematic understanding of the structural properties that allow for such improvements—and their origin—is lacking within the literature. For example, defects on the Li site have previously been shown to supress structural degradation, and subsequent capacity degradation, in Mg-substituted cathodes.<sup>4</sup> The origin of such Li-site defects, however, has not yet been determined. The

presence of Li-site defects in Fe-substituted cathodes, on the other hand, is disputed within the literature and, instead, their presence is said to be detrimental to performance.<sup>5,6</sup>

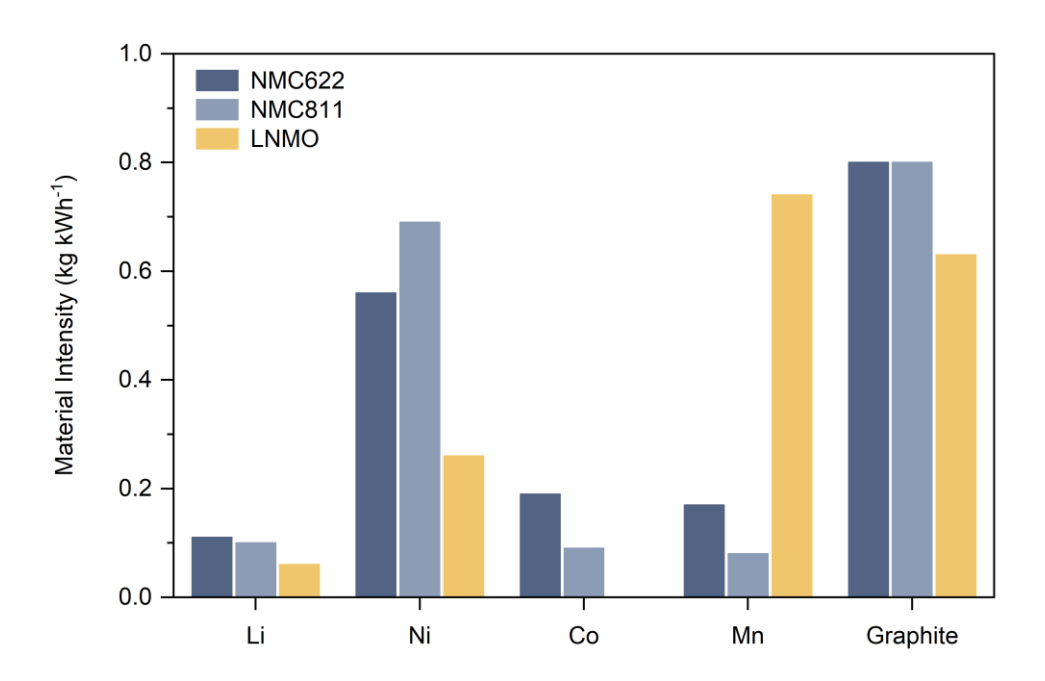


**Figure 4.1:** Comparing the intensity of different elements/materials (kg kWh<sup>-1</sup>) of LNMO to state-of-the-art NMC cathodes at the material level (i.e., this calculation does not consider the weight of inactive cell components. Material intensity at the cell level will be greater). See Appendix A for calculation details.

This chapter provides an in-depth study into the effect of substituents on the bulk structures of LiNi<sub>0.5-x</sub>M<sub>x</sub>Mn<sub>1.5</sub>O<sub>4</sub> (M = Fe, Mg, x = 0.05–0.2), which shows that the concentration of Li-site defects increases with substituent concentration and is higher in Mg-substituted samples. To our knowledge, this is the first report showing a correlation between the concentration of Lirich impurity phases and that of Li-site defects, where Mg is more likely to cause Li-site defects than Fe—evidenced both experimentally and computationally. Furthermore, possible charge compensators for charge-balancing Mn<sup>3+</sup> are explored and, while Mn<sup>3+</sup> is commonly linked to the presence of oxygen vacancies and/or Ni/Mn off-stoichiometry, our work shows that both are unlikely compensators for the charge reduction of Mn<sup>4+</sup> observed herein. This work not only provides valuable structural insight but can pave the way for the advanced structural design of LiNi<sub>0.5-x</sub>M<sub>x</sub>Mn<sub>1.5</sub>O<sub>4</sub> cathodes towards accelerated commercialisation.

Li-Site Defects Induce Formation of Li-Rich Impurity Phases: Implications for Charge Distribution and Performance of LiNi<sub>0.5-</sub> $_xM_xMn_{1.5}O_4$  Cathodes (M = Fe and Mg; x = 0.05-0.2)

Beth E. Murdock<sup>a,b,c</sup>, Jiayi Cen<sup>c,d</sup>, Alexander G. Squires<sup>c,e</sup>, Seán R. Kavanagh<sup>f</sup>, David O. Scanlon<sup>c,e</sup>, Li Zhang<sup>b,c</sup> and Nuria Tapia-Ruiz<sup>b,c\*</sup>

<sup>c</sup>The Faraday Institution, Quad One, Harwell Science and Innovation Campus, Didcot, OX11 0RA, UK

<sup>d</sup> Department of Chemistry and Thomas Young Centre, University College London, WC1H 0AJ, UK

#### **Abstract**

An understanding of the structural properties that allow for optimal cathode performance, and their origin, is necessary for devising advanced cathode design strategies and accelerating the commercialisation of next-generation cathodes. High-voltage, Fe- and Mg-substituted LiNi<sub>0.5</sub>Mn<sub>1.5</sub>O<sub>4</sub> cathodes offer a low-cost, Co-free, yet energy-dense alternative to commercial cathodes. In this work, the effect of substitution on several important structure properties is explored, including Ni/Mn ordering, charge distribution, and extrinsic defects. In the cation-disordered samples studied, a correlation is observed between increased Fe/Mg substitution, Li-site defects, and Li-rich impurity phase formation—the concentrations of which are greater for Mg-substituted samples. This is attributed to the lower formation energy of Mg<sub>Li</sub> defects when compared to Fe<sub>Li</sub> defects. Li-site defect-induced impurity phases consequently alter the charge distribution of the system, resulting in increased [Mn³+] with Fe/Mg substitution. In addition to impurity phases, other charge compensators are also investigated to explain the origin of Mn³+ (extrinsic defects, [Ni³+], oxygen vacancies and intrinsic off-stoichiometry), although their effects are found to be negligible.

<sup>&</sup>lt;sup>a</sup> Department of Chemistry, Lancaster University, Lancaster, LA1 4YB, UK

<sup>&</sup>lt;sup>b</sup> Department of Chemistry, Molecular Sciences Research Hub, Imperial College London, W12 0BZ, UK

<sup>&</sup>lt;sup>e</sup> School of Chemistry, University of Birmingham, Birmingham, B15 2TT, UK

<sup>&</sup>lt;sup>f</sup> Department of Materials and Centre for Processable Electronics, Imperial College London, SW7 2AZ, UK

<sup>\*</sup>Corresponding author: n.tapia-ruiz@imperial.ac.uk

#### 4.1 Introduction

Satisfying the increasing demands of transport electrification relies on the development of high energy-density cathode materials for lithium-ion batteries (LIBs). Spinel-type LiNi<sub>0.5</sub>Mn<sub>1.5</sub>O<sub>4</sub> (LNMO) cathodes have received particular attention due to their high operating voltage ( $\approx 4.7$  V vs Li<sup>+</sup>/Li) and high energy density (650 Wh kg<sup>-1</sup>).<sup>3</sup> Their widespread adoption in electric vehicles, however, is limited by their poor cycling stability, which results from a combination of structural instabilities, including electrolyte degradation, transition metal (TM) dissolution and surface densification.<sup>7–9</sup>

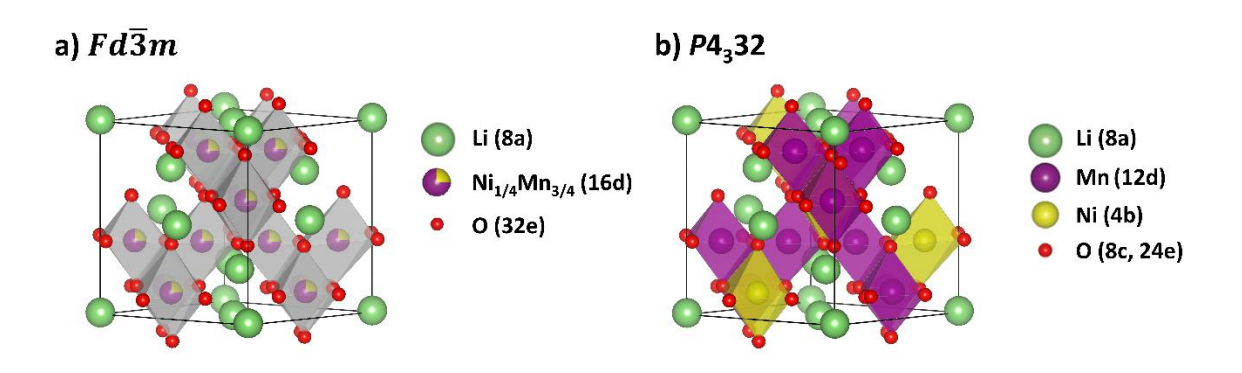


**Figure 4.2:** LNMO crystal structures: a) disordered ( $Fd\bar{3}m$ ); and b) ordered ( $P4_332$ ) LNMO.

A typical LNMO spinel structure consists of a cubic closed-packed array of oxygen, creating a series of octahedral (MO<sub>6</sub>) and tetrahedral (MO<sub>4</sub>) sites. Within the oxygen array, Li occupies the tetrahedral (8a) sites. The site location of Ni<sup>2+</sup> and Mn<sup>4+</sup> ions, on the other hand, depends on the synthetic conditions used to produce the material. An ordered arrangement of Ni and Mn ions across octahedral 4b and 12d Wyckoff sites, respectively, is the most thermodynamically stable phase ( $P4_332$  space group, **Figure 4.2b**). However, the use of high synthesis temperatures and fast cooling rates may encourage a disordered arrangement in which Ni and Mn become randomly distributed across octahedral 16d Wyckoff sites ( $Fd\overline{3}m$  space group, **Figure 4.2a**).<sup>3</sup> In addition to the presence of Ni ions on octahedral sites, some literature also reports Ni concentrations of  $\approx$  2% on tetrahedral 8a sites due to the similar crystal radii of tetrahedral Ni<sup>2+</sup> and Li<sup>+</sup> (0.69 and 0.73 Å, respectively).<sup>10–12</sup>

Cation ordering can have a direct influence on the electrochemical performance of these materials. Upon cycling, the ordered phase experiences discontinuous phase transitions between three different cubic phases related to LiNi<sub>0.5</sub>Mn<sub>1.5</sub>O<sub>4</sub>, Li<sub>0.5</sub>Ni<sub>0.5</sub>Mn<sub>1.5</sub>O<sub>4</sub> and Ni<sub>0.5</sub>Mn<sub>1.5</sub>O<sub>4</sub>. A cation-disordered arrangement, however, allows a solid solution behaviour from LiNi<sub>0.5</sub>Mn<sub>1.5</sub>O<sub>4</sub> to Li<sub>0.5</sub>Ni<sub>0.5</sub>Mn<sub>1.5</sub>O<sub>4</sub>, followed by a two-phase reaction. This not only minimises the lattice strain experienced upon cycling, which leads to capacity degradation,

but can also improve the kinetics of Li<sup>+</sup> ion de/intercalation. Cation disorder is typically accompanied by off-stoichiometry and increased concentrations of Mn<sup>3+</sup>, where Mn<sup>3+</sup> can improve the electronic conduction. This is thought to improve the rate performance.<sup>14</sup> High concentrations of Mn<sup>3+</sup>, however, can be detrimental to cycle life. This is not only because of the Jahn-Teller distortion effect associated with Mn<sup>3+</sup> ions, which can impact structural stability, but also because of the disproportionation of Mn<sup>3+</sup> and subsequent Mn<sup>2+</sup> dissolution.<sup>15</sup> This results in the loss of cathode active material and Mn deposition on the anode surface, which is detrimental to the stability of the solid electrolyte interphase.<sup>15</sup>

Various substitution strategies have been adopted to improve the performance of LNMO. For example, anionic substitution of oxygen with more electronegative anions, such as F<sup>-</sup>, can strengthen the metal-anion bonding, making the structure more stable and less prone to TM dissolution.<sup>16</sup> Additionally cationic substitution on either the Li tetrahedral site (e.g., Na<sup>+</sup>)<sup>17</sup> or the Ni/Mn octahedral site (e.g., Fe, Cr, Co)<sup>18</sup> has been shown to improve the structural stability and subsequent cycling stability of LNMO. In recent years, significant efforts towards codoping have been made, to offer combined benefits of the respective dopants, such as codoped Mo-F LNMO recently reported by Weng *et al.* to improve capacity retention from 87.7% to 95.6% (1C, 100 cycles, 3.5–4.95 V).<sup>19</sup>

Among those reported, Fe3+ and Mg2+ are of particular interest as substituents because of their high natural abundance and therefore, low cost, and sustainability.3 Despite the difference in redox activity and valence state, several reports show improved electrochemical performance upon  ${\rm Mg^{2+4,20,21}}$  and  ${\rm Fe^{3+6,22,23}}$  substitution. For example,  ${\rm Mg}$  substitution on both the 8a and 16c sites has been shown to prevent structural transitions upon cycling, induced by TM migration, which can effectively prevent TM dissolution and improve cycling stability.<sup>4</sup> Improved rate performance is also enabled through reduced charge transfer upon Mg substitution. 4,20,21 Fe, on the other hand, is reported to improve cycling stability by stabilising the cation-disordered phase and alleviating parasitic surface reactions. <sup>6,22,23</sup> The stabilised disorder structure, alongside increased concentrations of Mn<sup>3+</sup>, is also reported to improve electronic conductivity. 6,22,23 A cohesive view of the structural properties that lead to superior performance when using these substituents, however, is lacking within the literature, with many conflicting structural observations reported. This lack of understanding surrounding structure-property-performance relationships in substituted LNMO cathodes presents a bottleneck for advanced structural cathode design, which is crucial to delivering improved battery performance.

Several structural properties must be evaluated to understand the role of substituents in the electrochemical performance. These include 1) Ni/Mn ordering, where bulk disordered phases

typically exhibit superior performance by minimising discontinuous phase transformations and extending solid-solution regions upon cycling;<sup>24</sup> 2) impurity phase formation, where Ni-rich impurities are commonplace in LNMO and result in undesirable phase boundaries and loss of active material;<sup>3</sup> 3) Mn<sup>3+</sup> content, which must be tuned to balance the positive and negative effects of Mn<sup>3+</sup>;<sup>14</sup> 4) Oxygen vacancies, which not only influence the charge distribution but lead to surface reconstruction and the formation of thick surface layers on LNMO, leading to increased polarisation and diminished cycling stability;<sup>25</sup> 5) Ni<sup>3+</sup> content, which also influences charge distribution and limits the capacity available at high voltages;<sup>26</sup> and 6) the in/extrinsic defect chemistry, which evaluates substitutional (A<sub>B</sub>), interstitial (A<sub>i</sub>) and vacancy defects ( $V_B$ ), where A represents an ion substituted on site B or onto an interstitial site, i. For example, Mg substituted on the Li 8a site (Mg<sub>Li</sub> defect), Mg in the vacant 16c site (Mg<sub>i</sub> defect) or vacancies on the Li site ( $V_{Li}$  defect). Of particular interest is the presence of substitutional Li-site defects (A<sub>Li</sub>) which have been shown to inhibit structural degradation upon cycling, by limiting TM migration and subsequent dissolution.<sup>4</sup>

The similar X-ray scattering length of Ni and Mn atoms limits the use of X-ray diffraction (XRD) for such structural investigations. The clear distinction between Ni, Mn, Li and O atoms enabled through neutron diffraction (ND) studies, on the other hand, not only allows the determination of long-range Ni/Mn ordering—through the presence of superstructure peaks related to the decreased symmetry of  $P4_332$  phase—but also allows the investigation of substituent site location, by considering Fe and Mg 8a, 16d and 16c site occupancies ( $f_{8a}$ ,  $f_{16d}$ ,  $f_{16c}$ ). Rietveld refinement of the occupancies at different sites ( $f_{8a}$ ,  $f_{16d}$ ,  $f_{16c}$ ) and the resulting stoichiometries can give further insight into the charge distribution and cation deficiencies in the spinel phase and their relation to impurity phase formation. Despite the superiority of ND for such investigations, performing combined refinements against both ND and XRD data is optimal for determining site occupancy.<sup>27</sup> Even still, the complex co-existence of multiple cations on a given site limits the number of site defects that can be investigated through refinements against experimental data.<sup>27</sup> As such, computational insights are valuable in understanding the complex interplay between substitutional ( $A_B$ ), interstitial ( $A_I$ ) and vacancy defects ( $V_B$ ).

To establish the effect of Fe and Mg substitution on the bulk structure of LNMO, we present consolidating findings that emerge from both experimental and computational investigations. In this work, as-synthesised LiNi<sub>0.5-x</sub>M<sub>x</sub>Mn<sub>1.5</sub>O<sub>4</sub> cathodes (where M = Fe and Mg; and x = 0.05, 0.1, 0.15 and 0.2), denoted as Mx (e.g., Mg0.1), are analysed through combined ND-XRD Rietveld refinements. Such analysis is complemented by first-principles density functional theory (DFT) calculations which evaluate the substitution responses of LNMO under different

atomic chemical potentials, representing different experimental conditions subject to thermodynamic equilibrium. For such calculations, the Ni/Mn-ordered  $P4_332$  structural model was used. Although this structural model differs from the  $Fd\overline{3}m$  used for the synthesised samples—in correspondence with the temperature at which these samples were synthesised— it keeps the defect analysis on this complex quinary system tractable and avoids excessive computational demands for dealing with the undefined occupation of Ni/Mn across the 16d sites in the  $Fd\overline{3}m$  symmetry.

Through our combined approach we: 1) elucidate Mg/Fe site preference and evaluate the influence of increasing substituent concentration on the concentration of substitutional ( $A_B$ ), interstitial ( $A_i$ ) and vacancy defects ( $V_B$ ) at the equilibrium Fermi level under charge-neutral conditions (Section 4.3); 2) explore the effect of substitution on the concentration of Mn<sup>3+</sup> and evaluate several bulk structure properties—including unit cell size,  $V_o$ , Ni<sup>3+</sup> content, off-stoichiometry and impurity phase fractions—to search for its origin (Section 4.4); 3) investigate the impact of substitution on the electrochemical performance of LNMO, with the help of bulk structural insights provided in Sections 4.3 and 4.4.

#### 4.2 Experimental Methods

#### 4.2.1 Material Synthesis and Electrochemical Characterisation

LiNi<sub>0.5</sub>Mn<sub>1.5</sub>O<sub>4</sub> (LNMO), LiNi<sub>0.5-x</sub>Fe<sub>x</sub>Mn<sub>1.5</sub>O<sub>4</sub> (Fex) and LiNi<sub>0.5-x</sub>Mg<sub>x</sub>Mn<sub>1.5</sub>O<sub>4</sub> (Mgx) (x = 0.05, 0.1, 0.15 and 0.2) were synthesised via an oxalate co-precipitation method, and eletrodes prepared as previously outlined in Chapter 3 (Section 3.1 and 3.2.1).<sup>1</sup> All electrochemical testing was carried out in a temperature-controlled climate chamber (28°C, Memmert), where cells were rested for 12 h prior to the measurements. Standard galvanostatic cycling stability studies were carried out in two-electrode coin cells as outlined in Chapter 3.2.2 (1C, 3.5–4.9 V).

# 4.2.2 Powder X-ray and Neutron Diffraction

X-ray powder diffraction data were collected for all samples on a lab-based Rigaku SmartLab diffractometer in Bragg-Brentano geometry, using a glass sample holder, between  $2\theta = 10-90^{\circ}$  (0.1° min<sup>-1</sup>). Time-of-flight powder neutron diffraction (ND-ToF) data were collected for selected samples (x = 0, 0.1, 0.2, **Table 4.1**). Experiments were carried out at the ISIS spallation neutron and muon source on the General Materials (GEM) diffractometer.<sup>29</sup> For the experiments, powdered samples were packed in an MBraun glovebox under argon (H<sub>2</sub>O and O<sub>2</sub> < 0.1 ppm) into cylindrical vanadium cans ( $\varnothing = 6$  mm, h = 5.5 cm). Data were collected over

a wide Q-range (0.01–50 Å) across several banks, arranged at different angles to the detector. A data collection time of 8 h was used to provide a high signal-to-noise ratio at a high Q.

**Table 4.1:** Summary of X-ray and neutron diffraction data collected for each sample.

	LiNi <sub>0.5-x</sub> Fe	e <sub>x</sub> Mn <sub>1.5</sub> O <sub>4</sub>	$LiNi_{0.5-x}Mg_xMn_{1.5}O_4$	
X	XRD	ND	XRD	ND
0	<b>~</b>	<b>~</b>	<b>~</b>	<b>~</b>
0.05	<b>~</b>	×	<b>~</b>	×
0.1	<b>~</b>	<b>/</b>	<b>/</b>	<b>~</b>
0.15	<b>~</b>	×	<b>~</b>	×
0.2	<b>~</b>	<b>~</b>	<b>/</b>	<b>~</b>

Combined Rietveld refinements, in which ND-ToF bank 3 (24-45°), bank 4 (50-74°) and lab XRD data are simultaneously refined, were performed using GSAS software with the EXPGUI graphical interface for samples x = 0, 0.1 and 0.2 (**Table 4.1**). Refined parameters included lattice parameter (a), octahedral (16d) and tetrahedral (8a) site occupancy, isotropic atomic displacement parameters (ADP) ( $U_{iso}$ ), and oxygen xyz coordinates. Oxygen site occupancy was fixed to 1 and  $U_{iso}$  values of TM atoms were constrained to be equal. Backgrounds were fit using a Chebyshev polynomial function and peak shapes using a pseudo-Voight function. Estimated standard deviation (ESD) values of parameters related to peak intensity, which are generally accepted to be underestimated by a factor of ≈ 3, were scaled accordingly.<sup>32</sup> The absorption correction parameter was refined to account for <sup>6</sup>Li absorption in the neutron diffraction data. This correction factor was refined separately for each bank, with the result being small and consistent between banks. Note that the inclusion of an absorption correction factor in the structural refinement may result in a systematic underestimation of the ADP values, as the absorption correction factor is derived from the product of U and the scale factor.<sup>33</sup> However, due to the nature of the study, which considers an internal comparison between samples in which all sample refinements are treated in the same manner, the comparison between samples still holds. The same is true for comparing ESD values between refinements. The relatively high  $\chi^2$  value reported herein is a result of long ND-ToF data collection times and the large resulting number of data points, in which extremely minor differences between experimental and calculated patterns can cause a significant increase in the  $\chi^2$  value. In this case, R-factors are more indicative of the goodness-of-fit obtained.

For all other samples (x = 0.05 and 0.15), Le Bail refinements were performed to determine lattice parameters and phase fractions. Backgrounds were fit using a Chebyshev polynomial

function and peak shapes were fit using a pseudo-Voight function.  $U_{iso}$  values for all atoms were fixed to 0.005 Å<sup>2</sup> for all atoms, and site occupancies were fixed according to the stoichiometric formulation. The 16d octahedral sites were assumed for all substituents (i.e., Mg and Fe) during Le Bail refinements.

# 4.2.3 Mnx+ calculations (Figure 4.8)

The average Mn<sup>x+</sup> oxidation state in each sample was estimated from electrochemical data and from the stoichiometry that resulted from combined Rietveld refinement of X-ray and neutron diffraction data (**Tables A1–3**). The feasibility of the structural models, obtained through Rietveld refinements, was then determined by comparing Mn<sup>x+</sup> estimations from both methods.

Electrochemical estimates of  $Mn^{3+}$  concentrations in LNMO, Fex and Mgx (x = 0.1 and 0.2) were derived from the 4 V specific charge capacity region in the galvanostatic data (OCV–4.375 V, see **Figure 4.6**) as follows:

The mass Mn<sup>3+</sup> per g of active material (wt. % Mn<sup>3+</sup>) was first calculated through equation 4.1,

$$wt. \% Mn^{3+} = \frac{Mn^{3+}(g)}{LNMO(g)} = \frac{4 \text{ V region specific charge capacity (mAh } g_{LNMO}^{-1})}{Mn^{3/4+} \text{ theoretical specific capacity (mAh } g_{Mn}^{-1})}$$
(4.1)

The wt. % Mn<sup>3+</sup> was then converted to mol % Mn<sup>3+</sup> (moles of Mn<sup>3+</sup> per mol of active material) through equation 4.2, with units shown in equation 4.3 for clarity.

$$mol.\% Mn^{3+} = \frac{Mn^{3+}(mol)}{LNMO (mol)} = \frac{wt.\% Mn^{3+} \times MW_{LNMO}}{MW_{Mn}}$$
 (4.2)

$$mol.\% Mn^{3+} = \frac{mol_{Mn}}{mol_{LNMO}} = \frac{g_{Mn}/g_{LNMO} \times g_{LNMO}/mol_{LNMO}}{g_{Mn}/mol_{Mn}}$$
 (4.3)

Note that the initial charge capacity was chosen to eliminate any changes in [Mn<sup>3+</sup>] that may arise during cycling. The remaining Mn<sup>4+</sup> content was determined to be the difference between the total refined Mn content ( $\approx 1.5$  mol) and the estimated moles of Mn<sup>3+</sup>, as determined above. The average oxidation state was then calculated from the sum of products of the estimated molar quantities of Mn<sup>3+</sup> and Mn<sup>4+</sup> and their respective charges (Equation 4.4), as follows:

$$x in Mn^{x+} = \frac{4 Mol (Mn^{4+}) + 3 Mol (Mn^{3+})}{Mol (Mn_{total})}$$
(4.4)

The average oxidation state of Mn<sup>x+</sup> was also determined, through Equation 4.5, in which the sum of products of charge and refined moles of cations and anions must be equal to charge balance. Such calculations were performed while assuming a Ni<sup>2+</sup> oxidation state.

$$1Mol(Li^{+}) + 2Mol(Ni^{2+}) + yMol(M^{y+}) + xMol(Mn^{x+}) - 2Mol(O^{2-}) = 0$$
 (4.5)

where the charge (y) for M ( $Mg^{2+}$  and  $Fe^{3+}$ ) is 2 and 3, respectively.

## 4.2.4 Estimation of impurity phase fractions from Li deficiencies (Figure 4.13)

Assuming that all Li lost from the Li site precipitates to form a  $\text{Li}_2\text{MO}_3$  impurity phase, as opposed to migrating to the 16d site, then the *spinel phase : impurity phase* mole ratio should be  $\text{Li}_{1\text{-}z}\text{Ni}_{0.5}\text{Mn}_{1.5}\text{O}_4$  :  $\frac{z}{2}\text{Li}_2\text{MO}_3$ , where  $z = 1\text{-}f_{Li}$ . The wt.% of impurity per mol of LiNi<sub>0.5-x</sub>M<sub>x</sub>Mn<sub>1.5</sub>O<sub>4</sub> can then be calculated by Equation 4.6.

$$wt. \%(Li_2MO_3) = \frac{\left(\frac{z}{2}\right)MW(Li_2MO_3)}{\left(\frac{z}{2}\right)MW(Li_2MO_3) + MW(LiNi_{0.5-x}M_xMn_{1.5}O_4)}$$
(4.6)

#### 4.3 How Substitution Alters Site Preference and Defect Concentrations

#### 4.3.1 Mg and Fe site Preference in Substituted LNMO Materials

Through XRD and ND data, the structure of all the samples studied in this work (**Table 4.1**) can be indexed to an  $Fd\overline{3}m$  space group (**Figure 4.2, A1–5**), indicating that a spinel-type structure forms with bulk Ni/Mn disorder, regardless of substituent type or concentration.<sup>3</sup> In line with literature reports, such cation disorder is expected due to the high synthesis temperature and fast cooling rate used to produce these samples.<sup>34</sup> In the  $Fd\overline{3}m$  structure, TMs and other substituents typically occupy the octahedral 16d sites, while Li atoms occupy the tetrahedral 8a sites, and the interstitial 16c site remains vacant.

The site preference of Fe/Mg can be confirmed through defect calculations by comparing the site-dependent formation energies of their extrinsic defects, where lower formation energies correspond to stronger site preference (Equation B3, Appendix B). Calculated formation energies for substitutional ( $M_{Ni}$ ,  $M_{Mn}$  and  $M_{Li}$ ) and interstitial defects ( $M_i$ ) suggest that Mg/Fe site preference follows the order of  $Mg_{Ni} > Mg_{Li} > Mg_{Mn} \ge Mg_i$  and  $Fe_{Ni} \ge Fe_{Mn} > Fe_{Li} > Fe_i$  (**Figure 4.3**). For Mg-substituted samples, the formation energy ranges (corresponding to

varying synthesis conditions) do not overlap for different substitutional defects, which suggests a distinctive site preference for  $Mg_{Ni}$  (i.e., on the 4b sites in  $P4_332$  LNMO, corresponding to 16d sites in  $Fd\bar{3}m$  LNMO). The concentration of  $Mg_{Li}$  defects is, therefore, expected to be minor. In Fe-substituted LNMO, on the other hand, the formation energy ranges of  $Fe_{Mn}$  and  $Fe_{Ni}$  overlap, indicating a synthesis-dependent site preference. Fe is, therefore, less biased to sit on the Ni sites compared to Mg and likely exists across both the Ni and Mn sites. The high formation energies of interstitial  $Fe_i$  and  $Mg_i$  defects indicate that  $[M_i]$  is far lower than the concentration of substitutional defects in both Fe and Mg systems. This is consistent with our experimental results in which vacant 16c interstitial sites in the  $Fd\bar{3}m$  spinel remain unoccupied upon Fe/Mg substitution (**Tables A1–3**, Appendix A). Initial refinements allowing for 16c site occupancy led to non-physical site occupancies (> 1) and  $U_{Iso}$  (< 0), suggesting that these sites are not meaningfully occupied; they were therefore omitted from the final structural model.

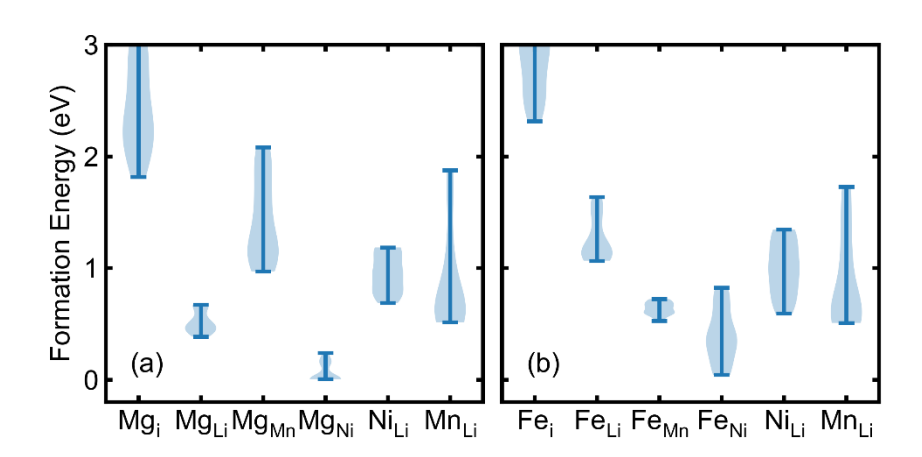


**Figure 4.3:** The distribution of formation energies of intrinsic (Ni<sub>Li</sub> and Mn<sub>Li</sub>) and extrinsic defects (M<sub>i</sub>, M<sub>Li</sub>, M<sub>Mn</sub>, M<sub>Ni</sub>) for M = Mg (a) and Fe (b) over all growth conditions (chemical potentials). Each formation energy corresponds to a single defect introduced into a  $2\times2\times2$  supercell (448 atoms), representing an approximate defect concentration of one dopant per 8 LNMO formula units, see Computational Methods in SI for details. Results and figures provided by Dr J. Cen.

Despite the good agreement between our experimental and computational findings, it is important to acknowledge the difference between the disordered structures observed experimentally and the ordered models used in computational analyses. The defect chemistry in disordered materials can be understood as an ensemble average across the possible

microstates such materials can adopt.<sup>35,36</sup> In this context, we employ the P4<sub>3</sub>32 ordered structure as a representative low-energy microstate of the disordered phase. This approach necessitates a qualitative interpretation of computational results due to the inherent discrepancies between the computational model and the as-synthesised material. Such qualitative analysis has shed light on point defect processes that affect the properties of doped LNMO. However, there is a pressing need for advancements in computational methods to enable the creation of quantitatively accurate models for defect analysis in compositionally complex disordered materials.

#### 4.3.2 Li (8a) Site Defect Response to Increased Substituent Concentration

Cation-disordered LNMO undergoes high-temperature synthesis during which Li vacancies can form in the structure, alongside the formation of impurity phases. This, combined with the similar sizes of Li and other cations within the substituted LNMO cathodes, may result in the formation of Li-site defects such as  $Ni_{Li}$ ,  $Mn_{Li}$  and  $M_{Li}$  (M = Fe and Mg), in which cations other than Li occupy the Li-site.

The similar crystal radius of Fe<sup>3+</sup> (0.63 Å) and Li<sup>+</sup> (0.73 Å) make Fe<sub>Li</sub> defects possible, yet discrepancies exist within the literature as to the site location of Fe. For instance, some literature suggests that Fe shows an increased propensity for the Li-8a site when  $x \ge 0.1$  in LiNi<sub>0.5-x</sub>Fe<sub>x</sub>Mn<sub>1.5</sub>O<sub>4</sub> through analysing the integrated intensity ratios of the (400)/(311) and (220)/(311) XRD peaks<sup>5</sup>, while others reports have used Mössbauer spectroscopy to suggest that Fe exists exclusively on the 16d sites in LiNi<sub>0.5-y</sub>Fe<sub>2y</sub>Mn<sub>1.5-y</sub>O<sub>4</sub>,  $0.2 \le y \le 0.4$ .<sup>6</sup> When considering Mg-substituted samples, few reports explore the site location of Mg.<sup>4,20,21,37</sup> However, one such exception reported the existence of Mg<sup>2+</sup> ions across both the Li 8a and typically vacant 16c sites (Mg<sub>Li</sub> and Mg<sub>i</sub> defects), as opposed to the 16d sites. This was shown through high-angle annular dark-field scanning transmission electron microscopy (STEM-HAADF) and ND, albeit with a large associated estimated standard deviation (ESD) of the site occupancy refined against ND data.<sup>4</sup> This is in contrast to both our computational (**Figure 4.3**) and experimental findings (**Table A1–3**, Appendix A), in which the interstitial 16c sites remain unoccupied. Occupancy of the Li 8a site in the as-synthesised samples, on the other hand, required further exploration.

Although the tetrahedral 8a site is occupied by Li alone in an ideal spinel structure, Li deficiencies in the refined structure unveil a more complex scenario (**Figure 4.4a**). Small Li deficiencies in the spinel phase (≈ 5–10%) are expected due to Li evaporation at high synthesis temperatures, and the formation of Li-containing impurity phases (see Section 4.4.5). However, when assuming that Li-site defects are absent, the refined Li deficiencies

that result from combined with XRD-ND refinements (1- $f_{Li(8a)}$ , **Table A1**, Appendix A) proceed as follows: LNMO (0 ± 2.4%) < Fe0.1 (2.8 ± 2.1%) < Fe0.2 (11.4 ± 2.1%) < Mg0.1 (15.1 ± 2.4%) < Mg0.2 (26.6 ± 2.4%). The lack of Li deficiency in LNMO, when using this structural model, suggests that a negligible amount of Li is lost through evaporation at the temperatures used in this work. It also suggests that the loss of Li through impurity phase formation is negligible, which is consistent with the formation of an impurity phase with low Li content (see Section 4.4.5). While the refined Li deficiency is lower than that anticipated for LNMO, it is larger than anticipated for the substituted samples, especially in the case of Mg0.2, which we explain with an increase in non-Li 8a site occupancy (i.e., Ni<sub>Li</sub> and M<sub>Li</sub> defects).

To account for the possibility of non-Li 8a site occupancy in LNMO refinements, Ni<sub>Li</sub> defects, in which small concentrations of Ni (< 6%) occupy the 8a site, are incorporated into the structural model. In addition to Ni<sub>Li</sub> defects, M<sub>Li</sub> defects (M = Fe and Mg; < 10%) were also considered in Mg/Fe-substituted samples. Mn<sub>Li</sub> defects, on the other hand, led to isotropic atomic displacement parameters ( $U_{iso}$ ) values > 0.1 Ų, which are greater than those expected for tightly bound metal oxides (0.001 Ų  $\geq U_{iso} \leq 0.025$  Ų).<sup>38</sup> We, therefore, ruled out the presence of Mn<sub>Li</sub> defects in the as-synthesised materials.

Data show that the ESD values of a "no-defect" scenario may be decreased when Li-site defects (Ni<sub>Li</sub> and M<sub>Li</sub>) are incorporated into the structure model (**Figure 4.4**), although goodness-of-fit parameters ( $\chi^2$  and R<sub>Wp(ND)</sub>), cell parameters, O<sub>xyz</sub> atomic positions, and 16d site occupancies (f<sub>16d</sub>) remain largely unaffected in all scenarios (**Table A1–3**, Appendix A). For instance, incorporating Ni<sub>Li</sub> defects into the structure model for LNMO causes f<sub>Li(8a)</sub> to decrease from 100 ± 2.4% to 99.2 ± 0.3%, where the ESD of f<sub>Li(8a)</sub> becomes 8 times smaller when Ni<sub>Li</sub> defects are incorporated (**Figure 4.4a–b**; and **Tables A1–3**, Appendix A). In Mg/Fesubstituted samples, refining either of the defect scenarios (Ni<sub>Li</sub> or M<sub>Li</sub>) not only reduces 1-f<sub>Li(8a)</sub> to be within the expected range (≈ 5–10%) but also results in a similar 8-fold reduction in f<sub>Li(8a)</sub> ESD values from ± 2.1%–2.4% to ± 0.3% (**Figure 4.4a–c**; and **Tables A1–3**, Appendix A), suggesting that Li-site defects are plausible in substituted samples.

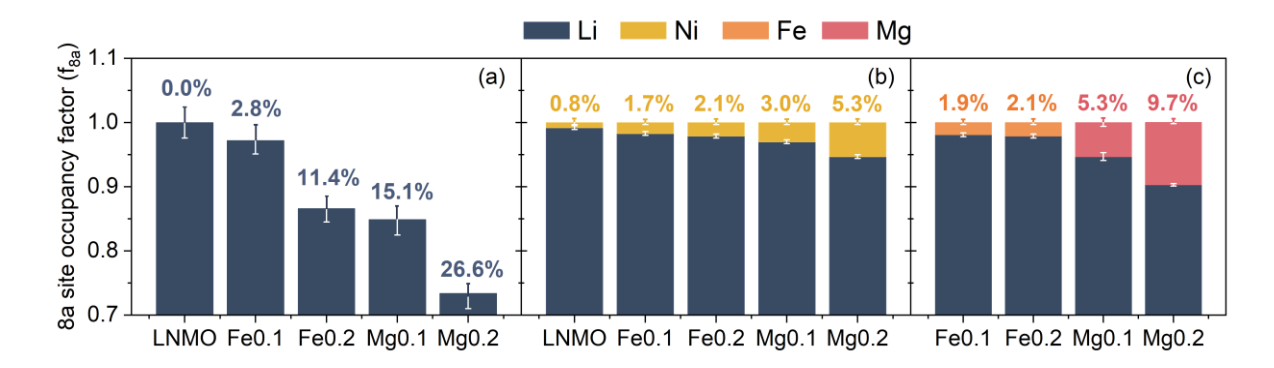


**Figure 4.4:** Changes in 8a site occupancy for samples LNMO, Fex and Mgx (x = 0.1 and 0.2) in different Li-site defect scenarios: (a) no defect; (b) Ni<sub>Li</sub> defect; and (c) M<sub>Li</sub> defect (M = Mg or Fe). Li-deficiencies (1-f<sub>Li(8a)</sub>) are indicated as percentages.

Improvements in ESD values are accompanied by a marginal improvement in the fit against XRD data when Li-site defects are incorporated into the structural model, alongside improvements in the  $R_{wp(XRD)}$  parameter (see **Figure A1–5**, Appendix A). In all cases—for the XRD peaks observed at  $2\theta = 36.4^{\circ}$  (311) and  $38^{\circ}$  (222)—the calculated peak intensity increases to better match the experimental data. Increased intensity of the (311) diffraction peak, and thus decreased intensity ratio between the (400)/(311) diffraction peaks, has been shown to correlate to the presence of cations, other than Li, on the 8a site.<sup>5,39</sup> Thus, the decreased intensity ratio I(400)/(311), again, suggests Li-site defects are present.

The concentration of Li-site defects in substituted samples is dependent on substituent type, concentration, and defect scenario. Comparing  $f_{(8a)}$  for both scenarios suggests that [Ni<sub>Li</sub>] and [M<sub>Li</sub>] increase with Fe/Mg concentration and that Mg promotes Li-site defects over Fe (**Figure 4.4b,c**). For example, in the M<sub>Li</sub> scenario we observe: Fe0.1 (1.9 ± 0.3%) < Fe0.2 (2.1 ± 0.3%) < Mg0.1 (5.3 ± 0.3%) < Mg0.2 (9.7 ± 0.3%) (**Figure 4.4c**; and **Table A3**, Appendix A). The greater non-Li  $f_{(8a)}$  in Mg-substituted samples may be related to the lower formation energy of Mg<sub>Li</sub> defects compared to Fe<sub>Li</sub> defects (**Figure 4.3**).

Despite the use of ND to enable distinction between Ni and Mn atoms, determining the likely defect scenario occurring in the samples is challenging. The neutron scattering length of Mg (5.375 fm) is approximately half that of Ni (10.3 fm).<sup>40</sup> To counteract the halving of neutron scattering length, the structural model doubles the site occupancy when switching from Ni<sub>Li</sub> defects to Mg<sub>Li</sub> defects, to produce a similar calculated peak intensity. The doubling of site occupancy is evidenced when comparing the Mg<sub>Li</sub> and Ni<sub>Li</sub> defect scenarios for Mg0.1 (**Figure 4.4b–c**), where  $f_{Mg(8a)} = 0.053$  is approximately double that of  $f_{Ni(8a)} = 0.03$ , respectively (i.e.,  $f_{Mg(8a)} \approx 2f_{Ni(8a)}$ ). Likewise,  $f_{Mg(8a)} = 0.097$  is approximately double that of  $f_{Ni(8a)} = 0.053$  in Mg0.2 for Mg<sub>Li</sub> and Ni<sub>Li</sub> defect scenarios, respectively. Similar issues occur for Fe0.1 and Fe0.2, where

 $f_{Fe(8a)} \approx f_{Ni(8a)}$  in Fe<sub>Li</sub> and Ni<sub>Li</sub> defect scenarios (**Figure 4.4b–c**), where the inability to distinguish between Fe and Ni, in this case, arises from the similar neutron scattering lengths of Fe (9.45 fm) and Ni (10.3 fm).<sup>40</sup> Furthermore, the coexistence of multiple Li-site defects (e.g., Ni<sub>Li</sub> + M<sub>Li</sub>) was also attempted in these studies but given its complexity, it could not be evaluated. These results highlight the limitations of ND-XRD refinements in determining 8a site occupancy.

From DFT results, directly comparing the effect of substituent type and concentrations on Lisite defects is also challenging. While the rise in total Li deficiency,  $[X_{\text{Li}}]$ , is sharper in the Mgsubstituted system—and dominated by MgLi defects—the overall contribution due to changes in [MgLi] is expected to be minor under thermodynamic equilibrium (**Figure 4.5b**). This is because of their higher formation energy when compared to charge-neutral MgNi defects, which shows no increase in  $[X_{\text{Li}}]$  since there is no charge-perturbation to the system (**Figure 4.3 and 4.5**). In comparison, the rise in  $[X_{\text{Li}}]$  for Fe-substituted samples, with increasing  $[Fe_{Mn}]$ , is shallower than with [MgLi] and is dominated by MnLi. Despite a shallower increase, the anticipated  $[Fe_{Mn}]$ , and therefore  $[X_{\text{Li}}]$ , is expected to be far more significant than  $[X_{\text{Li}}]$  from MgLi defects (**Figure 4.3b and 4.5d**). Increasing  $[Fe_{Ni}]$ , on the other hand, suppresses the formation of Li-site defects (**Figure 4.5c**).

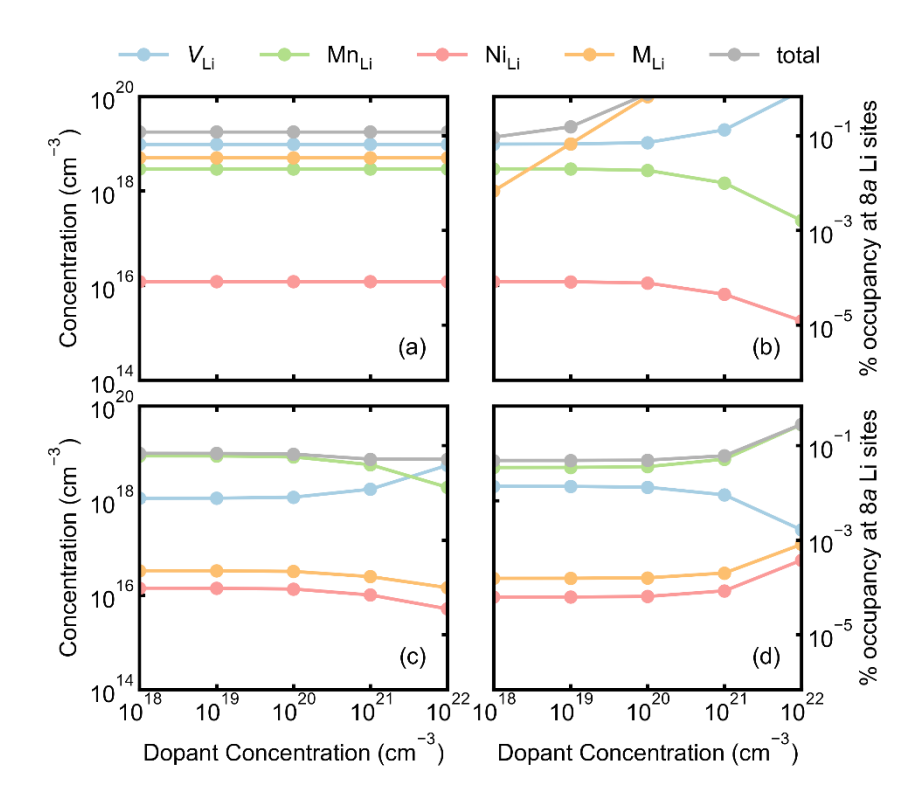


**Figure 4.5, DFT calculated Li deficiencies:** Calculated total concentration of  $X_{Li}$  defects, consisting of contributions from  $V_{Li}$ ,  $Mn_{Li}$ ,  $Ni_{Li}$  and  $M_{Li}$  defects as a function of increasing concentration of extrinsic defect species  $Mg_{Ni}$  (a) and  $Mg_{Li}$  (b) in Mg-doped system (M = Mg)

and defect species  $Fe_{Ni}$  (c) and  $Fe_{Mn}$  (d) in Fe-doped system (M = Fe), respectively. Results and figures provided by Dr J. Cen.

Although the dominating effect is hard to evaluate,  $[X_{Li}]$  in experimental systems could be more strongly affected by the loss of Li through impurity phase formation. Since the trend in calculated Li deficiency between different systems (pristine > Mg-substituted > Fe-substituted) does not follow that from experiments (i.e., Mg-substituted > Fe-substituted > LNMO), we speculate that Li-containing impurity phases, yielding a chemical potential different to the Mn<sup>3+</sup>-rich limit assumed in **Table B1** (Appendix B), contribute significantly to the observed the Li deficiencies.

# 4.4 Origin and Possible Charge Compensators for the Presence of Mn³+ ions in Substituted Samples

# 4.4.1 Mn<sup>3+</sup> Concentration Increases with Fe/Mg Content

The evolution of [Mn<sup>3+</sup>] in LNMO, Fex and Mgx (x = 0.05-0.2) can be explored through galvanostatic cycling (1C, 3.5-4.9 V, Figure 4.6a-b). During the charging process (Li extraction), all samples show a plateau at  $\approx 4$  V, characteristic of capacity provided through the Mn<sup>3+/4+</sup> redox reaction.<sup>41</sup> Two additional plateaux occur at 4.7 and 4.75 V and are characteristic of the Ni<sup>2+/3+</sup> and Ni<sup>3+/4+</sup> redox reactions, respectively.<sup>41</sup> The distinction between these reactions is more clearly evident from the dQ/dV data presented in Chapter 5, where the plateaux manifest as peaks at 4.0, 4.7 and 4.75 V (Figure 5.2). No further redox reactions are expected since Mg<sup>2+</sup> is redox inactive, and Fe<sup>3+/4+</sup> redox occurs outside of the operating voltage window used in this work (V > 4.9 V). The high-voltage Ni plateaux are similar for low Fe/Mg concentrations (x = 0-0.05), although these decrease with x due to the removal of redox-active Ni from the electrode formulation. The 4 V plateau, on the other hand, increases with x for both Fex and Mgx, which results in a slightly higher initial capacity for Fe0.05 and Mg0.05. The increase in the 4 V plateau indicates an increase in [Mn<sup>3+</sup>], which has been quantified in Figure 4.6d (the 4 V-region specific charge capacity is defined as the capacity obtained from OCV-4.375 V, as highlighted in Figure 4.6c). The larger initial 4 V capacity provided by the Fe-substituted samples compared to their analogous Mg-substituted samples suggests that the [Mn<sup>3+</sup>] is greater with Fe-substitution.

Increases in [Mn<sup>3+</sup>] can cause unit cell expansion since the crystal radius of Mn<sup>3+</sup> is larger than Mn<sup>4+</sup> (0.78 vs 0.67 Å).<sup>10</sup> The unit-cell lattice parameter (a) was subsequently refined either through combined ND-XRD Rietveld refinement (x = 0, 0.1 and 0.2) or Le Bail refinement (x = 0.05 and 0.15) against XRD data. The results show that when Fe and Mg are incorporated into the structure, a increases linearly with x, indicating unit cell expansion (**Figure 4.6e**).

Given the smaller octahedral crystal radii of Fe<sup>3+</sup> (0.69 Å) compared to Ni<sup>2+</sup> (0.83 Å),<sup>10</sup> such an increase in *a* is likely a result of increasing [Mn<sup>3+</sup>], as observed in other Fe-substituted LNMO.<sup>42</sup> Since the radius of Mg<sup>2+</sup> is marginally larger than Ni<sup>2+</sup> (0.86 and 0.83 Å, respectively), the major contributor to unit cell expansion in Mg-substituted samples is also expected to be increasing [Mn<sup>3+</sup>]. The greater unit cell expansion caused by Fe substitution when compared to Mg substitution may, therefore, suggest that [Mn<sup>3+</sup>] is greater in Fe-substituted samples. Such observations substantiate the evolution of [Mn<sup>3+</sup>] as determined by galvanostatic cycling.

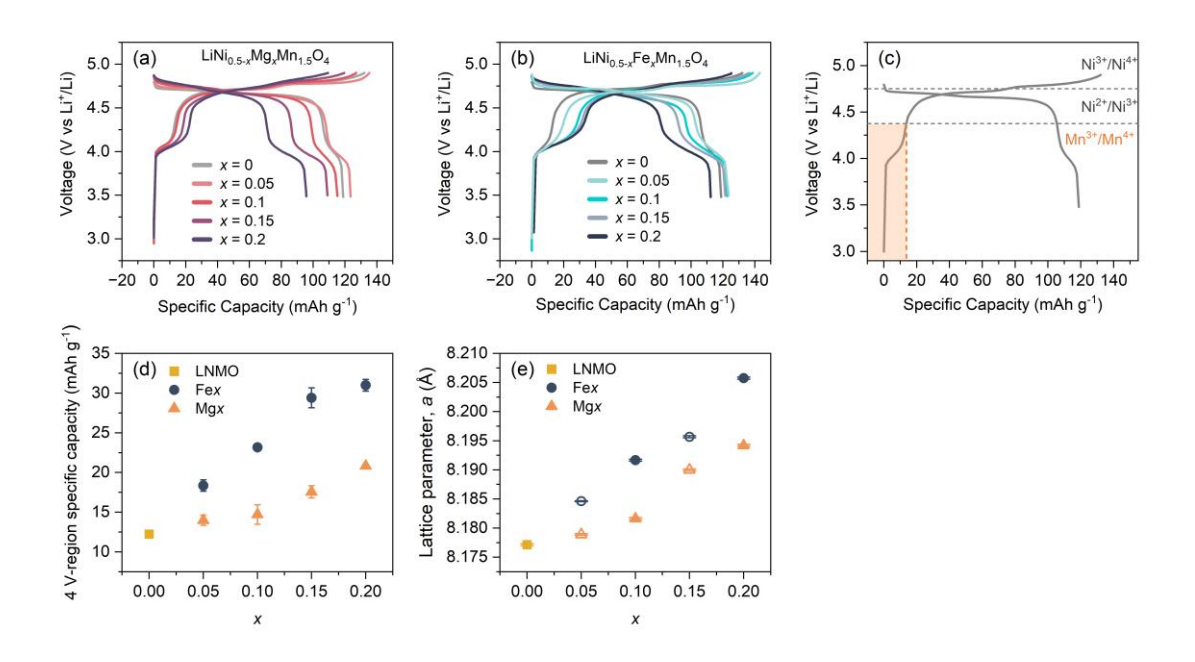


**Figure 4.6, Mn**<sup>3+</sup> **concentration increases with Fe/Mg content:** First-cycle voltage profiles of spinel/Li half cells (1C, 3.5–4.9 V) for a) Mgx and b) Fex (x = 0–0.2), where the capacity below 4.375 V as shown in (c) is used to derive the specific charge capacity related to Mn<sup>3+</sup> (4 V region) in Mgx and Fex samples, where error bars represent the standard deviation between cells (n = 3) d); and the corresponding changes in the lattice parameter, a, as a function of substituent concentration for samples Mgx, Fex e). The lattice parameter, a, was determined either through combined ND-XRD Rietveld refinement (filled symbol; x = 0, 0.1, and 0.2) or Le Bail refinement against XRD data (hollow symbol; x = 0.05 and 0.15).

DFT calculations corroborate the experimentally observed increase in [Mn³+], where calculated [Mn³+] also experiences an increase from LNMO  $(1.01\times10^{18} \text{ cm}^{-3}) < \text{Mg-substituted}$   $(6.40\times10^{20} \text{ cm}^{-3}) < \text{Fe-substituted samples}$   $(9.94\times10^{20} \text{ cm}^{-3})$ , **Table B1**, Appendix B). A further increase in [Mn³+] is observed in Fe-substituted systems upon increasing the concentrations of either Fe<sub>Ni</sub> or Fe<sub>Mn</sub> defects above  $10^{20} \text{ cm}^{-3}$  (i.e., comparable to major intrinsic defect concentrations, **Figure 4.7c,d**). Most notably, charge-neutral Fe<sub>Ni</sub><sup>0</sup> yields a strong rise in [Mn³+]

with a  $\approx$  1:1 ratio, as the incorporation of Fe<sup>3+</sup> into the Ni lattice site triggers the reduction of nearby Mn<sup>4+</sup> to Mn<sup>3+</sup>, to maintain charge neutrality. Furthermore, Fe<sub>Ni</sub> and Fe<sub>Mn</sub> defects have relatively low formation energies (**Figure 4.3**). Based on these observations, the experimentally observed increase in [Mn<sup>3+</sup>] is anticipated with increased Fe content due to increased concentrations of both Fe<sub>Ni</sub> and Fe<sub>Mn</sub> defects.

Unlike Fe substitution, increasing [MgNi] shows a flat response in [Mn³+], suggesting that the increased incorporation of Mg²+ into the Ni site does not trigger Mn⁴+ reduction (**Figure 4.7a**). This is expected as MgNi effectively exists in the charge-neutral state (i.e., MgNi⁰), providing no charge disturbance to the system. Increases in charge-balancing [Mn³+] are, instead, observed upon increasing [MgLi] above a threshold of ≈  $10^{20}$  cm³, corresponding to ≈ 0.7% Mg in the Li 8a site (**Figure 4.7b**). Given that refinements against experimental data show  $f_{Mg(8a)}$  considerably above 0.7% (Mg0.1 = 5.3% and Mg0.2 = 9.7%), increasing [MgLi] could be the cause of increasing [Mn³+]. The predictive power of DFT calculations on the dopant response, however, is limited to a low concentration (e.g., a few per cent), as defect/dopant-defect/dopant interactions are not accounted for under dilute dopant conditions. Therefore, other factors should also be considered to explain the increase in [Mn³+].

Aside from the charge disturbance induced by extrinsic defects, other factors may lead to increasing [Mn<sup>3+</sup>] in substituted samples. These include 1) an increase in Ni oxidation from the expected Ni<sup>2+</sup> present in the pristine samples; 2) an increase in  $V_0$  content; 3) off-stoichiometry and cation deficiencies; and 4) deviation from thermodynamic equilibrium, under which formation energies are evaluated, allowing the formation of Li-site defects (e.g., Mg<sub>Li</sub>).

# 4.4.2 Ni<sup>3+</sup> Concentration is Present in Substituted Samples and Independent of Fe/Mg content

Higher-valent Ni<sup>3+</sup> is suspected to be present in both substituted and unsubstituted LNMO based on DFT calculations. **Table B1** (Appendix B) shows that [Ni<sup>3+</sup>] is several orders of magnitude higher in both substituted systems than that of LNMO and is higher in the Mg-substituted system compared to the Fe-substituted system. While the exact values of [Ni<sup>3+</sup>] change under different chemical potential conditions, the same trend is observed by comparing [Ni<sup>3+</sup>] under the conditions corresponding to the highest concentration of [Ni<sup>3+</sup>] in pristine and Mg/Fe-substituted LNMO. This supports our hypothesis that increased [Mn<sup>3+</sup>] may arise from Ni oxidation upon Mg incorporation (see Section 4.3). Increasing Fe/Mg concentration through either [Mg<sub>Ni</sub>], [Mg<sub>Li</sub>], [Fe<sub>Ni</sub>] or [Fe<sub>Mn</sub>], however, sees a flat response in [Ni<sup>3+</sup>], suggesting that [Ni<sup>3+</sup>] is independent of Fe/Mg concentration (**Figure 4.6a–d**). Ni<sup>3+</sup> is,

therefore unlikely to be a major charge compensator for increases in [Mn³+] observed in substituted samples.

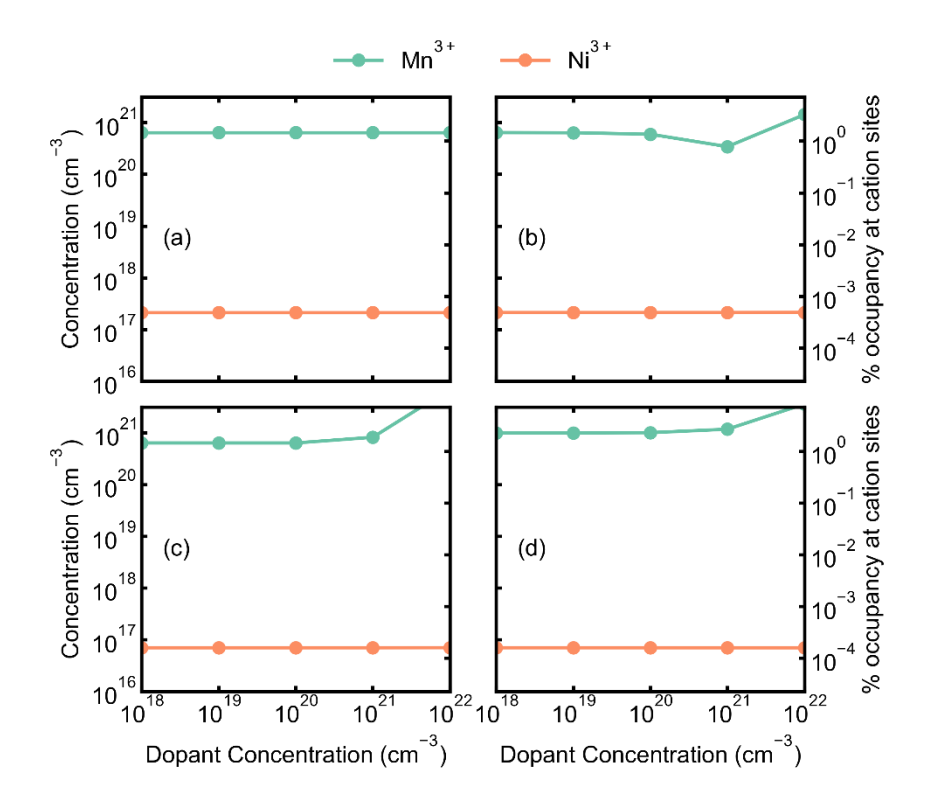


**Figure 4.7, DFT calculated Ni³+:** Calculated [Mn³+] and [Ni³+] in response to increased substituent concentration through tuning the concentration of extrinsic defect species  $Mg_{Ni}$  (a) and  $Mg_{Li}$  (b) in Mg-doped system and defect species  $Fe_{Ni}$  (c) and  $Fe_{Mn}$  (d) in Fe-doped systems, respectively. Results and figures provided by Dr J. Cen.

#### 4.4.3 V<sub>o</sub> are Almost Negligible

Computationally calculated  $V_0$  concentrations are low in pristine LNMO and further suppressed upon Mg/Fe-substitution ( $V_0$  in **Table B1**, Appendix B). Such negligible  $V_0$  concentrations are anticipated when considering a cation-ordered P4<sub>3</sub>32 structure. Oxygen loss at high synthesis temperatures used to synthesise cation-disordered arrangements, on the other hand, can increase  $V_0$  concentrations. However, attempts to refine oxygen occupancy values ( $f_{0(32e)}$ ) in Rietveld refinements against diffraction data ( $Fd\overline{3}m$ ), significantly overestimate [Mn<sup>3+</sup>] when compared to the estimates from electrochemical data and were, therefore, discounted (**Figure 4.8**). As a result, we anticipate that they are unlikely to be the

major charge compensators for the increased [Mn³+] observed in Mg/Fe-substituted LNMO samples.

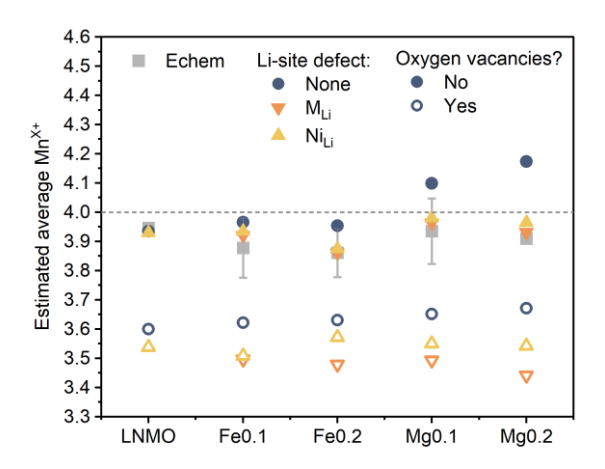


**Figure 4.8:** Estimated Mn<sup>x+</sup> oxidation state from the 4 V specific charge capacity region in the galvanostatic data (OCV–4.375 V, Echem data) and Rietveld refinements (Li-site defects: None,  $M_{Li}$  and  $Ni_{Li}$ ) both with (hollow) and without (filled) oxygen vacancies ( $V_0$ ). The comparison between structural refinements and electrochemical data suggests that  $V_0$  are overestimated within the refinement, resulting in overestimated Mn<sup>3+</sup> concentrations. Due to such anticipated overestimation, refinements with  $V_0$  are discounted. Refinements in which  $Mn^{x+} > Mn^{4+}$  are also discounted as they result from large, refined Li deficiencies (Figure 4.4).

The role of oxygen defects has also been doubted by several experimental studies. For example, through examining the voltage profiles and through thermogravimetric analysis data. While oxygen defects could be promoted by certain dopants, the literature suggests that they are not directly related to the Mn<sup>3+</sup> content in LNMO. For Mg-doped LNMO, computational studies have shown that the  $V_0$  formation is less energetically favourable when Mg occupies an octahedral site, making increased  $V_0$  in Mg-substituted LNMO unlikely. However,  $V_0$  could be promoted in a scenario where Mg ions occupy the Li tetrahedral sites (Mg<sub>Li</sub>) (see Section 4.3), resulting in vacant octahedral 16d sites ( $V_{Ni}$ ) (Figure 4.4). Nevertheless, at no point does [ $V_{Ni}$ ] calculated herein reach a magnitude comparable to other dominant intrinsic defects such as Li<sub>Ni</sub> and, as previously mentioned, [Mg<sub>Li</sub>] itself is expected to be extremely low, i.e.,  $V_0$  are expected to be minimal.

# 4.4.4 Off-Stoichiometry Drives an Increase in [Mn³+]

Reports show that Mn<sup>3+</sup> ions in LNMO can arise from Ni/Mn off-stoichiometry, in which there is a deficiency of Ni<sup>2+</sup> in the spinel structure alongside an excess of higher-valent Mn<sup>4+</sup>.<sup>46</sup> This causes a partial reduction of Mn<sup>4+</sup> to Mn<sup>3+</sup> to offset the charge excess. Such Ni/Mn off-

stoichiometry in LNMO can be explained computationally through [Mn<sub>Ni</sub>], which is a few orders of magnitude higher than [Ni<sub>Mn</sub>] (**Table B1**, Appendix B). This suggests that the intrinsic defect chemistry of LNMO drives the material to have a slight stoichiometric excess of Mn and a deficiency of Ni, thus increasing [Mn<sup>3+</sup>]. However, the only defect in substituted samples that might drive Ni/Mn off-stoichiometry, with a subsequent increase in [Mn<sup>3+</sup>], is  $Fe_{Mn}$  (**Figure B1**, Appendix B). Intrinsic off-stoichiometry, therefore, cannot explain the increase in [Mn<sup>3+</sup>] observed in Mg-substituted samples.

Computationally derived off-stoichiometry is directly related to Ni defect concentrations, where Ni defects contribute to Ni deficiency in the system. Total Ni deficiency ( $X_{Ni}$ ) can, therefore, be approximated by [ $X_{Ni}$ ] = [ $V_{Ni}$ ] + [ $L_{[Ni]}$ ] + [ $M_{Ni}$ ] (**Table B1**, Appendix B).  $X_{Ni}$  is not influenced by increasing [ $Mg_{Ni}$ ] (**Figure 4.9a**). An increase in [ $Mg_{Li}$ ], on the other hand, triggers an increase in [ $L_{[Ni]}$ ] as [ $V_{Li}$ ] also increases, suggesting preferential migration of Li to the Ni site as Mg begins to occupy the Li site (**Figure 4.9b and 4.5b**). In the case of Fe-substitution, [ $X_{Ni}$ ] can be increased by increasing either [ $Fe_{Ni}$ ] or [ $Fe_{Mn}$ ] (**Figure 4.9c**,d). However, the type of defect they promote differs. Increasing positively charged (n-type) [ $Fe_{Ni}$ ] raises the concentration of other negatively charged (p-type) defects ( $V_{Ni}$ ,  $L_{[Ni]}$ ) while suppressing the concentration of n-type defects ( $M_{NNi}$ ) to allow the system to equilibrate charge (**Figure 4.9c**). This leads to a decrease in Ni/Mn off stoichiometry with [ $Fe_{Ni}$ ] (**Figure B1c**, Appendix B). Conversely, increasing p-type [ $Fe_{Mn}$ ] will suppress other p-type defects ( $V_{Ni}$ ,  $L_{[Ni]}$ ) and encourage more n-type defects ( $M_{NNi}$ ,  $Fe_{Ni}$ ) in the system (**Figure 4.9d**), increasing Ni/Mn off-stoichiometry (**Figure 4.9d**; and **Figure B1d**, Appendix B). Given the similar formation energies of  $Fe_{Ni}$  and  $Fe_{Mn}$ , a balance between these two effects may therefore be realised.

Overall, calculations predicted high concentrations of anti-site  $Mn_{Ni}$  and  $Li_{Ni}$  defects, breaking the dopant dilute limit where defect-defect interactions become more significant. Therefore, results could potentially be different when considering defect interactions. It should be noted that  $Li_{Ni}$  defects could not be evaluated in refinements against an  $Fd\overline{3}m$  structure model due to the complex co-existence of Ni, Mn, M (M = Fe and Mg) and Li on one site (16d), which creates unsolvable equations in the refinement process due to the surplus of unknown variables, further highlighting the value of computational insight.

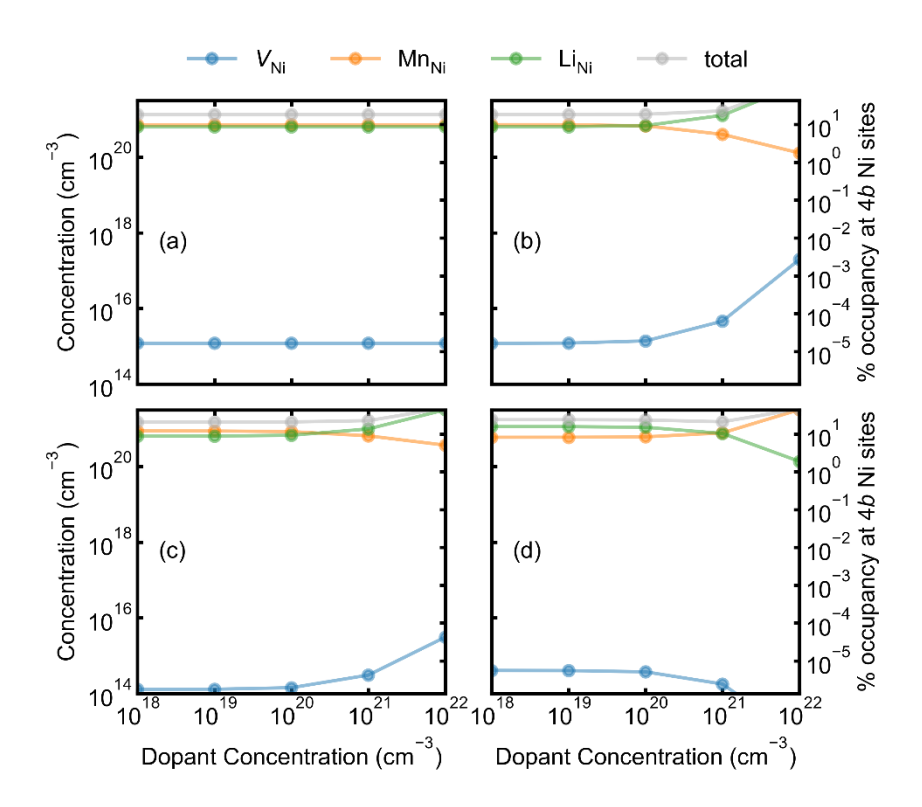


**Figure 4.9, DFT calculated Ni deficiency**: Calculated total concentration of  $X_{Ni}$  defects decomposed into contributions from  $V_{Ni}$ ,  $Mn_{Ni}$  and  $Li_{Ni}$  defects as a function of increasing concentration of extrinsic defect species  $Mg_{Ni}$  (a) and  $Mg_{Li}$  (b) in Mg-doped system (M = Mg) and defect species  $Fe_{Ni}$  (c) and  $Fe_{Mn}$  (d) in Fe-doped system (M = Fe), respectively. Results and figures provided by Dr J. Cen.

Through structure refinements, deficiencies are seen not only in Ni and Li but also in M (M = Fe and Mg; **Table A1–3**, Appendix A). Experimentally observed deficiencies are likely a result of impurity phase formation. To assess the need for charge-balancing Mn<sup>3+</sup> ions that arise due to off-stoichiometry and cation deficiencies/impurity phases, the charge surplus is calculated from refined stoichiometries (**Figure 4.10**). Except for the refinements without Li-site defects, charge surplus provided by Mn excess—in the presence of other cation deficiencies—shows an increasing trend from Mg0.1 < Mg0.2 < Fe0.1 < Fe0.2. Assuming full O site occupancy, the [Mn<sup>3+</sup>] required to balance such a surplus in charge should then also increase from Mg0.1 < Mg0.2 < Fe0.1 < Fe0.2, which is in line with the trend anticipated by the unit cell expansion and increased 4 V-region specific charge capacity (**Figure 4.6**). Based on **Figure 4.6**, the [Mn<sup>3+</sup>] should be the lowest in LNMO. The calculated charge surplus in LNMO, however, is higher than Mg0.1 and Mg0.2 in most cases, suggesting that [Mn<sup>3+</sup>] should be greater in LNMO than in the Mg-substituted samples. This discrepancy may be explained by the increase in [Ni<sup>3+</sup>] anticipated for the substituted samples (**Table B1**, Appendix B), which is not accounted

for in charge surplus calculations but would further increase charge-surplus for Mg0.1, Mg0.2, Fe0.1 and Fe0.2, perhaps above that of LNMO.

The trend in Ni deficiency as estimated computationally from the concentration of  $X_{\rm Ni}$  differs from that obtained experimentally (i.e., the pristine LNMO shows the greatest Ni deficiency). However, it should be noted that the computed contribution to Ni deficiency assumes thermodynamic equilibrium which may not be met in practice and does not account for any loss of Ni through impurity phase formation, which is sensitive to synthetic conditions. The conditions required to produce  $Fd\bar{3}m$  disordered LNMO typically lead to loss of Ni in the bulk due to Ni-rich impurity phase formation.

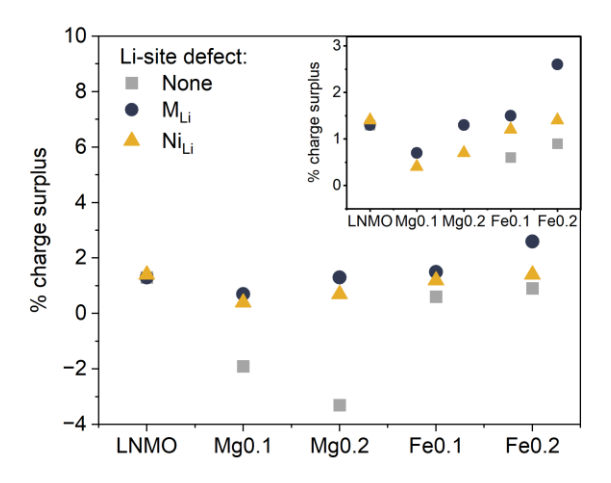


**Figure 4.10, Charge surplus**: % charge surplus from the expected +8 cation charge required to balance oxygen in full occupancy, as calculated from refined stoichiometries in scenarios that consider  $M_{Li}$  and  $M_{Li}$  (M = Mg and Fe).

### 4.4.5 Impurity Phases Exacerbate Off-stoichiometry.

Undesirable Ni-rich impurity phases are widely reported in LNMO materials, resulting in Ni deficiency within the spinel structure.<sup>3</sup> LNMO synthesised by the oxalic-acid co-precipitation method adopted in this work shows small impurity peaks at 37.5, 43.5, and 63.3° 20 in the XRD pattern. These impurity peaks can be indexed using two possible Ni-rich phases; Ni<sub>6</sub>MnO<sub>8</sub> ( $Fm\bar{3}m$ ) or Li<sub>x</sub>Ni<sub>1-x</sub>O ( $Fm\bar{3}m$ ), whose most intense peaks occur at similar 20 values (**Figure 4.11a**).<sup>12</sup> Due to the similar 20 values of peaks and the low impurity concentrations, it is not possible to unambiguously determine which of the two phases is present. Nevertheless, identification of this phase was enabled through ND, where LNMO shows impurity peaks at d = 0.97, 1.58 and 2.44 Å (**Figure 4.11c**). While Ni<sub>6</sub>MnO<sub>8</sub> and Li<sub>x</sub>Ni<sub>1-x</sub>O share peaks at d = 1.58 and 2.44 Å, the peak at d = 0.97 Å is only present in Ni<sub>6</sub>MnO<sub>8</sub>. A two-phase XRD-ND Rietveld refinement was therefore conducted with LNMO and Ni<sub>6</sub>MnO<sub>8</sub>,

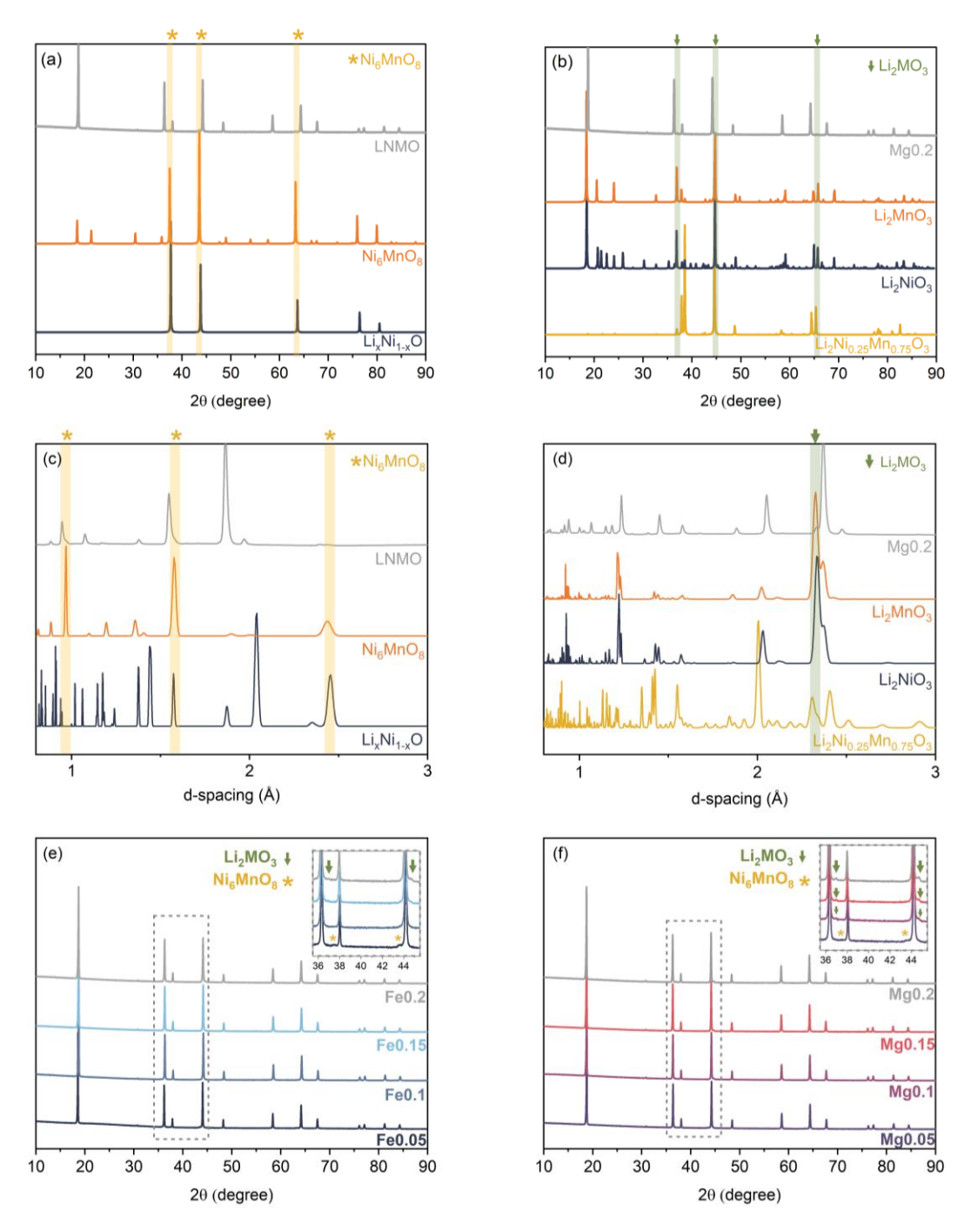


**Figure 4.11, Identification of impurity phases:** a) XRD and c) ND-TOF patterns of assynthesised LNMO and calculated patterns of typical Ni-rich impurity phases: Ni<sub>6</sub>MnO<sub>8</sub> (ICSD #41890) and Li<sub>x</sub>Ni<sub>1-x</sub>O (ICSD #40584). The location of impurity peaks present in LNMO are highlighted by yellow asterisks; b) XRD and d) ND-TOF patterns of Mg0.2 synthesised herein and calculated patterns of Li<sub>2</sub>MO<sub>3</sub>-type impurity phases: Li<sub>2</sub>MnO<sub>3</sub> (ICSD #132578), Li<sub>2</sub>NiO<sub>3</sub> (ICSD #29337) and Li<sub>2</sub>Ni<sub>0.25</sub>Mn<sub>0.75</sub>O<sub>3</sub> (ICSD #252826). Li<sub>2</sub>MO<sub>3</sub> impurity peaks present in Mg0.2 are highlighted by green arrows. XRD patterns of c) Fex and d) Mgx where x = 0.05-0.2. Insets show selected 2θ range in which impurity peaks are observed, indicated by yellow asterisks (Ni<sub>6</sub>MnO<sub>8</sub>) or green arrows (Li<sub>2</sub>MO<sub>3</sub>, M = Ni or Mn).

resulting in relative phase fractions of  $97.65 \pm 0.3$  wt.% and  $2.35 \pm 0.3$  wt.%, respectively. At such low impurity concentrations, it is unlikely that the presence of Ni<sub>6</sub>MnO<sub>8</sub> would significantly impact the electrochemical performance. However, in efforts to minimise the loss of active Ni and the resistance to Li<sup>+</sup>-ion diffusion caused by phase boundaries, it is desirable to eliminate impurity phases.<sup>47</sup>

Cationic substitution is often described as a method of reducing impurity phase fractions in LNMO.<sup>3</sup> In this work, substituting with either Fe or Mg at low concentrations (x = 0.05) reduces Ni-rich impurity phase formation, also observed at  $2\theta = 37.5$ , 43.5 and  $63.3^{\circ}$  (**Figure 4.11e, f**). Since ND data were not collected for Mg0.05 and Fe0.05, we cannot conclude if the phase corresponds to Ni<sub>6</sub>MnO<sub>8</sub> (as observed in LNMO) or Li<sub>x</sub>Ni<sub>1-x</sub>O. Increasing Fe or Mg concentration to  $x \ge 0.1$  eliminates this Ni-rich impurity before an additional Li<sub>2</sub>MO<sub>3</sub> impurity (C12/m1 space group; M = Ni and/or Mn) is introduced at  $2\theta = 36.9$ , 44.7 and  $65.7^{\circ}$ ; and d = 1.2 and 2.3 Å (**Figure 4.11e, f**). Lee *et al.* previously reported a Li<sub>2</sub>MO<sub>3</sub>-type impurity in their as-synthesised LNMO materials, yet their study was surrounding Li-rich Li<sub>1+x</sub>Ni<sub>0.5</sub>Mn<sub>1.5</sub>O<sub>4</sub> spinel materials.<sup>48</sup>

The concentration at which the Li-rich impurity phase appears depends on the substituent. In Mg-substituted samples, this phase appears at relatively low concentrations (x = 0.1, 1.7 wt.%), gradually increasing with Mg concentration (x = 0.2, 2.3 wt.%. **Figure 4.11f).** When substituting with Fe, on the other hand, phase pure samples are produced when x = 0.1-0.15. The additional impurity appears only at higher Fe concentrations (x = 0.2) in the XRD pattern, although at concentrations below the Rietveld refinement detection limit (**Figure 4.11e** This suggests that while both substituents suppress the Ni-rich impurity, Fe is more successful at reducing the formation of additional impurities under the reaction conditions used in this work.

Establishing the Li<sub>2</sub>MO<sub>3</sub> formulation, in which M = Ni or Mn or a combination thereof, is once again challenging due to the low impurity concentrations and similar XRD/ND patterns of the Li<sub>2</sub>MO<sub>3</sub> phases (**Figure 4.11d**). While Li<sub>2</sub>MnO<sub>3</sub>, Li<sub>2</sub>NiO<sub>3</sub> and Li<sub>2</sub>Mn<sub>0.75</sub>Ni<sub>0.25</sub>O<sub>3</sub> all match both the XRD and ND impurity peaks, the Li<sub>2</sub>Mn<sub>0.75</sub>Ni<sub>0.25</sub>O<sub>3</sub> phase shows its highest intensity peak at d = 2 Å (ND). This peak, however, is not present in the observed impurity, suggesting that the impurity is either Li<sub>2</sub>MnO<sub>3</sub> or Li<sub>2</sub>NiO<sub>3</sub>. Cyclic voltammetry was performed to differentiate Li<sub>2</sub>MnO<sub>3</sub> from Li<sub>2</sub>NiO<sub>3</sub>, since both impurities show irreversible oxygen loss at  $\approx$  4.6 V and 4.8 V, respectively (**Figure 4.12**).<sup>49,50</sup> However, such irreversible oxidation peaks were not observed. This may, again, be a result of very low impurity concentrations, as observed in other works.<sup>6,51</sup> Although the well-known insolubility of Ni at high synthesis temperatures, and the slight Ni-deficiency—both anticipated computationally and observed experimentally—

make Li<sub>2</sub>NiO<sub>3</sub> the more likely candidate, Li<sub>2</sub>MnO<sub>3</sub> and Li<sub>2</sub>NiO<sub>3</sub> remain indistinguishable from one another in the diffraction patterns. Nevertheless, the presence of a Li-containing impurity undoubtedly impacts Li concentrations in the main spinel phase, explaining observed Li deficiencies.

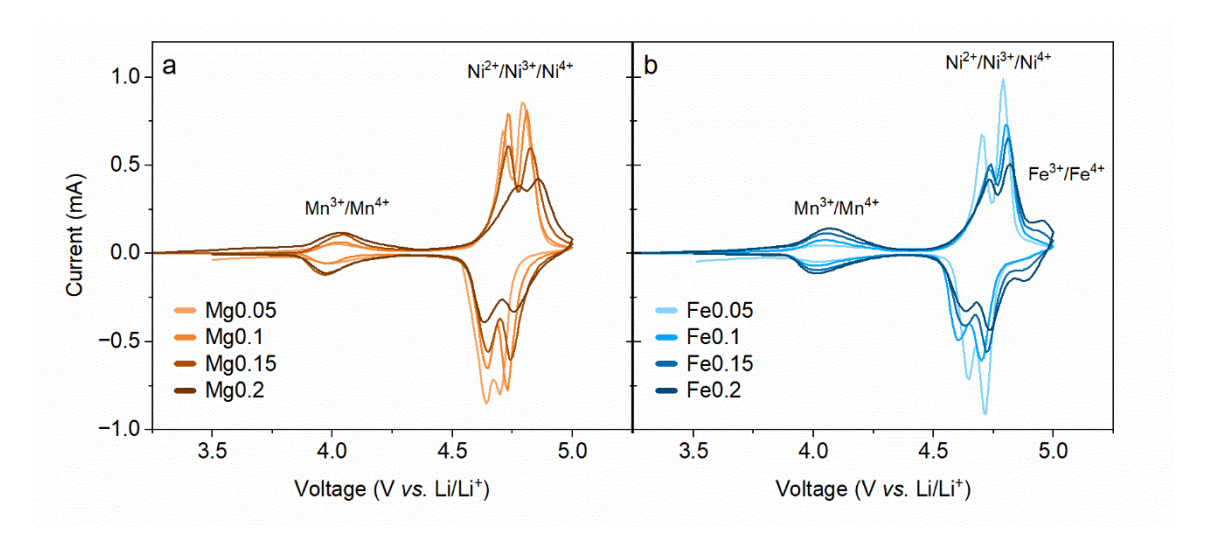


**Figure 4.12:** First-cycle cyclic voltammograms of a) Mgx and b) Fex (x = 0.05-0.2) collected in spinel/Li half-cells, using a voltage window of 3.5–5 V and a sweep rate of 0.1 mV s<sup>-1</sup>. Note that a higher cut-off voltage was used in these measurements compared to the galvanostatic cycling data shown in the manuscript to identify the Fe<sup>3+/4+</sup> redox reaction and thus, illustrate the successful incorporation of Fe in the spinel substituted samples (b).

Refined Li-deficiencies can be used to calculate the anticipated impurity phase fraction (wt.%), assuming that all loss of Li from the 8a site contributes to impurity formation as opposed to migrating to the Ni site (Li<sub>Ni</sub>) (see Section 4.2.4 for details). Such calculations again suggest that Li-site defects are present since the exclusion of Li-site defects significantly overestimates the impurity phase fraction (None, **Figure 4.13**). The incorporation of either Ni<sub>Li</sub> or M<sub>Li</sub> site defects, on the other hand, shows the expected trend in impurity phase fraction (i.e., Fe0.1 < Fe0.2 < Mg0.1 < Mg0.2). Data show that the wt.% for Mg-substituted samples, in which Mg is incorporated into the 8a site (Mg<sub>Li</sub>), show a close resemblance to the refined wt.% values. Calculated impurity phase fractions that exceed refined fractions, in the case of Mg0.2 with Mg<sub>Li</sub> defects, may suggest partial migration of Li to the 16d site, alongside precipitation into the impurity phase. Explaining calculated impurity phase fractions that are lower than refined fractions for Mg0.1 and 0.2 with Ni<sub>Li</sub> defects, on the other hand, is much harder since the calculated values lie outside of the refined error range. This may instead provide further support for the hypothesis that Mg occupies the 8a site in the presence of impurities (i.e.,

subject to non-equilibrium thermodynamics), where Mg<sub>Li</sub> defects are accompanied by small quantities of Li<sub>Ni</sub> defects.

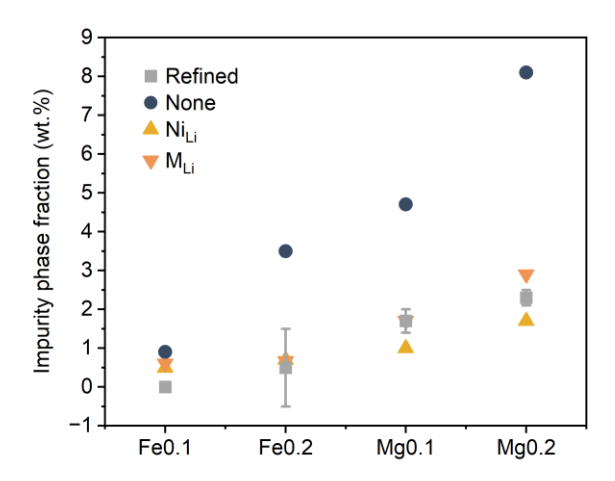
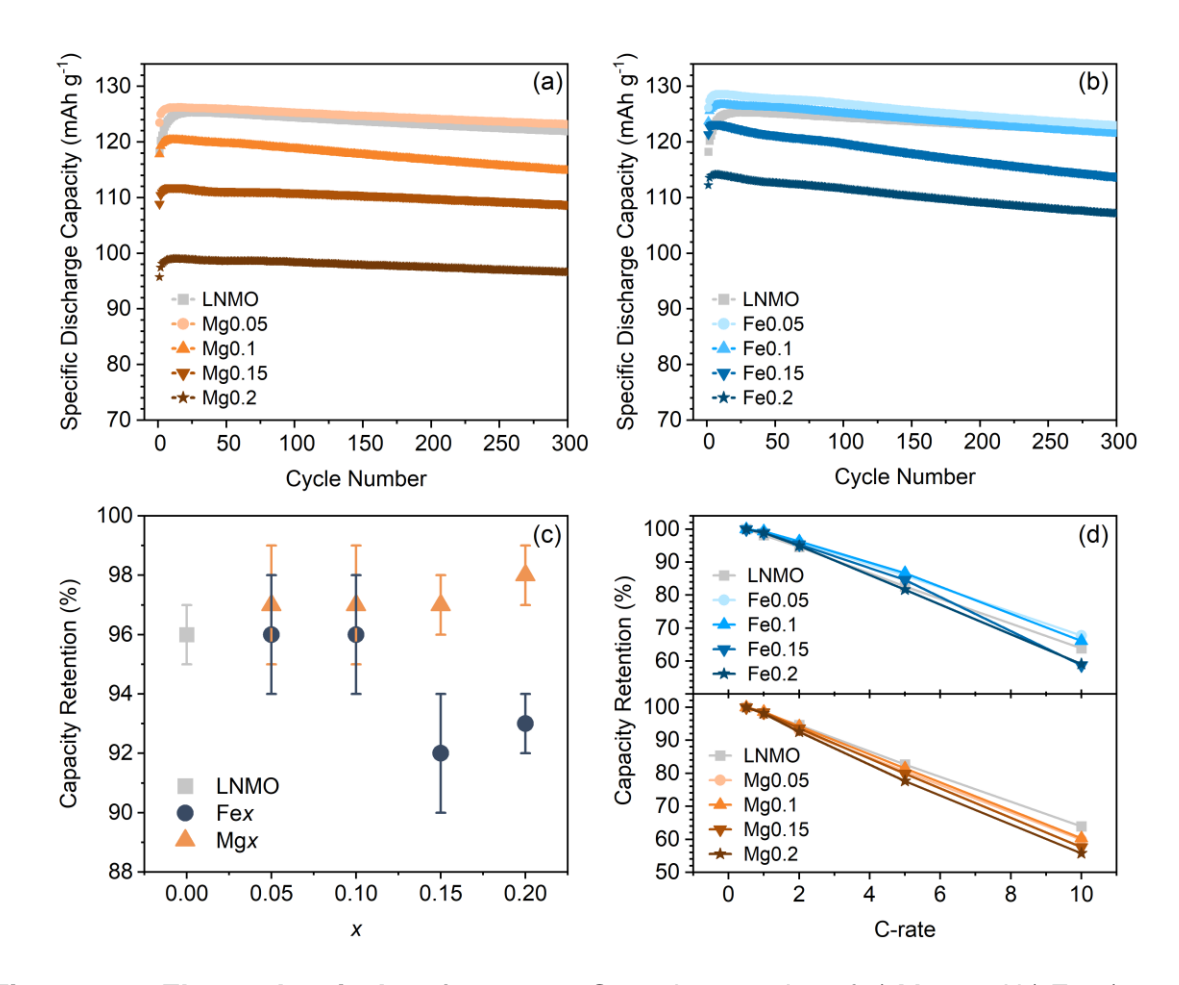


Figure 4.13, Estimated impurity phase fraction from refined Li deficiencies: Impurity phase fraction of  $Li_2MO_3$  in Fe0.1, Fe0.2\*, Mg0.1 and Mg0.2, as determined through combined Rietveld refinements (refined), and as estimated from refined Li deficiencies in refinements that consider sole-Li 8a site occupancy (None),  $Ni_{Li}$  and  $M_{Li}$  site defects (M = Fe and Mg). \* > 0.5 wt.% impurity is assumed for Fe0.2 as it is present in the XRD data but not in the NPD data. In the XRD pattern, the amount is too small to refine yet data collection on modern detectors, under conditions to provide a good signal-to-noise ratio allows detection of impurity phases as low as 0.5–1 wt.%.<sup>52</sup>

The concentration of the Li-rich impurity phase is not only related to Li-deficiencies in the spinel phase but appears to be correlated to an increased concentration of Li-site defects, which also increases with concentration and is greater in Mg-substituted samples. This suggests that either i) precipitation of Li into an impurity phase creates vacant Li sites which are then occupied by other cations or ii) substituents show some preference for the Li 8a site, thus displacing Li and resulting in a Li-rich impurity. Both are plausible since i) both MgLi and FeLi are deemed unlikely under thermodynamic equilibrium, but the formation of impurity phases would disrupt the equilibrium state and ii) MgLi defects are more probable than FeLi, due to their lower formation energy (Figure 4.3).

#### 4.5 Influence of Fe and Mg Substitution on Electrochemical Performance

In line with literature reports, high-crystallinity LNMO—produced through an oxalate coprecipitation method—leads to impressive rate performance, capacity and capacity retention at room temperature.<sup>28,53–55</sup> At slow rates of 0.5C, a high specific discharge capacity of 130 mAh g<sup>-1</sup> is observed (**Figure A7**, Appendix A), and is relatively well maintained with increased cycling rates (**Figure 4.14d**): 98.91% (1C), 94.93% (2C), 82.65% (5C), 63.86% (10C). A moderate rate of 1C was used to evaluate the long-term cycling stability of LNMO (3.5–4.9 V, **Figure 4.14a–c**). Without formation cycles, the as-synthesised LNMO shows an initial capacity of ≈ 120 mAh g<sup>-1</sup>. An increase in initial capacity, however, is observed over the first 20 cycles at ambient temperature (1C, **Figure 4.14a,b**). When using slower rates (0.5C, **Figure A6**, Appendix A), the increase in initial capacity is much less pronounced. Therefore, the capacity increase observed at 1C is likely due to some kinetic limitation in the pristine material.



**Figure 4.14, Electrochemical performance:** Capacity retention of a) Mgx and b) Fex (x = 0 - 0.2) (1C, 3.5–4.9 V, 28°C); c) Average capacity retention after 300 cycles (n = 3); and d) Capacity retention at different rates for Fex and Mgx from waterfall plots shown in Figure A6 (Appendix A).

Upon extended cycling, LNMO exhibits impressive capacity retention (≈ 96%, 1C. **Figure 4.14a–c**). Such high performance of LNMO is consistent with other LNMO materials produced through oxalate co-precipitation.<sup>53–55</sup> We note, however, that our LNMO outperforms many LNMO materials used as baseline samples in substitution studies, several of which are

highlighted in **Table 4.2**. <sup>20,22,56–60</sup>, Despite the difference in synthetic method, the highlighted studies produce LNMO with similar particle morphology. Slightly larger particles of our LNMO (1–3 μm)—a result of a high final calcination temperature of 900°C—may contribute to improved performance by minimising surface area available for parasitic surface reactions. <sup>55</sup> Improved capacity retention may also be attributed to the narrower voltage window (3.5–4.9 V) when compared to some other studies that use a wider voltage window (3.5–5 V, **Table 4.2**). As observed in the voltage profile, however, the high-voltage plateau of LNMO ends around 4.8 V (**Figure 4.5**). Minimal extra reversible capacity can, therefore, be obtained for LNMO beyond 4.9 V, yet electrolyte oxidation will be increased. Furthermore, notably low capacity retentions are observed when using slower cycling rates of 0.5C, which may be a result of longer time spent at high voltage where electrolyte oxidation and TM dissolution are most severe. <sup>61</sup>

**Table 4.2**: Relevant data comparison of LNMO performance reported in the literature.

Synthetic	Final	Morphology	Cycling	Peak discharge	Capacity	Ref.
method	calcination		conditions	capacity	retention	
				(mAh g <sup>-1</sup> )		
Sol-gel	800°C,	Polyhedral,	0.5C,	102	< 50%	56
(citric acid)	16 h	0.3–1 μm	3.5–5 V,			
			130 cycles			
Solid-state	800°C,	Polyhedral,	1C,	124	87.1%	57
(wet milling)	8 h	0.3–1 µm	3.5–5 V,			
			200 cycles			
Sol-gel	900°C,	Polyhedral,	1C,	112	92.7%	58
(citric acid)	12 h	nm–µm	3.5–4.9 V,			
			200 cycles			
Sol-gel	800°C,	Polyhedral,	0.5C,	115	68.2%	20
(Hydroxide)	30 h	0.3–1 µm	3.5–4.9 V,			
			100 cycles			
Solid-state	900°C,	Polyhedral,	1C,	102.5	90%	60
	8 h	< 1 µm	3.5–4.95 V,			
			200 cycles			
Hydroxide	900°C,	Octahedral,	1C,	130	92%	22
CO-	12 h (O <sub>2</sub> )	≈ 1 µm	3.5–5 V,			
precipitation			50 cycles			

Sol-gel	1000°C	Polyhedral,	0.5C,	133	79.5%	6
(citric acid)		> 1 µm	3.5–5 V,			
			300 cycles			
Sol-gel	900°C,	Octahedral,	0.2C,	130	94.8%	59
(citric acid)	15 h	≈ 4 µm	3.5–5 V,			
			100 cycles			
Oxalate	900°C,	Polyhedral,	1C,	125	96%	This
CO-	12 h	1–3 µm	3.5–4.9 V,			work
precipitation			300 cycles			

As expected, the specific discharge capacity decreases with Fe/Mg substitution, owing to a reduced high-voltage plateau, as the concentration of redox-active Ni is reduced (**Figure 4.6a,b**). This loss in capacity at high substituent concentrations is more significant in Mg-substituted samples when compared to analogous Fe-substituted samples. Differences in redox activity between Mg (inactive) and Fe (active) cannot explain capacity differences, since  $Fe^{3+/4+}$  redox occurs outside the voltage window used for galvanostatic cycling (> 4.9 V, **Figure 4.12**). Instead, the lower capacity of analogous Mg-substituted samples is likely due to a combination of 1) having less active Li/TM due to higher concentrations of a Li-rich impurity phase; 2) the presence of phase boundaries with such impurity phases, which can inhibit Li<sup>+</sup> diffusion; and 3) an increased occupancy of the 8a site with cations other than Li—as detailed above—which may block Li<sup>+</sup> diffusion across 8a-16c-8a-16c diffusion channels (i.e., less Li can be extracted from the spinel main phase). While the Ni plateau decreases, the plateau related to Mn<sup>3+</sup> increases with substituent concentration (**Figure 4.6**). This means that at low substituent concentrations (x = 0.05), initial discharge capacity increases slightly, but with increased substitution continues to decrease.

The impressive capacity retention of LNMO can be maintained with Fe/Mg substitution (**Figure 4.14a–c**). Contrary to many reports, however, neither Fe nor Mg substitution provide further improvements to the already-stable LNMO produced in this work.<sup>4,6,20,22,23,62</sup> Capacity retention of Mg substituted LNMO, instead, remains constant with increased Mg (and Mn<sup>3+</sup>) concentration ( $\approx 97\%$ , **Figure 4.14c**). Fe-substituted LNMO, on the other hand, shows comparable capacity retention at low concentrations (x = 0.05-0.1,  $\approx 96\%$ ; **Figure 4.14c**), but slightly reduced capacity retention at high concentrations (x = 0.15-0.2,  $\approx 92\%$ ; **Figure 4.14c**). This may be due to the notably higher concentrations of Mn<sup>3+</sup> observed in Fe0.15 and Fe0.2 (**Figure 4.6d**). In turn, this could lead to increased Mn<sup>3+</sup> disproportionation and subsequent Mn<sup>2+</sup> dissolution, where Mn can deposit as metallic Mn on the anode surface through the consumption of active Li.<sup>63</sup> The excellent capacity retention of these samples, at ambient

conditions, may be a result of half-cell testing, which provides a Li inventory that can mask the impact of TM dissolution.<sup>63</sup> Therefore, future work will aim to evaluate such samples in full cells and/or conditions which promote dissolution/degradation.

Despite the use of half-cell testing, several reports show that Mg substitution improves the capacity retention of LNMO.⁴.20,62 Previous work by Liang *et al.* on Mg-substituted LNMO, produced via solid-state method, showed that increased concentrations of Li-site defects improved the capacity retention of LNMO from 66.9 to 86.3% (Mg0.1) over 1500 cycles (≈ 80% after 300 cycles).⁴ We also observed an increased concentration of Li-site defects with Mg substitution. These site defects, however, do not appear to further improve the performance of our half cells under ambient conditions. Comparison with our work suggests that Mg shows a propensity for the Li site in non-stoichiometric LNMO, regardless of the synthetic method. Li-site defects have been shown to prevent surface reconstruction, but despite several reports that show improved cycling stability of Mg-substituted LNMO, several other reports find minimal improvements with Mg substitution.³7,57,59,64 Therefore, particle size/morphology and cycling conditions likely play a significant role in available improvements, where more significant improvements may be observed under accelerated ageing conditions.

Increased concentrations of  $Mn^{3+}$  are often reported to improve electronic conduction of LNMO, therefore, improving rate performance.<sup>3</sup> While  $Mn^{3+}$  does allow for improved conductivity of the fully-lithiated state, this only accounts for a small portion of the galvanostatic cycle.<sup>65</sup> Furthermore, Moorhead-Rosenberg *et al.* showed that the rate performance of the spinel structure is limited by Li<sup>+</sup> transport as opposed to the intrinsic electronic properties.<sup>65</sup> The importance of  $Mn^{3+}$  in improving rate performance is, therefore, dubious. This is reflected in our rate performance data (**Figure 4.14d**; and **Figure A6**, Appendix A). Despite increases in  $[Mn^{3+}]$  from LNMO < Mg0.05 < Fe0.05 < Fe0.1, the rate performance of the aforementioned samples is comparable. When further increasing the substituent concentration (i.e., x > 0.1 for Fe and x > 0.05 for Mg) the rate capability decreases, despite increases in  $[Mn^{3+}]$ . Differences in performance between samples cannot be attributed to microstructural differences since SEM images show that all samples display the same particle morphology (**Figure A7**, Appendix A). Instead, we anticipate that the loss of active Li/TM, alongside increased occupation of the 8a site with cations other than Li, may impede Li<sup>+</sup> diffusion and lead to an overall decrease in rate performance at increased concentrations.

Evaluation of the bulk structure suggests that the presence of Ni<sup>3+</sup> ions,  $V_o$  and, therefore, their influence on electrochemical performance are expected to be minimal. We acknowledge, however, the critical role of the electrode surface in the cycling stability of LNMO, particularly under accelerated ageing conditions. Notably,  $V_o$  that reside at the surface, which may not be

detected through bulk structure analysis used in this work, can exacerbate degradation at the surface of LNMO.<sup>25</sup> It is, therefore, part of our ongoing work to fully evaluate the surface of Fe/Mg-substituted LNMO under accelerated ageing conditions, with the help of the bulk structural insights presented in this study.

#### 4.6 Conclusions

This work aims to evaluate several structural properties to understand the role of the substituents in the electrochemical performance of  $LiNi_{0.5-x}M_xMn_{1.5}O_4$  cathode materials (M = Fe and Mg), for which a cohesive view is lacking. A combination of ND-XRD Rietveld refinements and first-principles defect calculations have provided insight into the following structural properties of these materials:

- 1) Ni/Mn ordering: All synthesised samples are indexed to the cation disordered  $Fd\overline{3}m$  space group, in which the 16c site remains vacant, as corroborated by the high calculated formation energy of interstitial  $M_i$  defects (M = Fe and Mg).
- 2) Mn³+ content increases with substitution and is greater in Fe-substituted samples when compared to analogous Mg-substituted samples.
- 3) Charge compensators for increasing Mn³+: V₀ are unlikely the dominant charge compensator and while the DFT-calculated [Ni³+] is greater in Mg-substituted LNMO, this does not increase with increased substitution (under a dilute limit which is lower than experimentally realised concentrations). Intrinsic off-stoichiometry also does not increase with substitution. Instead, off-stoichiometry and cation deficiencies that arise from impurity phase formation are likely to be the dominating charge compensators for increasing [Mn³+].
- **4) Impurity phase formation:** Li-containing impurity phases emerge with increased substitution and can be experimentally correlated to an increase in Li-site defects.
- 5) The extrinsic defect chemistry, as evaluated computationally, does not anticipate Lisite defects in the absence of impurity phases due to their relatively high formation energies. However, in the observed presence of impurities in the experimental data, the lower relative formation energy of Mg<sub>Li</sub> compared to Fe<sub>Li</sub> may explain the increase in Li-site defects in Mg-substituted samples.

We found that increased concentrations of Li-site defects caused by substitution do not significantly affect the cycling stability of our already well-performing LNMO. Furthermore, increased  $Mn^{3+}$  concentrations do not cause significant detriment to cycling stability in a half-cell configuration. A decrease in cycling stability is only observed at high Fe concentrations (x)

= 0.15–0.2), which could be linked to high concentrations of Mn<sup>3+</sup> ions, disproportionation and subsequent Mn<sup>2+</sup> dissolution. Finally, increased Mn<sup>3+</sup> offers no significant benefit to the rate capability. Instead, rate performance worsens with increased substitution because of i) loss of active material through impurity phases, and ii) increased occupation of the 8a site which may block the 8a-16c-8a-16c Li diffusion channel. Correlating the different structural features of these substituted LNMO cathodes, to differences in electrochemical performance under accelerated ageing conditions is part of ongoing work.

Furthermore, we have highlighted the limitations of a) using solely XRD or ND for identifying impurity phases and b) determining Li-site defects through combined XRD-ND Rietveld refinement. Such limitations make evaluating substituted LNMO structures challenging so efforts toward exploring/developing alternative methods would prove beneficial. While qualitative comparisons against DFT analysis have shed light on point defect processes that affect the properties of substituted LNMO, there is a pressing need for advancements in computational methods to enable the creation of quantitatively accurate models for defect analysis in compositionally complex disordered materials. Finally, our work shows that understanding the defect chemistry of the complex quinary system, such as the LNMO system explored here, requires combined efforts from researchers from both experimental and theoretical backgrounds.

#### 4.7 References

- B. E. Murdock, K. E. Toghill and N. Tapia-ruiz, *Adv. Energy Mater.*, 2021, **11**, 1–27.
- 2 Jeppe Winther Hedegaard, The Cathode Material for Next-Generation Lithium ion Batteries is Ready, https://www.topsoe.com/blog/the-cathode-material-for-next-generation-lithium-ion-batteries-is-ready.
- G. Liang, V. K. Peterson, K. W. See, Z. Guo and W. K. Pang, *J. Mater. Chem. A*, 2020,
   8, 15373–15398.
- G. Liang, Z. Wu, C. Didier, W. Zhang, J. Cuan, B. Li, K. Ko, P. Hung, C. Lu, Y. Chen, G. Leniec, S. M. Kaczmarek, B. Johannessen, L. Thomsen, V. K. Peterson, W. K. Pang and Z. Guo, *Angew. Chemie*, 2020, **132**, 10681–10689.
- 5 G. T. K. Fey, C. Z. Lu and T. Prem Kumar, *J. Power Sources*, 2003, **115**, 332–345.
- N. Kiziltas-Yavuz, M. Yavuz, S. Indris, N. N. Bramnik, M. Knapp, O. Dolotko, B. Das, H. Ehrenberg and A. Bhaskar, *J. Power Sources*, 2016, **327**, 507–518.
- 7 J. Ma, P. Hu, G. Cui and L. Chen, *Chem. Mater.*, 2016, **28**, 3578–3606.

- 8 H. Dong, Y. Zhang, S. Zhang, P. Tang, X. Xiao, M. Ma, H. Zhang, Y. Yin, D. Wang and S. Yang, *ACS Omega*, 2019, **4**, 185–194.
- 9 M. T. Nguyen, H. Q. Pham, J. A. Berrocal, I. Gunkel and U. Steiner, *J. Mater. Chem. A*, 2023, 7670–7678.
- 10 R. D. Shannon, *Acta Crystallogr.*, 1976, **A32**, 751–767.
- 11 Y. J. Gu, Y. Li, Y. B. Chen and H. Q. Liu, *Electrochim. Acta*, 2016, **213**, 368–374.
- T. Li, K. Chang, A. M. Hashem, A. E. Abdel-Ghany, R. S. El-Tawil, H. Wang, H. El-Mounayri, A. Tovar, L. Zhu and C. M. Julien, *Electrochem*, 2021, **2**, 95–117.
- J. Yoon, D. Kim, J. H. Um, M. Jeong, W. Oh and W. S. Yoon, *J. Alloys Compd.*, 2016,
   686, 593–600.
- 14 Y. Lin, J. Välikangas, R. Sliz, P. Molaiyan, T. Hu and U. Lassi, *Materials (Basel).*, 2023, **16**, 3116.
- 15 N. P. W. Pieczonka, Z. Liu, P. Lu, K. L. Olson, J. Moote, B. R. Powell and J. H. Kim, *J. Phys. Chem. C*, 2013, **117**, 15947–15957.
- 16 Y. Luo, H. Li, T. Lu, Y. Zhang, S. S. Mao, Z. Liu, W. Wen, J. Xie and L. Yan, *Electrochim. Acta*, 2017, **238**, 237–245.
- J. feng Wang, D. Chen, W. Wu, L. Wang and G. chuan Liang, *Trans. Nonferrous Met. Soc. China (English Ed.*, 2017, **27**, 2239–2248.
- 18 G. B. Zhong, Y. Y. Wang, Y. Q. Yu and C. H. Chen, *J. Power Sources*, 2012, **205**, 385–393.
- 19 Y. Weng and H. Zhang, *Ionics (Kiel)*., DOI:10.1007/s11581-023-05366-4.
- F. G. B. Ooms, E. M. Kelder, J. Schoonman, M. Wagemaker and F. M. Mulder, *Solid state ionics*, 2002, **153**, 143–153.
- 21 M. H. Liu, H. T. Huang, C. M. Lin, J. M. Chen and S. C. Liao, *Electrochim. Acta*, 2014, **120**, 133–139.
- 22 J. Liu and A. Manthiram, *J. Phys. Chem. C*, 2009, **113**, 15073–15079.
- 23 D. W. Shin, C. A. Bridges, A. Huq, M. P. Paranthaman and A. Manthiram, *Chem. Mater.*, 2012, **24**, 3720–3731.
- 24 J. H. Kim, S. T. Myung, C. S. Yoon, S. G. Kang and Y. K. Sun, *Chem. Mater.*, 2004, **16**, 906–914.

- D. Wang, C. Gao, X. Zhou, S. Peng, M. Tang, Y. Wang, L. Huang, W. Yang and X. Gao, *Carbon Energy*, 2023, **5**, 1–9.
- 26 Y. Chen, Y. Sun and X. Huang, *Comput. Mater. Sci.*, 2016, **115**, 109–116.
- 27 H. Liu, H. Liu, S. H. Lapidus, Y. S. Meng, P. J. Chupas and K. W. Chapman, *J. Electrochem. Soc.*, 2017, **164**, A1802–A1811.
- 28 D. Liu, J. Han and J. B. Goodenough, *J. Power Sources*, 2010, **195**, 2918–2923.
- 29 W. G. Williams, R. M. Ibberson, P. Day and J. E. Enderby, *Phys. B Condens. Matter*, 1997, **241–243**, 234–236.
- 30 A. C. Larson and R. B. Von Dreele, Los Alamos Natl. Lab. Rep. LAUR 86-748.
- 31 B. H. Toby, *J. Appl. Crystallogr.*, 2001, **34**, 210–213.
- 32 J. K. Cockcroft, Estimated Standard Deviations, http://pd.chem.ucl.ac.uk/pdnn/refine1/errors.htm, (accessed 5 May 2023).
- 33 A. W. Hewat, *Acta Crystallogr.*, 1979, **35**, 248–250.
- 34 E. S. Lee, K. W. Nam, E. Hu and A. Manthiram, *Chem. Mater.*, 2012, **24**, 3610–3620.
- P. Gorai, T. Famprikis, B. Singh, V. Stevanović and P. Canepa, *Chem. Mater.*, 2021, 33, 7484–7498.
- P. Gorai, H. Long, E. Jones, S. Santhanagopalan and V. Stevanović, *J. Mater. Chem. A*, 2020, **8**, 3851–3858.
- 37 M. M. Deng, B. K. Zou, Y. Shao, Z. F. Tang and C. H. Chen, *J. Solid State Electrochem.*, 2017, **21**, 1733–1742.
- 38 B. H. Toby, Argonne Natl. Laborartory.
- T. Ohzuku, K. Ariyoshi, S. Takeda and Y. Sakai, *Electrochim. Acta*, 2001, **46**, 2327–2336.
- 40 V. Sears, *Phys. Rev.*, 1992, **3**, 26–27.
- 41 H. Arai, K. Sato, Y. Orikasa, H. Murayama, I. Takahashi, Y. Koyama, Y. Uchimoto and Z. Ogumi, *J. Mater. Chem. A*, 2013, **1**, 10442–10449.
- 42 M. M. S. Sanad, H. A. Abdellatif, E. M. Elnaggar, G. M. El-Kady and M. M. Rashad, *Appl. Phys. A Mater. Sci. Process.*, 2019, **125**, 1–10.
- 43 P. Stüble, V. Mereacre, H. Geßwein and J. R. Binder, Adv. Energy Mater., ,

- DOI:10.1002/aenm.202203778.
- 44 J. Cen, B. Zhu, S. R. Kavanagh, A. G. Squires and D. O. Scanlon, *J. Mater. Chem. A*, 2023, 13353–13370.
- 45 Y. Chen, Y. Sun and X. Huang, *Comput. Mater. Sci.*, 2016, **115**, 109–116.
- 46 J. Cabana, F. O. Omenya, N. A. Chernova, D. Zeng, M. S. Whittingham and C. P. Grey, Chem. Mater., 2012, 24, 2952–2964.
- 47 Y. Luo, L. R. De Jesus, J. L. Andrews, A. Parija, N. Fleer, D. J. Robles, P. P. Mukherjee and S. Banerjee, *ACS Appl. Mater. Interfaces*, 2018, **10**, 30901–30911.
- 48 J. Lee, C. Kim and B. Kang, *NPG Asia Mater.*, , DOI:10.1038/am.2015.94.
- 49 M. Létiche, M. Hallot, M. Huvé, T. Brousse, P. Roussel and C. Lethien, *Chem. Mater.*, 2017, 29, 6044–6057.
- 50 R. Stoyanova, E. Zhecheva, R. Alcántara, J. L. Tirado, G. Bromiley, F. Bromiley and T. Boffa Ballaran, *Solid State Ionics*, 2003, **161**, 197–204.
- P. Sharma, C. Das, S. Indris, T. Bergfeldt, L. Mereacre, M. Knapp, U. Geckle, H. Ehrenberg and M. S. D. Darma, *ACS Omega*, 2020, **5**, 22861–22873.
- A. F. Gualtieri, G. Di. Gatta, R. Arletti, G. Artioli, P. Ballirano, G. Cruciani, A. Guagliardi, D. Malferrari, N. Masciocchi and P. Scardi, *Period. di Mineral.*, 2019, **88**, 147–151.
- 53 H. Liu, G. Zhu, L. Zhang, Q. Qu, M. Shen and H. Zheng, *J. Power Sources*, 2015, **274**, 1180–1187.
- 54 Y. Xiao, W. Xiang, J. Zhang, Y. Zhu and X. Guo, *Ionics (Kiel).*, 2016, **22**, 1361–1368.
- 55 Z. Liu, Y. Jiang, X. Zeng, G. Xiao, H. Song and S. Liao, *J. Power Sources*, 2014, **247**, 437–443.
- L. Balducci, H. Darjazi, E. Gonzalo, R. Cid, F. Bonilla and F. Nobili, *ACS Appl. Mater. Interfaces*, 2023, **15**, 55620–55632.
- 57 C. Ma, Int. J. Electrochem. Sci., 2019, 14, 7643–7651.
- 58 T. Chen, F. Lin, H. Wu, D. Zhou, J. Song and J. Guo, *J. Alloys Compd.*, 2023, **941**, 168825.
- 59 X. Cui, X. Zhou, W. Liang, K. Tuo, P. Wang, L. Zhang and S. Li, *Mater. Today Sustain.*, DOI:10.1016/j.mtsust.2021.100105.

- 60 J. Cheng, M. Li, Y. Wang, J. Li, J. Wen, C. Wang and G. Huang, *Chinese J. Chem. Eng.*, 2023, 61, 201–209.
- J. C. Hestenes, J. T. Sadowski, R. May and L. E. Marbella, *ACS Mater. Au*, 2023, **3**, 88–101.
- C. Locati, U. Lafont, L. Simonin, F. Ooms and E. M. Kelder, *J. Power Sources*, 2007, 174, 847–851.
- 63 J. H. Kim, N. P. W. Pieczonka, Z. Li, Y. Wu, S. Harris and B. R. Powell, *Electrochim. Acta*, 2013, **90**, 556–562.
- 64 W. Zhu, D. Liu, J. Trottier, C. Gagnon, A. Guerfi, C. M. Julien, A. Mauger and K. Zaghib, *J. Power Sources*, 2014, **264**, 290–298.
- Z. Moorhead-Rosenberg, A. Huq, J. B. Goodenough and A. Manthiram, *Chem. Mater.*, 2015, **27**, 6934–6945.

# Chapter 5 | Exploring the Surface Stability of Substituted LNMO Cathodes at Elevated Temperatures.

This chapter presents the article "Murdock, B.E., Menon, A.S., Booth, S.G., Fitzpatrick, J., Zhang, L., Piper, L.F.J., Cussen, S.A., and Tapia-Ruiz, N. Surface Stability of High-Voltage Spinel Cathodes Improved Through Mg Substitution Under Accelerated Ageing Conditions. *In Preparation*." which has been submitted for publication

As shown in Chapter 4, minimal improvement in capacity retention can be offered through cationic substitution, to LNMO produced in this work, at room temperature (1C, 3.5–4.9 V, 28°C).¹ Upon comparison with the literature, we found that this is likely due to the use of fast cycling rates, low upper-cut-off-voltages and ambient temperatures which limit the extent of electrolyte degradation.¹ Therefore, this article explores the improvements that can be offered under conditions that accelerate electrolyte degradation (50°C), by analysing the electrochemical performance, the electronic surface structure and the surface composition of LNMO, Fe0.05 and Mg0.05. Improved surface stability of Fe/Mg-substituted cathodes is often hypothesised to contribute to improvements in capacity retention.²-⁴ For example, Fe has been shown to migrate towards the surface of LNMO, where the Fe-enriched surface is said to limit the extent of surface degradation.³.⁵ However, a systematic study into the surface layer evolution is required to understand the role of substituents on the surface stability. Such a study is currently lacking in the literature.

In this chapter, we shed light on the improved surface stability of substituted LNMO cathodes, and its positive contribution to electrochemical performance. The surface structure and electrochemical performance of Fe-substituted LNMO are largely comparable to unsubstituted LNMO. This is in contrast to much of the literature, where differences are hypothesised to correlate to the differences in particle morphology and the similarity of the bulk structure of Fe0.05 and LNMO, as presented in Chapter 4. The Mg-substituted surface, on the other hand, shows marked improvements in both surficial and cycling stability. Such improvements are linked to improved TM3*d*-O2*p* hybridisation and the formation of a surface layer rich in C–O functionality, which is resistant to corrosion at high voltage. These findings not only demonstrate that the degradation mechanisms that occur at the Mg-substituted surface are unique, but also opens up potential avenues for advanced design of LNMO surfaces towards successful commercialisation.

# Surface Stability of High-Voltage Spinel Cathodes Improved Through Mg Substitution Under Accelerated Ageing Conditions

Beth E. Murdock<sup>1,2,3</sup>, Ashok S. Menon<sup>3,4</sup>, Samuel G. Booth<sup>3,5</sup> Jack Fitzpatrick<sup>1,2,3</sup>, Louis F. J. Piper<sup>3,4</sup>, Serena A. Cussen<sup>3,6</sup> and Nuria Tapia-Ruiz<sup>2,3\*</sup>

<sup>1</sup>Department of Chemistry, Lancaster University, Lancaster, LA1 4YB, UK

<sup>2</sup>Department of Chemistry, Molecular Sciences Research Hub, Imperial College London, W12 0BZ, UK

<sup>3</sup>The Faraday Institution, Quad One, Harwell Science and Innovation Campus, Didcot, OX11 0RA, UK

<sup>4</sup>Warwick Manufacturing Group, University of Warwick, Coventry, CV4 7AL, UK

<sup>5</sup>Department of Materials Science and Engineering, The University of Sheffield, Sir Robert Hadfield Building, Sheffield, S1 3JD, UK

<sup>6</sup>School of Chemistry, University College Dublin, Belfield, Dublin 4, Ireland

\*Corresponding author: n.tapia-ruiz@imperial.ac.uk

#### **Abstract**

LiNi<sub>0.5</sub>Mn<sub>1.5</sub>O<sub>4</sub> (LNMO) cathodes offer a cobalt-free, high-voltage alternative to current state-of-the-art Li-ion battery cathodes that are particularly well-suited for high-power applications due to their three-dimensional lithium-ion pathways and structural stability. However, degradation of commercial electrolytes at high voltages exacerbates capacity decay, where instability at the cathode surface leads to loss of active material, surface reconstructions, surface densification and observed increases in internal cell resistance. Cationic substitution has been proposed to enhance surface stability, thus limiting capacity decay. Here, we report the stabilising effect of Mg on the LNMO cathode surface during the early stages of cycling. We reveal that this decay mitigation is most pronounced in initial cycles, which we attribute to improved surface stability of Mg-substituted LNMO. Our studies indicate that this is correlated to improved TM3*d*-O2*p* hybridisation, enabled by the presence of Li-site defects, and the formation of a surface layer rich in C–O functionality for Mg-substituted LNMO, which is resistant to corrosion at high voltage. Examination of Fe-substituted and unsubstituted LNMO further validates the observation that C-O enriched surfaces in the case of Mg-LNMO allow

for improved stability. This work offers valuable insights into surface design for reducing degradation in high-voltage spinel cathodes.

#### **5.1 Introduction**

Future energy storage demands require the development of reliable, high-energy-density Liion batteries. As a result, next-generation cathode materials are seeing a push towards higher voltages that enable access to higher energy densities. By extending the upper voltage limit of the cathode, however, we also push the limits of conventional carbonate-based electrolytes, which are known to degrade at V > 4.2 V vs. Li<sup>+</sup>/Li.<sup>1</sup> This is a cause of concern for high-voltage spinel cathodes (LiNi<sub>0.5</sub>Mn<sub>1.5</sub>O<sub>4</sub>, LNMO)—with redox reactions occurring as high as 4.75 V—which, despite having high theoretical energy density (650 Wh kg<sup>-1</sup>), experience poor cycling stability.<sup>2</sup>

This poor cycling stability of LNMO cathodes is linked to electrolyte degradation at high voltages—a complex phenomenon which coincides with the dissolution of active transition metal ions (e.g., Ni²+ and Mn²+) from the cathode particles. Dissolution of Ni²+ and Mn²+ is observed after both storage and cycling of LNMO cells.³ This not only results in the loss of cathode active material but the dissolution of Mn²+ ions is particularly problematic in destabilising the anode surface layer, leading to capacity decay.³ Recent work has shown that HF formed at high voltages, due to electrolyte degradation, triggered Mn²+ dissolution, even though at V > 4.5 V all Mn ions are expected to be in the 4+ oxidation state.⁴ Furthermore, previous microscopy studies have also shown that the high-voltage surface reconstruction of LNMO, in which reduced transition metals migrate into the delithiated tetrahedral sites, forms a Mn₃O₄-like surface and thus a source of Mn³+.⁴,⁵ Mn³+ at the surface can then undergo HF-driven disproportionation to form surface  $\lambda$ -MnO₂ and dissolved Mn²+ ions. This correlates with reports which have shown the presence of HF in the electrolyte (at V ≈ 4.68 V vs. Li+Li),) shortly before the detection of Mn²+ ions, using a combination of nuclear magnetic resonance and electron paramagnetic resonance.⁴

Electrolyte degradation at the cathode is strongly influenced by the oxidative stability of the electrolyte solvent. In a conventional Li-ion cell, carbonate-based solvents such as ethylene carbonate (EC), typically oxidise at  $V > 4.2 \text{ V.}^1$  Such oxidation reaction produces a series of organic oligomers (e.g., polycarbonates and polyethylene oxide moieties) and organofluorine species, alongside H<sub>2</sub>O and other highly acidic species.<sup>6,7</sup> This results in the hydrolysis of the LiPF<sub>6</sub> electrolyte salt, forming HF, LiF, POF<sub>3</sub> and various Li<sub>x</sub>PO<sub>y</sub>F<sub>z</sub> species through subsequent reactions.<sup>6,7</sup> HF formation is followed by HF-etching of the cathode surface, resulting in the loss of active material and the accompanied production of further H<sub>2</sub>O, thus perpetuating a

continuous cycle of degradation, as outlined above.<sup>7</sup> A build-up of degradation species at the cathode surface forms a surface layer known as the cathode-electrolyte interphase (CEI). In some cases, the presence of a stable CEI on the surface can be beneficial in preventing continual electrolyte degradation.<sup>8,9</sup> However, the CEI layer formed on the LNMO surface is typically unstable, leading to significant surface densification, impeded Li<sup>+</sup> diffusion and progressive consumption of active material.<sup>8,9</sup> HF is also problematic for the stability of the aluminium current collectors, where HF corrosion—particularly during high-voltage operation—has been shown to form a thick and insulating AIF<sub>3</sub> layer, increasing the contact resistance between the cathode and the current collector and contributing to increased cell impedance.<sup>10</sup>

Much LNMO research is devoted to minimising degradation and dissolution at the electrode surface at high voltages through the use of surface coatings, high-voltage electrolytes/additives, particle engineering and elemental substitution.<sup>2,11,12</sup> Cationic substitution on the Ni-site with cheap and earth-abundant elements would not only potentially improve performance but also reduce the overall cathode cost. There have been reports that showed that the substitution of Ni with both Fe and Mg ions improves the cycling stability of LNMO, where potential migration of the substituents to the surface is sometimes offered as a contributor to improved stability, by facilitating the formation of a more stable CEI.<sup>13–15</sup> Indeed, migration of Fe to the LNMO surface has been observed previously.<sup>14,16</sup> However, verification and understanding of the CEI stability during cycling remain unreported.<sup>13–15</sup> Furthermore, suppression of Mn<sup>2+</sup> dissolution at high voltages is anticipated upon Mg substitution, since the presence of Li-site defects in Mg-substituted LNMO has been shown to prevent high-voltage surface reconstruction.<sup>13</sup>

Our earlier work, as presented in Chapter 4, confirmed the presence of Li-site defects in Mg-substituted LNMO and showed that Li-site defects also exist in Fe-substituted samples but at much lower concentrations. The concentration in unsubstituted LNMO, on the other hand, was negligible .<sup>17</sup> However, unsubstituted, Fe-substituted and Mg-substituted LNMO (LiNi $_{0.5-x}$ M $_x$ Mn $_{1.5}$ O $_4$ , where M = Fe or Mg; x = 0–0.2) exhibited comparable capacity retention under ambient conditions (~96% after 300 cycles at 1C, 3.5–4.9 V, Li $^+$ /Li half-cell)—despite differences in Li-site defects, impurity phase fractions, [Mn $^{3+}$ ] content, and initial capacities. We suggest that stability enhancement from Fe/Mg substitution in the samples studied may only become apparent under more demanding cycling conditions, such as higher temperatures, extended voltage ranges, and slower C-rates. Chapter 5, therefore, examines the influence of substitution on surface stability under elevated-temperature cycling.

In this work, the electrochemical performance of LiNi<sub>0.5-x</sub>M<sub>x</sub>Mn<sub>1.5</sub>O<sub>4</sub> (M = Fe and Mg; x = 0–0.05) is evaluated at elevated cycling temperatures (50 °C). To monitor degradation at the cathode surface, the CEI of unsubstituted, Mg-substituted, and Fe-substituted LNMO is investigated using a combination of synchrotron hard X-ray photoelectron spectroscopy (HAXPES) and soft X-ray absorption spectroscopy (sXAS) collected in the total electron yield (TEY) mode, while changes in cell impedance are tracked using electrochemical impedance spectroscopy (EIS). Our findings from experiments on both Mg- and Fe-substituted LNMO demonstrate the stabilising effect of Mg on the cathode surface, allowing for improved performance under accelerated ageing conditions. Fe, on the other hand, leads to minimal improvements in both capacity retention and surface stability.

#### 5.2 Experimental Methods

# **5.2.1 Material Synthesis and Electrochemical Characterisation**

LiNi<sub>0.5</sub>Mn<sub>1.5</sub>O<sub>4</sub> (LNMO), LiNi<sub>0.5-x</sub>Fe<sub>x</sub>Mn<sub>1.5</sub>O<sub>4</sub> (Fex) and LiNi<sub>0.5-x</sub>Mg<sub>x</sub>Mn<sub>1.5</sub>O<sub>4</sub> (Mgx) (x = 0.05, 0.1, 0.15 and 0.2) were synthesised via an oxalate co-precipitation method, and eletrodes prepared as previously outlined in Chapter 3 (Section 3.1 and 3.2.1).<sup>1</sup> All electrochemical testing was carried out in a temperature-controlled climate chamber (50°C, Memmert), where cells were rested for 12 h prior to the measurements. Standard galvanostatic cycling stability studies were carried out in two-electrode coin cells as outlined in Chapter 3.2.2 (1C, 3.5–4.9 V).

Potentiostatic electrochemical impedance spectroscopy (PEIS) was performed in three-electrode PAT-cell (EL-CELL®) using a spinel working electrode, Li counter electrode and Li reference electrode (see Chapter 3.2.5). Two EIS programs were adopted in this work: i) the detailed program, which follows work conducted by Pritzl *et al.*<sup>18</sup> and ii) the simplified program, used to limit time spent at high voltage. The detailed program involves collecting EIS data under blocking conditions (4.9 V vs Li<sup>+</sup>/Li) and non-blocking conditions (4.4 V vs Li<sup>+</sup>/Li, during the discharge process) for cycles 1–300, resulting in a total of 600 EIS measurements. The simplified program, on the other hand, only records EIS data under non-blocking conditions (4.4 V vs Li<sup>+</sup>/Li, during the discharge process) for selected cycles (cycles 1–5, 10, 25, and every 25 cycles thereafter), resulting in a total of 19 EIS measurements. For EIS measurements, both programs used a frequency range of 0.05 Hz–100 kHz and an amplitude of 10 mV. A rest period of 1 h was used before each EIS measurement to allow the system to equilibrate. Equivalent circuit fitting was then performed using the Aftermath software (Pine Research) using an  $R_{so}(R_{contacl}/Q_{contacl})(R_{pore}+CT_{non-blocking}/Q_{pore+CT-non-blocking})Q$  equivalent circuit

model (see **Figure 5.7d**). Note that while EIS was collected for every cycle when using the detailed program, circuit fitting was only performed on EIS data collected at cycles that correspond to those collected using the simplified programme.

# **5.2.2 Surface Characterisation**

For ex-situ surface analysis, spinel/Li half cells were disassembled after i) the 12 h rest period (OCV) or ii) after 1, 150 and 300 cycles. Extracted electrodes were thoroughly rinsed in dimethyl carbonate (DMC) in order to remove electrolyte residues and dried under vacuum overnight in the antechamber of a glovebox. Once dry, the electrode samples were mounted on the sample plates using double-sided Cu tape to ensure sufficient contact. Uncycled electrode (i.e., pristine electrodes, P) were also mounted. Samples plates were loaded into an ultrahigh vacuum chamber for transportation to avoid air exposure. Dual hard and soft X-ray experiments were conducted at the I09 beamline at Diamond Light Source (UK). 19 At I09, the electron analyser is mounted perpendicular to the direction of the X-ray propagation, which is at an almost grazing incident geometry to the sample surface. HAXPES data were collected at 2.2 keV and calibrated to the C-C (sp<sup>2</sup>) peak present in all samples in the form of CB (284.4 eV). Data processing and peak fitting were performed using the CasaXPS software, using a Shirley background. Electrodes without active material (C/PVDF reference) were used to determine the FWHM of the electrode species, where the active material was replaced with CB, resulting in a CB:PVDF ratio of 90:10. FWHM in cycled samples was constrained to be within  $\pm$  0.1 eV of similar species in pristine electrodes.

O K-edge, Ni L-edge and Mn L-edge sXAS data were collected from the same electrodes in total electron yield (TEY) mode. The intensity of all sXAS data was normalised with respect to the incident photon flux ( $III_0$ ). Pre-edge subtraction and post-edge normalisation of the O K-edge was performed using the ATHENA software. L-edge data were background subtracted in the OriginPro 2022 software, in which the baseline was created by the interpolation of manually selected background points. To aid in the comparison of relative intensity, selected post-edge-normalised data were subject to additional intensity normalisation (Intensity-normalised  $III_0$ , Figure 5.5h-j and Figure C2a-c). To account for lateral inhomogeneities, several electrode spots ( $n \ge 3$ ) were measured, and the average spectra presented in all cases.

#### **5.3 Electrochemical Performance**

As reported in our earlier work, LNMO prepared using a co-precipitation method with oxalic acid shows high rate performance and capacity retention under ambient conditions of  $\approx$  96% after 300 cycles at 1C (28 °C, 3.5–4.9 V), which, after an initial increase in capacity, delivers

a peak capacity of ≈ 125 mAh g<sup>-1</sup>.17 However, the capacity retention at elevated temperatures—used to accelerate ageing—decreases to ≈ 86% after 300 cycles (50 °C, 1C, 3.5-4.9 V, Figure 5.1a). To improve the high-temperature capacity retention of LNMO, several substituted spinel samples of composition LiNi<sub>0.5-x</sub> $M_xMn_{1.5}O_4$  (M = Fe and Mg; x = 0-0.2) were prepared (Figure C1, Appendix C). While all substituted samples showed improvements in high-temperature capacity retention, only samples prepared with low substituent concentrations provided improvements without a substantial loss of initial capacity (x = 0.05. Figure C1a-c, Appendix C). We, therefore, focus our current study on understanding the performance of  $LiNi_{0.5}Mn_{1.5}O_4$ (LNMO), LiNi<sub>0.45</sub>Mg<sub>0.05</sub>Mn<sub>1.5</sub>O<sub>4</sub> (Mg0.05)and LiNi<sub>0.45</sub>Fe<sub>0.05</sub>Mn<sub>1.5</sub>O<sub>4</sub> (Fe0.05) at 50 °C.

At 50 °C, the initial discharge capacities of LNMO, Fe0.05 and Mg0.05 are comparable (≈ 130 mAh g<sup>-1</sup>, **Figure 5.1a**). However, Mg0.05 shows a notable improvement in capacity retention over 300 cycles when compared to Fe0.05 and LNMO (94%, 88% and 86%, respectively. **Figure 5.1a**). To gain further insight into the rate of capacity degradation, the capacity retention (CR) from cycle to cycle is shown (Equation 5.1, **Figure 5.1c**), where the insets of **Figure 5.1c** highlight the variations observed during initial cycling (cycles 1–50) and long cycling (cycles 200–300).

$$CR = \left(\frac{C_{n+1}}{C_n}\right) \times 100 \tag{5.1}$$

All samples show initial CR values > 100%, indicating a slight increase in capacity over approximately the first 10 cycles. This behaviour is indicative of a cathode activation process, where the relatively fast cycling rate of 1C can limit the time available for lithium ions to fully access and intercalate into the cathode structure during the initial cycles. After activation the capacity then begins to degrade (i.e. CR < 100 %). From cycles 10-50, the average capacity retention values are the highest for Mg0.05 ( $\approx$  99.97%), followed by Fe0.05 ( $\approx$  99.95%) and LNMO ( $\approx$  99.92%). While these differences appear minor, such capacity loss accumulates exponentially with cycle number, since the total capacity retention is the product of CR from cycle 1 to cycle n (Equation 5.2).

$$\prod_{i=1}^{n} CR_i \tag{5.2}$$

This suggests that the rate of capacity degradation increases from Mg0.05 < Fe0.05 < LNMO. However, after initial cycling (i.e., > 50 cycles), the cycle-to-cycle variation in capacity is comparable for all three samples. We, therefore, attribute the enhanced long-term

performance of Mg0.05 to improved stability during the initial 50 cycles. This suggests that Mg substitution in LNMO can partially alleviate degradation processes which are most severe during initial cycling.

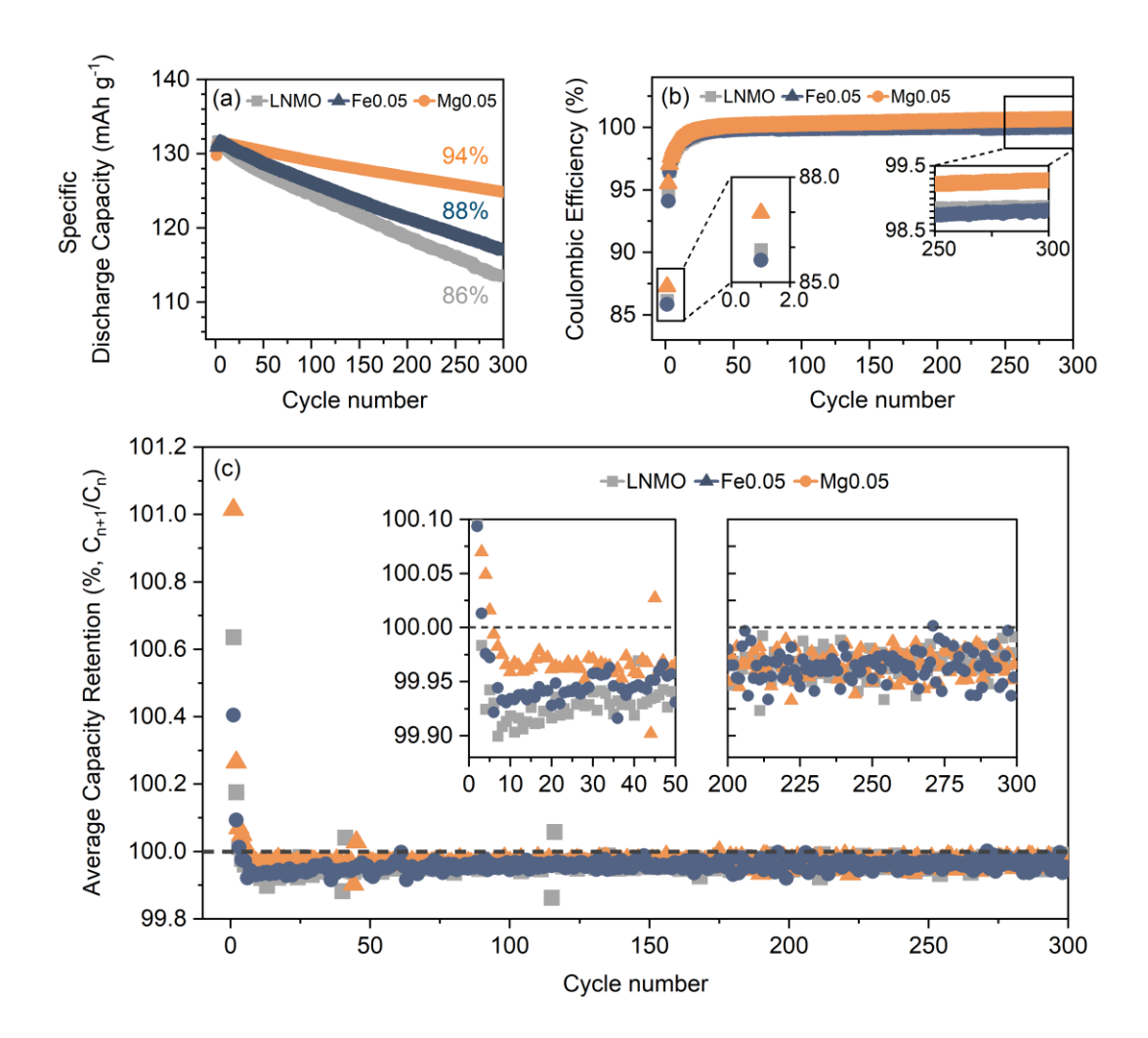


**Figure 5.1**: Long-term cycling performance of spinel/Li half-cells at 50 °C (1C, 3.5–4.9 V): a) cycling stability and b) corresponding coulombic efficiency values of LNMO (grey), Mg0.05 (orange) and Fe0.05 (blue) over 300 cycles; and c) average cycle-to-cycle variations (n > 3) in capacity retention ( $CR = (\frac{C_n+1}{C_n}) \times 100$ ), with insets highlighting the different rates of degradation from cycles 1–50 and 200–300.

To understand the contribution of unwanted oxidation processes to the observed differences in cycling stability, we compare the coulombic efficiency values (CE) of these materials. Low CE in LNMO-based full-cells is well reported and shown to correlate strongly to the loss of cyclable Li due to the destabilisation of the anode interphase by dissolved Mn<sup>2+</sup> ions.<sup>19,20</sup> However, unlike full-cells, half-cells have a large Li inventory, provided by the lithium counter electrode. As a result, spinel/Li half-cells are site-limited as opposed to inventory-limited.<sup>18</sup> In

other words, the capacity is primarily influenced by the amount of lithium which can be inserted into the cathode rather than the loss of Li. It is important to note, however, that while loss of cyclable Li is less of an issue in half-cells, degradation at the lithium electrode itself can still contribute to the loss of LiPF<sub>6</sub>. However, such effects are anticipated to be similar across the cells studied. In the framework presented by Tornheim *et al.*, coulombic efficiency in site-limited cells is influenced by the oxidation current,  $I_{ox}$ , where increases in  $I_{ox}$  (through electrolyte oxidation,  $O_2$  loss or current collector corrosion) can contribute to an increase in charge capacity and a decrease in discharge capacity.<sup>18</sup> This ultimately leads to lower CE at any given cycle.

All samples show low initial CE, indicating that a large amount of unwanted oxidation occurs at the cathode during the first cycle. However, initial CE is marginally higher for Mg0.05 (≈ 87%) when compared to LNMO and Fe0.05 (≈ 86%, **Figure 5.1b**), which suggests that Fe has minimal effect on the oxidation processes observed, whereas the presence of Mg can partially alleviate unwanted oxidation at the cathode surface. Despite low initial CE values, all samples show an increase in CE over the first 20 cycles, levelling off at 99.2% for Mg0.05, and 98.8% for both LNMO and Fe0.05. This demonstrates that unwanted oxidation processes at the cathode surface are most severe during initial cycling and could explain the increased rate of capacity degradation observed during the initial 50 cycles (Figure 5.1c). Furthermore, by the 300th cycle, the CE for Mg0.05 is only 0.4% higher than in LNMO compared to a 1% improvement observed for the 1st cycle, suggesting that the presence of Mg in LNMO is most influential during initial cycling. However, despite improvements, half-cell CEs for all samples are still below those required to meet full-cell industry standards (> 99.96%, full-cell), where CEs would likely decrease in full-cell configuration.<sup>21</sup> While the use of elevated temperatures in this work is expected to accelerate processes that contribute to  $I_{ox}$ , resulting in lower CE, half-cell CEs at ambient temperatures are still less than ideal (99.1-99.6%, Figure C1d, Appendix C).

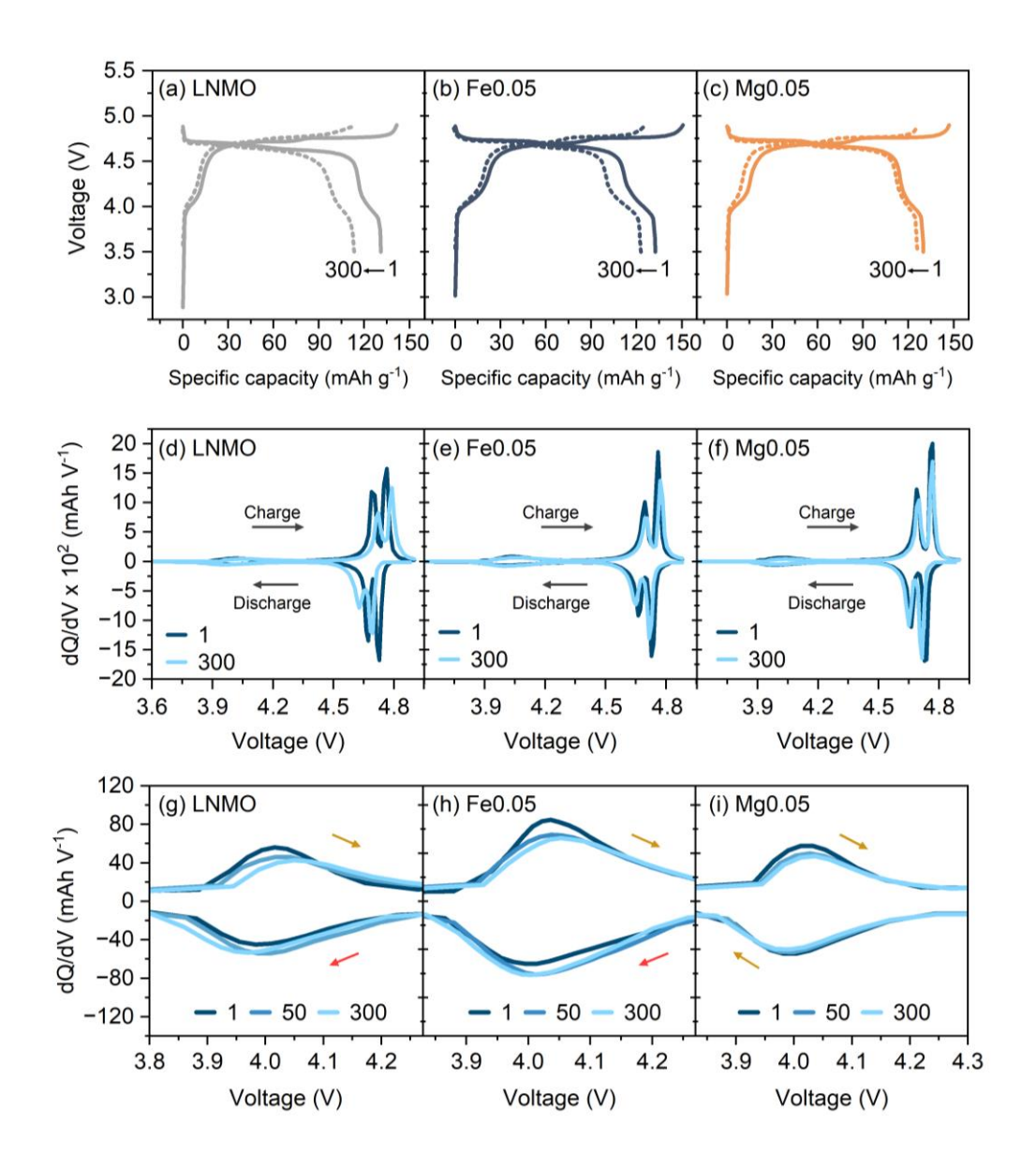


**Figure 5.2:** Voltage profiles of the 1<sup>st</sup> (solid) and 300<sup>th</sup> cycle (dashed) for a) LNMO, b) Fe0.05 and c) Mg0.05, obtained at 50 °C (1C, 3.5–4.9 V; dQ/dV vs. V plots corresponding to cycles 1 and 300 for d) LNMO, e) Fe0.05 and f) Mg0.05); enlarged dQ/dV vs. V, in the 4 V region mapping, the evolution of Mn<sup>3+/4+</sup>-related capacity from cycles 1–300 for g) LNMO, h) Fe0.05 and i) Mg0.05, where increases/decreases in intensity are indicated by red/yellow arrows respectively.

Further insight into the degradation of LNMO, Fe0.05 and Mg0.05 can be obtained from the charge/discharge voltage profiles, which consist of two high-voltage charge plateaux at  $\approx 4.7$  and 4.75 V, and a lower voltage charge plateau at  $\approx 4$  V (**Figure 5.2a-c**). These plateaux correspond to the Ni<sup>2+/3+</sup>, Ni<sup>3+/4+</sup> and Mn<sup>3+/4+</sup> redox couples, respectively.<sup>22</sup> The concentration of Mn<sup>3+</sup> in these samples increases with Fe/Mg concentration, leading to unit cell expansion, which was confirmed by diffraction data in our earlier work.

Increased Mn³+ concentrations are anticipated for Fe-substituted samples to maintain charge neutrality when substituting Ni²+ with Fe³+. When substituting Ni²+ with Mg²+, on the other hand, charge-balancing Mn³+ is not anticipated. Our previous work instead revealed that Mn³+ in Mg substituted LNMO increases to charge-balance cation deficiencies in the main spinel phase that result from impurity phases formation. Furthermore, we demonstrated a strong correlation between the formation Li-containing impurity phases and the formation of Li-site defects (i.e., Mg or Fe on the Li site)—the concentration of which were greater in Mg-substituted samples when compared to analogous Fe-substituted samples¹¹ The presence of Li-site defects is reported to be beneficial in preventing surface reconstruction. Despite the larger concentration of Li-site defects, however, the concentration of Mn³+ is greater for Fe0.05 than Mg0.05, as evidenced by the longer 4 V plateau. The presence of high concentrations of Mn³+ is often reported to have deleterious effects on cycling stability due to the infamous Mn³+ disproportionation and subsequent Mn²+ dissolution.²³

Differential capacity plots show well-defined peaks at 4, 4.7 and 4.75 V, corresponding to the plateaux observed in the voltage profiles (Figure 5.2d-i). In tracking the differential capacity in the 4 V-region, differences in Mn redox behaviour can be identified. For LNMO and Fe0.05, the 4 V discharge peak increases from cycle 1-50, while the 4 V discharge peak increases (Figure 5.2g-h). This behaviour can be attributed to Mn<sup>3+</sup> disproportionation, which can lead to the formation of electrochemically active Mn<sup>4+</sup> ions—as MnO<sub>2</sub> phases, for example—and soluble Mn<sup>2+</sup> ions, the latter of which dissolves into the electrolyte and is irreversibly lost. As a result, the redox-active Mn<sup>3+</sup> centres are depleted, explaining the diminishing charge peak, while the newly formed MnO<sub>2</sub> continues to contribute to the discharge process, leading to the increased discharge peak. From cycle 50–300, the 4 V peak intensities for LNMO and Fe0.05 remain relatively constant, suggesting that disproportionation is most severe during the initial 50 cycles. In contrast, for Mg0.05, both the 4 V charge and discharge peaks show a subtle decrease in intensity. This simultaneous reduction of intensity in both the charge and discharge peaks suggest that electrochemically active Mn<sup>4+</sup> ions are not formed to the same extent, implying that Mn<sup>3+</sup> disproportionation is less pronounced. Loss of intensity may instead be better correlated with a subtle loss of active Li.

The high-voltage peaks at 4.7 and 4.75 V also experience a loss in intensity after 300 cycles and may be explained by i) loss of active Ni/Li ions through dissolution and parasitic surface reactions or ii) inhibited Li<sup>+</sup> transport, preventing full oxidation/reduction of Ni. <sup>19,20</sup> In addition to changes in intensity, all three samples experience voltage polarisation, as evidenced by the shifts in the peak positions with respect to those observed in cycle 1. Such voltage polarisation suggests an increase in internal cell resistance—the origin of which could be a combination of surface layer resistance, charge transfer resistance and contact resistance—all of which can

lead to worsening electrode kinetics.<sup>24</sup> While all samples experience voltage polarisation and changes in peak intensity, both changes are most significant for the LNMO sample. Polarisation in Fe0.05, on the other hand, is reduced, while Mg0.05 demonstrates greater stability in both voltage and capacity. The improved stability of Mg0.05 suggests that Mg substitution not only prevents capacity fade but can also mitigate voltage decay and increases in cell impedance.

The compiled electrochemical characterisation provides several indications that the Mg0.05 sample might experience less electrolyte degradation, loss of active material and changes in internal cell resistance upon prolonged cycling under accelerated ageing conditions. The electrochemical evaluations of Fe0.05, on the other hand, suggest that Fe0.05 experiences similar degradation to LNMO—the possible reasons for which we explore later. To further investigate these differences, a combination of *ex-situ* surface analysis and electrochemical impedance spectroscopy was performed.

### 5.4 Ex-situ Surface Analysis

To evaluate the effect of Fe/Mg substitution on electrolyte degradation and surface stability of LNMO, *ex-situ* surface analyses were performed. The spinel electrode surfaces were analysed after several stages of cycling: in the pristine state (P); after soaking in the electrolyte for 12 h (OCV); and at the end of cycles 1, 150 and 300. Electrodes without active material—composed only of carbon black and PVDF (CB/PVDF)—were also soaked in the electrolyte to elucidate the role of inactive components on the chemical degradation of the electrolyte. Samples are labelled using the notation S-C, (sample-charge state) where S = C/PVDF, LNMO, Fe0.05 or Mg0.05 and C = P, OCV, 1, 150 or 300. Each electrode was analysed using both soft X-ray absorption spectroscopy in total electron yield mode (sXAS-TEY < 1 keV) and hard X-ray photoelectron spectroscopy (HAXPES, 2.2 keV).

#### **5.4.1 Hard X-ray Photoelectron Spectroscopy**

In the C1s, O1s and F1s HAXPES spectra, the C/PVDF-P electrode shows peaks characteristic of both CB and PVDF (**Figure 5.3**). The C1s peak at 284.4 eV can be attributed to the sp<sup>2</sup> carbon of CB.<sup>25</sup> As expected, the CB surface is slightly oxidised and contains a small amount of sp<sup>3</sup> carbon (284.8 eV) and oxygen functionality, with corresponding peaks in the C1s and O1s spectra at 287.5 eV and 531.5 eV (C=O) and 286 eV and 532.5 eV (C-O/O-H). Additional C1s peaks at 286.2eV and 290.8 eV are attributed to the CH<sub>2</sub> and CF<sub>2</sub> groups of the PVDF binder, respectively, where the C-F bonding is also evident in the F1s spectra by the presence of the peak at 687.8 eV.<sup>26</sup>

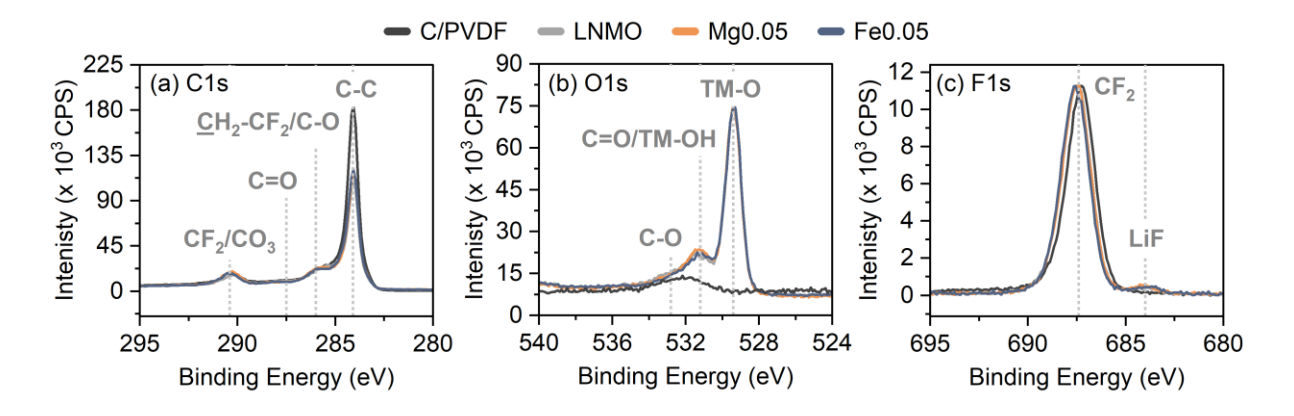


Figure 5.3: a) C1s, b) O1s and c) F1s HAXPES spectra of C/PVDF-P, LNMO-P, Fe0.05-P and Mg0.05-P.

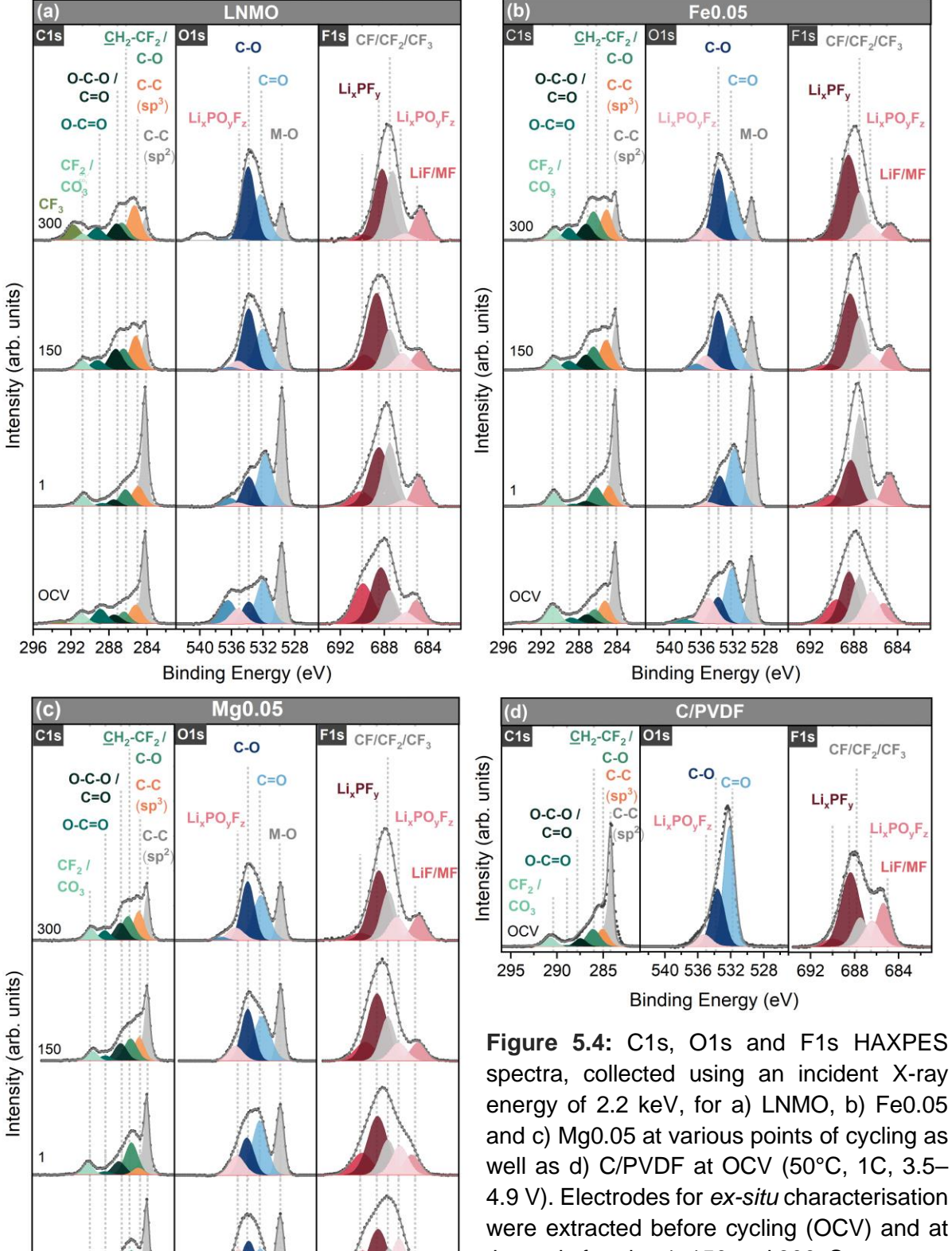
LNMO-P, Fe0.05-P and Mg0.05-P also show peaks consistent with PVDF and oxidised CB, alongside some notable differences in the spectra. Firstly, the electrodes containing active material show a lower intensity C-C (sp<sup>2</sup>) peak in the C1s spectra, since there is a lower concentration of CB in the electrode formulation compared to the C/PVDF electrode (10% vs. 90%). The C1s spectra are otherwise comparable, suggesting that CB at the surface of each electrode is oxidised to a similar extent. As a result, similarities in the O1s spectra, at 531.5 and 532.5 eV, are expected. However, the peak at 532.5 eV shows higher intensity for electrodes containing active material, indicating the presence of a functional group that does not contain carbon (i.e., is unlikely to be a carbonate signal). The increase in peak intensity is, therefore, most likely caused by the TM-OH terminating group at the cathode surface, as reported elsewhere.4 While surface hydroxyl groups can accelerate the production of HF, the hydroxyl concentration is comparable for all samples.<sup>27</sup> In addition to TM–OH bonding, TM–O bonding from within the spinel lattice is also observed in the O1s spectra ≈ 529 eV.<sup>28</sup> Finally, a small concentration of LiF is observed in the F1s spectra at 684.5 eV. This indicates slight dehydrofluorination of the PVDF binder during the slurry preparation process, where HF can further react with surface Li to form LiF.<sup>29</sup> However, there is no significant variation between the surface of LNMO-P, Mg0.05-P and Fe0.05-P prior to electrolyte exposure.

After exposure to the electrolyte, LNMO-OCV, Fe0.05-OCV and Mg0.05-OCV show additional surface species, which are indicative of electrolyte decomposition (**Figure 5.4**). Increases in sp<sup>3</sup> carbon (284.8 eV), C–O (286 eV), O–C–O/C=O (287.8 eV), O–C=O (288.5 eV) and CO<sub>3</sub> (290.2 eV) are observed in the C1s spectra, where such surface species originate from the decomposition/deposition of the electrolyte solvent.<sup>28,30,31</sup> Decomposition of the electrolyte salt is also observed, where hydrolysis of LiPF<sub>6</sub> in the presence of trace amounts of water leads to the formation of Li/TM fluorides (LiF/MF, 684.5 eV), Li<sub>x</sub>PO<sub>y</sub>F<sub>z</sub> (534.5 eV and 686.5 eV) and Li<sub>x</sub>PF<sub>y</sub> species (688.5 eV).<sup>28,30,31</sup> Such organic and inorganic species are also observed on the

CB/PVDF-OCV electrode (**Figure 5.4d**), demonstrating that chemical degradation of the electrolyte occurs at the surface of CB and/or PVDF in the absence of active material or an applied current.

Carbon additives are often shown to be unstable in the presence of organic electrolytes.  $^{32-34}$  In this work, the CB/PVDF-OCV electrode shows a higher intensity of the LiF peak, relative to CF<sub>2</sub>, when compared to LNMO-OCV, Mg0.05-OCV and Fe0.05-OCV which have much lower CB content. Since the PVDF content is the same for all electrodes, this suggests that CB in the electrode promotes LiF formation/deposition. The concentration of organic species, on the other hand, is greater for electrodes with active material, relative to the C–C(sp²) and TM–O peaks. This suggests that the presence of active material can facilitate the degradation of the electrolyte solvent, where H<sub>2</sub>O formed as a by-product of such solvent degradation may facilitate further hydrolysis of LiPF<sub>6</sub>. This could explain the increased concentration of Li<sub>x</sub>PO<sub>y</sub>F<sub>z</sub> observed for LNMO-OCV, Fe0.05-OCV and Mg0.05-OCV when compared to C/PVDF-OCV since Li<sub>x</sub>PO<sub>y</sub>F<sub>z</sub> is formed through more extensive hydrolysis of the electrolyte salt than LiF. These results show that both the CB additive and the active material contribute to electrolyte degradation. The influence of CB, however, is expected to be similar for LNMO, Fe0.05 and Mg0.05.

Although salt hydrolysis appears to occur at each of the cathode surfaces, differences in the  $\text{Li}_x\text{PO}_y\text{F}_z$  content are observed between LNMO, Fe0.05 and Mg0.05, where the  $\text{Li}_x\text{PO}_y\text{F}_z$  peak area (F1s spectra) increases from LNMO-OCV < Fe0.05-OCV < Mg0.05-OCV, relative to the CF2 peak.  $\text{Li}_x\text{PO}_y\text{F}_z$  species may prove beneficial for cycling stability, due to their ability to scavenge dissolved TM ions and, therefore, suppress electrode cross-talk. Such benefits have been demonstrated in several studies which employ  $\text{LiPO}_2\text{F}_2$ -forming additives with corresponding improvements in cycling stability. However, Li-containing additives typically come at a prohibitive cost, so the ability to form  $\text{Li}_x\text{PO}_y\text{F}_z$  preferentially at the Mg0.05 sample would be advantageous for reducing cell costs. Nevertheless, cross-talk effects are not always obvious in LNMO||Li half-cells which have a large Li inventory, often masking capacity loss that results from loss of active material. The direct impact of  $\text{Li}_x\text{PO}_y\text{F}_z$  concentrations on the cycling stability presented in Figure 5.1 is, therefore, unclear. However, monitoring their relative peak intensity during cycling may provide insight into the degradation differences experienced at each surface of the different samples.



OCV

296 292 288 284

540 536 532 528

Binding Energy (eV)

692

the end of cycles 1, 150 and 300. Spectra are area normalised to aid with the visualisation of relative intensity changes.

Differences in  $\text{Li}_x \text{PO}_y \text{F}_z$  relative peak intensity, as well as other inorganic species, are observed not only at OCV but also after the 1<sup>st</sup> cycle. For example, from Mg0.05-OCV to Mg0.05-1, the  $\text{Li}_x \text{PO}_y \text{F}_z$  peak area relative to  $\text{CF}_2$  decreases by  $\approx 40\%$ . This decrease, however, is far more significant for LNMO ( $\approx 70\%$ ) and Fe0.05 ( $\approx 80\%$ ). LNMO and Fe0.05 also see a notable decrease in peak intensity for LiF and  $\text{Li}_x \text{PF}_y$  species with respect to the CF2 peak. Such dissolution of inorganic species can result from HF attack, where an increase in [HF] is anticipated during the high-voltage operation, as demonstrated by Hestenes *et al.*<sup>4,36</sup> Greater retention of inorganic  $\text{Li}_x \text{PO}_y \text{F}_z$  on the Mg0.05-1 surface, therefore, suggests that HF attack may be partially suppressed, which, in turn, could be linked to a lesser extent of electrolyte degradation at high voltage.

Suppression of electrolyte degradation during the 1<sup>st</sup> cycle in the Mg0.05 sample is observed when comparing the C1s and O1s spectra of Mg0.05-OCV and Mg0.05-1. Very minor differences in the organic surface layer are observed after the 1<sup>st</sup> cycle, suggesting that i) the surface layer that forms at OCV is stable against high-voltage operation and ii) further degradation at the electrode surface does not occur. The concentration of organic surface species for LNMO-1 and Fe0.05-1, on the other hand, decreases relative to CB (C–C, sp²) and TM–O when compared to LMNO-OCV and Fe0.05-OCV. This suggests that the surface layer that forms on LNMO and Fe0.05 electrodes at OCV becomes partially stripped after the 1<sup>st</sup> cycle, which is expected due to corrosion of the CEI at high voltage.

Differences in the surface layer stability may be attributable to differences in the composition of the surface layer itself, where LNMO-OCV and Fe0.05-OCV show a surface layer rich in carbonates and sp³ C–C functionality, while Mg0.05-OCV has an organic surface layer rich in C–O functionality. This not only suggests that the electrolyte decomposition pathway on the Mg0.05 surface is different but also suggests that a surface layer rich in C–O functionality may be responsible for improved surface stability. The benefit of a C–O-rich surface has been demonstrated in other high-voltage systems. For example, Markevich *et al.* compared the use of an EC-based electrolyte with and without an FEC additive in combination with a high-voltage LiCoPO<sub>4</sub> cathode (C/5, 3.5–5.2 V, 30 °C).³0 They showed that without FEC the surface was rich in carbonates whereas incorporation of FEC led to improved capacity retention, attributed to a surface layer rich in C–O functionality. While in agreement with our findings, the improved oxidative stability observed in the Mg0.05 sample is somewhat surprising, given the lower oxidative stability of ethers when compared to carbonates.³7

The instability of the CEI layer is problematic for cycling stability, as it exposes the electrode surface to allow for continual degradation and build-up of degradation products. This is evident when tracking the surface layer evolution of LNMO and Fe0.05, which show a significant

decrease in C–C (sp², C1s) and TM–O (O1s) peak intensities relative to the observed surface species. This indicates a significant build-up of degradation products on the surface of LNMO and Fe0.05 with prolonged cycling. By contrast, the similar relative intensity of the C–C (sp², C1s) and TM–O (O1s) peaks are observed from Mg0.05-OCV to Mg0.05-150, followed by a marginal decrease from Mg0.05-150 to Mg0.05-300. This suggests that more extensive densification occurs at the surface of LNMO and Fe0.05 over 300 cycles at elevated temperatures, due to the formation of an unstable surface layer that allows for continual degradation. After prolonged cycling, the composition of the CEI layer is comparable for all three samples. This suggests that while the Mg0.05 surface is compositionally different during initial cycling, the processes that contribute to densification after long cycling are comparable. This is in agreement with the electrochemical analysis presented previously (**Figure 5.1**), where the rate of capacity degradation was improved for Mg0.05 during the initial cycling but was comparable to LNMO and Fe0.05 after long cycling.

Finally, unidentified peaks in the HAXPES spectra should also be noted. An additional F1s peak can be observed for all electrodes above 688 eV. While this has been attributed to organofluorine species (RCF $_x$ ) elsewhere in the literature, correlating peaks in the C1s (> 291 eV) spectra are not observed. This suggests that the F1s peak above 688 eV is likely absent of both C and O. Therefore, the origin of this peak could likely be electrolyte salt decomposition. Although unidentified, this peak decreases in intensity with prolonged cycling, relative to the CF $_2$  peak, which suggests that this species forms at OCV, before becoming buried within the CEI. Similarly, an unidentified O1s at high binding energy ( $\approx$  537 eV) is observed in LNMO, but decreases with cycling, and also appears sporadically in Fe0.05-OCV and Fe0.05-150 as well as Mg0.05-300. Since there is no obvious trend, the presence of this peak cannot be correlated to the electrochemical performance.

In summary, based on the HAXPES data presented, LNMO and Fe0.05 form an unstable, carbonate-rich surface layer at OCV which becomes partially stripped after the 1st cycle, likely due to the formation of acidic species during the initial charging process. This exposes the electrode surface, allowing for significant surface densification, which consumes active material and may impede Li<sup>+</sup> diffusion to the electrode. Densification at the Fe0.05 surface, however, is less severe which may explain the slight improvement in capacity retention. In contrast, the formation of a stable surface layer on Mg0.05-OCV, rich in C–O functionality, protects the surface during initial cycling, leading to a thinner surface layer after prolonged cycling. The degradation that occurs in the later cycles, however, is expected to be similar for all samples. Mg0.05 may, therefore, delay degradation as opposed to completely preventing it. This could offer a partial explanation for the improved cycling stability of Mg0.05 under accelerated ageing conditions, which is most notable during initial cycling. The reason for

differences in surface layer composition and surface layer formation mechanisms, however, remains unclear.

Despite literature reports that demonstrate improved cycling stability upon Fe-substitution in LNMO, our results reveal minimal improvements in capacity retention and surface stability, even at elevated temperatures. These limited improvements may be related to differences in synthetic methods used and resulting particle morphology. Fe-substituted LNMO reported in the literature typically shows polycrystalline morphology (PC). <sup>16,38</sup> In contrast, the method adopted herein produces materials that resemble a single crystal (SC) type morphology. <sup>17</sup> The stability of PC LNMO particles is significantly influenced by the anisotropic phase transitions that occur upon cycling which can lead to particle cracking at the grain boundaries, revealing fresh surfaces and contributing to surface-related degradation mechanisms. <sup>39</sup> Fe substitution in PC LNMO might, therefore, alleviate particle fracture as opposed to significantly alleviating electrolyte degradation, thus indirectly limiting the extent of degradation that is observed. SC particles, on the other hand, are more resistant to fracture, which may limit the improvement offered by Fe in this work. Understanding the influence of substitution on particle fracture would therefore be interesting for future investigations, to understand the synthesis-dependence of the enabled improvements that are beyond the scope of the current study.

#### **5.4.2 Soft X-ray Absorption Spectroscopy**

To explore the evolution of the transition metal oxidation state at the surface, sXAS data were collected using surface-sensitive total-electron-yield mode (TEY), with a detection depth of < 10 nm. Across all stages of cycling, LNMO, Fe0.05 and Mg0.05 show Ni *L*-edge spectra consistent with that of Ni<sup>2+</sup> (**Figure 5.5a-c**, Appendix C). The Mn *L*-edge spectra, on the other hand, show complex peak shapes which indicate the presence of Mn<sup>2+</sup>, Mn<sup>3+</sup> and Mn<sup>4+</sup> (**Figure 5.5d-j**). The relative intensities of the Mn<sup>2+</sup>, Mn<sup>3+</sup> and Mn<sup>4+</sup> peaks are identical for the three samples at OCV and show a dominant 2+/3+ character. This suggests that before electrochemical cycling, transition metal oxidation states at the surface are similar, despite known differences in bulk Mn<sup>3+</sup> content.<sup>17</sup>

Transition metal oxidation states are often correlated to the O *K*-edge spectra, which consist of two key features: the pre-edge (< 535 eV, peaks A and B in **Figure 5.6**) and a broad feature above 535 eV, arising from the hybridised O2*p*-TM4*sp* orbitals.<sup>40</sup> An additional feature at 534 eV (peak C in **Figure 5.6**), observed for LNMO and Fe0.05, is attributed to Li<sub>2</sub>CO<sub>3</sub> on the surface.<sup>41</sup> The pre-edge is related to the excitation of electrons from the O1s orbital to the unoccupied O2*p*-TM3*d* hybridised orbitals.<sup>40</sup> In LNMO spinel materials, the pre-edge represents a convolution of peaks related to Mn–O and Ni–O bonding. As a result, the intensity of the pre-edge peaks can be influenced by the TM oxidation states and TM–O covalency/

O2*p*-TM3*d* hybridisation. Greater O2*p*-TM3*d* hybridisation and orbital overlap indicate that more transitions from the O1s to the unoccupied O2*p*-TM3*d* hybridised orbitals can occur, leading to higher pre-edge peak intensity.<sup>40</sup> At a higher TM oxidation state, the number of unoccupied O2*p*-TM3*d* hybridised orbitals increases, which also contributes to a higher observed pre-edge peak intensity.<sup>40</sup>

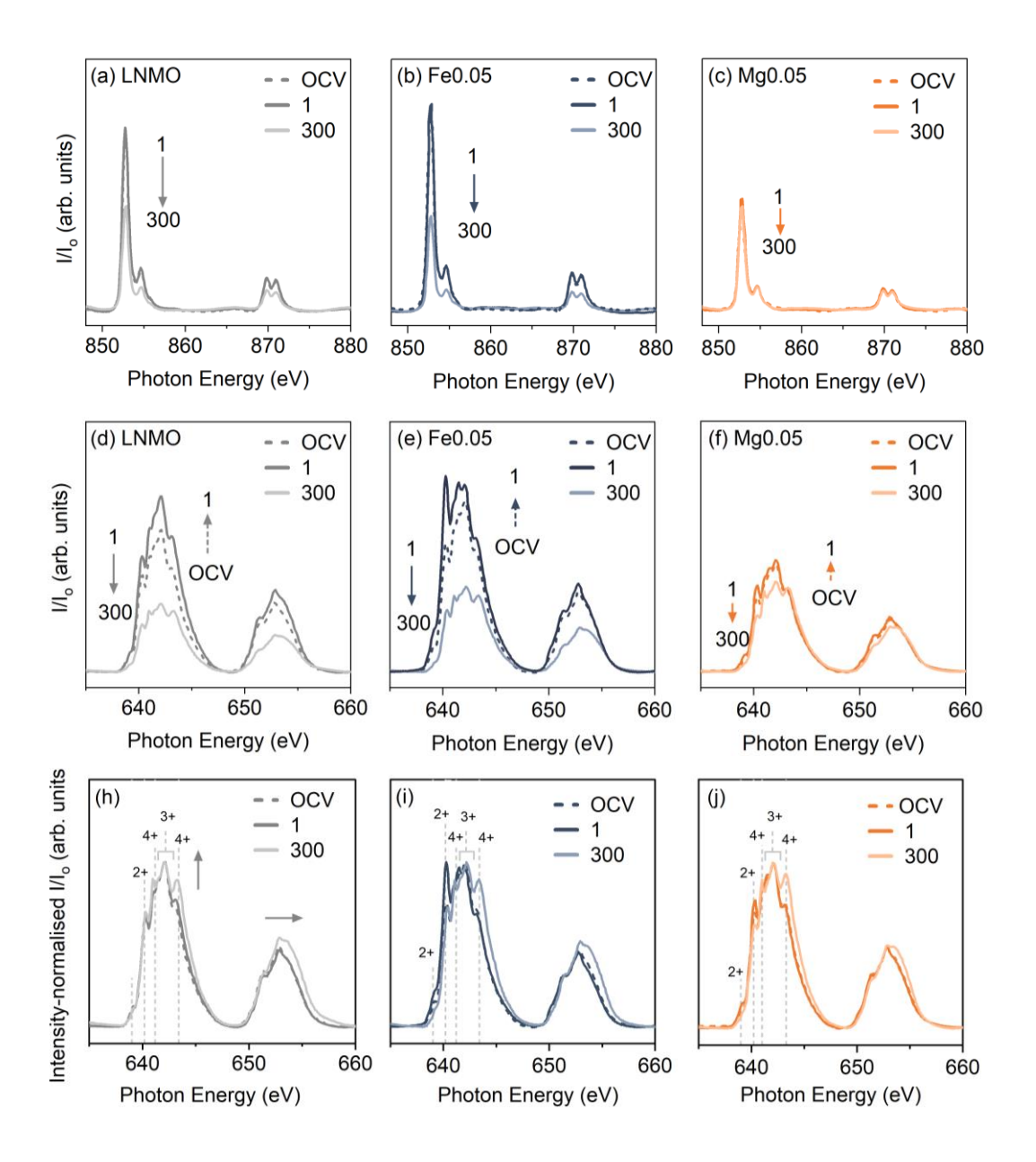


**Figure 5.5:** Ni *L*-edge (a-c) and Mn *L*-edge (d-f) sXAS-TEY spectra of *ex-situ* LNMO (grey; a, d, h), Fe0.05 (blue; b, e, i) and Mg0.05 (orange; c, f j) electrodes at various points of cycling (50°C, 1C, 3.5–4.9 V): before cycling (OCV); and after cycles 1, 150 and 300. The intensity normalised Mn *L*-edge h) LNMO, i) Fe0.05 and j) Mg0.05 highlight changes in relative intensity.

The pre-edge of Mg0.05-OCV resembles that of an Mn<sub>3</sub>O<sub>4</sub>-like surface, which correlates well with the dominant Mn<sup>2+/3+</sup> peaks observed in the Mn *L*-edge spectra.<sup>4</sup> Mn<sub>3</sub>O<sub>4</sub>-like surfaces are often reported to appear during the delithiation process in LNMO materials, as TMs migrate into the empty tetrahedral sites. 4,5 Recent works, however, demonstrate the presence of a Mn<sub>3</sub>O<sub>4</sub>-like surface in pristine LNMO samples, which can result from lithium/oxygen deficiencies that transpire during synthesis. 42 Previous structural characterisation of our spinel samples revealed the presence of Li deficiencies. 17 Such Li deficiencies were most prominent in Mg-substituted samples due to the formation of Li-site defects (e.g., Mg on the Li site, MgLi). The presence of a Mn<sub>3</sub>O<sub>4</sub>-like surface at OCV is, therefore, likely caused by lithium deficiencies in the Mg0.05 sample. Unlike Mg0.05, the pre-edge of LNMO-OCV and Fe0.05-OCV resembles that of MnO (Mn<sup>2+</sup>), with a lower intensity of peak A (530 eV).<sup>4</sup> However, given that the electronic structure around Mn is identical for all samples (Figure C2b, Appendix C), the lower intensity of peak A in the O K-edge spectra observed for LNMO-OCV and Fe0.05-OCV may reveal differences in the oxygen electronic structure when compared to Mg0.05, as opposed to TM oxidation states. Observed changes in oxygen electronic structure might therefore be associated with alternative factors that can influence the extent to which the O2p and TM3d orbitals overlap, such as local structure, bond strength, and covalecy.

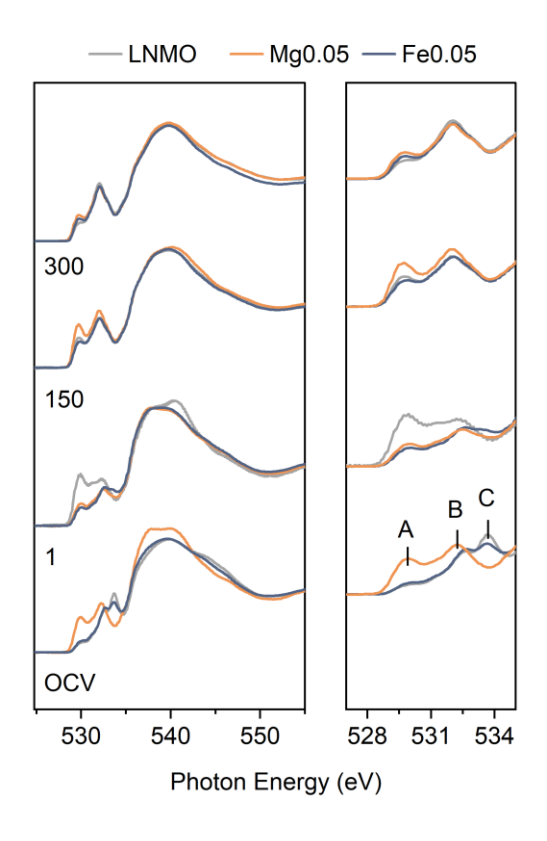


**Figure 5.6**: O *K*-edge sXAS-TEY spectra of *ex-situ* LNMO (grey), Fe0.05 (blue) and Mg0.05 (orange) electrodes at various stages of cycling (50°C, 1C, 3.5–4.9 V): before cycling (OCV), and after cycles 1, 150 and 300.

Improved O2p-TM3d orbital overlap in Mg0.05 may be related to the presence of Li-site defects, which are thought to prevent the migration of Mn into the tetrahedral sites. <sup>17</sup> The orbital overlap in MnO<sub>6</sub> octahedra is generally stronger than in Mn–O<sub>4</sub> tetrahedra since the octahedral geometry permits the  $e_g$  orbitals of Mn to point directly at the oxygen atoms, allowing for strong  $\sigma$ -bonding with the oxygen p orbitals. By contrast, the  $e_g$  and  $t_{2g}$  orbitals of Mn in the tetrahedral environment do not overlap as effectively, resulting in weaker bonding interactions. We, therefore, expect to observe a lower pre-edge intensity. As a result, the lower pre-edge intensity of LNMO-OCV and Fe0.05-OCV may indicate some migration of Mn from octahedral to tetrahedral sites, reducing the overall O2p-TM3d hybridisation. Furthermore, previous computational work on isostructural LiMn<sub>2</sub>O<sub>4</sub> has demonstrated that the presence of bulk Mn<sub>Li</sub> defects (i.e., Mn on the tetrahedral site) does not impact the oxidation state of Mn, but rather causes the charge localised on oxygen to decrease. <sup>43</sup> This supports our observation that changes in the oxygen electronic structure and TMO<sub>x</sub> geometry can occur without alternating the TM oxidation state.

Insufficient overlap of the O2p and TM3d orbitals is thought to limit the stability of the TM–O bonding in LNMO, thus facilitating TM migration and dissolution. 44,45 To prevent such processes, previous works have successfully adopted doping strategies which aim to promote TM-O orbital hybridisation in LNMO, through the use of Ge or P, for example. 44,45 Upon Ge doping, Liang et al. observed minimal changes in the pre-edge features (O K-edge) with cycling, while the pre-edge of LNMO changed in intensity.<sup>37</sup> A similar scenario is observed for Mg0.05, which shows consistent pre-edge features throughout cycling with slight variations in relative intensity that reflect subtle changes in the Mn oxidation state (Figure 5.6). Stability in the oxygen electronic environment for Mg0.05 is perhaps unusual given the ability of Mg to promote oxygen redox in other reported cathode materials, where DFT modelling has predicted that LiMq<sub>0.5</sub>Mn<sub>1.5</sub>O<sub>4</sub> should result in irreversible O<sub>2</sub> loss as opposed to oxygen redox.<sup>46</sup> In this work, however, Mg-substituted samples demonstrate good cycling stability even at high Mg concentrations (x = 0.2, Figure C1, Appendix C). Unlike Mg0.05, LNMO and Fe0.05, show pronounced differences in pre-edge features from OCV to cycle 1. This indicates that the changes in the oxygen environment at the surface of LNMO and Fe0.05 are induced during the 1<sup>st</sup> cycle.

We observe that the Mn oxidation state from Mg0.05-OCV to Mg0.05-1 remains stable for Mg0.05, with negligible variation in relative peak intensity (**Figure 5.5j**). Similar stability is observed for LNMO, while Fe0.05 shows an increase in Mn<sup>2+</sup> ions upon cycling (**Figure 5.5h**-i). The higher concentration of Mn<sup>2+</sup> can be correlated to the increased concentration of Mn<sup>3+</sup> in the Fe0.05 structure, as reported in our previous work and observed in the voltage profiles (**Figure 5.2**).<sup>17</sup> The greater Mn<sup>3+</sup> concentration, therefore, contributes to greater Mn<sup>3+</sup>

disproportionation and Mn<sup>2+</sup> deposition on the surface.<sup>4</sup> After 300 cycles, all samples show a similar distribution of Mn oxidation state with a relative increase in Mn<sup>4+</sup> contribution (**Figure 5.5h-i**). Mn<sup>4+</sup> could be formed i) to charge balance loss of active material or ii) as a product of Mn<sup>3+</sup> disproportionation, forming soluble Mn<sup>2+</sup> species alongside MnO<sub>2</sub> at the surface.<sup>4</sup> The similarity in the distribution of Mn<sup>2+</sup>, Mn<sup>3+</sup> and Mn<sup>4+</sup> ions after 300 cycles suggests that the Mn species in all three samples experience similar degradation.

The intensity of the Mn *L*-edge spectral peaks (I/I<sub>0</sub>, without intensity normalisation) for Mg0.05 is almost constant after 300 cycles (**Figure 5.5f**, Appendix C). LNMO and Fe0.05, on the other hand, show an increase in I/I<sub>0</sub> after the 1<sup>st</sup> cycle followed by a significant decrease after 300 cycles (**Figure 5.5d–e**, Appendix C). This is consistent with HAXPES results (**Figure 5.4**), which reveal an increase in peak intensity after the 1<sup>st</sup> cycle attributed to the partial stripping of the surface layer, allowing Mn within the electrode to provide a larger contribution to the observed spectra. The surface layer build-up that occurs after extended cycling reduces the intensity of Mn *L*-edge spectra. The stable surface layer on Mg0.05, on the other hand, is reflected by the stable Mn *L*-edge intensity. Similar changes in I/I<sub>0</sub> are also observed in the respective Ni *L*-edge spectra (**Figure 5.5a-c**), suggesting that both Ni and Mn at the surface LNMO and Fe0.05 become buried under the thickening CEI.

#### 5.5 Contribution of Cell Resistance to Voltage Polarisation

To understand the influence of surface reconstruction and densification on voltage polarisation and cell impedance, LNMO and Mg0.05 were selected for further impedance measurements due to their notable differences in electrochemical performance and surface stability. EIS was performed at several points during long cycling of LNMO and Mg0.05.

The typical Nyquist plot of LNMO under non-blocking conditions shows a high-frequency intercept, with two semicircles in the high- to mid-frequency region, and a tail related to solid-state diffusion in the bulk of the electrode (**Figure 5.7**). Several evaluations of the impedance response in LNMO have demonstrated that the first high-frequency semicircle—visible at all states of charge—is correlated to contact resistance. Corrosion of the current collector by HF leads to the formation of insulating AIF<sub>3</sub>-like species and an increase in contact resistance with cycling.<sup>10,24,47</sup> Such conclusions have been made from 2-electrode half-cell and 3-electrode full-cell setups in LiPF<sub>6</sub>-based electrolytes (LP57 and LP30, respectively).<sup>10,24,47</sup> The high-frequency intercept of this semicircle represents solution resistance,  $R_{sol}$ , accounting for the impedance of the electrolyte. The second semicircle, which is only evident under non-blocking conditions where charge-transfer can occur (**Figure 5.7**), represents a convolution of electrode pore resistance ( $R_{pore}$ ) and charge transfer resistance ( $R_{CT}$ ), the combination of which is referred to as  $R_{cathode}$ .<sup>24</sup>

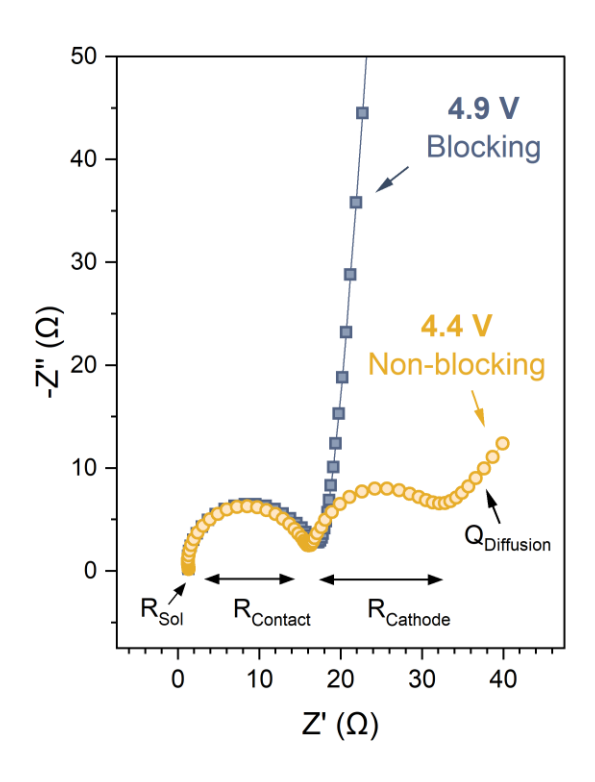


**Figure 5.7:** Exemplar Nyquist plot highlighting  $R_{sol}$ ,  $R_{Contact}$  and  $R_{cathode}$  under blocking (4.9 V) and non-blocking conditions (4.4 V), where the high-frequency semi-circle ( $R_{contact}$ ) is independent of state of charge, whereas the mid-frequency semi-circle ( $R_{cathode}$ ) is dependent on state of charge.

A procedure for the deconvolution of  $R_{pore}$  from  $R_{CT}$  has been outlined in great detail by Pritzl et al.<sup>24</sup> For such deconvolution EIS data must be collected at 2 different points for any given cycle. The first EIS data point is collected under blocking conditions, i.e., where no charge-transfer reactions can take place. For LNMO, blocking conditions can be achieved by measuring EIS in the fully delithiated state (e.g., 4.9 V, **Figure 5.7**). The second EIS data point is collected under non-blocking conditions, i.e., where charge-transfer reactions can take place (e.g., 4.4 V,  $\approx$  10% SOC, where charge transfer resistance is typically low).<sup>24</sup> To allow the system to reach a steady state, the aforementioned potentials were held for 1 h before the EIS measurement. As we observe here, holding the cell at the upper voltage limit, where degradation will be most severe, undoubtedly influences the recorded cell impedance.

In this work, a simplified program was adopted in which EIS for selected cycles was only measured under non-blocking conditions (4.4 V), to minimise the influence of potential hold at high voltage and to ensure reasonable correlation with ex-situ surface characterisation. As such, an equivalent circuit model (ECM) fitting was performed with a simple  $R_{sol}(R_{contact}/Q_{contact})(R_{pore}+CT_{non-blocking}/Q_{pore+CT-non-blocking})Q$  circuit (**Figure 5.8d**), where the first

semicircle represents  $R_{contact}$  and the second semi-circle remains a convolution of  $R_{pore}$  and  $R_{CT}$  and will be referred to as  $R_{cathode}$ . Although the model has been simplified, electrolyte degradation is expected to contribute to both  $R_{pore}$  and  $R_{CT}$ ; fragments from electrolyte degradation will partially block the electrode pores, reducing the effective electrolyte conductivity (increase in  $R_{pore}$ ), and build-up of species at the surface will impede charge transfer (increase in  $R_{CT}$ ). Increases in  $R_{cathode}$  can, therefore, still provide insight into the influence of electrolyte degradation and surface densification on cell impedance and voltage polarisation. Finally, in this work, the tail is modelled using a constant phase element (Q) as opposed to a Warburg element (W), where W represents semi-infinite diffusion. This is because the angle of the tail deviates from the idealised 45° angle. Such deviation in the tail angle indicates restricted (finite), non-ideal diffusion into the electrode.

To first demonstrate the influence of the impedance program on the recorded resistances, the simplified program (EIS@4.4 V for selected cycles) is compared to the detailed program (EIS@4.4 V+4.9 V, every cycle), using LNMO as a case study (see section 5.2.1 for full details). Note that the same ECM is applied to both datasets to compare  $R_{sol}$ ,  $R_{contact}$  and  $R_{cathode}$ .

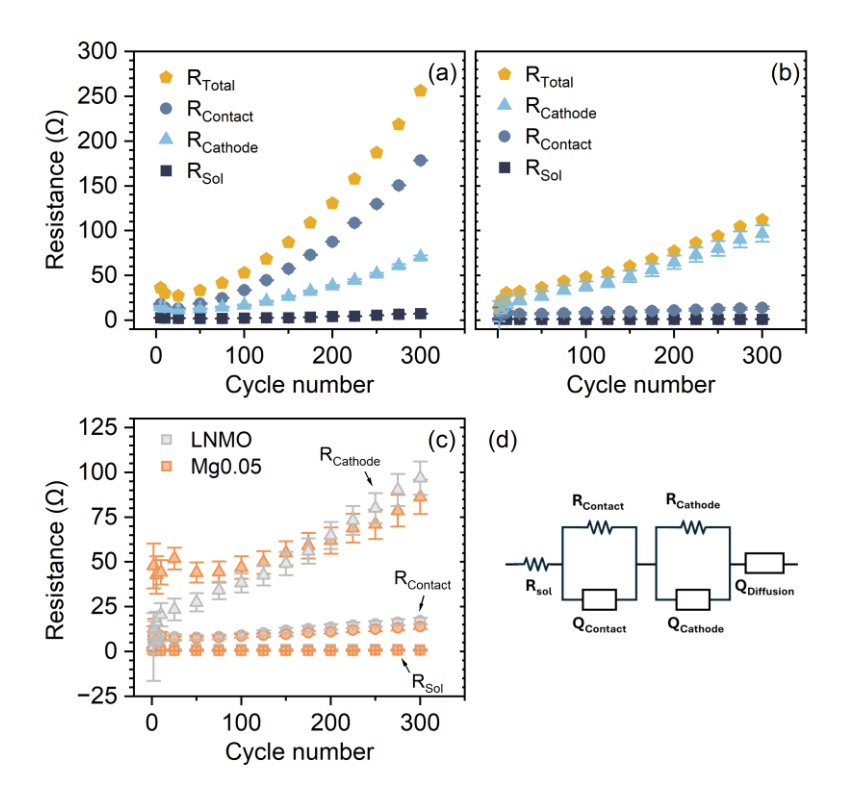


**Figure 5.8:** Evolution of resistances in spinel/Li/Li 3-electrode half cells (50°C, 1C, 3.5–4.9 V) from EIS collected at 4.4 V (discharge) for a) LNMO using the detailed program, b) LNMO using the simplified program and c) a comparison of LNMO and Mg0.05 using the simplified

program, where the evolution of EIS spectra can be found in Appendix C, Figure C3. The detailed program involves measuring EIS at 4.9 V and at 4.4 V (discharge) for every cycle, while the simplified program involves measuring EIS at 4.4 V, only for selected cycles. While the detailed program collects multiple datasets per cycle, only data which corresponds to those collected in the simplified program are presented in (b). EIS fitting was performed using the equivalent circuit model (d).

Comparison between the detailed and simplified programs yields two important observations. The first observation is the influence of program choice on the dominant source of resistance. When using the detailed program, the evolution of resistances correlates well with those previously reported by Pritzl et al.<sup>24</sup> In this case, the dominant source of resistance is R<sub>contact</sub>.  $R_{cathode}$ , on the other hand, increased to a much lesser extent, while  $R_{sol}$  remains constant (Figure 5.8a). In contrast, when the program is simplified to limit time at high voltage, R<sub>cathode</sub> dominates the increases in resistance, while  $R_{contact}$  increases to a lesser extent and, again, R<sub>sol</sub> remains reasonably constant (Figure 5.8b). This observation can be explained by two known implications of high-voltage operation. Firstly, the continual formation of HF in the highvoltage region, which is known to corrode the current collector, will be more problematic when using the detailed program. 10 The longer time spent at high voltage, therefore, contributes to greater R<sub>contact</sub> when compared to the simplified program. Secondly, the CEI layer is also subject to degradation and is known to be unstable in the high-voltage region.<sup>36</sup> The longer time spent at high voltage is therefore expected to cause R<sub>cathode</sub> to be lower when using the detailed program, as the CEI is degraded. Protection of both the current collector and the CEI from corrosion at high voltage, when using the simplified program, therefore causes inverse contributions to resistance; lowering  $R_{contact}$  while allowing  $R_{cathode}$  to have a more notable contribution.

The second observation is that the magnitude of total resistance at selected cycles is greater for the detailed program. In this regard, we acknowledge the limitations of using a simplified programme and how protection of the system from the impacts of high-voltage operation will ultimately lead to lower reported resistances. However, we also demonstrate the importance of matching the time scale of the impedance program to the time scale used for *ex-situ* characterisation.

The simplified program was employed to track and compare the evolution of  $R_{sol}$ ,  $R_{contact}$ , and  $R_{Cathode}$  for LNMO and Mg0.05 (**Figure 5.8c**). Both samples showed relatively low and comparable  $R_{sol}$  and  $R_{contact}$ . However, notable differences in  $R_{Cathode}$  are observed over the 300 cycles. During the first 100 cycles, Mg0.05 shows a higher  $R_{Cathode}$  than LNMO, yet the magnitude of  $R_{cathode}$  for Mg0.05 remains reasonably constant. With continued cycling,

however, Mg0.05 experiences a steady increase in  $R_{cathode}$ . LNMO, on the other hand, shows a much lower  $R_{Cathode}$  during the first 100 cycles. However, unlike Mg0.05, LNMO experiences an increase in  $R_{cathode}$ , which continues throughout cycling. The rate at which  $R_{cathode}$  increases is greater for LNMO. EIS measurements correlate well with ex-situ HAXPES characterisation, where Mg0.05 showed a stable surface layer during the initial cycles followed by a marginal increase in surface layer thickness after 300 cycles. Higher initial  $R_{cathode}$  for Mg0.05, therefore, likely results from the denser CEI that forms at the surface before cycling. However, the protective nature of this surface is highlighted by the stability in the  $R_{cathode}$  during the first 100 cycles, after which point the rise in cell impedance correlates well with the slight thickening of the CEI observed for Mg0.05-300. In contrast, the unstable surface layer observed on LNMO during initial cycling leaves the surface subject to continual degradation, and with continued degradation at the surface comes the continual increase in  $R_{cathode}$ .

#### 5.6 Conclusions

This work aims to reveal the improved stability of the cation-substituted LNMO cathode surfaces, as previously hypothesised in the literature. Fe and Mg are employed as earth-abundant substituents, offering varying levels of improvement to the capacity retention of LNMO under accelerated ageing conditions; i.e., marginal improvements for Fe (88%) and more notable improvements for Mg0.05 (94%). The rate of degradation for all samples was most severe during initial cycling (cycles 1–50), and while Mg—and to some extent Fe—can initially slow the rate of degradation, all samples experience similar degradation in later cycles (cycles 50–300). Reduced degradation during initial cycles for Mg0.05 has many possible origins and in this work, we demonstrate the improved stability of the Mg0.05 surface to be one of the causes for improvement.

Changes in the oxygen electronic structure at the surface, and the creation of new active Mn<sup>4+</sup> sites during initial cycling, suggest that LNMO and Fe0.05 likely experience some bulk/surface structural arrangement—both of which are suppressed for Mg0.05. Improved surface structure for Mg0.05 may be related to an increased concentration of Li-site defects, which can inhibit TM migration. With longer cycling, however, all samples experience an increase in Mn<sup>4+</sup> ions with cycling (sXAS); either to account for the loss of active material or from Mn<sup>3+</sup> disproportionation, which ultimately leads to loss of Mn<sup>3+/4+</sup>-related capacity. Loss of Ni<sup>2+/4+</sup> capacity is also observed, alongside voltage polarisation and can be explained by differences in CEI stability and composition.

The Mg0.05 surface, rich in C–O functionality, remains stable during the first 100 cycles, allowing for negligible changes in cell resistance and voltage polarisation. The carbonate-rich CEI on LNMO and Fe0.05, on the other hand, is shown to be unstable, allowing for continued

degradation, surface densification and increases in cell resistance. While this suggests that the C–O enriched surface allows for improved stability, the origin of C–O enrichment remains unclear. However, such findings open possible avenues for advanced CEI design.

This work also highlights that time spent at high voltage dominates recorded contributions to cell impedance, where increased time at high voltage leads to high contact resistance and lower cathode resistance, likely due to HF corrosion of both the current collector and CEI. The significant increase in contact resistance that results from high voltage operation highlights the need for alternative corrosion-resistant current collectors. In this work, however—in which time at high voltage was limited—cathode resistance dominates.

Here, we acknowledge the limitations of the controlled nature of this study, where the use of half-cell testing and limited time at high voltage mask the true effects of high-voltage degradation and TM dissolution. While the internal comparison clearly demonstrates the improved surface stability of Mg0.05, future work should aim to evaluate performance and surface stability under 'real-world' conditions (i.e., incorporating full-cell testing, slower C-rates, and potential holds in the charged state).

#### 5.7 References

- B. E. Murdock, J. Cen, A. G. Squires, S. R. Kavanagh, D. O. Scanlon, L. Zhang and N. Tapia-Ruiz, *Adv. Mater.*, 2024, **36**, 2400343.
- G. Liang, Z. Wu, C. Didier, W. Zhang, J. Cuan, B. Li, K. Ko, P. Hung, C. Lu, Y. Chen, G. Leniec, S. M. Kaczmarek, B. Johannessen, L. Thomsen, V. K. Peterson, W. K. Pang and Z. Guo, *Angew. Chemie*, 2020, **132**, 10681–10689.
- 3 J. Liu and A. Manthiram, *J. Phys. Chem. C*, 2009, **113**, 15073–15079.
- 4 L. Balducci, H. Darjazi, E. Gonzalo, R. Cid, F. Bonilla and F. Nobili, *ACS Appl. Mater. Interfaces*, 2023, **15**, 55620–55632.
- 5 D. W. Shin, C. A. Bridges, A. Huq, M. P. Paranthaman and A. Manthiram, *Chem. Mater.*, 2012, **24**, 3720–3731.
- 6 I. Azcarate, W. Yin, C. Méthivier, F. Ribot, C. Laberty-Robert and A. Grimaud, *J. Electrochem. Soc.*, 2020, **167**, 080530.
- G. Liang, V. K. Peterson, K. W. See, Z. Guo and W. K. Pang, *J. Mater. Chem. A*, 2020, 8, 15373–15398.
- 8 N. P. W. Pieczonka, Z. Liu, P. Lu, K. L. Olson, J. Moote, B. R. Powell and J. H. Kim, *J. Phys. Chem. C*, 2013, **117**, 15947–15957.

- 9 J. C. Hestenes, J. T. Sadowski, R. May and L. E. Marbella, *ACS Mater. Au*, 2023, **3**, 88–101.
- M. Lin, L. Ben, Y. Sun, H. Wang, Z. Yang, L. Gu, X. Yu, X. Q. Yang, H. Zhao, R. Yu, M. Armand and X. Huang, *Chem. Mater.*, 2015, 27, 292–303.
- B. L. D. Rinkel, D. S. Hall, I. Temprano and C. P. Grey, *J. Am. Chem. Soc.*, 2020, **142**, 15058–15074.
- 12 Y. Liao, H. Zhang, Y. Peng, Y. Hu, J. Liang, Z. Gong, Y. Wei and Y. Yang, *Adv. Energy Mater.*, 2024, **14**, 2304295.
- U. Nisar, J. Bansmann, M. Hebel, B. Reichel, M. Mancini, M. Wohlfahrt-Mehrens, M. Hölzle and P. Axmann, *Chem. Eng. J.*, DOI:10.1016/j.cej.2024.152416.
- 14 H. Wang, X. Li, F. Li, X. Liu, S. Yang and J. Ma, *Electrochem. commun.*, 2021, **122**, 106870.
- D. Pritzl, A. E. Bumberger, M. Wetjen, J. Landesfeind, S. Solchenbach and H. A. Gasteiger, *J. Electrochem. Soc.*, 2019, **166**, A582–A590.
- N. N. Intan, K. Klyukin and V. Alexandrov, *J. Electrochem. Soc.*, 2018, **165**, A1099–A1103.
- 17 D. Zhao, S. Song, X. Ye, P. Wang, J. Wang, Y. Wei, C. Li, L. Mao, H. Zhang and S. Li, *Appl. Surf. Sci.*, 2019, **491**, 595–606.
- J. Landesfeind, D. Pritzl and H. A. Gasteiger, J. Electrochem. Soc., 2017, 164, A1773– A1783.
- 19 T. L. Lee and D. A. Duncan, *Synchrotron Radiat. News*, 2018, **31**, 16–22.
- 20 A. Tornheim and D. C. O'Hanlon, *J. Electrochem. Soc.*, 2020, **167**, 110520.
- 21 P. Jehnichen, K. Wedlich and C. Korte, Sci. Technol. Adv. Mater., 2019, 20, 1–9.
- W. Bao, W. Yao, Y. Li, B. Sayahpour, B. Han, G. Raghavendran, R. Shimizu, A. Cronk, M. Zhang, W. Li and Y. S. Meng, *Energy Environ. Sci.*, 2024, 4263–4272.
- 23 Z. Lin, T. Liu, X. Ai and C. Liang, *Nat. Commun.*, 2018, **9**, 8–12.
- 24 H. Arai, K. Sato, Y. Orikasa, H. Murayama, I. Takahashi, Y. Koyama, Y. Uchimoto and Z. Ogumi, *J. Mater. Chem. A*, 2013, **1**, 10442–10449.
- 25 J. Ma, P. Hu, G. Cui and L. Chen, *Chem. Mater.*, 2016, **28**, 3578–3606.

- 26 X. Chen, X. Wang and D. Fang, *Fullerenes Nanotub. Carbon Nanostructures*, 2020, **28**, 1048–1058.
- 27 S. Sarkar, S. Garain, D. Mandal and K. K. Chattopadhyay, *RSC Adv.*, 2014, **4**, 48220–48227.
- 28 I. A. Shkrob and D. P. Abraham, *J. Phys. Chem. C*, 2016, **120**, 15119–15128.
- 29 S. Dalavi, M. Xu, B. Knight and B. L. Lucht, *Electrochem. Solid-State Lett.*, 2011, **15**, A28.
- 30 S. Roberts, L. Chen, B. Kishore, C. E. J. Dancer, M. J. H. Simmons and E. Kendrick, *J. Colloid Interface Sci.*, 2022, **627**, 427–437.
- E. Markevich, G. Salitra, K. Fridman, R. Sharabi, G. Gershinsky, A. Garsuch, G. Semrau, M. A. Schmidt and D. Aurbach, *Langmuir*, 2014, **30**, 7414–7424.
- E. Björklund, C. Xu, W. M. Dose, C. G. Sole, P. K. Thakur, T.-L. Lee, M. F. L. De Volder,C. P. Grey and R. S. Weatherup, *Chemsitry Mater.*, 2022, 34, 1987–2494.
- 33 Y. H. Liu, W. C. Chen, C. H. Hsueh and C. L. Hsu, *Mater. Today Chem.*, 2022, **25**, 100934.
- 34 J. Syzdek, M. Marcinek and R. Kostecki, *J. Power Sources*, 2014, **245**, 739–744.
- R. Younesi, A. S. Christiansen, R. Scipioni, D.-T. Ngo, S. B. Simonsen, K. Edström, J. Hjelm and P. Norby, *J. Electrochem. Soc.*, 2015, **162**, A1289–A1296.
- 36 S. Klein, P. Harte, S. van Wickeren, K. Borzutzki, S. Röser, P. Bärmann, S. Nowak, M. Winter, T. Placke and J. Kasnatscheew, *Cell Reports Phys. Sci.*, , DOI:10.1016/j.xcrp.2021.100521.
- 37 T. Yoon, J. Soon, T. Jin, J. Heon and S. M. Oh, *J. Power Sources*, 2021, **503**, 230051.
- 38 D. Ruan, Z. Cui, J. Fan, D. Wang, Y. Wu and X. Ren, *Chem. Sci.*, 2024, **15**, 4238–4274.
- 39 E. M. Erickson, W. Li, A. Dolocan and A. Manthiram, *ACS Appl. Mater. Interfaces*, 2022, **12**, 16451–16461.
- 40 F. Zou, Z. Cui, H. C. Nallan, J. G. Ekerdt and A. Manthiram, *ACS Appl. Energy Mater.*, 2021, **4**, 13297–13306.
- W. N. Wang, D. Meng, G. Qian, S. Xie, Y. Shen, L. Chen, X. Li, Q. Rao, H. Che, J. Liu,
  Y. S. He, Z. F. Ma and L. Li, *J. Phys. Chem. C*, 2020, 124, 27937–27945.

- 42 F. Frati, M. O. J. Y. Hunault and F. M. F. De Groot, *Chem. Rev.*, 2020, **120**, 4056–4110.
- 43 R. Qiao, Y. De Chuang, S. Yan and W. Yang, *PLoS One*, 2012, **7**, 3–8.
- 44 X. Liu, M. Maffre, D. Tie, N. P. Wagner, N. C. Félix, R. Azmi, K. Stokes, P. E. Vullum, J. Bailly, S. Pal, G. Evans, M. Buga, M. Hahlin, K. Edström, S. Clark and A. Vlad, J. Electrochem. Soc., 2023, 170, 100527.
- 45 X. Li, J. Wang, S. Zhang, L. Sun, W. Zhang, F. Dang, H. J. Seifert and Y. Du, *ACS Omega*, 2021, **6**, 21255–21264.
- 46 T. Fu, Y. Li, Z. Yao, T. Guo, S. Liu, Z. Chen, C. Zheng and W. Sun, *Small*, 2024, 2402339.
- 47 G. Liang, E. Olsson, J. Zou, Z. Wu, J. Li, C.-Z. Lu, A. M. D'Angelo, B. Johannessen, L. Thomsen, B. Cowie, V. K. Peterso, Q. Cai, W. K. Pang and Z. Guo, *Angew. Chemie Int. Ed.*, 2022, 61, e202201969.
- 48 X. M. Shi, E. Watanabe, M. Okubo and A. Yamada, *Chem. Mater.*, 2020, **32**, 7181–7187.
- 49 C. Bizot, M. A. Blin, P. Guichard, P. Soudan, J. Gaubicher and P. Poizot, *Electrochem. commun.*, DOI:10.1016/j.elecom.2021.107008.
- 50 P. Iurilli, C. Brivio and V. Wood, *J. Power Sources*, 2021, **505**, 229860.

# **Chapter 6 | Conclusions**

The goal of this PhD thesis was to progress the development of advanced cathode materials for LIBs, towards a more diverse battery supply chain, through a deep understanding of their structure-property-performance relationships. Therefore, it first became necessary to evaluate the criticality and sustainability of state-of-the-art cathodes as well as several other advanced cathode materials in order to select a cathode material for further investigations that could help distribute the demand for battery metals across several elements (Chapter 2).

Chapter 2 found that state-of-the-art NMC materials—which are increasingly rich in Ni—present a future supply risk for Ni on top of the existing Li and Co supply risk, due to the large demand for NMC materials. To reduce supply risk across the battery landscape, it, therefore, becomes important to add more diversity to the array of state-of-the-art cathode materials on offer by developing materials that possess a lower content of Li, Ni and Co. To this end, LFP and LMFP are (re)gaining popularity, with significant industry and academic research dedicated to their advancements. LNMO, on the other hand, represents an underdeveloped cathode material which is not only Co-free but also low in Li and Ni. Reductions in material demand offered by LNMO extend beyond the cathode material since its high voltage means that fewer battery cells are required to produce a pack with the same energy as its lower-voltage counterparts (e.g., NMC).

Despite the many benefits of LNMO—including good energy density (650 Wh kg<sup>-1</sup>), high voltage, high rate performance and low material demand—its commercialisation is currently limited by its poor cycling stability. The remainder of this thesis was, therefore, focussed on understanding and improving the capacity degradation of LNMO, using cationic substitution as the method of improvement to mitigate the need for additional components (e.g., surface coatings), whilst potentially allowing further reduction of Ni content. As such, Ni was substituted with varying amounts of Fe and Mg—LiNi<sub>0.5</sub>Mn<sub>1.5</sub>O<sub>4</sub> (LNMO), LiNi<sub>0.5-x</sub>Fe<sub>x</sub>Mn<sub>1.5</sub>O<sub>4</sub> (Fex) and LiNi<sub>0.5-x</sub>Mg<sub>x</sub>Mn<sub>1.5</sub>O<sub>4</sub> (Mgx) (x = 0.05, 0.1, 0.15 and 0.2)—which were chosen as earth-abundant substituents. While Fe- and Mg-substitution have been shown to improve capacity retention in the literature, a clear and systematic understanding of the structural properties that allow for such improvements—and their origin—was lacking. The overarching research questions from which Chapters 4–5 are constructed were, therefore, what is the influence of substituent type/concentration on 4) the structure and 5) the surface?

Chapter 4 presents an in-depth XRD/ND investigation into the structure of LNMO, Mgx and Fex (x = 0.05, 0.1, 0.15 and 0.2). Of particular interest was determining which structural sites

the substituents occupied—the octahedral TM site or the tetrahedral Li site, thus creating Lisite defects—and the influence on electrochemical performance. Through the structural investigations presented in Chapter 4, the concentration of Li-site defects was shown to increase with substituent concentration for both Fe and Mg. Mg, however, showed higher relative Li-defect concentrations indicating a site preference of Mg for the Li site. This conclusion was made from Li site occupancy factors, obtained from combined Rietveld refinement against both neutron and X-ray diffraction data. However, from refinements alone, we highlight the inability to distinguish whether these Li-site defects originated from the substituents themselves (M<sub>Li</sub> defects) or simply from Li-Ni antisite mixing (Ni<sub>Li</sub> defects). Nonetheless, complimentary computational investigations suggest that Mg<sub>Li</sub> and Ni<sub>Li</sub> are preferred in Mg-substituted and Fe-substituted samples, respectively, due to their lower formation energies.

A further limitation of this work is the subtle improvement to the fit against experimental data offered when incorporating Li-site defects. Extensive analysis of the refinement results, however, provides several indications for their existence. For example, by analysing the implications of charge distribution and the correlation of Li-site defects and Li-containing impurity phase formation, we were able to rule out refinements without Li-site defects included. Further experimental techniques, such as Mössbauer spectroscopy to track the location of Fe, could therefore enhance the existing evidence provided in this work.

Li-site defects induced the formation of a Li-rich impurity phase ( $Li_2MO_3$ , M = Ni or Mn). This led to a loss of cations from the structure, resulting in an increase in [Mn<sup>3+</sup>]—which was otherwise unexpected for Mg-substituted samples due to the identical charge of Ni<sup>2+</sup> and Mg<sup>2+</sup>. However, while Mn<sup>3+</sup> increased with substituent concentration, we observed no significant effect on either rate performance or cycling stability, despite the positive and negative impacts of Mn<sup>3+</sup> that are reported on rate performance and cycling stability, respectively. Increases in the capacity related to Mn<sup>3+</sup> were counteracted by a loss in the capacity related to Ni substitution of Ni with Fe and Mg leading to a significant overall loss of capacity at high concentrations which means that Fe/Mg-substitution cannot be used to further reduce the Ni content beyond x = 0.05. Capacity retention, on the other hand, is largely independent of substituent concentration.

Given the limited improvements in performance offered by Fe/Mg at room temperature, when using a cycling rate and voltage window which can limit the extent degradation (1C, 3.5–4.9 V, 300 cycles), Chapter 5 was focussed on evaluating the performance under conditions that accelerate electrolyte degradation and enhance surface reactivity (50°C). This allowed the influence of Fe/Mg (x = 0.05) on surface degradation to be revealed. As expected, the cycling

stability of LNMO decreases at elevated temperatures, with Fe0.05 showing mild performance improvements. Mg0.05, on the other hand, showed notable improvements. Improved stability at the surface was shown to contribute to the improved capacity retention in early cycles (1–50), where Mg0.05 forms a surface layer at OCV which is rich in C–O functionality and resistant to HF corrosion at high voltages. Mg0.05 also exhibited enhanced O2*p*-TM3*d* hybridisation and a more stable electronic environment around oxygen. We hypothesise that this is correlated to the presence of MgLi site defects, as characterised in Chapter 4, which can prevent surface reconstruction.

In evaluating the cell resistances, Chapter 5 reveals the importance of matching the time scale of the EIS measurements to the time scale at which electrodes used for *ex-situ* surface characterisation are cycled. This is because longer time spent at high voltage can lead to dissolution of the surface layer, and corrosion of the current collector, by HF formed during high-voltage operation. This not only increases contact resistance, as the current collector becomes corroded, but also reduces cathode resistance, as the surface layer dissolves. While it is important to understand how these cathodes respond to severe high-voltage operation, similar experimental time scales are preferred if a good correlation between the recorded resistances and the *ex-situ* surface characterisation is required.

The insights into the bulk structure, surface and electrochemical performance of Fe- and Mg-substituted cathodes presented throughout Chapters 4–5, have successfully enabled a comparison of the structure-surface-performance relationships that exist in LNMO, Fex and Mgx cathodes. This has allowed the identification of both bulk and surface structures that can enable improved capacity retention of Mg-substituted LNMO (1C, 3.5–4.9 V), namely MgLi defects and the formation corrosion-resistant surface layer rich in C–O functionality, which likely originate for PEO-like moieties. The findings presented in this work not only successfully answer the original research questions but also expose new and exciting avenues for future research.

# **Chapter 7 | Future Work**

As highlighted in Chapter 2, the increased demand for LIBs intenisifies the criticality of the metals used in their cathodes. A unified effort across several important players will be required to best manage resources. Given the lead time of technological readiness, material development and commercialisation strategies would greatly benefit from a deep understanding of the potential impact new cathode materials can have on supply risk, when used alongside state-of-the-art cathode materials. In addition to models which project supply and demand from current data, a retrospective approach could be more beneficial for creating a material development strategy which allows optimal use of resources. For example, based on the anticipated future supply, retrospective models may be able to determine what share of the market different cathodes—both new and existing—should take in order to limit supply risk. From such analysis, funding can be directed to accelerate the commercialisation of the materials that will be most influential in ensuring a more sustainable battery supply chain. Such decisions will not only be valuable in informing academic research, but also for developing a unified global strategy for resource management at a company/policy level.

Throughout Chapters 4 and 5, the cycling procedures adopted inadvertently protected the studied cathodes from the true impacts of high-voltage operation. Future work should therefore investigate similar samples using a range of cycling procedures and cell setups including slow rate cycling (< 1C), to observe whether Fe/Mg can reduce the detrimental impacts associated with longer time spent at high voltage, and full-cell testing, to understand the influence of Fe/Mg on the extent of Mn<sup>2+</sup> dissolution. Such full cell testing would be particularly valuable when paired with a graphite anode where the impacts of Mn dissolution should be obvious. Further HAXPES characterisation of *ex-situ* anode materials can provide insight into the dissolution and deposition of metals, originating from the cathode, onto the anode surface.

As demonstrated in this work, the exact location of substituents is crucial to understanding their working mechanisms. Such analysis, however, is challenging with the techniques currently available. Having said that, this work established a strong correlation between Li-site defects and the concentration of the Li-containing impurity phase. While determining the presence of Li-site defects in this work required advanced neutron diffraction characterisation, this could build the foundations for a simple and more streamlined approach to determining the concentration of Li-site defects in substituted LNMO cathodes from X-ray diffraction data alone, by refining the wt. % of the Li-based impurity. This approach, however, requires the correlation to be demonstrated on a greater number of samples, varying in composition and

synthetic method. In addition, the development of new characterisation techniques that allow the easy identification of the substituent site location will be beneficial to this field of research.

Given the stability enabled by the surface layer formed on Mg0.05 in Chapter 5, it would be valuable to identify film-forming additives that can produce a CEI with a similar composition, which is shown to be resistant to corrosion at high voltage. Such film-forming additives can not only be implemented alongside LNMO cathodes, but also to other cathode materials that are subjected to high voltages. Such avenues of research could be further enhanced by a deeper understanding of the CEI formation mechanism that occurs at the Mg-substituted surface that allows the formation of a CEI rich in C–O functionality, which contrasted with the carbonate-rich surface formed on the unsubstituted and Fe-substituted materials.

Limited improvements in performance offered in this work are suspected to have some synthesis dependence—particularly in the case of Fe-substituted LNMO which showed comparable performance to LNMO at both room temperature and elevated temperatures. This may be a result of the particle morphology which resembles that of a SC morphology, which is known to show better resistance to particle fracture, therefore reducing the amount of electrolyte degradation at newly exposed surfaces. Understanding the effect of substitution on particle fracture in both PC and SC-type morphologies and their correlation to electrolyte degradation. Such analysis could be combined with techno-economic and life cycle analysis to determine the optimal combination of composition, particle morphology, materials cost and processing cost.

Finally, the development of alternative current collectors that are resistant to corrosion at high voltage would not only be valuable but a necessity for the successful commercialisation of LNMO-based cathodes. Given the low cost and availability of AI, however, alternatives should aim to be cost-competitive while also avoiding the use of scarce/critical materials.

# Appendix A | Supporting Experimental Data for Chapter 4

#### Estimated material intensity (kg kWh<sup>-1</sup>)

The amount of cathode required to produce 1 kWh of energy at the material level (i.e., only considering the mass of the cathode itself) for different cathodes was estimated based on their practical energy densities using Equation A1 (kg<sub>cathode</sub> kWh<sup>-1</sup>): NMC622 (650 Wh kg<sup>-1</sup>), NMC811 (700 Wh kg<sup>-1</sup>), LNMO (610 Wh kg<sup>-1</sup>). The mass of each element contained in each kg<sub>cathode</sub> was then calculated by Equation A2. The mass of each element required per kWh can then be calculated from Equation A3 (kg<sub>element</sub> kWh<sup>-1</sup>). Finally, to estimate the amount of anode required to balance the charge provided by the cathode, it is first necessary to calculate the capacity ratio between the cathode (Q<sub>cathode</sub>) and the anode (Q<sub>anode</sub>). This can then be multiplied by the amount of cathode required, as shown in Equation A4, to determine kg<sub>anode</sub> kWh<sup>-1</sup>. This calculation provides a rough estimate of the material intensity. The actual material intensity will be higher per kWh due to the presence of inactive components which add additional mass.

$$kg_{cathode} kWh^{-1} = \frac{1000}{Wh kg^{-1}}$$
 (A1)

$$kg_{element} kg_{cathode}^{-1} = \frac{mol \, ratio_{element} \cdot Mw_{element}}{Mw_{cathode}}$$
 (A2)

$$kg_{element} kWh^{-1} = kg_{element} kg_{cathode}^{-1} \cdot kg_{cathode} kWh^{-1}$$
 (A3)

$$kg_{anode} kWh^{-1} = \frac{Q_{anode}}{Q_{cathode}} \cdot kg_{cathode} kWh^{-1}$$
 (A4)

#### **Supporting Figures**

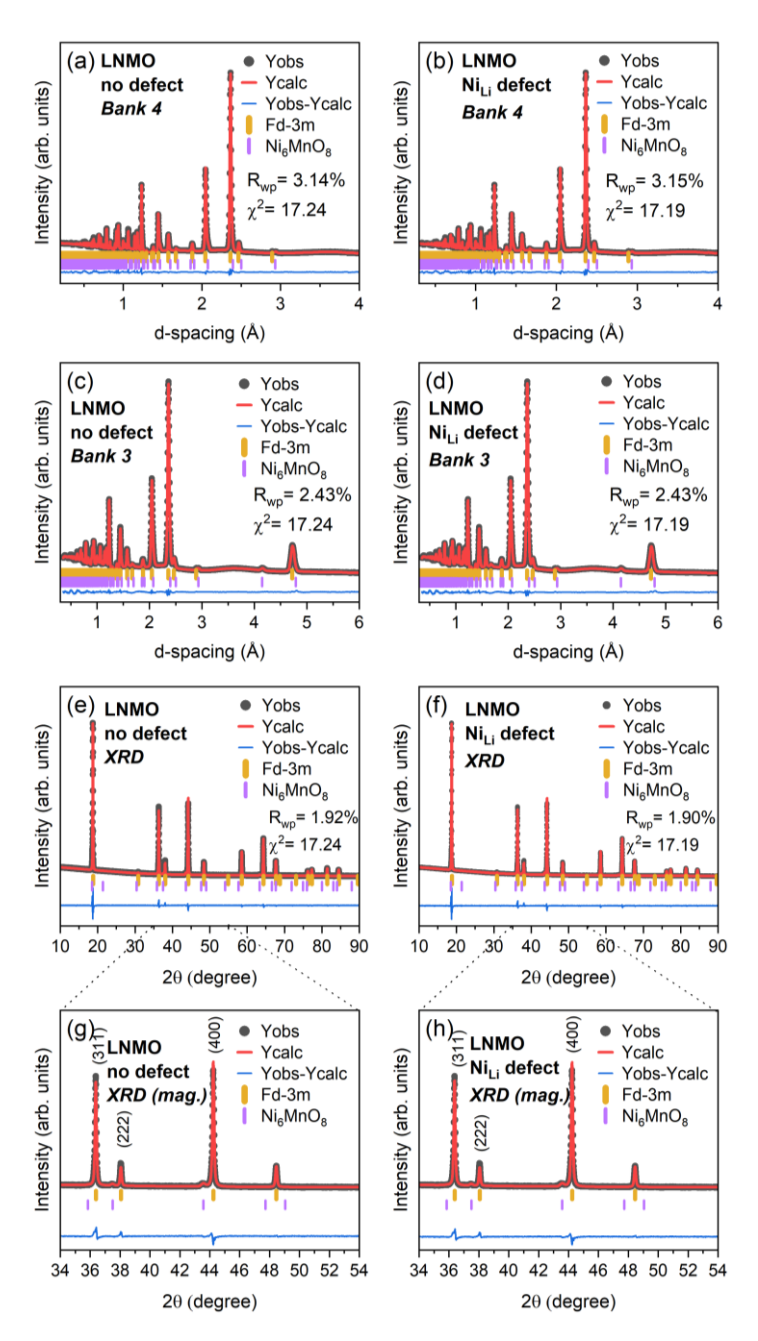


**Figure A1.** Combined ND-XRD Rietveld refinement against data collected at room temperature for LNMO. Structure models are based on the  $Fd\overline{3}m$  space group and consider a Ni<sub>6</sub>MnO<sub>8</sub> impurity and the following Li-site defects (A<sub>Li</sub>): no defect (a, c, e and g); and Ni<sub>Li</sub> defect (b, d, f and h). ND refinements of bank 4 (a–b) and bank 3 (c–d) show no change with defect scenario. XRD data (e–h) show a very subtle increase in the calculated (311) peak intensity when incorporating Ni<sub>Li</sub> defects, as highlighted in the magnified plots (g–h).

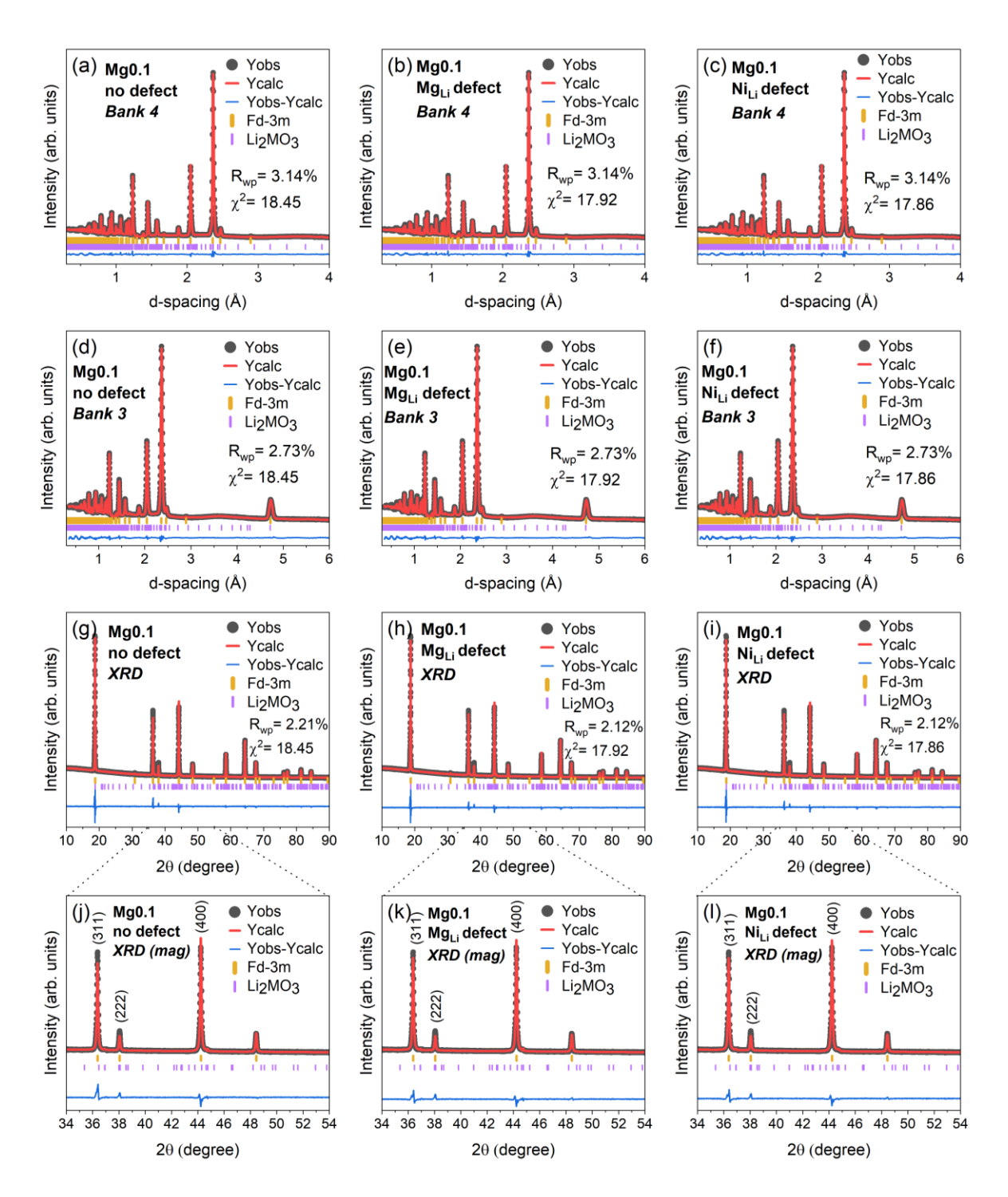


**Figure A2.** Combined ND-XRD Rietveld refinement against data collected at room temperature for Mg0.1. Structure models are based on the  $Fd\overline{3}m$  space group and consider a Li<sub>2</sub>MO<sub>3</sub> impurity (M = Mn and Ni) and the following Li-site defects (A<sub>Li</sub>): no defect (a, d, g and j); Mg<sub>Li</sub> defect (b, e, h and k); and Ni<sub>Li</sub> defect (c, f, i and l). ND refinements of bank 4 (a–c) and bank 3 (d–f) show no change with defect scenario. XRD data (g–l) show an increase in the calculated (311) peak intensity when incorporating Mg<sub>Li</sub>/Ni<sub>Li</sub> defects, as highlighted in the magnified plots (j–l). Peak intensities, however, do not alter significantly between Ni<sub>Li</sub> and Mg<sub>Li</sub> scenarios (k–l).

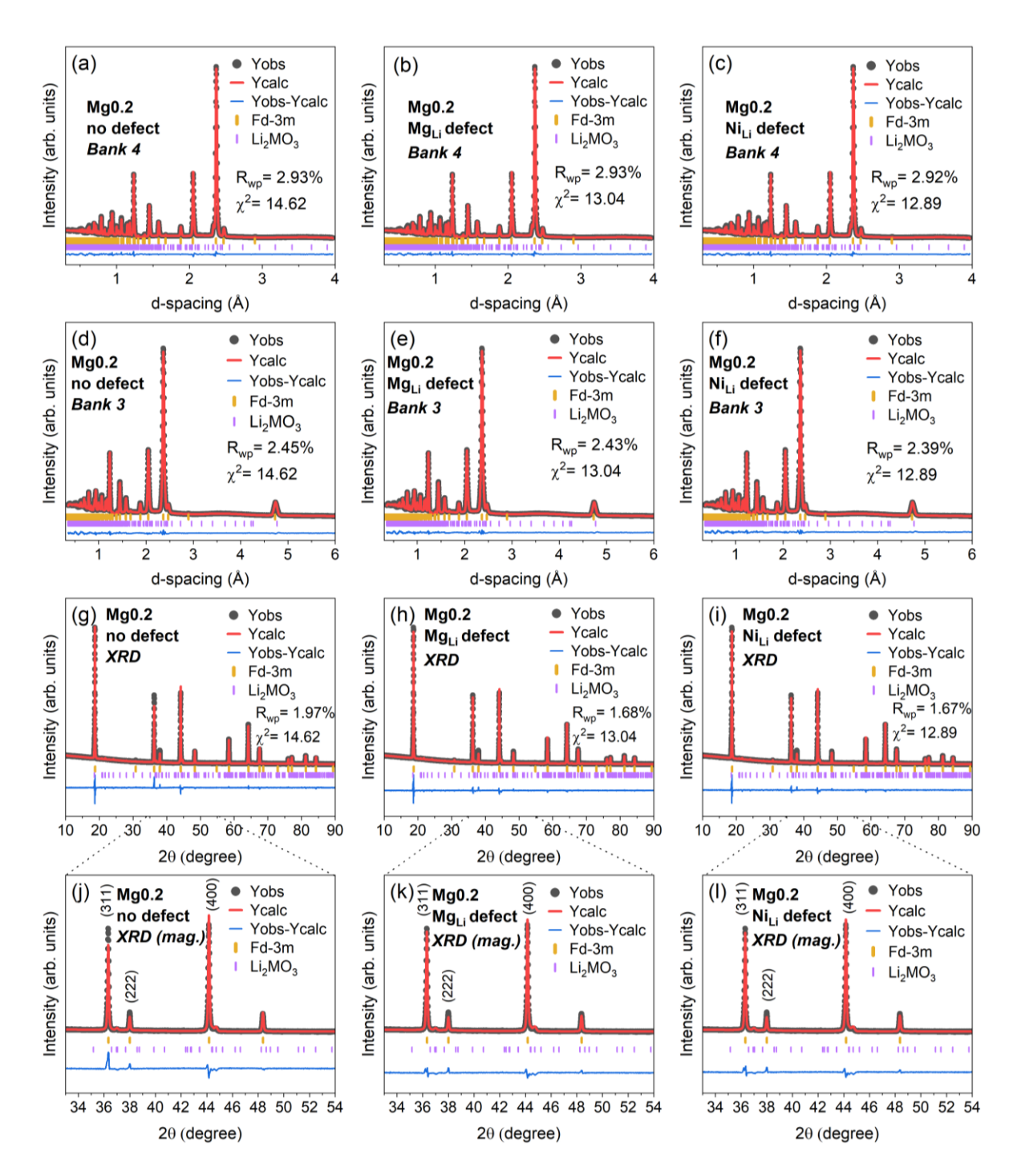


**Figure A3.** Combined ND-XRD Rietveld refinement against data collected at room temperature for Mg0.2. Structure models are based on the  $Fd\overline{3}m$  space group and consider a Li<sub>2</sub>MO<sub>3</sub> impurity (M = Mn and Ni) and the following Li-site defects (A<sub>Li</sub>): no defect (a, d, g and j); Mg<sub>Li</sub> defect (b, e, h and k); and Ni<sub>Li</sub> defect (c, f, i and l). ND refinements of bank 4 (a–c) and bank 3 (d–f) show no change with defect scenario. XRD data (g–l) show an increase in the calculated (311) peak intensity when incorporating Mg<sub>Li</sub>/Ni<sub>Li</sub> defects, as highlighted in the magnified plots (j–l). Peak intensities, however, do not alter significantly between Ni<sub>Li</sub> and Mg<sub>Li</sub> scenarios (k–l).

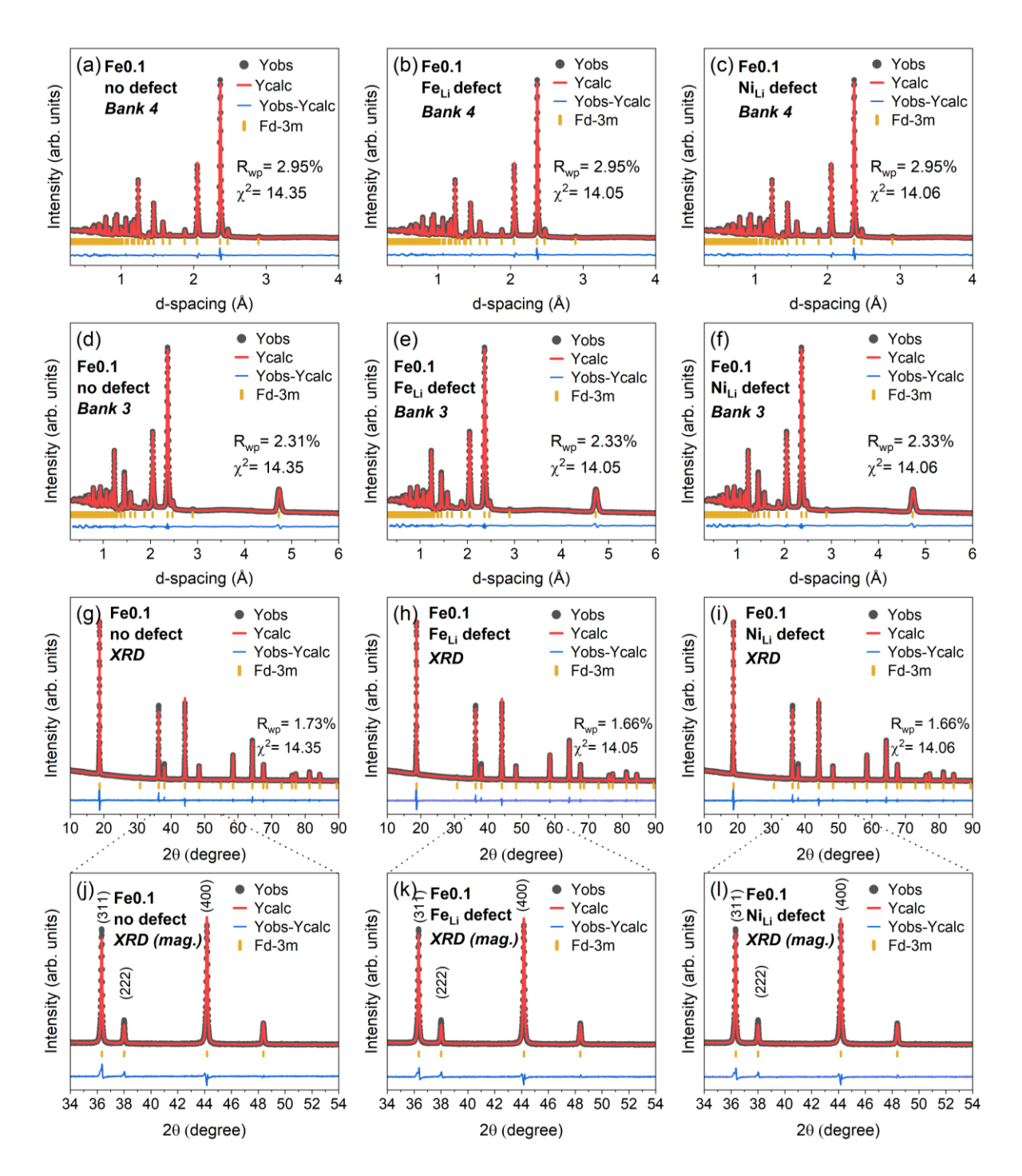


**Figure A4.** Combined ND-XRD Rietveld refinement against data collected at room temperature for Fe0.1. Structure models are based on the  $Fd\overline{3}m$  space group and consider the following Li-site defects (A<sub>Li</sub>): no defect (a, d, g and j); Fe<sub>Li</sub> defect (b, e, h and k); and Ni<sub>Li</sub> defect (c, f, i and l). ND refinements of bank 4 (a–c) and bank 3 (d–f) show no change with defect scenario. XRD data (g–l) show an increase in the calculated (311) peak intensity when incorporating Fe<sub>Li</sub>/Ni<sub>Li</sub> defects, as highlighted in the magnified plots (j–l). Peak intensities, however, do not alter significantly between Ni<sub>Li</sub> and Fe<sub>Li</sub> scenarios (k–l).

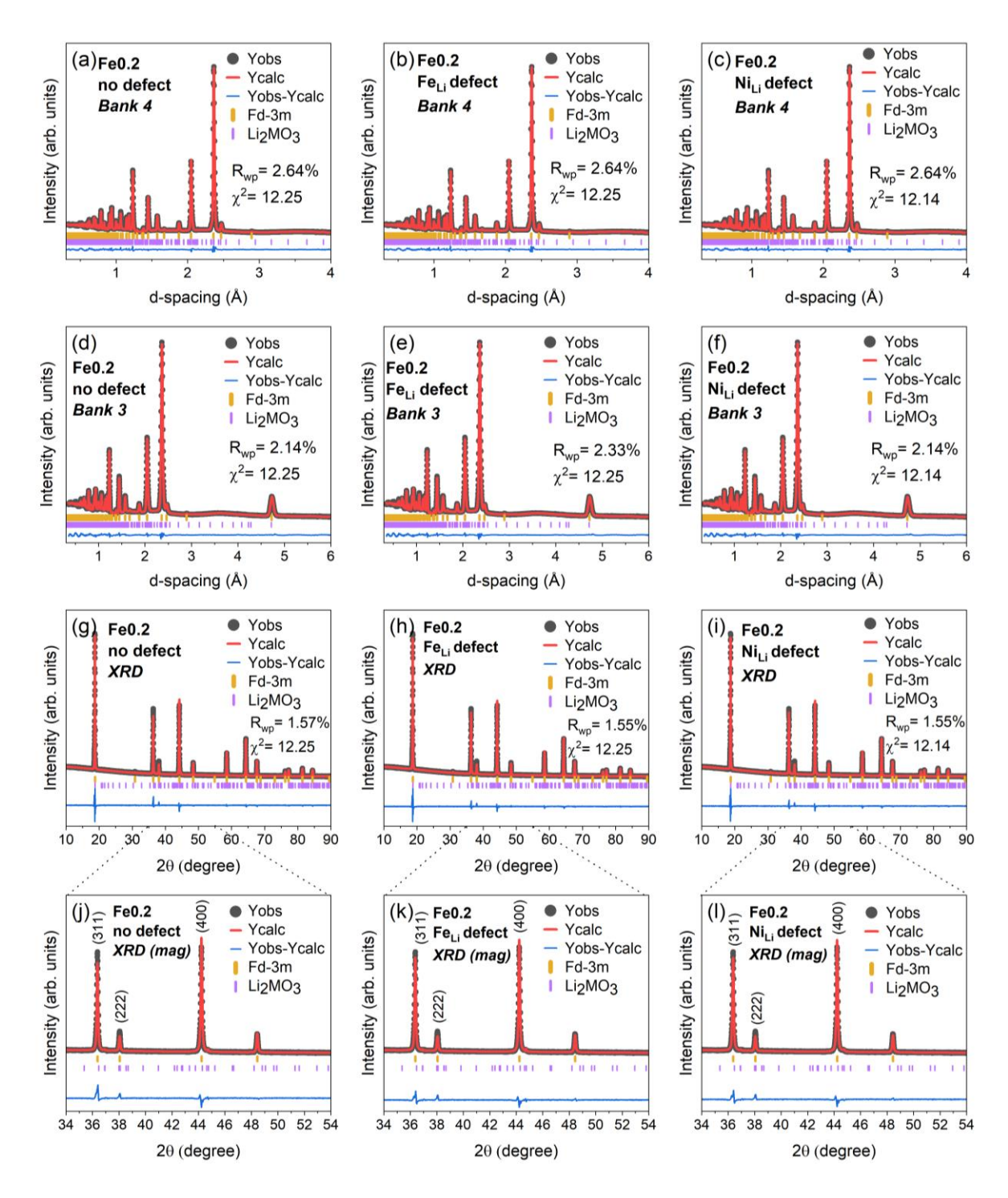


**Figure A5.** Combined ND-XRD Rietveld refinement against data collected at room temperature for Fe0.2. Structure models are based on the  $Fd\overline{3}m$  space group and consider a Li<sub>2</sub>MO<sub>3</sub> impurity (M = Mn and Ni) and the following Li-site defects (A<sub>Li</sub>): no defect (a, d, g and j); Fe<sub>Li</sub> defect (b, e, h, k); and Ni<sub>Li</sub> defect (c, f, i and l). ND refinements of bank 4 (a–c) and bank 3 (d–f) show no change with defect scenario. XRD data (g–l) show an increase in the calculated (311) peak intensity when incorporating Fe<sub>Li</sub>/Ni<sub>Li</sub> defects, as highlighted in the magnified plots (j–l). Peak intensities, however, do not alter significantly between Ni<sub>Li</sub> and Fe<sub>Li</sub> scenarios (k–l).

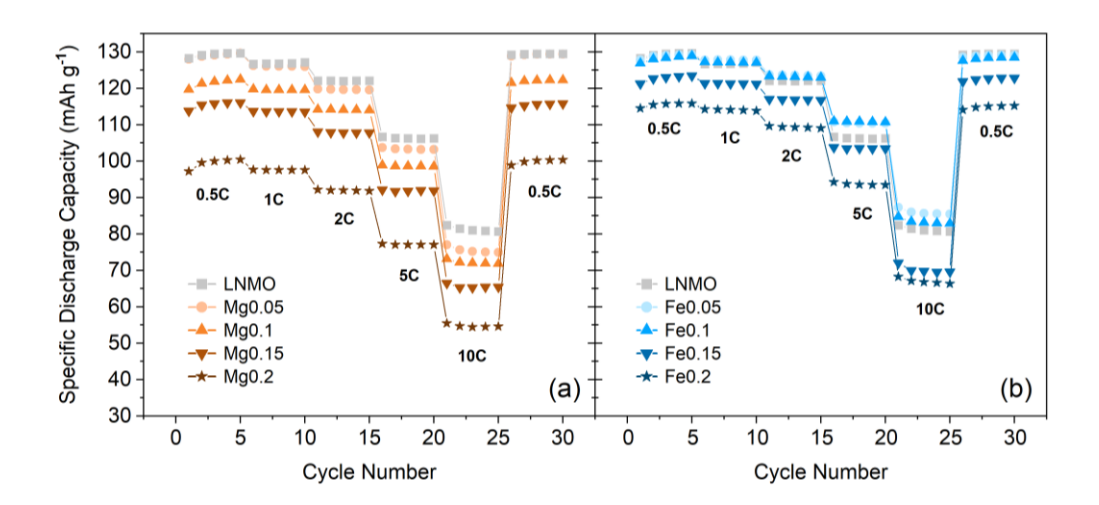


**Figure A6:** Rate capability of a) Mgx and b) Fex (x = 0-0.2) collected in spinel/Li half-cells, using a voltage window of 3.5–4.9 V.

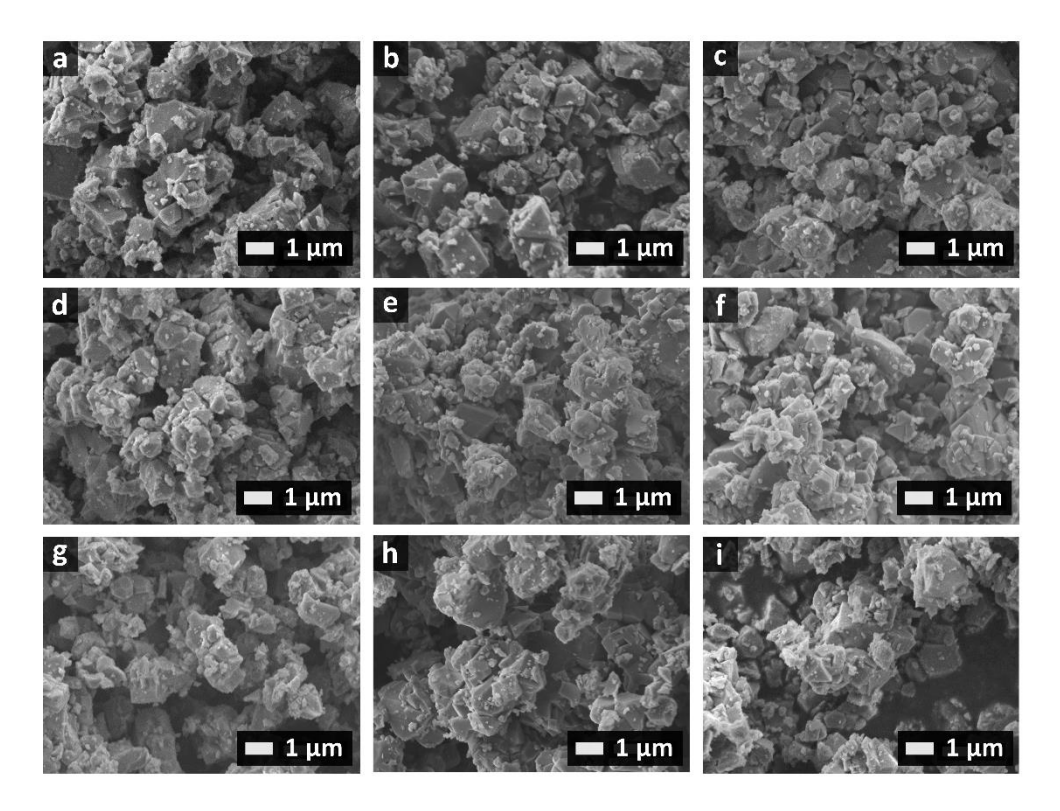


**Figure A7.** SEM images of a) Fe0.05; b) Fe0.1; c) Fe0.15; d) Fe0.2; e) Mg0.05; f) Mg0.1; g) Mg0.15; h) Mg0.2; and i) LNMO.

# **Supporting Tables**

**Table A1:** Crystallographic data obtained from Rietveld refinement against diffraction data on samples LNMO, Mg0.1, Mg0.2, Fe0.1 and Fe0.2 with no Li site defect. ESD values for refined parameters are provided in parentheses.

		Mg0.1	Mg0.2	Fe0.1	Fe0.2	LNMO
X <sup>2</sup>		18.45	14.62	14.35	12.25	17.24
R <sub>wp</sub> %	ND-TOF bank 4	3.14	2.93	2.95	2.64	3.14
	ND-TOF bank 3	2.74	2.45	2.31	2.14	2.43
	XRD	2.21	1.97	1.73	1.57	1.92
f <sub>(8a)</sub>	Li	0.849(24)	0.734(24)	0.972(21)	0.886(21)	1.000(24)
f <sub>(16d)</sub>	Mn	0.760(1)	0.763(1)	0.760(1)	0.758(1)	0.775(1)
	Ni	0.190(1)	0.137(1)	0.190(1)	0.142(1)	0.225(1)
	M (M = Mg, Fe)	0.040(1)	0.087(1)	0.040(1)	0.092(1)	-
f <sub>(32e)</sub>	0	1.000	1.000	1.000	1.000	1.000
100*Uiso	Li	1.945(104)	2.227(125)	1.908(82)	1.493(84)	1.576(76)
(Ų)	Ni, Mn, Mg/Fe	0.524(40)	0.395(33)	0.405(41)	0.592(35)	0.527(40)
	0	1.152(12)	1.195(12)	1.147(11)	1.172(11)	1.070(11)
xyz	8a	0.125000	0.125000	0.125000	0.125000	0.125000
	16d	0.500000	0.500000	0.500000	0.500000	0.500000
	32e	0.262996(18)	0.262991(17)	0.262952(18)	0.262999(17)	0.262931(18)
a (Å)		8.181623(59)	8.194190(56)	8.191654(59)	8.205752(64)	8.177138(57)

**Table A2.** Crystallographic data obtained from Rietveld refinement against diffraction data on samples LNMO, Mg0.1, Mg0.2, Fe0.1 and Fe0.2 in a Ni<sub>Li</sub> defect scenario. ESD values for refined parameters are provided in parentheses.

		Mg0.1	Mg0.2	Fe0.1	Fe0.2	LNMO
χ <sup>2</sup>		17.86	12.89	14.06	12.14	17.19
R <sub>wp</sub> %	ND-TOF bank 4	3.14	2.92	2.95	2.64	3.15
	ND-TOF bank 3	2.73	2.39	2.33	2.14	2.43
	XRD	2.12	1.67	1.66	1.55	1.90
f <sub>(8a)</sub>	Li	0.970(3)	0.947(3)	0.983(3)	0.979(3)	0.992(3)
	Ni	0.03(3)	0.053(3)	0.017(3)	0.021(3)	0.008(3)
f <sub>(16d)</sub>	Mn	0.760(1)	0.763(1)	0.759(1)	0.758(1)	0.775(1)
	Ni	0.190(1)	0.137(1)	0.191(1)	0.141(1)	0.225(1)
	M (M = Mg, Fe)	0.040(1)	0.087(1)	0.041(1)	0.090(1)	-
f <sub>(32e)</sub>	0	1.000	1.000	1.000	1.000	1.000
100*Uiso	Li	1.458(73)	1.235(65)	1.166(61)	1.475(60)	1.158(64)
(Ų)	Ni, Mn, Mg/Fe	0.653(40)	0.529(32)	0.440(40)	0.802(36)	0.534(39)
	0	1.144(12)	1.182(11)	1.135(11)	1.172(10)	1.070(11)
xyz	8a	0.125000	0.125000	0.125000	0.125000	0.125000
	16d	0.500000	0.500000	0.500000	0.500000	0.500000
	32e	0.263011(16)	0.263011(18)	0.262956(16)	0.263013(15)	0.262933(17)
a (Å)		8.181600(59)	8.194217(52)	8.191655(59)	8.205747(64)	8.177232(57)

**Table A3.** Crystallographic data obtained from Rietveld refinement against diffraction data on samples Mg0.1, Mg0.2, Fe0.1 and Fe0.2 in an  $M_{Li}$  defect scenario (M = Mg and Fe). ESD values for refined parameters are provided in parentheses.

		Mg0.1	Mg0.2	Fe0.1	Fe0.2
$\chi^2$		17.92	12.95	14.05	12.25
R <sub>wp</sub> %	ND-TOF bank 4	3.14	2.92	2.95	2.64
	ND-TOF bank 3	2.73	2.40	2.33	2.14
	XRD	2.12	1.68	1.66	1.55
f <sub>(8a)</sub>	Li	0.947(6)	0.903(6)	0.981(3)	0.979(3)
	M (M = Mg, Fe)	0.053(6)	0.097(6)	0.019(3)	0.021(3)
f <sub>(16d)</sub>	Mn	0.760(1)	0.763(1)	0.759(1)	0.758(1)
	Ni	0.190(1)	0.137(1)	0.191(1)	0.141(1)
	M (M = Mg, Fe)	0.04(1)	0.087(1)	0.041(1)	0.090(1)
f <sub>(32e)</sub>	0	1.000	1.000	1.000	1.000
100*Uiso	Li	1.363(73)	1.275(89)	1.172(82)	1.528(61)
$(\mathring{A}^2)$	Ni, Mn, Mg/Fe	0.626(40)	0.484(32)	0.447(40)	0.792(36)
	0	1.143(12)	1.179(11)	1.133(11)	1.175(10)
xyz	8a	0.125000	0.125000	0.125000	0.125000
	16d	0.500000	0.500000	0.500000	0.500000
	32e	0.263008(18)	0.263018(16)	0.262957(16)	0.263016(15)
a(Å)		8.181611(59)	8.194218(53)	8.191655(59)	8.205749(64)

# Appendix B | Supporting Computational Methods and Data for Chapter 4

The methodology provided in Appendix B was written by Dr J. Cen, and is provided for completeness.

#### **Computational Methods**

First-principles DFT calculations were performed using spin-polarised plane-wave DFT as implemented in the Vienna ab initio Simulation Package<sup>1-3</sup> (VASP) code (version 5.4.4). PAW pseudopotentials<sup>4,5</sup> (version PBE 5.4) of Li sv, Mn pv, Ni pv, Fe pv, Mg and O were used to model the core electrons. Calculations were performed with the GGA (PBEsol) + U method<sup>6,7</sup>, where *U* values for *d*-orbitals of Mn, Ni and Fe were set to 3.9 eV, 6.0 eV and 4.0 eV, respectively, according to previous literature studies.<sup>8,9</sup> The initial primitive structure of P4<sub>3</sub>32 LNMO obtained from Materials Project<sup>10</sup> contains 8 formula units of LiNi<sub>0.5</sub>Mn<sub>1.5</sub>O<sub>4</sub> (56 atoms). All calculations in this work used a plane-wave cut-off of 550 eV and defect calculations used a cubic 2×2×2 (448-atom) supercell with Γ-only **k**-point grid, consistent with our previous intrinsic defect study. 11 Tolerances of 10-5 eV and 10-2 eV Å-1 were applied to electronic and ionic convergence, respectively. The force tolerance was raised to 2x10<sup>-2</sup> eV Å<sup>-1</sup> for interstitial defects. Defect calculations were generated and analysed using the doped Python package. 12 A lean version of the ShakeNBreak 13 approach was used to aid the location of the ground-state defect structures. 14,15 Notably, the ground-state defect structure of MgLi<sup>0</sup> (with an Mn<sup>3+</sup> formation near the defect site) was accessed by the ShakeNBreak approach, without considering standard defect structure relaxations. The ferrimagnetic spin configuration (Ni↓ Mn↑) was initialised for all defects with fixed-volume relaxations. 16

The formation energy of a defect *X* in charge state *q* is defined as:

$$E^f(X^q) = E_{\text{tot}}(X^q) - E_{\text{tot}}(\text{host}) - \sum_i n_i \mu_i + q(E_{\text{vbm}} + \mu_e) + \Delta^q, \tag{B1}$$

where  $E_{\rm tot}(X^q)$  and  $E_{\rm tot}({\rm host})$  are the total energies of a defect supercell and the defect-free (i.e., host) supercell respectively.  $\mu_i$  is the atomic chemical potential of species i, and  $n_i$  is the number of atoms of species i that have been added  $(n_i>0)$  or removed  $(n_i<0)$  to form the defects. Sets of  $\mu_i$  can be found by calculating the chemical potential limits of the host compound and they represent different experimental conditions.  $^{17}$   $\mu_e$  is the electronic chemical potential (i.e., the Fermi level), referenced to the valence band maximum (VBM) of the host  $(E_{\rm vbm})$ .  $\Delta^q$  is a correction term to account for the finite-cell-size effect on the total energies of charged defects.  $^{18,19}$  The Freysoldt, Neugebauer and Van de Walle  $^{20,21}$  (FNV) charge correction scheme was used to be consistent with the previous intrinsic defect study.  $^{11}$ 

The defect formation energies should be evaluated at the equilibrium Fermi level which is determined self-consistently under the charge neutrality condition using py-sc-fermi:<sup>22,23</sup>

$$\sum_{X,q} qc(X^q) + n_h - n_e = 0 \tag{B2}$$

where the net charge of a system takes into account all defect species (X) with charge q, free electrons ( $n_e$ ) and free holes ( $n_h$ ). The free carrier concentrations are determined according to the Fermi-Dirac distribution function.<sup>24</sup> The concentration c of a defect in thermodynamic equilibrium at temperature T is related to its formation energy  $E^f$ :11,25

$$c = N_{\text{sites}} N_{\text{config}} \exp\left(\frac{-E^f}{k_B T}\right)$$
 (B3)

 $N_{
m sites}$  is the number of symmetry-inequivalent sites in the lattice per unit volume where the defect can be incorporated.  $N_{
m config}$  is the number of equivalent configurations (i.e., degeneracy) and  $k_{
m B}$  is the Boltzmann's constant. Defect concentrations for pristine, Mg- and Fe-substituted LNMO are given in **Table B1**.

#### **Supporting Figures and Tables**

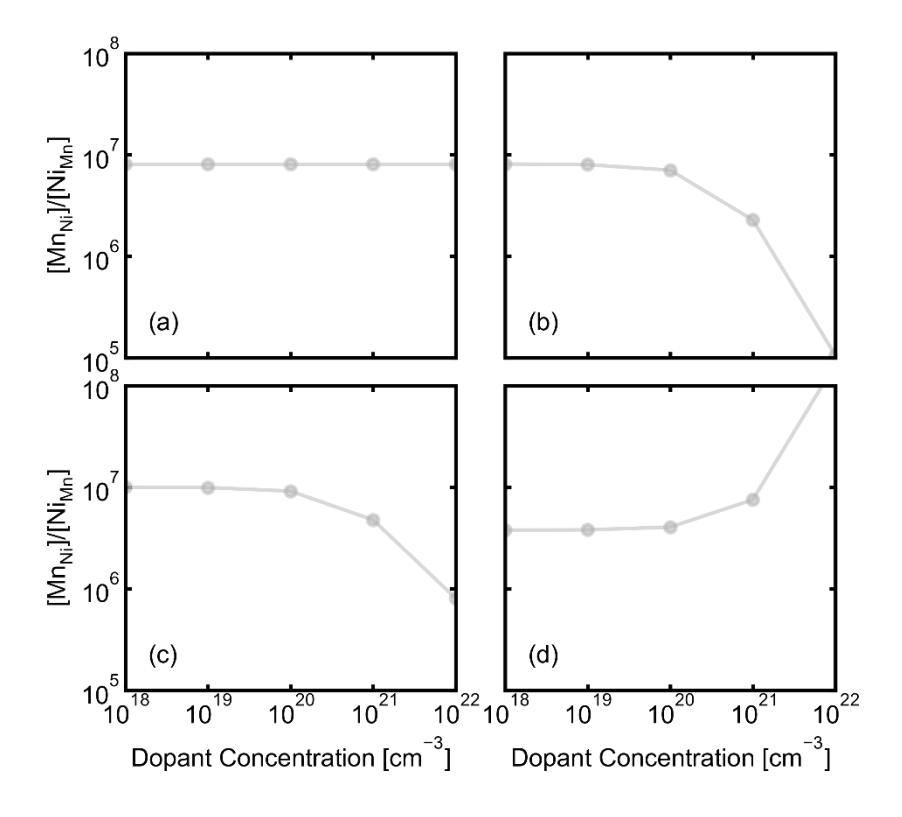


**Figure B1:** Calculated  $[Mn_{Ni}]/[Ni_{Mn}]$  ratio in response to increased substituent concentration through tuning the concentration of extrinsic defect species  $Mg_{Ni}$  (a) and  $Mg_{Li}$  (b) in  $Mg_{Ci}$ 

substituted system and defect species  $Fe_{Ni}$  (c) and  $Fe_{Mn}$  (d) in Fe-doped systems, respectively. Results and figure provided by Dr J. Cen.

**Table B1:** Calculated concentrations of relevant defect species at the chemical potential/growth conditions with the highest concentration of Mn<sup>3+</sup> in pristine and Mg/Fe-doped LNMO. Defect concentrations are dependent on the growth conditions, thus the chosen chemical potential conditions allow comparison between the pristine and doped samples.

	Systems	Pristine	Mg-doped	Fe-doped
	Mn³+	1.01×10 <sup>18</sup>	6.40×10 <sup>20</sup>	9.94×10 <sup>20</sup>
	Ni <sup>3+</sup>	5.66×10 <sup>3</sup>	2.12×10 <sup>17</sup>	6.99×10 <sup>16</sup>
	$Ni_{Mn}$	5.95×10 <sup>16</sup>	8.93×10 <sup>13</sup>	1.57×10 <sup>14</sup>
	Vo	$3.70 \times 10^{15}$	1.17×10 <sup>10</sup>	3.50×10 <sup>11</sup>
	$V_{Ni}$	8.96×10 <sup>9</sup>	1.21×10 <sup>15</sup>	4.07×10 <sup>14</sup>
m-3)	$Mn_{Ni}$	1.53×10 <sup>19</sup>	7.22×10 <sup>20</sup>	$5.99 \times 10^{20}$
) u	Li <sub>Ni</sub>	1.29×10 <sup>19</sup>	$6.39 \times 10^{20}$	1.15×10 <sup>21</sup>
Concentration (cm <sup>-3</sup> )	Total X <sub>Ni</sub>	2.82×10 <sup>19</sup>	1.36×10 <sup>21</sup>	1.75×10 <sup>21</sup>
cent	$V_{Li}$	3.94×10 <sup>15</sup>	9.84×10 <sup>18</sup>	1.99×10 <sup>18</sup>
Conc	$Mn_{Li}$	$3.79 \times 10^{19}$	2.94×10 <sup>18</sup>	5.00×10 <sup>18</sup>
<u> </u>	$Ni_{Li}$	4.50×10 <sup>18</sup>	1.21×10 <sup>16</sup>	$9.09 \times 10^{15}$
	$M_Li$	0	5.06×10 <sup>18</sup>	2.26×10 <sup>16</sup>
	Total X <sub>Li</sub>	4.24×10 <sup>19</sup>	1.79×10 <sup>19</sup>	7.02×10 <sup>18</sup>
	Total non-Li 8a	4.24×10 <sup>19</sup>	8.01×10 <sup>18</sup>	5.03×10 <sup>18</sup>
	occupancy	4.24810		

#### **Supporting references**

- 1 G. Kresse and J. Hafner, *Phys. Rev. B*, 1993, **47**, 558–561.
- 2 G. Kresse and J. Furthmüller, Comput. Mater. Sci., 1996, 6, 15–50.
- 3 G. Kresse and J. Furthmüller, *Phys. Rev. A*, 1996, **54**, 11169–11186.
- 4 P. E. Blöchl, *Phys. Rev. B*, 1994, **50**, 17953–17979.
- G. Kresse and D. Joubert, *Phys. Rev. B Condens. Matter Mater. Phys.*, 1999, **59**, 1758–1775.
- J. P. Perdew, A. Ruzsinszky, G. I. Csonka, O. A. Vydrov, G. E. Scuseria, L. A. Constantin, X. Zhou and K. Burke, *Phys. Rev. Lett.*, 2008, **100**, 1–4.

- S. Dudarev and G. Botton, *Phys. Rev. B Condens. Matter Mater. Phys.*, 1998, **57**, 1505–1509.
- 8 G. Hautier, S. P. Ong, A. Jain, C. J. Moore and G. Ceder, *Phys. Rev. B Condens. Matter Mater. Phys.*, , DOI:10.1103/PhysRevB.85.155208.
- 9 T. Mueller, G. Hautier, A. Jain and G. Ceder, *Chem. Mater.*, 2011, **23**, 3854–3862.
- A. Jain, S. P. Ong, G. Hautier, W. Chen, W. D. Richards, S. Dacek, S. Cholia, D. Gunter,
   D. Skinner, G. Ceder and K. A. Persson, *APL Mater.*, DOI:10.1063/1.4812323.
- 11 J. Cen, B. Zhu, S. R. Kavanagh, A. G. Squires and D. O. Scanlon, *J. Mater. Chem. A*, 2023, 13353–13370.
- S. R. Kavanagh, A. G. Squires, A. Nicolson, I. Mosquera-Lois, A. M. Ganose, B. Zhu, K. Brlec, A. Walsh and D. O. Scanlon, *J. Open Source Softw.*, 2024, **9**, 6433.
- 13 I. Mosquera-Lois, S. R. Kavanagh, A. Walsh and D. O. Scanlon, *J. Open Source Softw.*, 2022, **7**, 4817.
- I. Mosquera-Lois, S. R. Kavanagh, A. Walsh and D. O. Scanlon, *npj Comput. Mater.*, ,
   DOI:10.1038/s41524-023-00973-1.
- 15 I. Mosquera-Lois and S. R. Kavanagh, *Matter*, 2021, **4**, 2602–2605.
- 16 C. G. Van De Walle and J. Neugebauer, *J. Appl. Phys.*, 2004, **95**, 3851–3879.
- 17 J. Buckeridge, D. O. Scanlon, A. Walsh and C. R. A. Catlow, *Comput. Phys. Commun.*, 2014, **185**, 330–338.
- 18 K. Hoang and M. Johannes, *Chem. Mater.*, 2016, **28**, 1325–1334.
- 19 S. Kim, S. N. Hood, J. S. Park, L. D. Whalley and A. Walsh, *JPhys Energy*, 2020, **2**, 1–8.
- 20 C. Freysoldt, J. Neugebauer and C. G. Van de Walle, *Phys. Status Solidi Basic Res.*, 2011, **248**, 1067–1076.
- C. Freysoldt, J. Neugebauer and C. G. Van De Walle, *Phys. Rev. Lett.*, 2009, **102**, 1–4.
- A. G. Squires, D. O. Scanlon and B. J. Morgan, J. Open Source Softw., 2023, 8, 4962.
- 23 J. Buckeridge, Comput. Phys. Commun., 2019, **244**, 329–342.
- 24 C. Kittel and H. Kroemer, *Thermal Physics*, American Association of Physics Teachers,

1998.

25 I. Mosquera-Lois, S. R. Kavanagh, J. Klarbring, K. Tolborg and A. Walsh, *Chem. Soc. Rev.*, 2023, **52**, 5812–5826.

# Appendix C | Supporting Experimental Data for Chapter 5

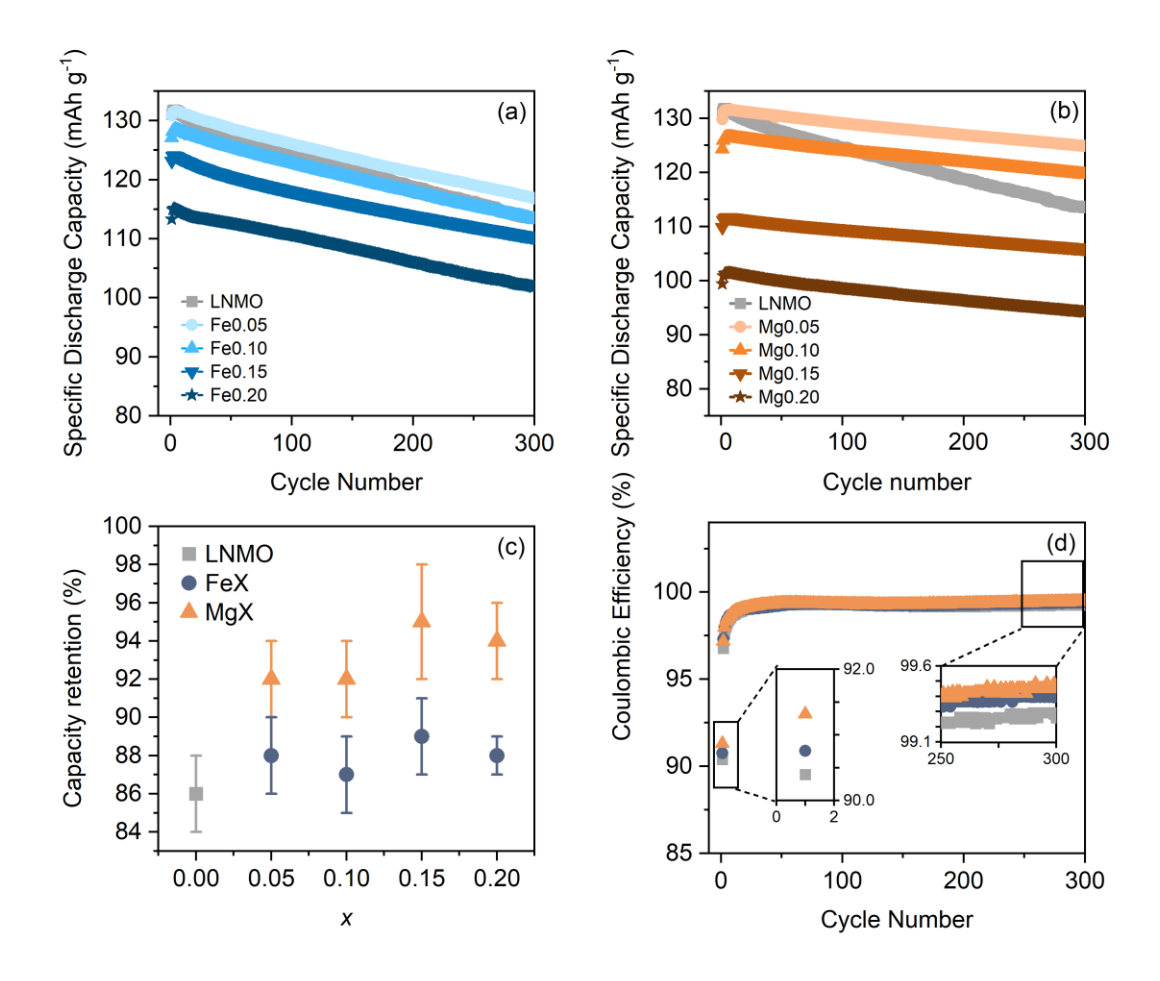


**Figure C1**: Electrochemical performance of spinel/Li half cells (1C, 3.5-4.9 V). High-temperature (50°C) cycling stability of a) Mgx and b) Fex (x = 0-0.2), with average capacity retention after 300 cycles (n = 4) shown in (c); and d) coulombic efficiencies at ambient temperature (28°C). Previously reported cycling stability and rate performance at ambient temperature are presented in Chapter 4.

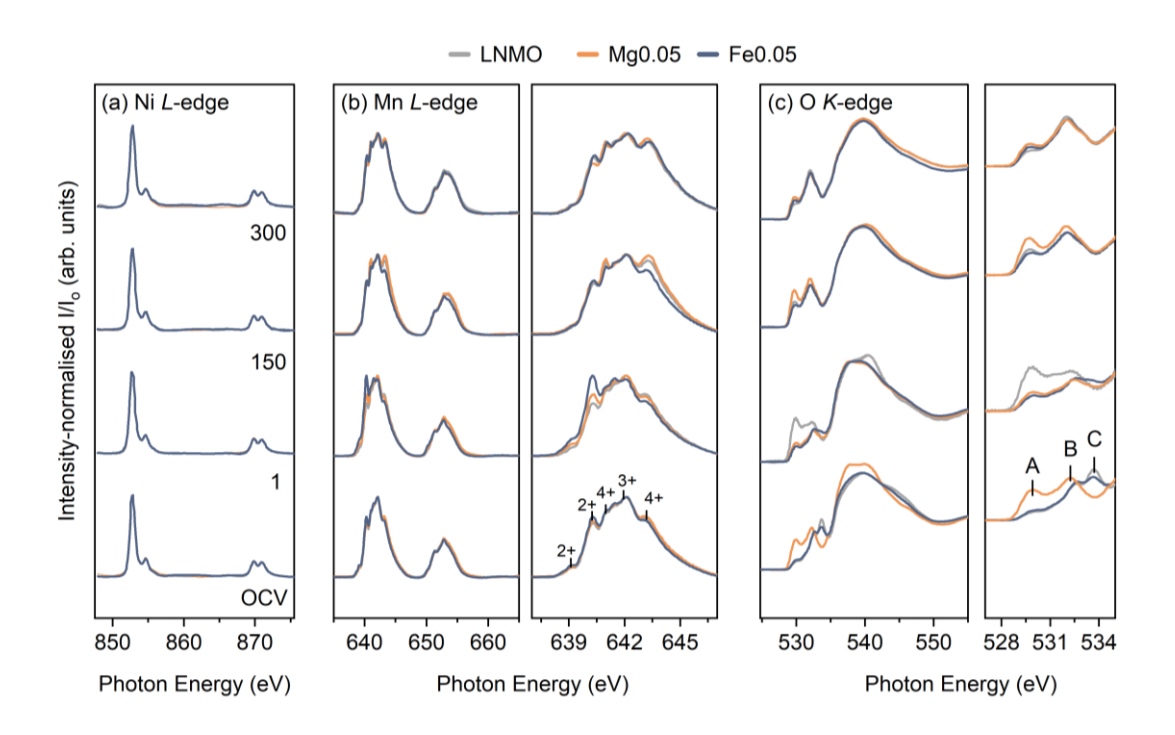


**Figure C2**: Intensity normalised a) Ni *L*-edge, b) Mn *L*-edge and c) O *K*-edge sXAS-TEY spectra of *ex-situ* LNMO (grey), Fe0.05 (blue) and Mg0.05 (orange) electrodes at various points of cycling (50°C, 1C, 3.5–4.9 V): before cycling (OCV); and after cycles 1, 150 and 300.

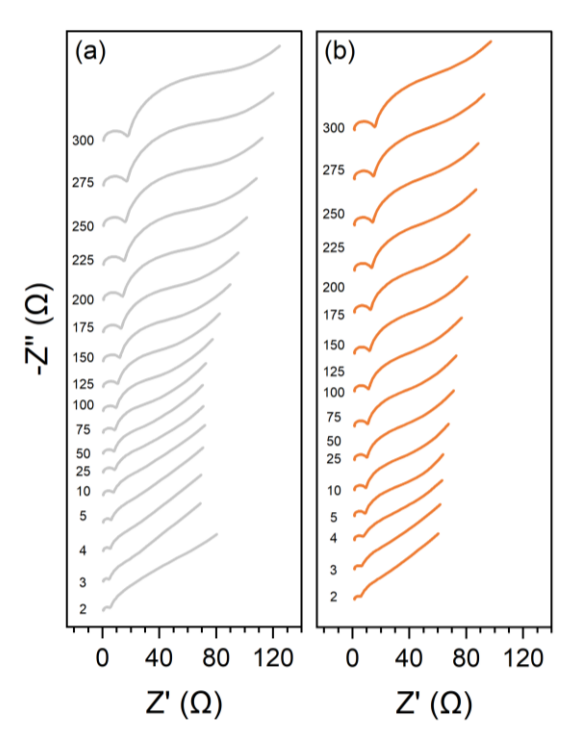


**Figure C3**: Evolution of EIS spectra for a) LNMO and b) Mg0.05 over 300 cycles used to determine  $R_{sol}$ ,  $R_{contact}$  and  $R_{cathode}$  presented in Figure 5.6. EIS data were collected using the simplified program.

### **Consolidated List of References**

Adenusi, H., Chass, G. A., Passerini, S., Tian, K. V., & Chen, G. (2023). Lithium Batteries and the Solid Electrolyte Interphase (SEI)—Progress and Outlook. Advanced Energy Materials, 13, 2203307.

Ahmed, S., Nelson, P. A., Gallagher, K. G., Susarla, N., & Dees, D. W. (2017). Cost and energy demand of producing nickel manganese cobalt cathode material for lithium ion batteries. Journal of Power Sources, 342, 733–740. https://doi.org/10.1016/j.jpowsour.2016.12.069

Alvarado, J., Schroeder, M. A., Zhang, M., Borodin, O., Gobrogge, E., Olguin, M., Ding, M. S., Gobet, M., Greenbaum, S., Meng, Y. S., & Xu, K. (2018). A carbonate-free, sulfone-based electrolyte for high-voltage Li-ion batteries. Materials Today, 21(4), 341–353. https://doi.org/10.1016/j.mattod.2018.02.005

Arai, H., Sato, K., Orikasa, Y., Murayama, H., Takahashi, I., Koyama, Y., Uchimoto, Y., & Ogumi, Z. (2013). Phase transition kinetics of LiNi0.5Mn1.5O4electrodes studied by in situ X-ray absorption near-edge structure and X-ray diffraction analysis. Journal of Materials Chemistry A, 1(35), 10442–10449. https://doi.org/10.1039/c3ta11637a

Atkins, P. W. (6519 B.C.E.). Physical Chemistry. In Oxford University Press (Vol. 625, Issue 6). https://doi.org/10.1016/0016-0032(61)90576-2

Azcarate, I., Yin, W., Méthivier, C., Ribot, F., Laberty-Robert, C., & Grimaud, A. (2020). Assessing the Oxidation Behavior of EC:DMC Based Electrolyte on Non-Catalytically Active Surface. Journal of The Electrochemical Society, 167(8), 080530. https://doi.org/10.1149/1945-7111/ab8f57

Babbitt, C. W. (2020). Sustainability perspectives on lithium-ion batteries. Clean Technologies and Environmental Policy, 22(6), 1213–1214. https://doi.org/10.1007/s10098-020-01890-3

Baker, M. L., Mara, M. W., Yan, J. J., Hodgson, K. O., Hedman, B., & Solomon, E. I. (2017). K- and L-edge X-ray absorption spectroscopy (XAS) and resonant inelastic X-ray scattering (RIXS) determination of differential orbital covalency (DOC) of transition metal sites. Coordination Chemistry Reviews, 345, 182–208. https://doi.org/10.1016/j.ccr.2017.02.004

Balducci, L., Darjazi, H., Gonzalo, E., Cid, R., Bonilla, F., & Nobili, F. (2023). Evaluation of Electronic-Ionic Transport Properties of a Mg/Zr-Modified LiNi0.5Mn1.5O4 Cathode for Li-Ion Batteries. ACS Applied Materials and Interfaces, 15(48), 55620–55632. https://doi.org/10.1021/acsami.3c10480

Bao, W., Yao, W., Li, Y., Sayahpour, B., Han, B., Raghavendran, G., Shimizu, R., Cronk, A., Zhang, M., Li, W., & Meng, Y. S. (2024). Insights into lithium inventory quantification of LiNio.5Mn1.5O4-graphite full cells. Energy and Environmental Science, 4263–4272. https://doi.org/10.1039/d4ee00842a

Berar, J. F., & Lelann, P. (1991). E.S.D.'s and estimated probable error obtained in rietveld refinements with local correlations. Journal of Applied Crystallography, 24(pt 1), 1–5. https://doi.org/10.1107/S0021889890008391

Bernhart, W. (2019). Battery Recycling is a Key Market of the Future: Ist it also an Oppourtunity for Europe? Roland Berger. https://www.rolandberger.com/en/Insights/Publications/Battery-recycling-is-a-key-market-of-the-future-Is-it-also-an-opportunity-for.html

BGS. (n.d.). Uk and World Mineral datasets and statistics. Retrieved January 11, 2021, from https://www.bgs.ac.uk/datasets/uk-and-world-mineral-statistics-datasets/

Bizot, C., Blin, M. A., Guichard, P., Soudan, P., Gaubicher, J., & Poizot, P. (2021). Aluminum current collector for high voltage Li-ion battery. Part II: Benefit of the En' Safe® primed current collector technology. Electrochemistry Communications, 126. https://doi.org/10.1016/j.elecom.2021.107008

Björklund, E., Xu, C., Dose, W. M., Sole, C. G., Thakur, P. K., Lee, T.-L., De Volder, M. F. L., Grey, C. P., & Weatherup, R. S. (2022). Cycle-Induced Interfacial Degradation and Transition-Metal Cross-Over in LiNio.8 Mno.1 Coo.1 O2–Graphite Cells. Chemsitry of Materials, 34(5), 1987–2494.

Blöchl, P. E. (1994). Projector augmented-wave method. Physical Review B, 50(24), 17953–17979. https://doi.org/10.1103/PhysRevB.50.17953

Buckeridge, J. (2019). Equilibrium point defect and charge carrier concentrations in a material determined through calculation of the self-consistent Fermi energy. Computer Physics Communications, 244, 329–342. https://doi.org/10.1016/j.cpc.2019.06.017

Buckeridge, J., Scanlon, D. O., Walsh, A., & Catlow, C. R. A. (2014). Automated procedure to determine the thermodynamic stability of a material and the range of chemical potentials necessary for its formation relative to competing phases and compounds. Computer Physics Communications, 185(1), 330–338. https://doi.org/10.1016/j.cpc.2013.08.026

Cabana, J., Omenya, F. O., Chernova, N. A., Zeng, D., Whittingham, M. S., & Grey, C. P. (2012). Composition-Structure Relationships in the Li-Ion Battery Electrode Material LiNio.5Mn1.5O4. Chemistry of Materials, 24, 2952–2964.

Calisaya-Azpilcueta, D., Herrera-Leon, S., Lucay, F. A., & Cisternas, L. A. (2020). Assessment of the supply chain under uncertainty: The case of Lithium. Minerals, 10(7), 1–20. https://doi.org/10.3390/min10070604

Carver, R., Childs, J., Steinberg, P., Mabon, L., Matsuda, H., Squire, R., McLellan, B., & Esteban, M. (2020). A critical social perspective on deep sea mining: Lessons from the emergent industry in Japan. Ocean and Coastal Management, 193(February), 105242. https://doi.org/10.1016/j.ocecoaman.2020.105242

Cen, J., Zhu, B., Kavanagh, S. R., Squires, A. G., & Scanlon, D. O. (2023). Cation disorder dominates the defect chemistry of high-voltage LiMn1.5Ni0.5O4 (LMNO) spinel cathodes. Journal of Materials Chemistry A, 13353–13370. https://doi.org/10.1039/d3ta00532a

Chen, P., Yang, F., Cao, Z., Jhang, J., Gao, H., Yang, M., & Huang, K. D. (2019). Reviving Aged Lithium-Ion Batteries and Prolonging their Cycle Life by Sinusoidal Waveform Charging Strategy. Batteries & Supercaps, 2(8), 673–677. https://doi.org/10.1002/batt.201900022

Chen, R., Witte, R., Heinzmann, R., Ren, S., Mangold, S., Hahn, H., Hempelmann, R., Ehrenberg, H., & Indris, S. (2016). Identifying the redox activity of cation-disordered Li-Fe-V-Ti oxide cathodes for Li-ion batteries. Physical Chemistry Chemical Physics, 18(11), 7695–7701. https://doi.org/10.1039/c6cp00131a

Chen, T., Lin, F., Wu, H., Zhou, D., Song, J., & Guo, J. (2023). Zn-Y co-doped LiNi0.5Mn1.5O4 cathode materials with high electrochemical performance. Journal of Alloys and Compounds, 941, 168825. https://doi.org/10.1016/j.jallcom.2023.168825

Chen, X., Wang, X., & Fang, D. (2020). A review on C1s XPS-spectra for some kinds of carbon materials. Fullerenes Nanotubes and Carbon Nanostructures, 28(12), 1048–1058. https://doi.org/10.1080/1536383X.2020.1794851

Chen, Y., Sun, Y., & Huang, X. (2016a). Origin of the Ni/Mn ordering in high-voltage spinel LiNi0.5Mn1.5O4: The role of oxygen vacancies and cation doping. Computational Materials Science, 115, 109–116. https://doi.org/10.1016/j.commatsci.2016.01.005

Chen, Y., Sun, Y., & Huang, X. (2016b). Origin of the Ni/Mn ordering in high-voltage spinel LiNi0.5Mn1.5O4: The role of oxygen vacancies and cation doping. Computational Materials Science, 115, 109–116. https://doi.org/10.1016/j.commatsci.2016.01.005

Cheng, J., Li, M., Wang, Y., Li, J., Wen, J., Wang, C., & Huang, G. (2023). Effects of Al and Co doping on the structural stability and high temperature cycling performance of LiNio.5Mn1.5O4 spinel cathode materials. Chinese Journal of Chemical Engineering, 61, 201–209. https://doi.org/10.1016/j.cjche.2023.02.020

Chong, J., Xun, S., Song, X., Liu, G., & Battaglia, V. S. (2013). Surface stabilized LiNio.5Mn1.5O4 cathode materials with high-rate capability and long cycle life for lithium ion batteries. Nano Energy, 2(2), 283–293. https://doi.org/10.1016/j.nanoen.2012.09.013

Chong, J., Xun, S., Zhang, J., Song, X., Xie, H., Battaglia, V., & Wang, R. (2014). Li3PO4-Coated LiNi0.5Mn 1.5O4: A stable high-voltage cathode material for lithium-ion batteries. Chemistry - A European Journal, 20(24), 7479–7485. https://doi.org/10.1002/chem.201304744

Ciez, R. E., & Whitacre, J. F. (2019). Examining different recycling processes for lithium-ion batteries. Nature Sustainability, 2(2), 148–156. https://doi.org/10.1038/s41893-019-0222-5

Clark, D. T., Feast, W. J., Tweedale, P. J., & Thomas, H. R. (1980). ESCA applied to polymers. XXVI. Investigation of a series of aliphatic, aromatic, and fluorine-containing polycarbonates. Journal of Polymer Science, 18(6), 1651–2031.

Clément, R. J., Lun, Z., & Ceder, G. (2020). Cation-disordered rocksalt transition metal oxides and oxyfluorides for high energy lithium-ion cathodes. Energy and Environmental Science, 13(2), 345–373. https://doi.org/10.1039/c9ee02803j

Climate Change 2014 Synthesis Report. (2014). In IPCC.

Cobalt. (2021). Trading Economics. https://tradingeconomics.com/commodity/cobalt

Cobalt Price. (2020). Metalary. https://www.metalary.com/cobalt-price

Cockcroft, J. K. (2006). Estimated Standard Deviations. Powder Diffraction on the Web. http://pd.chem.ucl.ac.uk/pdnn/refine1/errors.htm

Costa, C. M., Lizundia, E., & Lanceros-Méndez, S. (2020). Polymers for advanced lithium-ion batteries: State of the art and future needs on polymers for the different battery components. Progress in Energy and Combustion Science, 79, 100846. https://doi.org/10.1016/j.pecs.2020.100846

Cui, X., Zhou, X., Liang, W., Tuo, K., Wang, P., Zhang, L., & Li, S. (2022). Exploring the action mechanism of magnesium in different cations sites for LiNi0.5Mn1.5O4 cathode materials. Materials Today Sustainability, 17. https://doi.org/10.1016/j.mtsust.2021.100105

Cullity, B. D., & Stock, S. R. (2001). Elements of X-ray diffraction (3rd ed.). Prentice-Hall.

Dalavi, S., Xu, M., Knight, B., & Lucht, B. L. (2011). Effect of Added LiBOB on High Voltage (LiNi0.5Mn1.5O4) Spinel Cathode. Electrochemical and Solid-State Letters, 15, A28. https://doi.org/10.1149/2.015202esl

Deng, M. M., Zou, B. K., Shao, Y., Tang, Z. F., & Chen, C. H. (2017). Comparative study of the electrochemical properties of LiNi0.5Mn1.5O4 doped by bivalent ions (Cu2+, Mg2+, and Zn2+). Journal of Solid State Electrochemistry, 21(6), 1733–1742. https://doi.org/10.1007/s10008-017-3545-z

Deng, S., Wang, B., Yuan, Y., Li, X., Sun, Q., Doyle-Davis, K., Banis, M. N., Liang, J., Zhao, Y., Li, J., Li, R., Sham, T. K., Shahbazian-Yassar, R., Wang, H., Cai, M., Lu, J., & Sun, X. (2019). Manipulation of an ionic and electronic conductive interface for highly-stable high-voltage cathodes. Nano Energy, 65(August), 103988. https://doi.org/10.1016/j.nanoen.2019.103988

Deng, Y., Mou, J., Wu, H., Jiang, N., Zheng, Q., Lam, K. H., Xu, C., & Lin, D. (2017). A superior Li2SiO3-Composited LiNi0.5Mn1.5O4 Cathode for High-Voltage and High-Performance Lithium-ion Batteries. Electrochimica Acta, 235, 19–31. https://doi.org/10.1016/j.electacta.2017.03.066

Desjardins, J. (2017). The Cathode is the Key to Advancing Lithium-Ion Technology. Visual Capitalist. https://www.visualcapitalist.com/cathode-advancing-lithium-ion/

Ding, Y., Cano, Z. P., Yu, A., Lu, J., & Chen, Z. (2019). Automotive Li-Ion Batteries: Current Status and Future Perspectives. Electrochemical Energy Reviews, 2(1), 1–28. https://doi.org/10.1007/s41918-018-0022-z

Distinguishing charge rates for next-generation batteries. (2021). Quantum Scape. https://www.quantumscape.com/resources/blog/distinguishing-charge-rates-for-next-generation-batteries/

Doi, T., Shimizu, Y., Hashinokuchi, M., & Inaba, M. (2016). LiBF 4 -Based Concentrated Electrolyte Solutions for Suppression of Electrolyte Decomposition and Rapid Lithium-Ion Transfer at LiNi 0.5 Mn 1.5 O 4 /Electrolyte Interface . Journal of The Electrochemical Society, 163(10), A2211–A2215. https://doi.org/10.1149/2.0331610jes

Doi, T., Shimizu, Y., Hashinokuchi, M., & Inaba, M. (2017). Dilution of Highly Concentrated LiBF 4 /Propylene Carbonate Electrolyte Solution with Fluoroalkyl Ethers for 5-V LiNi 0.5 Mn 1.5 O 4 Positive Electrodes . Journal of The Electrochemical Society, 164(1), A6412–A6416. https://doi.org/10.1149/2.0611701jes

Dong, Hongxu, & Koenig, G. M. (2017). Compositional control of precipitate precursors for lithium-ion battery active materials: Role of solution equilibrium and precipitation rate. Journal of Materials Chemistry A, 5(26), 13785–13798. https://doi.org/10.1039/c7ta03653a

Dong, Hongyu, Zhang, Y., Zhang, S., Tang, P., Xiao, X., Ma, M., Zhang, H., Yin, Y., Wang, D., & Yang, S. (2019). Improved High Temperature Performance of a Spinel LiNi0.5Mn1.5O4 Cathode for High-Voltage Lithium-Ion Batteries by Surface Modification of a Flexible Conductive Nanolayer. ACS Omega, 4(1), 185–194. https://doi.org/10.1021/acsomega.8b02571

Du, P., Wan, J., Qu, J., Xie, H., Wang, D., & Yin, H. (2024). Passivation and corrosion of Al current collectors in lithium-ion batteries. Npj Materials Degradation, 8(1). https://doi.org/10.1038/s41529-024-00453-x

Dudarev, S., & Botton, G. (1998). Electron-energy-loss spectra and the structural stability of nickel oxide: An LSDA+U study. Physical Review B - Condensed Matter and Materials Physics, 57(3), 1505–1509. https://doi.org/10.1103/PhysRevB.57.1505

Dunn, J. B., James, C., Gaines, L., Gallagher, K., Dai, Q., & Kelly, J. C. (2015). Material and Energy Flows in the Production of Cathode and Anode Materials for Lithium Ion Batteries. Argonne National Laborartory, 53(9), 1689–1699. http://publications.lib.chalmers.se/records/fulltext/245180/245180.pdf%0Ahttps://hdl.handle.net/20.500.12380/245180%0Ahttp://dx.doi.org/10.1016/j.jsames.2011.03.003%0Ahttps://doi.org/10.1016/j.gr.2017.08.001%0Ahttp://dx.doi.org/10.1016/j.precamres.2014.12

Edge, J. S., O'Kane, S., Prosser, R., Kirkaldy, N. D., Patel, A. N., Hales, A., Ghosh, A., Ai, W., Chen, J., Yang, J., Li, S., Pang, M. C., Bravo Diaz, L., Tomaszewska, A., Marzook, M. W., Radhakrishnan, K. N., Wang, H., Patel, Y., Wu, B., & Offer, G. J. (2021). Lithium ion battery degradation: what you need to know. Physical Chemistry Chemical Physics, 23(14), 8200–8221. https://doi.org/10.1039/d1cp00359c

Elgrishi, N., Rountree, K. J., McCarthy, B. D., Rountree, E. S., Eisenhart, T. T., & Dempsey, J. L. (2018). A Practical Beginner's Guide to Cyclic Voltammetry. Journal of Chemical Education, 95(2), 197–206. https://doi.org/10.1021/acs.jchemed.7b00361

Elshkaki, A., Reck, B. K., & Graedel, T. E. (2017). Anthropogenic nickel supply, demand, and associated energy and water use. Resources, Conservation and Recycling, 125(June), 300–307. https://doi.org/10.1016/j.resconrec.2017.07.002

Entwistle, T., Sanchez-Perez, E., Murray, G. J., Anthonisamy, N., & Cussen, S. A. (2022). Co-precipitation synthesis of nickel-rich cathodes for Li-ion batteries. Energy Reports, 8, 67–73. https://doi.org/10.1016/j.egyr.2022.06.110

Erickson, E. M., Li, W., Dolocan, A., & Manthiram, A. (2022). Insights into the Cathode–Electrolyte Interphases of High-Energy-Density Cathodes in Lithium-Ion Batteries.

ACS Applied Materials and Interfaces, 12, 16451–16461. https://pubs.acs.org/doi/epdf/10.1021/acsami.0c00900

Farjana, S. H., Huda, N., Mahmud, M. A. P., & Lang, C. (2019). A global life cycle assessment of manganese mining processes based on EcoInvent database. Science of the Total Environment, 688, 1102–1111. https://doi.org/10.1016/j.scitotenv.2019.06.184

Farjana, S. H., Huda, N., Parvez Mahmud, M. A., & Saidur, R. (2019). A review on the impact of mining and mineral processing industries through life cycle assessment. Journal of Cleaner Production, 231, 1200–1217. https://doi.org/10.1016/j.jclepro.2019.05.264

Fey, G. T. K., Lu, C. Z., & Prem Kumar, T. (2003). Preparation and electrochemical properties of high-voltage cathode materials, LiMyNi0.5-yMn1.5O4 (M = Fe, Cu, Al, Mg; y = 0.0-0.4). Journal of Power Sources, 115(2), 332–345. https://doi.org/10.1016/S0378-7753(03)00010-7

Frati, F., Hunault, M. O. J. Y., & De Groot, F. M. F. (2020). Oxygen K-edge X-ray Absorption Spectra. Chemical Reviews, 120(9), 4056–4110. https://doi.org/10.1021/acs.chemrev.9b00439

Freire, M., Diaz-Lopez, M., Bordet, P., Colin, C. V., Lebedev, O. I., Kosova, N. V., Jordy, C., Chateigner, D., Chuvilin, A. L., Maignan, A., & Pralong, V. (2018). Investigation of the exceptional charge performance of the 0.93Li4-: XMn2O5-0.07Li2O composite cathode for Liion batteries. Journal of Materials Chemistry A, 6(12), 5156–5165. https://doi.org/10.1039/c8ta00234g

Freysoldt, C., Neugebauer, J., & Van de Walle, C. G. (2011). Electrostatic interactions between charged defects in supercells. Physica Status Solidi (B) Basic Research, 248(5), 1067–1076. https://doi.org/10.1002/pssb.201046289

Freysoldt, C., Neugebauer, J., & Van De Walle, C. G. (2009). Fully Ab initio finite-size corrections for charged-defect supercell calculations. Physical Review Letters, 102(1), 1–4. https://doi.org/10.1103/PhysRevLett.102.016402

Fu, T., Li, Y., Yao, Z., Guo, T., Liu, S., Chen, Z., Zheng, C., & Sun, W. (2024). Enhancing Orbital Interaction in Spinel LiNi 0.5 Mn 1.5 O4 Cathode for High-Voltage and High-Rate Lilon Batteries. Small, 2402339.

Fu, X., Beatty, D. N., Gaustad, G. G., Ceder, G., Roth, R., Kirchain, R. E., Bustamante, M., Babbitt, C., & Olivetti, E. A. (2020). Perspectives on Cobalt Supply through 2030 in the Face of Changing Demand. Environmental Science and Technology, 54(5), 2985–2993. https://doi.org/10.1021/acs.est.9b04975

Fujita, T., Chen, H., Wang, K. tuo, He, C. lin, Wang, Y. bin, Dodbiba, G., & Wei, Y. zhou. (2021). Reduction, reuse and recycle of spent Li-ion batteries for automobiles: A review. International Journal of Minerals, Metallurgy and Materials, 28(2), 179–192. https://doi.org/10.1007/s12613-020-2127-8

Gaines, L. (2014). The future of automotive lithium-ion battery recycling: Charting a sustainable course. Sustainable Materials and Technologies, 1, 2–7. https://doi.org/10.1016/j.susmat.2014.10.001

Gaines, L., Richa, K., & Spangenberger, J. (2018). Key issues for Li-ion battery recycling. MRS Energy & Sustainability, 5(1), 1–14. https://doi.org/10.1557/mre.2018.13

Gao, H., Yan, Q., Xu, P., Liu, H., Li, M., Liu, P., Luo, J., & Chen, Z. (2020). Efficient Direct Recycling of Degraded LiMn2O4Cathodes by One-Step Hydrothermal Relithiation. ACS Applied Materials and Interfaces, 12(46), 51546–51554. https://doi.org/10.1021/acsami.0c15704

Garole, D. J., Hossain, R., Garole, V. J., Sahajwalla, V., Nerkar, J., & Dubal, D. P. (2020). Recycle, Recover and Repurpose Strategy of Spent Li-ion Batteries and Catalysts: Current Status and Future Opportunities. ChemSusChem, 13(12), 3079–3100. https://doi.org/10.1002/cssc.201903213

Gengenbach, T. R., Major, G. H., Linford, M. R., & Easton, C. D. (2021). Practical guides for x-ray photoelectron spectroscopy (XPS): Interpreting the carbon 1s spectrum. Journal of Vacuum Science & Technology A: Vacuum, Surfaces, and Films, 39(1). https://doi.org/10.1116/6.0000682

Gifford, S. (2019). Building a Responsible Cobalt Supply Chain. Faraday Insights, 2018.

Gong, J., Wang, Q., & Sun, J. (2017). Thermal analysis of nickel cobalt lithium manganese with varying nickel content used for lithium ion batteries. Thermochimica Acta, 655(June), 176–180. https://doi.org/10.1016/j.tca.2017.06.022

Goodenough, J. B., & Park, K. S. (2013). The Li-ion rechargeable battery: A perspective. Journal of the American Chemical Society, 135(4), 1167–1176. https://doi.org/10.1021/ja3091438

Gorai, P., Famprikis, T., Singh, B., Stevanović, V., & Canepa, P. (2021). Devil is in the Defects: Electronic Conductivity in Solid Electrolytes. Chemistry of Materials, 33(18), 7484–7498. https://doi.org/10.1021/acs.chemmater.1c02345

Gorai, P., Long, H., Jones, E., Santhanagopalan, S., & Stevanović, V. (2020). Defect chemistry of disordered solid-state electrolyte Li10GeP2S12. Journal of Materials Chemistry A, 8(7), 3851–3858. https://doi.org/10.1039/c9ta10964a

Gourley, S. W. D., Or, T., & Chen, Z. (2020). Breaking Free from Cobalt Reliance in Lithium-Ion Batteries. IScience, 23(9), 101505. https://doi.org/10.1016/j.isci.2020.101505

gov.uk. (2021). Waste batteries: producer responsibility. https://www.gov.uk/guidance/waste-batteries-producer-responsibility#:~:text=It's illegal to send waste,sale on the UK market.

Government Office for Science. (2022). A brief guide to futures thinking and foresight. https://www.gov.uk/government/publications/futures-thinking-and-foresight-a-brief-guide%0Ahttps://assets.publishing.service.gov.uk/government/uploads/system/uploads/attac hment data/file/964195/A brief guide to futures thinking and foresight.pdf

Grant, A., Whittaker, M., & Aaron, C. (n.d.). Inside Tesla 's Lithium Clay Salt Extraction Process. Jade Cove Partners. Retrieved February 10, 2021, from https://www.jadecove.com/research/teslasaltclay

Greczynski, G., & Hultman, L. (2017). C 1s Peak of Adventitious Carbon Aligns to the Vacuum Level: Dire Consequences for Material's Bonding Assignment by Photoelectron Spectroscopy. ChemPhysChem, 18(12), 1491–1660.

Greczynski, G., & Hultman, L. (2022). A step-by-step guide to perform x-ray photoelectron spectroscopy. Journal of Applied Physics, 132(1). https://doi.org/10.1063/5.0086359

Gruber, P. W., Medina, P. A., Keoleian, G. A., Kesler, S. E., Everson, M. P., & Wallington, T. J. (2011). Global lithium availability: A constraint for electric vehicles? Journal of Industrial Ecology, 15(5), 760–775. https://doi.org/10.1111/j.1530-9290.2011.00359.x

Gu, Y. J., Li, Y., Chen, Y. B., & Liu, H. Q. (2016). Comparison of Li/Ni antisite defects in Fd-3 m and P4332 nanostructured LiNi0.5Mn1.5O4 electrode for Li-ion batteries. Electrochimica Acta, 213, 368–374. https://doi.org/10.1016/j.electacta.2016.06.124

Gualtieri, A. F., Gatta, G. Di., Arletti, R., Artioli, G., Ballirano, P., Cruciani, G., Guagliardi, A., Malferrari, D., Masciocchi, N., & Scardi, P. (2019). Quantitative phase analysis using the Rietveld method: Towards a procedure for checking the reliability and quality of the results. Periodico Di Mineralogia, 88(2), 147–151. https://doi.org/10.2451/2019PM870

Gulley, A. L., McCullough, E. A., & Shedd, K. B. (2019). China's domestic and foreign influence in the global cobalt supply chain. Resources Policy, 62(June 2018), 317–323. https://doi.org/10.1016/j.resourpol.2019.03.015

Gummow, R. J., de Kock, A., & Thackeray, M. M. (1994). Improved capacity retention in rechargeable 4 V lithium/lithium-manganese oxide (spinel) cells. Solid State Ionics, 69(1), 59–67. https://doi.org/10.1016/0167-2738(94)90450-2

Gummow, Rosalind J., Vamvounis, G., Kannan, M. B., & He, Y. (2018). Calcium-Ion Batteries: Current State-of-the-Art and Future Perspectives. Advanced Materials, 30(39), 1–14. https://doi.org/10.1002/adma.201801702

Guo, X., Zhang, J., & Tian, Q. (2020). Modeling the potential impact of future lithium recycling on lithium demand in China: A dynamic SFA approach. Renewable and Sustainable Energy Reviews, October, 110461. https://doi.org/10.1016/j.rser.2020.110461

Habib, K., Hansdóttir, S. T., & Habib, H. (2020). Critical metals for electromobility: Global demand scenarios for passenger vehicles, 2015–2050. Resources, Conservation and Recycling, 154(December 2019), 104603. https://doi.org/10.1016/j.resconrec.2019.104603

Harper, G., Sommerville, R., Kendrick, E., Driscoll, L., Slater, P., Stolkin, R., Walton, A., Christensen, P., Heidrich, O., Lambert, S., Abbott, A., Ryder, K., Gaines, L., & Anderson, P. (2019). Recycling lithium-ion batteries from electric vehicles. Nature, 575(7781), 75–86. https://doi.org/10.1038/s41586-019-1682-5

Hasan, S., Islam, M. S., Bashar, S. M. A., Al Noman Tamzid, A., Hossain, R. Bin, Haque, M. A., & Rahaman, M. F. (2023). Beyond Lithium-Ion: The Promise and Pitfalls of BYD's Blade Batteries for Electric Vehicles. E3S Web of Conferences, 469, 00005. https://doi.org/10.1051/e3sconf/202346900005

Hautier, G., Ong, S. P., Jain, A., Moore, C. J., & Ceder, G. (2012). Accuracy of density functional theory in predicting formation energies of ternary oxides from binary oxides and its implication on phase stability. Physical Review B - Condensed Matter and Materials Physics, 85(15). https://doi.org/10.1103/PhysRevB.85.155208

Hawkins, T. R., Singh, B., & Guillaume Majeau-Bettez, A. H. S. (2013). Comparative Environmental Life Cycle Assessment of Conventional and Electric Vehicles. Journal of Industrial Ecology, 17(1), 53–64.

Haynes, W. M. (2016). CRC Handbook of Chemistry and Physics (97th ed.). CRC Press.

Helbig, C., Bradshaw, A. M., Wietschel, L., Thorenz, A., & Tuma, A. (2018). Supply risks associated with lithium-ion battery materials. Journal of Cleaner Production, 172, 274–286. https://doi.org/10.1016/j.jclepro.2017.10.122

Hestenes, J. C., Sadowski, J. T., May, R., & Marbella, L. E. (2023). Transition Metal Dissolution Mechanisms and Impacts on Electronic Conductivity in Composite LiNio.5Mn1.5O4 Cathode Films. ACS Materials Au, 3(2), 88–101. https://doi.org/10.1021/acsmaterialsau.2c00060

Hewat, A. W. (1979). Absorption corrections for neutron diffraction. Acta Crystallography, 35, 248–250.

Hoang, K., & Johannes, M. (2016). Defect Physics and Chemistry in Layered Mixed Transition Metal Oxide Cathode Materials: (Ni,Co,Mn) vs (Ni,Co,Al). Chemistry of Materials, 28(5), 1325–1334. https://doi.org/10.1021/acs.chemmater.5b04219

Hou, P., Zhang, H., Zi, Z., Zhang, L., & Xu, X. (2017). Core-shell and concentration-gradient cathodes prepared via co-precipitation reaction for advanced lithium-ion batteries. Journal of Materials Chemistry A, 5(9), 4254–4279. https://doi.org/10.1039/c6ta10297b

Huang, B., Pan, Z., Su, X., & An, L. (2018). Recycling of lithium-ion batteries: Recent advances and perspectives. Journal of Power Sources, 399(July), 274–286. https://doi.org/10.1016/j.jpowsour.2018.07.116

Intan, N. N., Klyukin, K., & Alexandrov, V. (2018). Theoretical Insights into Oxidation States of Transition Metals at (001) and (111) LiNi 0.5 Mn 1.5 O 4 Spinel Surfaces. Journal of The Electrochemical Society, 165(5), A1099–A1103. https://doi.org/10.1149/2.1251805jes

Iurilli, P., Brivio, C., & Wood, V. (2021). On the use of electrochemical impedance spectroscopy to characterize and model the aging phenomena of lithium-ion batteries: a critical review. Journal of Power Sources, 505, 229860. https://doi.org/10.1016/j.jpowsour.2021.229860

Jain, A., Ong, S. P., Hautier, G., Chen, W., Richards, W. D., Dacek, S., Cholia, S., Gunter, D., Skinner, D., Ceder, G., & Persson, K. A. (2013). Commentary: The materials project: A materials genome approach to accelerating materials innovation. APL Materials, 1(1). https://doi.org/10.1063/1.4812323

Jehnichen, P., Wedlich, K., & Korte, C. (2019). Degradation of high-voltage cathodes for advanced lithium-ion batteries—differential capacity study on differently balanced cells. In Science and Technology of Advanced Materials (Vol. 20, Issue 1, pp. 1–9). https://doi.org/10.1080/14686996.2018.1550625

Jeppe Winther Hedegaard. (2019). The Cathode Material for Next-Generation Lithium ion Batteries is Ready. Topsoe. https://www.topsoe.com/blog/the-cathode-material-for-next-generation-lithium-ion-batteries-is-ready

Jordans, F. (2021). Why automakers are joining the push against deep seabed mining. CS Monitors. https://www.csmonitor.com/Environment/2021/0331/Why-automakers-are-joining-the-push-against-deep-seabed-mining

Kader, Z. A., Marshall, A., & Kennedy, J. (2021). A review on sustainable recycling technologies for lithium-ion batteries. Emergent Materials, 725–735. https://doi.org/10.1007/s42247-021-00201-w

Kallitsis, E., Korre, A., Kelsall, G., Kupfersberger, M., & Nie, Z. (2020). Environmental life cycle assessment of the production in China of lithium-ion batteries with nickel-cobalt-manganese cathodes utilising novel electrode chemistries. Journal of Cleaner Production, 254, 120067. https://doi.org/10.1016/j.jclepro.2020.120067

Kaur, G., & Gates, B. D. (2022). Review—Surface Coatings for Cathodes in Lithium Ion Batteries: From Crystal Structures to Electrochemical Performance. Journal of The Electrochemical Society, 169(4), 043504. https://doi.org/10.1149/1945-7111/ac60f3

Kavanagh, S. R., Squires, A. G., Nicolson, A., Mosquera-Lois, I., Ganose, A. M., Zhu, B., Brlec, K., Walsh, A., & Scanlon, D. O. (2024). doped: PythonToolkit for Robust and Repeatable Charged Defect Supercell Calculations. Journal of Open Source Software, 9(96), 6433. https://doi.org/10.21105/joss.06433

Kelly, J. C., Dai, Q., & Wang, M. (2019). Globally regional life cycle analysis of automotive lithium-ion nickel manganese cobalt batteries. Mitigation and Adaptation Strategies for Global Change, 371–396. https://doi.org/10.1007/s11027-019-09869-2

Kim, J. H., Myung, S. T., Yoon, C. S., Kang, S. G., & Sun, Y. K. (2004). Comparative Study of LiNi0.5Mn1.5O 4-δ and LiNi0.5Mn1.5O4 Cathodes Having Two Crystallographic Structures: Fd3m and P4332. Chemistry of Materials, 16(5), 906–914. https://doi.org/10.1021/cm035050s

Kim, Jung Hyun, Pieczonka, N. P. W., Li, Z., Wu, Y., Harris, S., & Powell, B. R. (2013). Understanding the capacity fading mechanism in LiNi0.5Mn 1.5O4/graphite Li-ion batteries. Electrochimica Acta, 90, 556–562. https://doi.org/10.1016/j.electacta.2012.12.069

Kim, S., Hood, S. N., Park, J. S., Whalley, L. D., & Walsh, A. (2020). Quick-start guide for first-principles modelling of point defects in crystalline materials. JPhys Energy, 2(3), 1–8. https://doi.org/10.1088/2515-7655/aba081

Kim, S. W., Seo, D. H., Ma, X., Ceder, G., & Kang, K. (2012). Electrode materials for rechargeable sodium-ion batteries: Potential alternatives to current lithium-ion batteries. Advanced Energy Materials, 2(7), 710–721. https://doi.org/10.1002/aenm.201200026

KITAJOU, A., TANAKA, K., MIKI, H., KOGA, H., OKAJIMA, T., & OKADA, S. (2016). Improvement of Cathode Properties by Lithium Excess in Disordered Rocksalt Li2+2xMn1−xTi1−xO4. Electrochemistry, 84(8), 597–600. https://doi.org/10.5796/electrochemistry.84.597

Kittel, C., & Kroemer, H. (1998). Thermal Physics. American Association of Physics Teachers.

Kiziltas-Yavuz, N., Yavuz, M., Indris, S., Bramnik, N. N., Knapp, M., Dolotko, O., Das, B., Ehrenberg, H., & Bhaskar, A. (2016). Enhancement of electrochemical performance by simultaneous substitution of Ni and Mn with Fe in Ni-Mn spinel cathodes for Li-ion batteries. Journal of Power Sources, 327, 507–518. https://doi.org/10.1016/j.jpowsour.2016.07.047

Klein, S., Harte, P., van Wickeren, S., Borzutzki, K., Röser, S., Bärmann, P., Nowak, S., Winter, M., Placke, T., & Kasnatscheew, J. (2021). Re-evaluating common electrolyte additives for high-voltage lithium ion batteries. Cell Reports Physical Science, 2(8). https://doi.org/10.1016/j.xcrp.2021.100521

Ko, G., Jeong, S., Park, S., Lee, J., Kim, S., Shin, Y., Kim, W., & Kwon, K. (2023). Doping strategies for enhancing the performance of lithium nickel manganese cobalt oxide cathode materials in lithium-ion batteries. Energy Storage Materials, 60(May), 102840. https://doi.org/10.1016/j.ensm.2023.102840

Kresse, G., & Furthmüller, J. (1996a). Efficiency of ab-initio total energy calculations for metals and semiconductors using a plane-wave basis set. Computational Materials Science, 6(1), 15–50. https://doi.org/10.1016/0927-0256(96)00008-0

Kresse, G., & Furthmüller, J. (1996b). Efficient iterative schemes for ab initio total-energy calculations using a plane-wave basis set. Physical Review A, 54(16), 11169–11186. https://doi.org/10.1021/acs.jpca.0c01375

Kresse, G., & Hafner, J. (1993). Ab initio molecular dynamics for liquid metals. Physical Review B, 47(1), 558–561. https://doi.org/10.1103/PhysRevB.47.558

Kresse, G., & Joubert, D. (1999). From ultrasoft pseudopotentials to the projector augmented-wave method. Physical Review B - Condensed Matter and Materials Physics, 59(3), 1758–1775. https://doi.org/10.1103/PhysRevB.59.1758

Lander, L., Cleaver, T., Rajaeifar, M. A., Nguyen-Tien, V., Elliott, R. J. R., Heidrich, O., Kendrick, E., Edge, J. S., & Offer, G. (2021). Financial viability of electric vehicle lithium-ion battery recycling. IScience, 24(7), 102787. https://doi.org/10.1016/j.isci.2021.102787

Landesfeind, J., Pritzl, D., & Gasteiger, H. A. (2017). An Analysis Protocol for Three-Electrode Li-Ion Battery Impedance Spectra: Part I. Analysis of a High-Voltage Positive Electrode. Journal of The Electrochemical Society, 164(7), A1773–A1783. https://doi.org/10.1149/2.0131709jes

LaRocca, G. M. (2020). Working Paper ID-067 Global Value Chains: Lithium in Lithium-ion Batteries for Electric Vehicles U . S . international Trade Commission Global Value Chains: Vehicles. July.

Larson, A. C., & Von Dreele, R. B. (2004). General Structure Analysis System (GSAS),. Los Alamos National Laboratory Report LAUR 86-748, 748.

Lazanas, A. C., & Prodromidis, M. I. (2023). Electrochemical Impedance Spectroscopy—A Tutorial. ACS Measurement Science Au, 3(3), 162–193. https://doi.org/10.1021/acsmeasuresciau.2c00070

Lebens-Higgins, Z. W., Halat, D. M., Faenza, N. V., Wahila, M. J., Mascheck, M., Wiell, T., Eriksson, S. K., Palmgren, P., Rodriguez, J., Badway, F., Pereira, N., Amatucci, G. G., Lee, T. L., Grey, C. P., & Piper, L. F. J. (2019). Surface Chemistry Dependence on Aluminum Doping in Ni-rich LiNi0.8Co0.2-yAlyO2 Cathodes. Scientific Reports, 9(1), 1–12. https://doi.org/10.1038/s41598-019-53932-6

Lèbre, É., Stringer, M., Svobodova, K., Owen, J. R., Kemp, D., Côte, C., Arratia-Solar, A., & Valenta, R. K. (2020). The social and environmental complexities of extracting energy transition metals. Nature Communications, 11(1), 1–8. https://doi.org/10.1038/s41467-020-18661-9

Lee, E. S., Nam, K. W., Hu, E., & Manthiram, A. (2012). Influence of cation ordering and lattice distortion on the charge-discharge behavior of LiMn 1.5 Ni 0.5 O 4 Spinel between 5.0 and 2.0 v. Chemistry of Materials, 24(18), 3610–3620. https://doi.org/10.1021/cm3020836

Lee, J., Kim, C., & Kang, B. (2015). High electrochemical performance of high-voltage LiNi0.5Mn1.5O4 by decoupling the Ni/Mn disordering from the presence of Mn3+ ions. NPG Asia Materials, 7(8). https://doi.org/10.1038/am.2015.94

Lee, R., & Gifford, S. (2020). The importance of coherent regulatory and policy strategies for the recycling of EV batteries. Faraday Insights, 8.

Lee, T. L., & Duncan, D. A. (2018). A Two-Color Beamline for Electron Spectroscopies at Diamond Light Source. Synchrotron Radiation News, 31(4), 16–22. https://doi.org/10.1080/08940886.2018.1483653

- Lei, Z., Naveed, A., Lei, J., Wang, J., Yang, J., Nuli, Y., Meng, X., & Zhao, Y. (2017). High performance nano-sized LiMn1-:XFexPO4 cathode materials for advanced lithium-ion batteries. RSC Advances, 7(69), 43708–43715. https://doi.org/10.1039/c7ra08993g
- Létiche, M., Hallot, M., Huvé, M., Brousse, T., Roussel, P., & Lethien, C. (2017). Tuning the Cation Ordering with the Deposition Pressure in Sputtered LiMn1.5Ni0.5O4 Thin Film Deposited on Functional Current Collectors for Li-Ion Microbattery Applications. Chemistry of Materials, 29(14), 6044–6057. https://doi.org/10.1021/acs.chemmater.7b01921
- Li, C., Zhao, Y., Zhang, H., Liu, J., Jing, J., Cui, X., & Li, S. (2013). Compatibility between LiNio.5Mn1.5O4 and electrolyte based upon lithium bis(oxalate)borate and sulfolane for high voltage lithium-ion batteries. Electrochimica Acta, 104, 134–139. https://doi.org/10.1016/j.electacta.2013.04.075
- Li, M., Wang, C., Chen, Z., Xu, K., & Lu, J. (2020). New Concepts in Electrolytes. Chemical Reviews. https://doi.org/10.1021/acs.chemrev.9b00531
- Li, S., Yan, J., Pei, Q., Sha, J., Mou, S., & Xiao, Y. (2019). Risk identification and evaluation of the long-term supply of manganese mines in China based on the VW-BGR method. Sustainability (Switzerland), 11(9), 1–23. https://doi.org/10.3390/su11092683
- Li, T., Chang, K., Hashem, A. M., Abdel-Ghany, A. E., El-Tawil, R. S., Wang, H., El-Mounayri, H., Tovar, A., Zhu, L., & Julien, C. M. (2021). Structural and Electrochemical Properties of the High Ni Content Spinel LiNiMnO4. Electrochem, 2(1), 95–117. https://doi.org/10.3390/electrochem2010009
- Li, W., Erickson, E. M., & Manthiram, A. (2020). High-nickel layered oxide cathodes for lithium-based automotive batteries. Nature Energy, 5(1), 26–34. https://doi.org/10.1038/s41560-019-0513-0
- Li, X., Wang, J., Zhang, S., Sun, L., Zhang, W., Dang, F., Seifert, H. J., & Du, Y. (2021). Intrinsic Defects in LiMn2O4: First-Principles Calculations. ACS Omega, 6(33), 21255–21264. https://doi.org/10.1021/acsomega.1c01162
- Li, Z. Q., Liu, Y. F., Liu, H. X., Zhu, Y. F., Wang, J., Zhang, M., Qiu, L., Guo, X. D., Chou, S. L., & Xiao, Y. (2024). Kinetically controlled synthesis of low-strain disordered micro-nano high voltage spinel cathodes with exposed {111} facets. Chemical Science, 15, 11302–11310. https://doi.org/10.1039/d4sc02754j
- Liang, G., Olsson, E., Zou, J., Wu, Z., Li, J., Lu, C.-Z., D'Angelo, A. M., Johannessen, B., Thomsen, L., Cowie, B., Peterso, V. K., Cai, Q., Pang, W. K., & Guo, Z. (2022). Introducing 4s–2p Orbital Hybridization to Stabilize Spinel Oxide Cathodes for Lithium-Ion Batteries.

Angewandte Chemie International Edition, 61, e202201969. https://onlinelibrary.wiley.com/doi/epdf/10.1002/anie.202201969

Liang, G., Peterson, V. K., See, K. W., Guo, Z., & Pang, W. K. (2020). Developing high-voltage spinel LiNi 0.5 Mn 1.5 O 4 cathodes for high-energy-density lithium-ion batteries: current achievements and future prospects. Journal of Materials Chemistry A, 8, 15373–15398. https://doi.org/10.1039/d0ta02812f

Liang, G., Wu, Z., Didier, C., Zhang, W., Cuan, J., Li, B., Ko, K., Hung, P., Lu, C., Chen, Y., Leniec, G., Kaczmarek, S. M., Johannessen, B., Thomsen, L., Peterson, V. K., Pang, W. K., & Guo, Z. (2020). A Long Cycle-Life High-Voltage Spinel Lithium-Ion Battery Electrode Achieved by Site-Selective Doping. Angewandte Chemie, 132(26), 10681–10689. https://doi.org/10.1002/ange.202001454

Liao, Y., Zhang, H., Peng, Y., Hu, Y., Liang, J., Gong, Z., Wei, Y., & Yang, Y. (2024). Electrolyte Degradation During Aging Process of Lithium-Ion Batteries: Mechanisms, Characterization, and Quantitative Analysis. Advanced Energy Materials, 14(18), 2304295. https://onlinelibrary.wiley.com/doi/abs/10.1002/aenm.202304295#:~:text=The degradation of the electrolytes,1) Loss of lithium inventory.

Lin, M., Ben, L., Sun, Y., Wang, H., Yang, Z., Gu, L., Yu, X., Yang, X. Q., Zhao, H., Yu, R., Armand, M., & Huang, X. (2015). Insight into the atomic structure of high-voltage spinel Lini0.5mn1.5o4 cathode material in the first cycle. Chemistry of Materials, 27(1), 292–303. https://doi.org/10.1021/cm503972a

Lin, X., Khosravinia, K., Hu, X., Li, J., & Lu, W. (2021). Lithium Plating Mechanism, Detection, and Mitigation in Lithium-Ion Batteries. Progress in Energy and Combustion Science, 87(September 2020). https://doi.org/10.1016/j.pecs.2021.100953

Lin, Y., Välikangas, J., Sliz, R., Molaiyan, P., Hu, T., & Lassi, U. (2023). Optimized Morphology and Tuning the Mn3+ Content of LiNi0.5Mn1.5O4 Cathode Material for Li-lon Batteries. Materials, 16(8), 3116. https://doi.org/10.3390/ma16083116

Lin, Z., Liu, T., Ai, X., & Liang, C. (2018). Aligning academia and industry for unified battery performance metrics. Nature Communications, 9(1), 8–12. https://doi.org/10.1038/s41467-018-07599-8

Lithium. (2021). Trading Economics. https://tradingeconomics.com/commodity/lithium
Lithium statistics and information. (2020). In U.S. Geological Survey,2020 (Vol. 53, Issue 9).

Liu, Chaofeng, Neale, Z. G., & Cao, G. (2016). Understanding electrochemical potentials of cathode materials in rechargeable batteries. Materials Today, 19(2), 109–123. https://doi.org/10.1016/j.mattod.2015.10.009

Liu, Chunwei, Lin, J., Cao, H., Zhang, Y., & Sun, Z. (2019). Recycling of spent lithium-ion batteries in view of lithium recovery: A critical review. Journal of Cleaner Production, 228(1), 801–813. https://doi.org/10.1016/j.jclepro.2019.04.304

Liu, Cong, Wu, M., Liu, Y., Lu, Z., Yang, Y., Shi, S., & Yang, G. (2018). Effect of ball milling conditions on microstructure and lithium storage properties of LiNi0.5Mn1.5O4 as cathode for lithium-ion batteries. Materials Research Bulletin, 99(November 2017), 436–443. https://doi.org/10.1016/j.materresbull.2017.11.048

Liu, D., Han, J., & Goodenough, J. B. (2010). Structure, morphology, and cathode performance of Li 1-x [Ni 0.5 Mn 1.5 ]O 4 prepared by coprecipitation with oxalic acid. Journal of Power Sources, 195(9), 2918–2923. https://doi.org/10.1016/j.jpowsour.2009.11.024

Liu, Haidong, Naylor, A. J., Ashok Sreekumar Menon, W. R. B., Edström, K., & Younesi, R. (2020). Understanding the Roles of Tris(trimethylsilyl) Phosphite(TMSPi) in LiNi0.8Mn0.1Co0.1O2 (NMC811)/Silicon–Graphite(Si–Gr) Lithium-Ion Batteries. Advanced Materials Interfaces, 7, 2000277.

Liu, Hao, Liu, H., Lapidus, S. H., Meng, Y. S., Chupas, P. J., & Chapman, K. W. (2017). Sensitivity and Limitations of Structures from X-ray and Neutron-Based Diffraction Analyses of Transition Metal Oxide Lithium-Battery Electrodes. Journal of The Electrochemical Society, 164(9), A1802–A1811. https://doi.org/10.1149/2.0271709jes

Liu, Hongmei, Zhu, G., Zhang, L., Qu, Q., Shen, M., & Zheng, H. (2015). Controllable synthesis of spinel lithium nickel manganese oxide cathode material with enhanced electrochemical performances through a modified oxalate co-precipitation method. Journal of Power Sources, 274, 1180–1187. https://doi.org/10.1016/j.jpowsour.2014.10.154

Liu, J., & Manthiram, A. (2009). Understanding the improved electrochemical performances of Fe-substituted 5 V spinel cathode LiMn1.5Ni0.5O4. Journal of Physical Chemistry C, 113(33), 15073–15079. https://doi.org/10.1021/jp904276t

Liu, M. H., Huang, H. T., Lin, C. M., Chen, J. M., & Liao, S. C. (2014). Mg gradient-doped LiNi0.5Mn1.5O4 as the cathode material for Li-ion batteries. Electrochimica Acta, 120, 133–139. https://doi.org/10.1016/j.electacta.2013.12.065

Liu, Xiaosong, & Weng, T. C. (2016). Synchrotron-based x-ray absorption spectroscopy for energy materials. MRS Bulletin, 41(6), 466–472. https://doi.org/10.1557/mrs.2016.113

Liu, Xuelian, Maffre, M., Tie, D., Wagner, N. P., Félix, N. C., Azmi, R., Stokes, K., Vullum, P. E., Bailly, J., Pal, S., Evans, G., Buga, M., Hahlin, M., Edström, K., Clark, S., & Vlad, A. (2023). Surface, Structural, and Electrochemical Analysis of High-Voltage Spinel Cathode LiNi 0.5 Mn 1.5 O 4 Evolution Upon Ambient Storage Conditions . Journal of The Electrochemical Society, 170(10), 100527. https://doi.org/10.1149/1945-7111/ad0263

Liu, Y. H., Chen, W. C., Hsueh, C. H., & Hsu, C. L. (2022). Elucidating the function of modified carbon blacks in high-voltage lithium-ion batteries: impact on electrolyte decomposition. Materials Today Chemistry, 25, 100934. https://doi.org/10.1016/j.mtchem.2022.100934

Liu, Z., Jiang, Y., Zeng, X., Xiao, G., Song, H., & Liao, S. (2014). Two-step oxalate approach for the preparation of high performance LiNi 0.5Mn1.5O4 cathode material with high voltage. Journal of Power Sources, 247, 437–443. https://doi.org/10.1016/j.jpowsour.2013.09.002

Locati, C., Lafont, U., Simonin, L., Ooms, F., & Kelder, E. M. (2007). Mg-doped LiNi0.5Mn1.5O4 spinel for cathode materials. Journal of Power Sources, 174(2), 847–851. https://doi.org/10.1016/j.jpowsour.2007.06.196

Lu, X., Lian, G. J., Parker, J., Ge, R., Sadan, M. K., Smith, R. M., & Cumming, D. (2024). Effect of carbon blacks on electrical conduction and conductive binder domain of next-generation lithium-ion batteries. Journal of Power Sources, 592, 233916. https://doi.org/10.1016/j.jpowsour.2023.233916

Luo, Ying, Li, H., Lu, T., Zhang, Y., Mao, S. S., Liu, Z., Wen, W., Xie, J., & Yan, L. (2017). Fluorine gradient-doped LiNi0.5Mn1.5O4 spinel with improved high voltage stability for Li-ion batteries. Electrochimica Acta, 238, 237–245. https://doi.org/10.1016/j.electacta.2017.04.043

Luo, Yuting, De Jesus, L. R., Andrews, J. L., Parija, A., Fleer, N., Robles, D. J., Mukherjee, P. P., & Banerjee, S. (2018). Roadblocks in Cation Diffusion Pathways: Implications of Phase Boundaries for Li-Ion Diffusivity in an Intercalation Cathode Material. ACS Applied Materials and Interfaces, 10(36), 30901–30911. https://doi.org/10.1021/acsami.8b10604

Ma, C. (2019). The Electrochemical Performance of Mg-F Co-doped Spinel LiNi0.5Mn1.5O4 Cathode Materials for Lithium-Ion Battery. International Journal of Electrochemical Science, 14, 7643–7651. https://doi.org/10.20964/2019.08.39

Ma, G., Wang, L., He, X., Zhang, J., Chen, H., Xu, W., & Ding, Y. (2018). Pseudoconcentrated Electrolyte with High Ionic Conductivity and Stability Enables High-Voltage Lithium-Ion Battery Chemistry. ACS Applied Energy Materials, 1(10), 5446–5452. https://doi.org/10.1021/acsaem.8b01020

Ma, J., Hu, P., Cui, G., & Chen, L. (2016). Surface and Interface Issues in Spinel LiNio.5Mn1.5O4: Insights into a Potential Cathode Material for High Energy Density Lithium Ion Batteries. Chemistry of Materials, 28(11), 3578–3606. https://doi.org/10.1021/acs.chemmater.6b00948

Madec, L., & Martinez, H. (2018). Impact of the metal electrode size in half-cells studies: Example of graphite/Li coin cells. Electrochemistry Communications, 90(April), 61–64. https://doi.org/10.1016/j.elecom.2018.04.007

Major, G. H., Fairley, N., Sherwood, P. M. A., Linford, M. R., Terry, J., Fernandez, V., & Artyushkova, K. (2020). Practical guide for curve fitting in x-ray photoelectron spectroscopy. Journal of Vacuum Science & Technology A, 38(6). https://doi.org/10.1116/6.0000377

Marcelo, A., Goffaux, N., & Hoffman, K. (2020). How clean can the nickel industry become? McKinsey Insights, September, 1–6.

Markevich, E., Salitra, G., Fridman, K., Sharabi, R., Gershinsky, G., Garsuch, A., Semrau, G., Schmidt, M. A., & Aurbach, D. (2014). Fluoroethylene Carbonate as an Important Component in ElectrolyteSolutions for High-Voltage Lithium Batteries: Role of SurfaceChemistry on the Cathode. Langmuir, 30, 7414–7424. https://pubs.acs.org/doi/epdf/10.1021/la501368y

May, I. V., Kleyn, S. V., & Vekovshinina, S. A. (2019). Assessment of impact of accumulated environmental damage to the quality of soil, surface and groundwater, agricultural products resulted from the mining enterprise. IOP Conference Series: Earth and Environmental Science, 315(6). https://doi.org/10.1088/1755-1315/315/6/062024

Mayyas, A., Steward, D., & Mann, M. (2019). The case for recycling: Overview and challenges in the material supply chain for automotive li-ion batteries. Sustainable Materials and Technologies, 19, e00087. https://doi.org/10.1016/j.susmat.2018.e00087

Mccusker, L. B., Von Dreele, R. B., Cox, D. E., Louër, D., & Scardi, P. (1999). Rietveld refinement guidelines. Journal of Applied Crystallography, 32(1), 36–50. https://doi.org/10.1107/S0021889898009856

McKinsey&Company. Lithium (2018).and cobalt-a tale of two commodities. June. McKinsey&Company Metals Mining, and https://www.mckinsey.com/~/media/mckinsey/industries/metals and mining/our insights/lithium and cobalt a tale of two commodities/lithium-and-cobalt-a-tale-of-twocommodities.ashx

McKinsey. (2021). Has South East Asia taken a firm grip on the nickel value chain? October 2019, 2019.

Merritt, E. A. (2012). To B or not to B: A question of resolution? Acta Crystallographica Section D: Biological Crystallography, 68(4), 468–477. https://doi.org/10.1107/S0907444911028320

Metallary. (n.d.). Iron Price. Retrieved January 11, 2021, from https://www.metalary.com/iron-price/

Mohtadi, R., & Mizuno, F. (2014). Magnesium batteries: Current state of the art, issues and future perspectives. Beilstein Journal of Nanotechnology, 5(1), 1291–1311. https://doi.org/10.3762/bjnano.5.143

Moore, D. (2021). Lithium-ion battery waste fires costing UK over 150m a year. Circular. https://www.circularonline.co.uk/news/lithium-ion-battery-waste-fires-costing-uk-over-150m-a-year/

Moorhead-Rosenberg, Z., Huq, A., Goodenough, J. B., & Manthiram, A. (2015). Electronic and Electrochemical Properties of Li1-xMn1.5Ni0.5O4 Spinel Cathodes As a Function of Lithium Content and Cation Ordering. Chemistry of Materials, 27(20), 6934–6945. https://doi.org/10.1021/acs.chemmater.5b01356

Morgan, D. J. (2023). XPS insights: Sample degradation in X-ray photoelectronspectroscopy. Surface and Interface Analysis, 55, 331–335.

Mosquera-Lois, I., & Kavanagh, S. R. (2021). In search of hidden defects. Matter, 4(8), 2602–2605. https://doi.org/10.1016/j.matt.2021.06.003

Mosquera-Lois, I., Kavanagh, S. R., Klarbring, J., Tolborg, K., & Walsh, A. (2023). Imperfections are not 0 K: free energy of point defects in crystals. Chemical Society Reviews, 52(17), 5812–5826. https://doi.org/10.1039/d3cs00432e

Mosquera-Lois, I., Kavanagh, S. R., Walsh, A., & Scanlon, D. O. (2022). ShakeNBreak: Navigating the defect configurational landscape. Journal of Open Source Software, 7(80), 4817. https://doi.org/10.21105/joss.04817

Mosquera-Lois, I., Kavanagh, S. R., Walsh, A., & Scanlon, D. O. (2023). Identifying the ground state structures of point defects in solids. Npj Computational Materials, 9(1). https://doi.org/10.1038/s41524-023-00973-1

Mueller, T., Hautier, G., Jain, A., & Ceder, G. (2011). Evaluation of tavorite-structured cathode materials for lithium-ion batteries using high-throughput computing. Chemistry of Materials, 23(17), 3854–3862. https://doi.org/10.1021/cm200753g

Murdock, B. E., Armstrong, C. G., Smith, D. E., Tapia-Ruiz, N., & Toghill, K. E. (2022). Misreported non-aqueous reference potentials: The battery research endemic. Joule, 6(5), 928–934. https://doi.org/10.1016/j.joule.2022.04.009

Murdock, B. E., Cen, J., Squires, A. G., Kavanagh, S. R., Scanlon, D. O., Zhang, L., & Tapia-Ruiz, N. (2024). Li-Site Defects Induce Formation ofLi-Rich Impurity Phases: Implications for Charge Distribution and Performance of LiNi0.5–xMxMn1.5O4 Cathodes (M = Fe and Mg; x = 0.05–0.2). Advanced Materials, 36, 2400343.

Murdock, B. E., Toghill, K. E., & Tapia-ruiz, N. (2021). A perspective on the Sustainability Cathode Materials used in Lithium-ion Batteries. Advanced Energy Materials, 11(37), 1–27. https://doi.org/10.1002/aenm.202102028

Myung, S. T., Maglia, F., Park, K. J., Yoon, C. S., Lamp, P., Kim, S. J., & Sun, Y. K. (2017). Nickel-Rich Layered Cathode Materials for Automotive Lithium-Ion Batteries: Achievements and Perspectives. ACS Energy Letters, 2(1), 196–223. https://doi.org/10.1021/acsenergylett.6b00594

Nagler, S. E., Stoica, A. D., Stoica, G. M., An, K., Skorpenske, H. D., Rios, O., Hendin, D. B., & Bower, N. W. (2019). Time-of-Flight Neutron Diffraction (TOF-ND) Analyses of the Composition and Minting of Ancient Judaean "Biblical" Coins. Journal of Analytical Methods in Chemistry, 2019(1), 164058.

Narins, T. P. (2017). The battery business: Lithium availability and the growth of the global electric car industry. Extractive Industries and Society, 4(2), 321–328. https://doi.org/10.1016/j.exis.2017.01.013

Nguyen, M. T., Pham, H. Q., Berrocal, J. A., Gunkel, I., & Steiner, U. (2023). An electrolyte additive for the improved high voltage performance of LiNi0.5Mn1.5O4 (LNMO) cathodes in Li-ion batteries. Journal of Materials Chemistry A, 7670–7678. https://doi.org/10.1039/d2ta09930f

Nickel. (2021). Trading Economics. https://tradingeconomics.com/commodity/nickel

Nisar, U., Bansmann, J., Hebel, M., Reichel, B., Mancini, M., Wohlfahrt-Mehrens, M., Hölzle, M., & Axmann, P. (2024). Borate modified Co-free LiNio.5Mn1.5O4 cathode material: A pathway to superior interface and cycling stability in LNMO/graphite full-cells. Chemical Engineering Journal, 493(March). https://doi.org/10.1016/j.cej.2024.152416

Nisar, U., Muralidharan, N., Essehli, R., Amin, R., & Belharouak, I. (2021). Valuation of Surface Coatings in High-Energy Density Lithium-ion Battery Cathode Materials. Energy Storage Materials, 38(November 2020), 309–328. https://doi.org/10.1016/j.ensm.2021.03.015

Nishi, Y. (2001). Lithium ion secondary batteries; Past 10 years and the future. Journal of Power Sources, 100(1–2), 101–106. https://doi.org/10.1016/S0378-7753(01)00887-4

Nitta, N., Wu, F., Lee, J. T., & Yushin, G. (2015). Li-ion battery materials: Present and future. Materials Today, 18(5), 252–264. https://doi.org/10.1016/j.mattod.2014.10.040

Noh, M., & Cho, J. (2013). Optimized Synthetic Conditions of LiNi 0.5 Co 0.2 Mn 0.3 O 2 Cathode Materials for High Rate Lithium Batteries via Co-Precipitation Method . Journal of The Electrochemical Society, 160(1), A105–A111. https://doi.org/10.1149/2.004302jes

Nordelöf, A., Poulikidou, S., Chordia, M., de Oliveira, F. B., Tivander, J., & Arvidsson, R. (2019). Methodological approaches to end-of-life modelling in life cycle assessments of lithium-ion batteries. Batteries, 5(3). https://doi.org/10.3390/batteries5030051

Ohzuku, T., Ariyoshi, K., Takeda, S., & Sakai, Y. (2001). Synthesis and characterization of 5 V insertion material of Li[FeyMn2-y]O4 for lithium-ion batteries. Electrochimica Acta, 46(15), 2327–2336. https://doi.org/10.1016/S0013-4686(00)00725-8

Olivetti, E. A., Ceder, G., Gaustad, G. G., & Fu, X. (2017). Lithium-Ion Battery Supply Chain Considerations: Analysis of Potential Bottlenecks in Critical Metals. Joule, 1(2), 229–243. https://doi.org/10.1016/j.joule.2017.08.019

Ooms, F. G. B., Kelder, E. M., Schoonman, J., Wagemaker, M., & Mulder, F. M. (2002). High-voltage LiMgNIMnO4 spinels for Li-ion batteries. Solid State Ionics, 153, 143–153.

Perdew, J. P., Ruzsinszky, A., Csonka, G. I., Vydrov, O. A., Scuseria, G. E., Constantin, L. A., Zhou, X., & Burke, K. (2008). Restoring the density-gradient expansion for exchange in solids and surfaces. Physical Review Letters, 100(13), 1–4. https://doi.org/10.1103/PhysRevLett.100.136406

Perks, C., & Mudd, G. (2019). Titanium, zirconium resources and production: A state of the art literature review. Ore Geology Reviews, 107(February), 629–646. https://doi.org/10.1016/j.oregeorev.2019.02.025

Piątek, J., Afyon, S., Budnyak, T. M., Budnyk, S., Sipponen, M. H., & Slabon, A. (2020). Sustainable Li-Ion Batteries: Chemistry and Recycling. Advanced Energy Materials, 2003456. https://doi.org/10.1002/aenm.202003456

Pieczonka, N. P. W., Liu, Z., Lu, P., Olson, K. L., Moote, J., Powell, B. R., & Kim, J. H. (2013). Understanding transition-metal dissolution behavior in LiNi 0.5 Mn 1.5 O 4 high-voltage spinel for lithium ion batteries. Journal of Physical Chemistry C, 117(31), 15947–15957. https://doi.org/10.1021/jp405158m

Pritzl, D., Bumberger, A. E., Wetjen, M., Landesfeind, J., Solchenbach, S., & Gasteiger, H. A. (2019). Identifying Contact Resistances in High-Voltage Cathodes by Impedance Spectroscopy. Journal of The Electrochemical Society, 166(4), A582–A590. https://doi.org/10.1149/2.0451904jes

Qiao, R., Chuang, Y. De, Yan, S., & Yang, W. (2012). Soft X-Ray Irradiation Effects of Li2O2, Li2CO3 and Li2O Revealed by Absorption Spectroscopy. PLoS ONE, 7(11), 3–8. https://doi.org/10.1371/journal.pone.0049182

Ramesha, R. N., Bosubabu, D., Karthick Babu, M. G., & Ramesha, K. (2020). Tuning of Ni, Mn, and Co (NMC) content in 0.4(LiNixMnyCozo2)-0.4(Li2MnO3) toward stable high-capacity lithium-rich cathode materials. ACS Applied Energy Materials, 3(11), 10872–10881. https://doi.org/10.1021/acsaem.0c01897

Richa, K., Babbitt, C. W., & Gaustad, G. (2017). Eco-Efficiency Analysis of a Lithium-Ion Battery Waste Hierarchy Inspired by Circular Economy. Journal of Industrial Ecology, 21(3), 715–730. https://doi.org/10.1111/jiec.12607

Rinkel, B. L. D., Hall, D. S., Temprano, I., & Grey, C. P. (2020). Electrolyte oxidation pathways in lithium-ion batteries. Journal of the American Chemical Society, 142(35), 15058–15074. https://doi.org/10.1021/jacs.0c06363

Roberto Sifon-arevalo. (2019). Why lithium has turned from gold to dust for investors. S&P Global. https://www.spglobal.com/en/research-insights/articles/why-lithium-has-turned-from-gold-to-dust-for-investors

Roberts, S., Chen, L., Kishore, B., Dancer, C. E. J., Simmons, M. J. H., & Kendrick, E. (2022). Mechanism of gelation in high nickel content cathode slurries for sodium-ion batteries. Journal of Colloid and Interface Science, 627, 427–437. https://doi.org/10.1016/j.jcis.2022.07.033

Ruan, D., Cui, Z., Fan, J., Wang, D., Wu, Y., & Ren, X. (2024). Recent advances in electrolyte molecular design for alkali metal batteries. Chemical Science, 15(12), 4238–4274. https://doi.org/10.1039/d3sc06650a

Sanad, M. M. S., Abdellatif, H. A., Elnaggar, E. M., El-Kady, G. M., & Rashad, M. M. (2019). Understanding structural, optical, magnetic and electrical performances of Fe- or Cosubstituted spinel LiMn 1.5 Ni 0.5 O 4 cathode materials. Applied Physics A: Materials Science and Processing, 125(2), 1–10. https://doi.org/10.1007/s00339-019-2445-8

Sarkar, S., Garain, S., Mandal, D., & Chattopadhyay, K. K. (2014). Electro-active phase formation in PVDF-BiVO4 flexible nanocomposite films for high energy density storage application. RSC Advances, 4(89), 48220–48227. https://doi.org/10.1039/c4ra08427f

Schmuch, R., Wagner, R., Hörpel, G., Placke, T., & Winter, M. (2018). Performance and cost of materials for lithium-based rechargeable automotive batteries. Nature Energy, 3(4), 267–278. https://doi.org/10.1038/s41560-018-0107-2

Sears, V. (1992). Neutron scattering lengths and cross sections. Physical Review, 3(3), 26–27. https://doi.org/10.1103/PhysRev.85.555

Sezgin, Z. (2013). Ecological modernization at the intersection of environment and energy. International Journal of Energy Economics and Policy, 3(SPECIAL ISSUE), 93–101.

Shang, K. (2020). Nickel sulphate: In high-nickel batteries, safety comes into question. Roskill. https://roskill.com/news/nickel-sulphate-in-high-nickel-batteries-safety-comes-into-question/

Shannon, R. D. (1976). Revised Effective Ionic Radii and Systematic Studies of Interatomie Distances in Halides and Chaleogenides. Acta Crystallography, A32, 751–767.

Sharma, P., Das, C., Indris, S., Bergfeldt, T., Mereacre, L., Knapp, M., Geckle, U., Ehrenberg, H., & Darma, M. S. D. (2020). Synthesis and characterization of a multication doped Mn spinel, LiNio.3Cuo.1Feo.2Mn1.4O4, as 5 v positive electrode material. ACS Omega, 5(36), 22861–22873. https://doi.org/10.1021/acsomega.0c02174

Shi, X. M., Watanabe, E., Okubo, M., & Yamada, A. (2020). Does Spinel Serve as a Rigid Framework for Oxygen Redox? Chemistry of Materials, 32(17), 7181–7187. https://doi.org/10.1021/acs.chemmater.0c00599

Shin, D. W., Bridges, C. A., Huq, A., Paranthaman, M. P., & Manthiram, A. (2012). Role of Cation Ordering and Surface Segregation in High-Voltage Spinel LiMn LiMn 1.5Ni 0.5-xM xO 4(M = Cr, Fe, and Ga) Cathodes for Lithium-Ion Batteries. Chemistry of Materials, 24(19), 3720–3731. https://doi.org/10.1021/cm301844w

Shin, H., Park, J., Sastry, A. M., & Lu, W. (2015). Degradation of the solid electrolyte interphase induced by the deposition of manganese ions. Journal of Power Sources, 284, 416–427. https://doi.org/10.1016/j.jpowsour.2015.03.039

Shkrob, I. A., & Abraham, D. P. (2016). Electrocatalysis Paradigm for Protection of Cathode Materials in High-Voltage Lithium-Ion Batteries. Journal of Physical Chemistry C, 120, 15119–15128. https://pubs.acs.org/doi/epdf/10.1021/acs.jpcc.6b05756

Shu, Y., Xie, Y., Yan, W., Meng, S., Sun, D., Jin, Y., & He, K. (2019). Synergistic effect of surface plane and particle sizes on the electrochemical performance of LiNi0.5Mn1.5O4 cathode material via a facile calcination process. Journal of Power Sources, 433(April), 226708. https://doi.org/10.1016/j.jpowsour.2019.226708

Song, Y., Wang, N., & Yu, A. (2019). Temporal and spatial evolution of global iron ore supply-demand and trade structure. Resources Policy, 64(November 2017), 101506. https://doi.org/10.1016/j.resourpol.2019.101506

Sonter, L. J., Dade, M. C., Watson, J. E. M., & Valenta, R. K. (2020). Renewable energy production will exacerbate mining threats to biodiversity. Nature Communications, 11(1), 6–11. https://doi.org/10.1038/s41467-020-17928-5

Sovacool, B. K. (2021). Who are the victims of low-carbon transitions? Towards a political ecology of climate change mitigation. Energy Research and Social Science, 73(December 2020), 101916. https://doi.org/10.1016/j.erss.2021.101916

Sovacool, B. K., Hook, A., Martiskainen, M., Brock, A., & Turnheim, B. (2020). The decarbonisation divide: Contextualizing landscapes of low-carbon exploitation and toxicity in Africa. Global Environmental Change, 60(May 2019), 102028. https://doi.org/10.1016/j.gloenvcha.2019.102028

Speirs, J., Contestabile, M., Houari, Y., & Gross, R. (2014). The future of lithium availability for electric vehicle batteries. Renewable and Sustainable Energy Reviews, 35, 183–193. https://doi.org/10.1016/j.rser.2014.04.018

Squires, A. G., Scanlon, D. O., & Morgan, B. J. (2023). py-sc-fermi: self-consistent Fermi energies and defect concentrations from electronic structure calculations. Journal of Open Source Software, 8(82), 4962. https://doi.org/10.21105/joss.04962

Steward, D., Mayyas, A., & Mann, M. (2019). Economics and challenges of Li-ion battery recycling from end-of-life vehicles. Procedia Manufacturing, 33, 272–279. https://doi.org/10.1016/j.promfg.2019.04.033

Stoyanova, R., Zhecheva, E., Alcántara, R., Tirado, J. L., Bromiley, G., Bromiley, F., & Boffa Ballaran, T. (2003). Lithium/nickel mixing in the transition metal layers of lithium nickelate: High-pressure synthesis of layered Li[LixNi1-x]O 2 oxides as cathode materials for lithium-ion batteries. Solid State Ionics, 161(3–4), 197–204. https://doi.org/10.1016/S0167-2738(03)00280-7

Stüble, P., Mereacre, V., Geßwein, H., & Binder, J. R. (2023). On the Composition of LiNio.5Mn1.5O4 Cathode Active Materials. Advanced Energy Materials, 13(10). https://doi.org/10.1002/aenm.202203778

Su, C. C., He, M., Redfern, P. C., Curtiss, L. A., Shkrob, I. A., & Zhang, Z. (2017). Oxidatively stable fluorinated sulfone electrolytes for high voltage high energy lithium-ion batteries. Energy and Environmental Science, 10(4), 900–904. https://doi.org/10.1039/c7ee00035a

Sun, Y. K., Myung, S. T., Park, B. C., & Amine, K. (2006). Synthesis of spherical nano- To microscale core-shell particles Li[(Ni 0.8Co 0.1Mn 0.1) 1-x(Ni 0.5Mn 0.5) x]O 2 and their applications to lithium batteries. Chemistry of Materials, 18(22), 5159–5163. https://doi.org/10.1021/cm061746k

Syzdek, J., Marcinek, M., & Kostecki, R. (2014). Electrochemical activity of carbon blacks in LiPF6-based organic electrolytes. Journal of Power Sources, 245, 739–744. https://doi.org/10.1016/j.jpowsour.2013.07.033

Tan, D. H. S., Xu, P., & Chen, Z. (2020). Enabling sustainable critical materials for battery storage through efficient recycling and improved design: A perspective. MRS Energy & Sustainability, 7(1), 1–13. https://doi.org/10.1557/mre.2020.31

Tesla partners with nickel mine amid shortage fears. (2021). BBC News. https://www.bbc.co.uk/news/business-56288781

Thies, C., Kieckhäfer, K., Spengler, T. S., & Sodhi, M. S. (2019). Assessment of social sustainability hotspots in the supply chain of lithium-ion batteries. Procedia CIRP, 80, 292–297. https://doi.org/10.1016/j.procir.2018.12.009

Titanium Dioxide (TiO2) Production and Manufacturing Process. (n.d.). Independant Commodity Intellegence Services (ICIS).

Toby, B. H. (n.d.). GSAS Parameters & Controls: What to Refine when? (Refinement Recipes). Argonne National Laborartory. https://www.aps.anl.gov/sites/default/files/APS-Uploads/XSD/Powder-Diffraction-Crystallography/5ParametersRecipes.pdf

Toby, B. H. (2001). EXPGUI, a graphical user interface for GSAS. Journal of Applied Crystallography, 34, 210–213. https://doi.org/10.5229/jecst.2013.4.1.34

Toby, B. H. (2006). R factors in Rietveld analysis: How good is good enough? . Powder Diffraction, 21(1), 67–70. https://doi.org/10.1154/1.2179804

Tornheim, A., & O'Hanlon, D. C. (2020). What do Coulombic Efficiency and Capacity Retention Truly Measure? A Deep Dive into Cyclable Lithium Inventory, Limitation Type, and Redox Side Reactions. Journal of The Electrochemical Society, 167(11), 110520. https://doi.org/10.1149/1945-7111/ab9ee8

U.S. Geological Survey. (n.d.). Commodity Statistics and Information. Retrieved January 11, 2021, from https://www.usgs.gov/centers/nmic/commodity-statistics-and-information

United Nations. (2015). Paris Declaration on Electro-Mobility and Climate Change & Call to Action. https://unfccc.int/news/the-paris-declaration-on-electro-mobility-and-climate-change-and-call-to-action

Van De Walle, C. G., & Neugebauer, J. (2004). First-principles calculations for defects and impurities: Applications to III-nitrides. Journal of Applied Physics, 95(8), 3851–3879. https://doi.org/10.1063/1.1682673

van den Brink, S., Kleijn, R., Sprecher, B., & Tukker, A. (2020). Identifying supply risks by mapping the cobalt supply chain. Resources, Conservation and Recycling, 156(January), 104743. https://doi.org/10.1016/j.resconrec.2020.104743

Vignarooban, K., Kushagra, R., Elango, A., Badami, P., Mellander, B. E., Xu, X., Tucker, T. G., Nam, C., & Kannan, A. M. (2016). Current trends and future challenges of electrolytes for sodium-ion batteries. International Journal of Hydrogen Energy, 41(4), 2829–2846. https://doi.org/10.1016/j.ijhydene.2015.12.090

Vikström, H., Davidsson, S., & Höök, M. (2013). Lithium availability and future production outlooks. Applied Energy, 110, 252–266. https://doi.org/10.1016/j.apenergy.2013.04.005

Wang, D., Gao, C., Zhou, X., Peng, S., Tang, M., Wang, Y., Huang, L., Yang, W., & Gao, X. (2023). Enhancing reversibility of LiNi0.5Mn1.5O4 by regulating surface oxygen deficiency. Carbon Energy, 5(11), 1–9. https://doi.org/10.1002/cey2.338

Wang, H., Li, X., Li, F., Liu, X., Yang, S., & Ma, J. (2021). Formation and modification of cathode electrolyte interphase: A mini review. Electrochemistry Communications, 122, 106870. https://doi.org/10.1016/j.elecom.2020.106870

Wang, J. feng, Chen, D., Wu, W., Wang, L., & Liang, G. chuan. (2017). Effects of Na+ doping on crystalline structure and electrochemical performances of LiNio.5Mn1.5O4 cathode material. Transactions of Nonferrous Metals Society of China (English Edition), 27(10), 2239–2248. https://doi.org/10.1016/S1003-6326(17)60250-4

Wang, S. (2020). Metal Mining for Lithium-ion Battery Production of Electric Vehicles and Its Impact on Global Land Use: A Review. Icssm, 21–31.

Wang, W. N., Meng, D., Qian, G., Xie, S., Shen, Y., Chen, L., Li, X., Rao, Q., Che, H., Liu, J., He, Y. S., Ma, Z. F., & Li, L. (2020). Controlling particle size and phase purity of "single-crystal" LiNio.5Mn1.5O4 in molten-salt-assisted synthesis. Journal of Physical Chemistry C, 124(51), 27937–27945. https://doi.org/10.1021/acs.jpcc.0c09313

Weng, Y., & Zhang, H. (2024). Enhancement of the electrochemical performance of LiNio.5Mn1.5O4 cathode materials for Li-ion battery by Mo-F co-doping. Ionics. https://doi.org/10.1007/s11581-023-05366-4

Wentker, M., Greenwood, M., & Leker, J. (2019). A bottom-up approach to lithium-ion battery cost modeling with a focus on cathode active materials. Energies, 12(3), 1–18. https://doi.org/10.3390/en12030504

Weydanz, W., & Ag, S. (2009). Power Tools: Batteries. Siemens AG, 46–52. https://booksite.elsevier.com/brochures/ecps/PDFs/PowerTools\_Batteries.pdf

Williams, W. G., Ibberson, R. M., Day, P., & Enderby, J. E. (1997). GEM - General Materials Diffractometer at ISIS. Physica B: Condensed Matter, 241–243, 234–236. https://doi.org/10.1016/S0921-4526(97)00561-9

Winslow, K. M., Laux, S. J., & Townsend, T. G. (2018). A review on the growing concern and potential management strategies of waste lithium-ion batteries. Resources, Conservation and Recycling, 129(October 2017), 263–277. https://doi.org/10.1016/j.resconrec.2017.11.001

Wu, F., Zhou, H., Bai, Y., Wang, H., & Wu, C. (2015). Toward 5 v Li-Ion Batteries: Quantum Chemical Calculation and Electrochemical Characterization of Sulfone-Based High-Voltage Electrolytes. ACS Applied Materials and Interfaces, 7(27), 15098–15107. https://doi.org/10.1021/acsami.5b04477

Xia, F., Zeng, W., Peng, H., Wang, H., Sun, C., Zou, J., & Wu, J. (2023). Revealing structural degradation in layered structure oxides cathode of lithium ion batteries via in-situ transmission electron microscopy. Journal of Materials Science and Technology, 154, 189–201. https://doi.org/10.1016/j.jmst.2023.02.005

Xiao, Y., Xiang, W., Zhang, J., Zhu, Y., & Guo, X. (2016). Synthesis of spinel LiNi0.5Mn1.5O4 as advanced cathode via a modified oxalate co-precipitation method. Ionics, 22(8), 1361–1368. https://doi.org/10.1007/s11581-016-1659-4

Xiao, Z., Liu, J., Fan, G., Yu, M., Liu, J., & Gou, X. (2020). Lithium bis (oxalate) borate additive in the electrolyte to improve Li-rich layered oxide cathode materials †. MATERIALS CHEMISTRY FRONTIERS, 4, 1689–1696. https://doi.org/10.1039/d0qm00094a

Xu, M., Lu, D., Garsuch, A., & Lucht, B. L. (2012). Improved Performance of LiNi 0.5 Mn 1.5 O 4 Cathodes with Electrolytes Containing Dimethylmethylphosphonate (DMMP). Journal of The Electrochemical Society, 159(12), A2130–A2134. https://doi.org/10.1149/2.077212jes

Xu, P., Dai, Q., Gao, H., Liu, H., Zhang, M., Li, M., Chen, Y., An, K., Meng, Y. S., Liu, P., Li, Y., Spangenberger, J. S., Gaines, L., Lu, J., & Chen, Z. (2020). Efficient Direct Recycling of Lithium-Ion Battery Cathodes by Targeted Healing. Joule, 4(12), 2609–2626. https://doi.org/10.1016/j.joule.2020.10.008

Xue, L., Ueno, K., Lee, S. Y., & Angell, C. A. (2014). Enhanced performance of sulfone-based electrolytes at lithium ion battery electrodes, including the LiNi0.5Mn1.5O4 high voltage cathode. Journal of Power Sources, 262, 123–128. https://doi.org/10.1016/j.jpowsour.2014.03.099

Yamada, A., Chung, S. C., & Hinokuma, K. (2001). Optimized LiFePO4 for Lithium Battery Cathodes. Journal of The Electrochemical Society, 148(3), A224. https://doi.org/10.1149/1.1348257

Yamada, Y. (2017). Developing new functionalities of superconcentrated electrolytes for lithium-ion batteries. Electrochemistry, 85(9), 559–565. https://doi.org/10.5796/electrochemistry.85.559

Yamada, Y., Furukawa, K., Sodeyama, K., Kikuchi, K., Yaegashi, M., Tateyama, Y., & Yamada, A. (2014). Unusual stability of acetonitrile-based superconcentrated electrolytes for fast-charging lithium-ion batteries. Journal of the American Chemical Society, 136(13), 5039–5046. https://doi.org/10.1021/ja412807w

Yang, M., Zhao, X., Yao, C., Kong, Y., Ma, L., & Shen, X. (2016). Nanostructured cation disordered Li2FeTiO4/graphene composite as high capacity cathode for lithium-ion batteries. Materials Technology, 31(9), 537–543. https://doi.org/10.1080/10667857.2016.1192372

Yang, R., Chang, L., Luo, S., Bi, X., Yang, W., Cai, K., Wei, A., & Hou, Z. (2024). A critical revelation of lithium ferromanganese phosphate (LMFP) performance in a Mn-rich cathode for Li-ion batteries using Fe equivalents to occupy a Mn site. Journal of Materials Chemistry C, 12(14), 4961–4976. https://doi.org/10.1039/d4tc00049h

Yao, Y., Zhu, M., Zhao, Z., Tong, B., Fan, Y., & Hua, Z. (2018). Hydrometallurgical Processes for Recycling Spent Lithium-Ion Batteries: A Critical Review. ACS Sustainable Chemistry and Engineering, 6(11), 13611–13627. https://doi.org/10.1021/acssuschemeng.8b03545

Yoon, J., Kim, D., Um, J. H., Jeong, M., Oh, W., & Yoon, W. S. (2016). Effect of local structural changes on rate capability of LiNio.5Mn1.5O4-δ cathode material for lithium ion batteries. Journal of Alloys and Compounds, 686, 593–600. https://doi.org/10.1016/j.jallcom.2016.06.044

Yoon, S.-J., Park, K.-J., Lim, B.-B., Yoon, C. S., & Sun, Y.-K. (2015). Improved Performances of Li[Ni 0.65 Co 0.08 Mn 0.27 ]O 2 Cathode Material with Full Concentration Gradient for Lilon Batteries . Journal of The Electrochemical Society, 162(2), A3059–A3063. https://doi.org/10.1149/2.0101502jes

Yoon, T., Soon, J., Jin, T., Heon, J., & Oh, S. M. (2021). Dissolution of cathode – electrolyte interphase deposited on LiNi 0 . 5 Mn 1 . 5 O 4 for lithium-ion batteries. Journal of Power Sources, 503, 230051.

Younesi, R., Christiansen, A. S., Scipioni, R., Ngo, D.-T., Simonsen, S. B., Edström, K., Hjelm, J., & Norby, P. (2015). Analysis of the Interphase on Carbon Black Formed in High Voltage Batteries. Journal of The Electrochemical Society, 162(7), A1289–A1296. https://doi.org/10.1149/2.0761507jes

Yue, M., Azam, S., Zhang, N., Dahn, J. R., & Yang, C. (2024). Residual NMP and Its Impacts on Performance of Lithium-Ion Cells. Journal of The Electrochemical Society, 171(5), 050515. https://doi.org/10.1149/1945-7111/ad4396

Zeng, X., Li, M., Abd El-Hady, D., Alshitari, W., Al-Bogami, A. S., Lu, J., & Amine, K. (2019). Commercialization of Lithium Battery Technologies for Electric Vehicles. Advanced Energy Materials, 9(27), 1–25. https://doi.org/10.1002/aenm.201900161

Zeng, Z., Murugesan, V., Han, K. S., Jiang, X., Cao, Y., Xiao, L., Ai, X., Yang, H., Zhang, J. G., Sushko, M. L., & Liu, J. (2018). Non-flammable electrolytes with high salt-to-solvent ratios for Li-ion and Li-metal batteries. Nature Energy, 3(8), 674–681. https://doi.org/10.1038/s41560-018-0196-y

Zhang, B., Xu, S., Lu, Z., Zhang, Z., Chen, L., & Zhang, D. (2023). Na vacancies and Li doping synergistically constructed P2-type Na0.5Li0.1Ni0.2Mn0.7O2 as high-performance cathode material for sodium-ion batteries. Materials Letters, 350(April), 134870. https://doi.org/10.1016/j.matlet.2023.134870

Zhang, F., Zhou, X., Fu, X., Wang, C., Wang, B., Liang, W., Wang, P., Huang, J., & Li, S. (2021). Which is the winner between the single-crystalline and polycrystalline LiNio.80Coo.15Alo.05O2 cathode in the lithium-ion battery? Materials Today Energy, 22, 100873. https://doi.org/10.1016/j.mtener.2021.100873

Zhang, J. N., Li, Q., Wang, Y., Zheng, J., Yu, X., & Li, H. (2018). Dynamic evolution of cathode electrolyte interphase (CEI) on high voltage LiCoO2 cathode and its interaction with Li anode. Energy Storage Materials, 14(December 2017), 1–7. https://doi.org/10.1016/j.ensm.2018.02.016

Zhang, S., Deng, C., Fu, B. L., Yang, S. Y., & Ma, L. (2010). Synthetic optimization of spherical Li[Ni1/3Mn1/3Co1/3]O2 prepared by a carbonate co-precipitation method. Powder Technology, 198(3), 373–380. https://doi.org/10.1016/j.powtec.2009.12.002

Zhang, X., Li, L., Fan, E., Xue, Q., Bian, Y., Wu, F., & Chen, R. (2018). Toward sustainable and systematic recycling of spent rechargeable batteries. Chemical Society Reviews, 47(19), 7239–7302. https://doi.org/10.1039/c8cs00297e

Zhang, Y., Liu, J., Xu, W., Lu, Y., Ma, H., Cheng, F., & Chen, J. (2022). Gradient doping Mg and AI to stabilize Ni-rich cathode materials for rechargeable lithium-ion batteries. Journal of Power Sources, 535(January), 231445. https://doi.org/10.1016/j.jpowsour.2022.231445

Zhao, D., Song, S., Ye, X., Wang, P., Wang, J., Wei, Y., Li, C., Mao, L., Zhang, H., & Li, S. (2019). New insight into the mechanism of LiPO2F2 on the interface of high-voltage cathode LiNi0.5Mn1.5O4 with truncated octahedral structure. Applied Surface Science, 491(May), 595–606. https://doi.org/10.1016/j.apsusc.2019.06.146

Zheng, Q., Yamada, Y., Shang, R., Ko, S., Lee, Y. Y., Kim, K., Nakamura, E., & Yamada, A. (2020). A cyclic phosphate-based battery electrolyte for high voltage and safe operation. Nature Energy, 5(4), 291–298. https://doi.org/10.1038/s41560-020-0567-z

Zhong, G. B., Wang, Y. Y., Yu, Y. Q., & Chen, C. H. (2012). Electrochemical investigations of the LiNi 0.45M 0.10Mn 1.45O 4 (M = Fe, Co, Cr) 5 v cathode materials for lithium ion batteries. Journal of Power Sources, 205, 385–393. https://doi.org/10.1016/j.jpowsour.2011.12.037

Zhou, W., Apkarian, R., Wang, Z. L., & Joy, D. (2007). Fundamentals of scanning electron microscopy (SEM). Scanning Microscopy for Nanotechnology: Techniques and Applications, 1–40. https://doi.org/10.1007/978-0-387-39620-0\_1

Zhu, W., Liu, D., Trottier, J., Gagnon, C., Guerfi, A., Julien, C. M., Mauger, A., & Zaghib, K. (2014). Comparative studies of the phase evolution in M-doped LixMn 1.5Ni0.5O4 (M = Co, Al, Cu and Mg) by in-situ X-ray diffraction. Journal of Power Sources, 264, 290–298. https://doi.org/10.1016/j.jpowsour.2014.03.122

Zou, F., Cui, Z., Nallan, H. C., Ekerdt, J. G., & Manthiram, A. (2021). Long-Term Cycling of a Mn-Rich High-Voltage Spinel Cathode by Stabilizing the Surface with a Small Dose of Iron. ACS Applied Energy Materials, 4(11), 13297–13306. https://doi.org/10.1021/acsaem.1c02903

Zou, Z., Xu, H., Zhang, H., Tang, Y., & Cui, G. (2020). Electrolyte Therapy for Improving the Performance of LiNi0.5Mn1.5O4 Cathodes Assembled Lithium-Ion Batteries. ACS Applied Materials and Interfaces, 12(19), 21368–21385. https://doi.org/10.1021/acsami.0c02516